The University Of Sheffield.

The Effect of Changing Particle Size Distribution and Layer Thickness on the Density of Parts Manufactured Using the Laser Powder Bed Fusion Process

By:

Abdullah Yahia M Alfaify

Thesis submitted in partial fulfilment of the requirements for the degree of "Doctor of Philosophy"

The University of Sheffield
Advanced Manufacturing Research Centre

March 2019

ABSTRACT

Powder Bed Fusion (PBF) is a metal additive manufacturing process where parts, described using a CAD data file, are fabricated layer by layer by melting metal powder. Selection of the ideal process parameters for the pulsed laser powder bed fusion (L-PBF) processes is of paramount importance, as there are a vast amount of parameters that have a direct impact on an eventual quality of fabricated parts. The aim of the present study is to present a systematic method of optimising the selection of the process parameters. The research comprehensively investigates the effect on final part density of changing (i) the particle size distribution of the primary powder, (ii) the layer thickness and (iii) the location of the fabricated part on the build platform. All these should help the prediction of the density/porosity of the parts and control their density for their desired applications.

In previous studies, volumetric energy density (VED) or scan speed have been used as the control variables for selecting the appropriate applied energy. The VED is not always completely accurate and able to identify the optimum energy that leads to fully dense parts. Consequently it should be used more as a guideline for finding the region in which to operate. A similar value of VED can be obtained using various combinations of laser power, scan speed and layer thickness. However, some values of scan speed, for instance, are not able to produce sufficient melt. To produce components with acceptable mechanical performance requires a comprehensive understanding of process parameters and their interactions.

In this work, the process parameters (layer thickness (LT), laser power (LP), point distance (PD), exposure time (ET) and hatching distance (HD)) were considered and studied comprehensively, and individually, to provide a better understanding of the effects of each process parameter on the final built part. Titanium alloy Ti-6Al-4V ELI and 316L Stainless Steel are used throughout this research. The Taguchi experimental design method and the Response Surface Method (RSM) were used to determine and optimise the effect of the selected input parameters, and also to investigate the impact of changing critical parameters on the density of parts manufactured. The influence on the part density was selected as the output to be measured to identify the most statistically

significant parameters. This was then followed up by in-depth studies focusing on individual parameters.

The results show the ideal combinations of process parameters which can provide fully or near fully dense parts. These process parameter combinations are used to fabricate samples at different layer thicknesses and from a different range of particle size distributions. The effect of changing the layer thickness and particle size distribution was then investigated. It was found possible to fabricate parts with relative density above 99% for layer thickness ranges from 30µm up to 100µm, with appropriate tuning of the process parameters. A clear correlation between the number and shape of pores and the process parameters was identified. Generally, large and irregular pores are usually a result of the lack-of-fusion process due to inadequate melt energy being applied, which can be a result of large PD, HD and LT or short ET. The small and circular pores are mainly due to a result of exaggerated overlapping in HD, PD or elongated ET. These relations are not only due to the effect of the individual process parameter (e.g. PD, HD etc.), but also the interactions between process parameters themselves. These were also found to critically affect the porosity. Then, the study develops regression models and verifies them experimentally. The proposed models were validated and used to accurately predict part density.

Finally, a first-of-its-kind study about build location effect was conducted. This shows that part location has a significant impact on sample quality. Potential reasons for the effect of build location are discussed. Spatter was found to be the major factor that causes a variation of the density of parts built in different locations on the platform. The best build location for both materials was found to be close to the inlet of the gas flow. This position minimises the influence of spatter. The study provides a deeper understanding of the variation of the density of a part built in different locations on the build platform and the effect of that on reproducibility. The study also raises awareness about building in angled orientations.

The results from this research offer a valuable understanding of ways to optimise the selection of processing parameters, for fabricating parts using PBF with high density/low porosity. It leads to a better understanding of concerns which need to be taken into account for optimal operation. The focus is not restricted to the process parameters of the PBF machine and the PSD of the primary powder used, but also

highlights the significance of ensuring correct part orientation/location as all these parameters influence the part density of the fabricated part.

ACKNOWLEDGEMENTS

First and foremost, I would like to thank my supervisor, Professor Keith Ridgway, for providing me the opportunity to work with him, for his constructive insightful suggestions, and his continuous guidance throughout my journey. His support has made the journey significantly easier and allowed me to reach this stage of completion. His supervision and guidance has helped me drastically both professionally and personally in my life. Also, I would like to express my gratitude to my co-supervisor, Dr James Hughes for his valuable guidance and support throughout my PhD research journey.

I am thankful for the financial support of my government, Kingdom of Saudi Arabia, and for giving me the opportunity to study and live in UK.

Special thanks go to Chris Ridgway for her generous support, in administrative, logistic and family support. She has been a constant support for me and my family, especially during the health problem of my son. She waved out so much stress and her warm words and support are unforgettable.

In addition to this, I would like to acknowledge the support from all the technical and administrative staff at the AMRC who helped me throughout my journey. Their support is highly appreciated and gratefully acknowledged. Special thanks to people at NAMTEC and DPG for their technical support. At NAMTEC, I would like to thank Dr Adrian Sharman for his help in powder characterisation, Dr Kristina Parry for teaching me how to use Pycnometer for density measurement, Holger Krain for micrographic imaging, and Dr Syed Islam for his informative guidance during the writing stage. At DPG, I would like to thank and acknowledge the support from Abdul Haque for technical help on the Renishaw AM machine and Lee Moore for providing me with great technical support and tools during my work at the workshop. I would like to extend my gratitude to my dear friends at the AMRC for their love and support throughout the whole journey. I am sincerely grateful for the opportunity to complete my PhD at the AMRC with great people, great facilities and campus, perfect integration with all AMRC groups and professional dealing.

I would also thank relatives and friends for their encouraging words and continuous support throughout my time in the UK.

I want to express my deepest appreciation to my parents and siblings who have always given their instrumental support and patience while I have been away from them. Their love has and will always be with me.

Last and most importantly, I would like to thank my beloved wife, Bashaer, for her faithful and spiritual support, encouraging words, timely support, the patience she had when difficult moments were present and for all the sacrifices she has made for me.

LIST OF PUBLICATIONS

[1] A. Y. Alfaify, J. Hughes, and K. Ridgway, “Critical evaluation of the pulsed selective laser melting process when fabricating Ti64 parts using a range of particle size distributions,” Additive Manufacturing, vol. 19, pp. 197–204, 2018.

[2] A. Y. Alfaify, J. Hughes, and K. Ridgway, “Controlling the Porosity of 316L Stainless Steel Parts Manufactured via the Powder Bed Fusion Process,” Rapid Prototyping Journal, vol. 25 (1), pp. 162-175, 2019.

TABLE OF CONTENTS

LIST OF FIGURES

LIST OF TABLES

NOMENCLATURE

AM	Additive Manufacturing
BBD	Box-Behnken Design
CAD	Computer Aided Design
CCD	Central Composite Design
CI	Confidence Interval
D_{10}	Volume-based Size which 10% of the Particle Size Distribution lies below
D_{50}	Volume-based Size which 50% of the Particle Size Distribution lies below
D_{90}	Volume-based Size which 90% of the Particle Size Distribution lies below
DOE	Design of Experiments
ELI	Extra Low Interstitials
ET	Exposure Time (s)
HD	Hatching Distance (mm)
LP	Laser Power (W)
L-PBF	Laser Powder Bed Fusion
LT	Layer Thickness (mm)
PBF	Powder Bed Fusion
PD	Point Distance (mm)
PI	Prediction Interval
PSD	Particle Size Distribution
RD	Relative Density (%)
RSM	Response Surface Methodology
SP	Laser Beam Spot Size (mm)
SS	Scan Speed (mm/s)
VED	Volumetric Energy Density (J/mm^3)

1. INTRODUCTION

1.1. Background

Metal Additive Manufacturing (AM) technologies have gained significant attention from both academia and industry over the last three decades. The capability of the technologies to shorten lead time, manufacture complex parts effortlessly, reduce waste and reduce the buy-to-fly ratio attracts many sectors such as aerospace, automotive and medical industries to adopt AM technologies. The Powder-Bed Fusion (PBF) process is superior at producing the complex designs among all other AM technologies ([1]; [2]). However, predicting and understanding the mechanical properties of additively manufactured parts is yet to be fully established. Governing the density of parts enables greater control and prediction of other mechanical properties which are directly influenced by the amount of porosity and the shape and distribution of porosity throughout the part. Ultimate tensile strength, elongation, hardness and fatigue are all influenced by the amount, shape and distribution of porosity. The particular challenge in PBF is selecting appropriate process parameters values for producing defective-free parts [3] and finding their correct correlation with the porosity [4]. Thus, the primary focus of this study was to investigate the density of parts fabricated using the PBF process and how the density is influenced by changing certain process and operational parameters. Certain applications require full density parts to avoid failure, such as aerospace components, while porous or controlled porosity parts are acceptable and even desirable in other applications such as medical implants, where controlled porosity implants are required for better osseointegration with human bone.

Factors that influence the quality of fabricated parts and their densities in the PBF process are classified into two main categories: process parameters and powder properties. The main process parameters can be combined and expressed as volumetric energy density (VED). The VED can be defined as the energy used to melt a unit volume of powder. There are, however, other process parameters which are not included in VED calculation even though they have a direct and significant influence on the process. For instance, working temperature, chamber pressure and surrounding gas type. Metal powder characterisation such as the size, shape and distribution of powder particles can also lead to different part quality.

1.2. Identifying Issues

Despite the exponential growth in adopting metal additive manufacturing technologies in end-user applications, a lack of confidence in the quality of parts has hindered many manufacturers from adopting them. For instance, there is still a need to understand the relationships between metal powder properties, such as particle size distribution, and the process parameters of the PBF process. A vast amount of research has and is being carried out to develop a better understanding of process parameter optimisation. However, minimal work has been conducted to investigate the effect of changing powder characteristics with process parameters on the density/porosity of fabricated parts. Thus the effect on the porosity of fabricated parts when material, powder particle size distribution (PSD), layer thickness and energy input are changed also needs to be established. The main experimental research investigations rely on trial and error methods, which are costly and time consuming. Using statistical methods for process optimisation is crucial to evaluate the applicability of AM on new materials in a methodical and efficient manner.

The review of previous work confirms that this is the first systematic research programme that uses the design of experiment (DOE) methods to investigate the effect of process parameters of the PBF process using a pulsed (modulated/discontinuous) laser on the density of Ti-6Al-4V and 316L alloys. In pulsed Laser PBF (L-PBF) systems, scan speed can be obtained by varying the exposure time and point distance [5]. Density (porosity) is the quality that was investigated with varying process parameters of layer thickness, laser power, point distance, exposure time and hatching distance for a range of particle size distribution (PSD) powders.

1.3. Aims and Objectives

The main objective of this research is to investigate the influence of changing layer thickness (LT) for a range of particle size distributions (PSD) of Ti-6Al-4V ELI and 316L-SS powders on fabricating fully or near fully dense parts using the Laser Powder Bed Fusion (L-PBF) process. The energy density applied to the powder bed will be controlled by varying the process parameters.

The following steps (milestones) are set to achieve this research objective:

- Optimise the process parameters for each metal material to develop the optimum process parameter combinations to obtain fully dense parts.

- Fabricate parts using process parameters found in the optimisation phase for different particles size distributions (PSD) and layer thicknesses (LT) for a range of energy densities.

- Discover the correlation between process parameters and metal powder property.

- Develop a process parameter selection models and correlation equation for each material, PSD powder and LT. These models should aid practitioners for selecting the correct process parameter combinations according to metal material properties and powder characterisation.

1.4. Main Contributions (Findings)

This work addressed the main the effects of changing the particle size distribution, layer thickness and melt energy on fabricated parts. It demonstrated the influence of process parameters differs according to the properties of the processing material. The effect of process parameters on shape and size of the pores were studied intensively for Stainless Steel (316L-SS). The correlation between the resulting density and the material properties were also addressed for each particle size distribution and layer thickness. Part relative density of greater than or equal to 99% has been achieved for all particle size distributions and layer thicknesses for both materials (Ti-6Al-4V ELI and 316L-SS). Finally, the first study of the impacts of build location on the platform was conducted. This resulted in a greater understanding and justification of the reasons for the variation of density of fabricated parts located at different positions on the build platform.

1.5. Research Outline

Following the introduction given in this chapter (Chapter 1), the literature review is presented in Chapter 2. The review is subdivided into sections. The first section gives a fundamental description about additive manufacturing and its available technologies. The next section focuses on metal additive manufacturing and on the materials used throughout this study and their applications. The third section provides a detailed review

of previous work concerning process parameters studies and their effect on the fabricated parts.

Each of the process parameters considered are reviewed in a subsection with the final subsection giving a review of using volumetric energy density as an indicator to study the effect of the process parameters on a fabricated part. In section four, a detailed review of the porosity and its main types are discussed. Also, the desire and benefits of having porous structures for some application is reviewed. The effect of changing particle size distribution and layer thickness on part porosity is reviewed in section five. The final section summarises the literature review and develops a research hypothesis.

Chapter 3 describes the materials used and methods followed in this study. It starts with a section on the material characterisation followed by a section which describes the laser powder bed fusion system used to carry out the experimental work. In section 3, a detailed description of the Design of Experiment methods is presented. The steps taken to fabricate the samples are illustrated in section four. Finally, section five describes evaluation method of the powder bed fused samples.

The results of the process parameter optimisation are presented in Chapter 4. The chapter also provides a detailed investigation of the effect of process parameters on the part density at a micro level. The chapter ends with a comprehensive discussion about process parameter optimisation and the influence on the density of the fabricated part.

In Chapter 5, the results of regression analysis are presented. The regression models are shown to successfully predict the density of parts with a high acceptable level of accuracy. Then, a correlation model for each particle size distribution powder and layer thickness are developed and studied. An extensive discussion is conducted which shows the impact of changing the particle size distribution and/or the layer thickness on the resultant density.

Chapter 6 presents the analysis of the build location for the all builds conducted throughout this research. The results reveal the paramount importance of the build location on the build platform. A detailed discussion is presented at the end of the chapter. Some possible reasons that may contribute to the variation of the parts built in different locations are discussed in detail and linked to the literature.

Finally conclusion and recommendations for the future work are presented in Chapter 7 and Chapter 8, respectively.

2. LITERATURE REVIEW

2.1. Additive Manufacturing: Overview

Additive manufacturing (AM) has been an interesting topic for academia and industry for about three decades. Dramatic advancements in the technology have been made over that period, and now we are at a stage with the technology in which if you can imagine the item, you can most likely print it. Additive manufacturing is also known as Additive Fabrication, Additive Processes, Additive Techniques, Additive Layer Manufacturing, Layer Manufacturing, Rapid Prototyping, Rapid Manufacturing, 3D Printing, and Freeform Fabrication. According to the standard ISO/ASTM 52900:2015(E) [6], Additive Manufacture is defined as:

> *"A process of joining materials to make parts from 3D model data, usually layer upon layer, as opposed to subtractive manufacturing and formative manufacturing methodologies."*

It can be divided into different systems according to the materials that are used in AM fabrication such as polymer, metal and ceramic or according to the form of raw materials such as solid-based, liquid-based or powder-based system ([1]; [7]). In metal AM, material has two forms which are solid (wire and sheet) and powder. The technologies used with latter form of raw material can be powder-bed or powder-feed. The AM is classified into seven process categories: Binder Jetting, Direct Energy Deposition, Material Extrusion, Material Jetting, Powder Bed Fusion, Sheet Lamination and Vat Polymerisation. Table 2-1 shows the definition of each AM process category and some examples for the current technologies.

Table 2-1: Definition and examples for the current technologies of each AM process category [6]

AM Process Category	*Definition*	*Examples for Technologies*
Binder Jetting	Additive manufacturing process in which a liquid bonding agent is selectively deposited to join powder materials.	Binder Jetting (BJ)
Direct Energy Deposition	Additive manufacturing process in which focused thermal energy is used to fuse materials by melting as they are being deposited.	Laser Engineering Net Shaping (LENS); Laser Metal Deposition (LMD)
Material Extrusion	Additive manufacturing process in which material is selectively dispensed through a nozzle or orifice.	Fused Deposition Modelling (FDM) or Fused Filament Fabrication (FFF)
Material Jetting	Additive manufacturing process in which droplets of build material are selectively deposited.	Material Jetting (MJ); Drop on Demand (DoD)
Powder Bed Fusion	Additive manufacturing process in which thermal energy selectively fuses regions of a powder bed.	Selective Laser Sintering (SLS); Selective Laser Melting (SLM); Direct Metal Laser Sintering (DMLS); Electron Beam Melting (EBM)
Sheet Lamination	Additive manufacturing process in which sheets of material are bonded to form a part.	Laminated Object Manufacturing (LOM); Ultrasonic Additive Manufacturing (UAM)
Vat Polymerisation	Additive manufacturing process in which liquid photopolymer in a vat is selectively cured by light-activated polymerization.	Stereolithography (SLA); Direct Light Processing (DLP)

The history of producing a 3 Dimensional (3D) part in a layer manner goes back to the beginning of the 20th century (1902). Peacock patented the idea of making horseshoes using a metal lamination method under the name of "method of making composition horseshoes". The idea of a powder bed fusion machine was invented by Ross

Housholder in 1979 and he obtained a patent for the technology in 1981 which is known as the moulding process for forming a three-dimensional object [8]. The casting material and the mould material are deposited in layers. Then selective solidification for the casting material can be achieved by a source of heat with selected mask or by using a controlled heat scanning process. In this process, sand can be used as the mould material to support the casting material. However, a printer that makes 3D objects from a CAD model was invented by Charles Hall in 1984 and patent for the technology was granted in 1986 under name Stereo Lithography. A year later, the first ever commercialised system in the world was introduced in 1987, which was a SLA 3D System [9]. The powder bed fusion machine that fabricates a part from CAD model using plastic, metal, ceramic or polymer materials was patented by Carl R. Deckard in 1989 [10] and 1990 [11]. During the last 30 years, numerous AM systems, applications, materials and software's have been introduced to meet growing worldwide demand. It took 20 years for the global market to reach one billion dollar. The second billion dollar market valuation was reached within the next 5 years. However, within the next 3 years, specifically in 2016, the global market of AM technology was six billion dollars. It is estimated that the global market of AM will reach 26 billion dollars by 2022 (Wohlers Associates, Inc. 2017).

2.1.1. Metal Powder Bed Fusion

The Metal Powder Bed Fusion (PBF) process is used to fabricate metal parts directly from metal powder by joining layers of powder. There are three main steps in metal PBF: (1) spreading the powder as a layer, (2) selectively melting the powder according to a CAD file and (3) lowering the platform. These steps are repeated until the part is completely built. The sources of melting energy are Electron or Laser beams. There are different systems classified under the technologies of energy source, fabrication process, and the form of raw materials are listed in the work of Frazier [12] and Herderick [13].

At present Electron Beam Melting technology (EBM) is substantially quicker in fabricating a part in comparison to laser powder bed fusion (L-PBF) technologies but with reduced accuracy and surface quality [13]. Even though EBM has unique characteristics and advantages, especially compared with wrought processes, it still has some challenges in relation to the process stability and producing quality parts

consistently. Also, the EBM is a complicated process at elevated temperatures, which requires deep a understanding to model and simulate and improve its performance and obtain consistent part quality [14]. On the other hand, laser technologies such as selective laser sintering (SLS), direct metal laser sintering (DMLS) and selective laser melting (SLM) are superior where building finer details or small features is important. Technically, as electrons are affected by the atoms of surrounding gas, it is therefore necessary for builds to be conducted under vacuum to avoid the deflection of the beam, whereas for the laser system, it can pass through a transparent gas without being affected and therefore does not require a vacuum. The Electron beam is guided by a magnetic coil therefore the beam deflection is instantaneous. This is advantageous to the speed of scanning the powder layer. In contrast, the laser beam is directed by a Galvanometer therefore the scan speed is limited by the speed of the Galvanometer. The Electron beam process is limited to being used in conductive metals whereas laser can be used on a variety of materials. The main differences between the two EBM and L-PBF are summarised in Table 2-2.

Table 2-2: The key differences between EBM and L-PBF [1]

Characteristic	***Electron beam melting***	***Laser powder bed fusion***
Thermal source	Electron beam	Laser beam
Atmosphere	Vacuum	Inert gas
Scanning	Deflection coils	Galvanometers
Energy absorption	Conductivity-limited	Absorptivity-limited
Scan speeds	Very fast, magnetically-driven	Limited by galvanometer inertia
Energy costs	Moderate	High
Surface finish	Moderate to poor	Excellent to moderate
Feature resolution	Moderate	Excellent
Materials	Metals (conductors)	Polymers, metals and ceramics

2.1.2. Laser Powder Bed Fusion (L-PBF)

2.1.2.1. Laser Sources

Laser (Light Amplification by Stimulated Emission of Radiation) is classified according to the gain medium: gas, solid state, excimer, dye, fibre or semiconductor. It is constructed from three main parts: a pump energy source, a gain medium, and two or more mirrors that form an optical resonator. Lasers used in metal powder bed fusion systems are mainly of three types: gas (CO_2), Nd:YAG (solid state) and Yb-fibre (fibre).

A CO_2 laser consists of a discharge tube, electric pump source and optics (reflection mirror, output mirror and lenses). The CO_2 gain medium fills the discharge unit. The laser is stimulated by pumping the tube electrically to generate infrared with wavelength from 9.0 to 11.0μm.

The Nd:YAG laser (Neodymium-doped Yttrium Aluminium Garnet laser) solid-state laser is generated by optically pumping energy using a flash light such as Xenon or laser diode along the axis of the Nd:YAG rod to produce near infrared wavelength (1.064μm). The output coupling mirror passes the light beam which can be delivered by flexible optical fibre.

A rare-earth doped optical fibre is the gain medium for fibre laser. Due to the high quantum efficiency, Yb-Fibres are the most suitable of the rare-earth gain fibres. The Yb-fibre is pumped by laser diodes produce a near-infrared wavelength beam (1.03-1.07μm). The schematics of the three lasers are shown in Figure 2-1 [15].

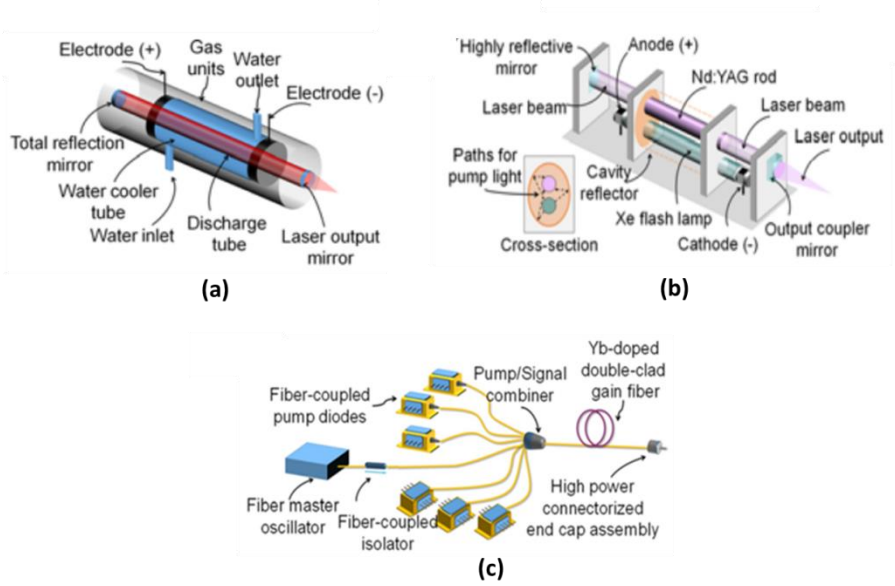

Figure 2-1: Schematics of laser components of a (a) CO_2 laser, (b) Nd:YAG laser, (c) Yd-fibre laser [15]

Of the three laser types used in the metal powder bed fusion process, the Nd; YAG and Yd-fibre laser are most commonly used due to their short wavelength which is more easily absorbed by powder particle compared to the CO_2 laser. The majority of the commercial powder bed fusion systems recently produced are equipped with the Yb-fibre laser as it is cheaper to repair and has a longer maintenance period [15].

2.1.2.2. Laser Powder Bed Fusion (L-PBF) Process

The main focus in this work is metal additive manufacturing using the Laser Powder Bed Fusion (L-PBF) processes. The research of fabricating metal parts using the L-PBF process was unsuccessful until the early 1990s. The characteristics of metal (such as high thermal conductivity, tendency to oxidise, low beam absorptivity) compared to polymer made the fabrication processes significantly more difficult. The powder absorptivity was improved by using a Ytterbium fibre laser which has a wavelength of 1.06µm while the CO_2 laser has a wavelength of 10µm [1]. This resulted in full melt for the metal powder particles and more efficient scanning over the powder layer. SLM is an advanced process from the SLS [16], where the powder particles are completely melted instead of partially melted (sinter). The main concept of laser powder bed fusion processes is the same. In an inert atmosphere in which the Oxygen level is near to zero, a thin layer of the metal powder is spread using a roller or raking mechanisms. Then, a

guided laser beam melts the cross-sectional area according to the CAD file definition. Finally the build platform is lowered by distance representing the layer thickness. The steps are repeated until the part is completed. Figure 2-2 shows a schematic of the laser powder bed fusion machine.

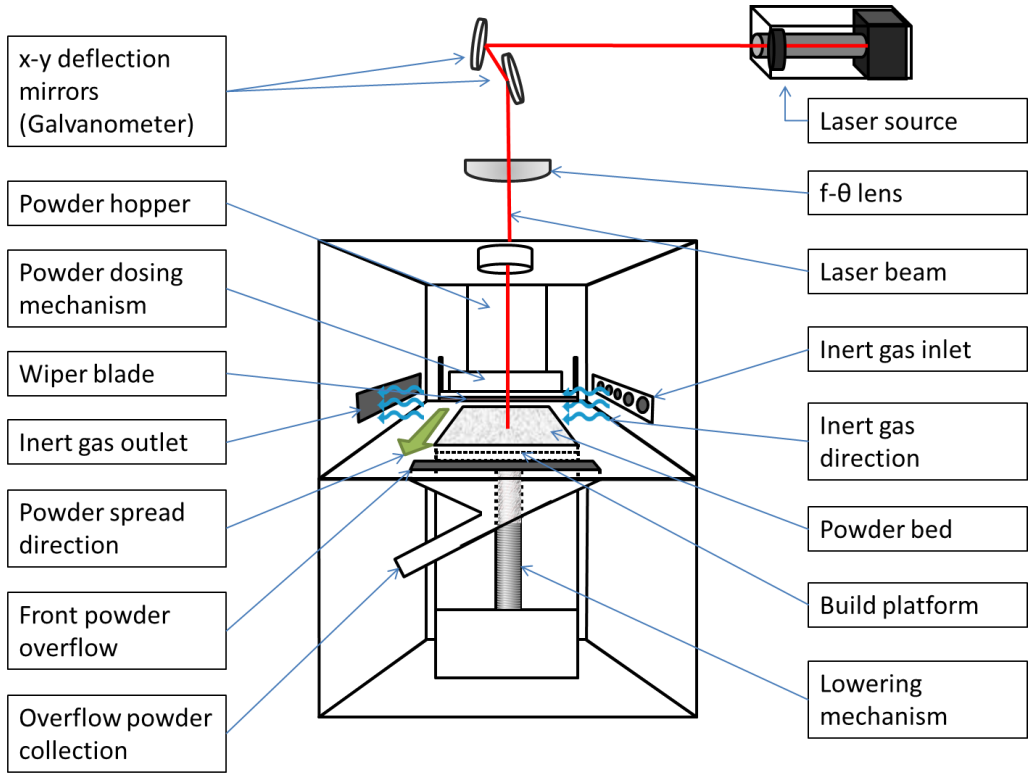

Figure 2-2: Schematic of laser powder bed fusion machine showing the main process components

2.2. Metal Additive Manufacturing Alloys

The number of metal materials available for AM is growing impressively each year. Frazier [12] mentioned a range of alloys that are commercially used in AM processing. They were grouped according to the based material such as Titanium based, Aluminium based, Tool Steels, Nickel based, Stainless Steel and refractory alloys. Also there are Copper based alloys, Cobalt based alloys and precious metal alloys [17]. Under each of these groups there is a list of alloys. The AM alloys need intensive investigation of process parameters to verify that they are suitable and provide a stable process. A brief review of the history and application of the materials used in this research is in the following subsections.

2.2.1. Titanium Alloys: History, Applications and Powder Bed Fusion Fabrication

The Titanium element was first discovered by William George in 1790, in Cornwall, United Kingdom, and published in 1791. The element was later named by German chemist Heinrich Klaporth "Titanium", in 1795 [18]. The extraction of Titanium was costly process until recently. In 1948, Titanium was produced commercially for the first time. Nowadays, there are tens of Titanium alloys which have been developed. They are classified according to the nominal compositions [19]. Titanium alloys have excellent corrosion resistance and high strength to weight ratio so that it is preferable candidate in many applications to replace Steel, Aluminium and Nickle alloys. While there are more than 100 Titanium alloys, Ti-6Al-4V alloy is the most popular of the titanium alloys used. It is a common material that has been used in many applications for decades due to its lightweight and corrosion resistance properties. It dominates more than 50% of the usage of the Titanium, the majority in aerospace industries [20]. For instance, Ti-6Al-4V is used in airframe structures, fan discs and blades, and compressor disc, blades and stators [21]. In the automotive industry, Ti-6Al-4V is a good replacement for the steel in the body, outlet valves, intake valves, turbochargers and connection rods [21]. In biological usage, the first discovery of the potential use of Titanium alloy in medical applications was in 1965 by a Swedish doctor named Per-Ingvar Brånemark. After years of research on animals and analysing the results, Brånemark presented the findings in 1982 which showed that Titanium is a feasible material that can be used in the medical sector and implemented in the human body [22]. Nowadays, Ti-6Al-4V is the most popular medical material used in medical implants, dentistry, surgical tools, fixation, joint replacement, skull repair and others.

While a large number of metallic materials have been fabricated using AM technologies, Ti-6Al-4V has received major attention due to its wide variety of industrial applications. Ti-6Al-4V ELI is a higher purity version of the Ti-6Al-4V. ELI is a short term of Extra Low Interstitials, where the level of oxygen, nitrogen and carbon is carefully controlled (reduced). This improves the ductility and fracture toughness and therefore workability [19]. This also makes the alloy more suitable for the dental and medical applications (Arcam: Ti6Al4V ELI Titanium Alloy).

2.2.1.1. Titanium Crystal Stracutre

Titanium is a polymorphous material for which there are two different crystal structures. There is the hexagonal close packed (HCP) crystal structure which is referred to as the α-phase, and the body centred cubic (BCC) crystal structure which is referred to as the β-phase (Figure 2-3). The transformation occurs at 882°C, above which the BCC structure exists, and below this the HCP exists [23].

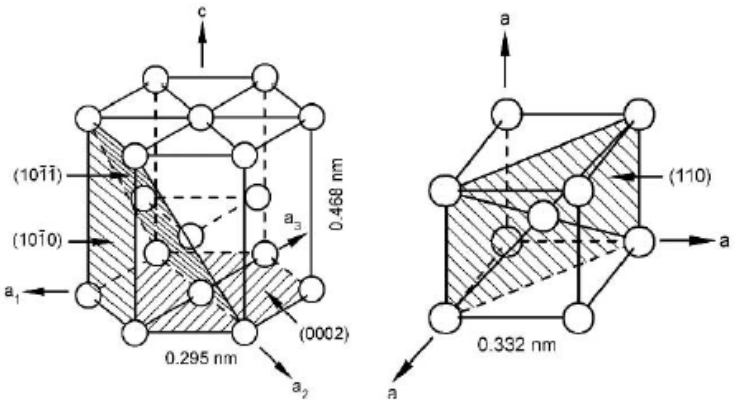

Figure 2-3: Hexagonal close packed (HCP) crystal structure, and body centred cubic (BCC) [23]

The alloys of titanium are classified according to the stabilizing additive used and its effect on increasing or decreasing the α/β transformation temperature. The different stabilising elements along with the phase they stabilise are shown in Figure 2-4. As titanium alloys are cooled relatively slowly, from the β phase region into the α + β region, the α phase begins to nucleate on the β grain boundaries. The microstructure is termed as lamellar α + β, for which an example of Ti-6AL-4V can be seen in Figure 2-5.

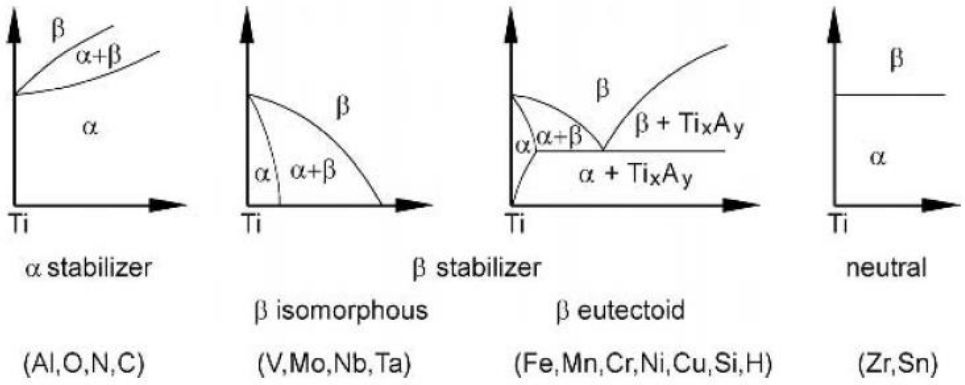

Figure 2-4: Different alloying elements and the corresponding phase diagrams for titanium [23]

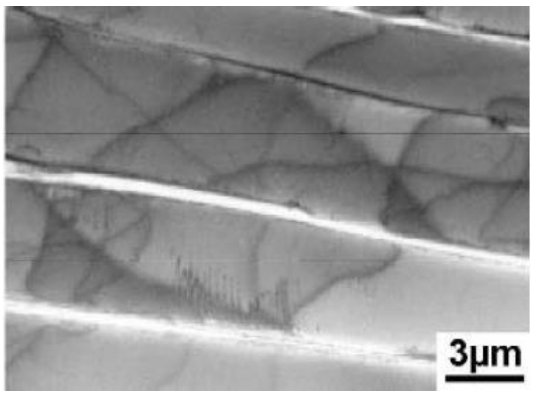

Figure 2-5: TEM showing the boundary layer between the β phase and the corresponding α phase growth [23]

Ti-6Al-4V is one of the most popular titanium alloys used globally, with currently half of the titanium products being made with this particular alloy [24]. During the L-PBF process, the vast fluctuations in heating and cooling during the fabrication of layers affect the microstructure of the part, which is not homogenous. This is due to the thermal history experienced by the layers. Generally, parts fabricated using Ti-6Al-4V via L-PBF show elongated β grain boundaries that are filled with α martensitic laths [25]. This presence of α martensitic is due to the rapid cooling which occurs during the SLM process for each layer. During the process laser melts the powder to create a melt pool, which than rapidly cools and solidifies [26]. The rotational change of each layer also plays a part, with a clear difference seen between from 67° to 90° [26]. One of the main desirable features to be controlled in L-PBF is the potential to manipulate the microstructure throughout the building process towards the desired phases and grain sizes.

2.2.2. Stainless Steel Alloys: History, Applications and Powder Bed Fusion Fabrication

Stainless Steel alloys mainly contains low amount of Carbon (0.03-0.1%) and 11-30 % of Chromium [27]. There are three main families of Stainless Steel alloys. These are classified according to the amount of Chromium they contain: Ferritic Stainless Steel (Cr 10.5-29%), Austenitic Stainless Steel (at least 16%) and Martensitic Stainless Steel (up to 16%). Other elements such as Nickel, Carbon, molybdenum, Titanium and Copper are added in different proportions to modify the physical and mechanical properties [28]. For instance, Duplex Stainless Steel is a family of Stainless Steel which

has an increased amount of Nickle 1.4-7% and Chromium 20.1-25.4%. The result is a family which has mixed microstructures between Ferritic and Austenitic [29]. Steel has a long history of use in the past (thousands years), Stainless Steel alloys, however, has been known and commercially developed only since the early 1900s. The alloy was originally discovered and developed in Germany and England in approximately 1910. Between 1910-1915, Harry Brearley, Sheffield, England, studied the industrial uses and applications of Stainless Steel. The alloys were commercially produced later in the US in 1945. Since then the production technologies and capacity have been improved to meet the demand which has increased over the years ([27]; [30]). In 2017, The production of the Stainless Steel alloys was around 48.1 million metric tons worldwide [31].

The usage of Stainless Steel in manufacturing continuously increases. It ranges from small products up to nuclear reactors and buildings. Stainless Steel has good corrosion resistance, machinability, and wide range of strength and stability characteristics at cryogenic and elevated temperatures. Stainless Steel is the third most commonly used material after Aluminium and Steel [32]. The applications of Stainless Steel are countless ranging from consumer products such as kitchen equipment, utensils, sinks, dishwasher, washing machines and others, to industrial equipment such as nuclear, chemical and oil industries, transportation, building and construction, energy production and medical uses ([33]; [34]).

Stainless Steel was found to be a good candidate alloy to be fabricated by the AM process. The PBF process have been successfully used to fabricate different Ferrous-based alloys; 316L Stainless Steel being one of them [35]. For instance, Zhong et al. [36] investigated fabricating International Thermonuclear Experimental Reactor (ITER) In-Vessel components from 316L-SS powder using the PBF process. Their results showed that the mechanical properties of the 316L-SS PBFed parts fulfilled the required criteria of the ITER at room and elevated temperatures. Even the cellular structure and its effect on the mechanical properties needs to be understood in details, the feasibility of using the alloy and the PBF process is viable alternative.

2.2.2.1. Stainless Steel Crystal Stracutre

Steel is an alloy based on iron and carbon, with other alloying elements present too (e.g. Si, Mn, P, S, and Cr etc.). As the carbon content increases, the Ultimate Tensile Strength also increases, however, the Toughness decreases. When chromium is added to approximately 12wt %, the corrosion resistance is now present and the alloy is termed stainless steel. For 316L stainless steel, the chromium content is 18% and Nickel is 10%, placing the structure in the austenitic region (Figure 2-6). 316L is often preferred for its relatively low cost.

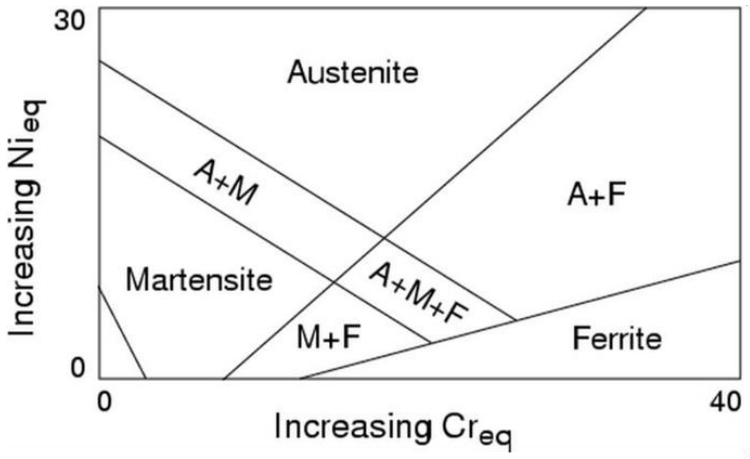

Figure 2-6: Stainless steel microstructure diagram [37]

Research has been conducted by Liverani et al. [38] which shows generally that 316L-SS parts fabricated using L-PBF result in the presence of a FCC austenite phase. This was confirmed using XRD measurements. The effect of orientation was further investigated and was shown to affect the relative intensity of austenite peaks. The orientation of the build (45° and 90°) was shown to influence the preferred crystal orientation plane [38]. A distinct complex columnar structure would form, which has been ascribed to the vast temperature gradients present during the solidification process (as the laser beam moves away from the melt pool after melting the powder) [39]. The presence of microstructure formation can be seen in Figure 2-7.

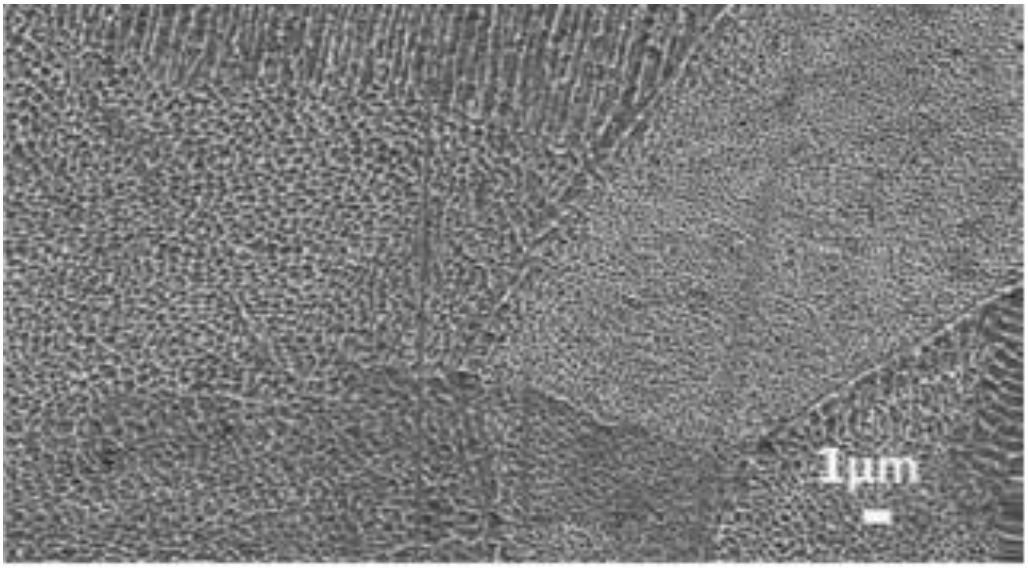

Figure 2-7: The presence of fine columnar microstructure [39]

2.2.3. Characteristics of Metal Powder

Powder-bed fused parts are strongly influenced by the powder characteristics as shown in several articles such as [40];[41]. A narrow powder Particle Size Distribution (PSD) has the advantage of improving powder flowability which is an essential characteristic in PDF systems that rely on gravity to feed the powder dose. However, flowability is not solely affected by the PSD and there are other factors which also contribute. Powder morphology is a key contributor towards powder flow with spherical particles having a higher tendency to flow better and faster than non-spherical and irregular particle shapes which tend to have poor flowability. PSD, flowability and morphology all impact on the packing density and depositing a homogenous powder layer during the process [41]. Powder particle size distribution (PSD) influences the packing density and powder flowability.

Using a narrow PSD improves the powder flowability, but decreases the packing density which impacts the final fabricated part density [42]. A wider range of powder distribution increases layer packing density, therefore, improves part density, but may result in poor flowability. The laser absorptivity by the powder improves with the presence of fine particles in a wide PSD powder. This was shown by the work of King et al. [43]. When a laser beam strikes a large particle, the majority of the beam is reflected causing poor absorption and less heat transfer. In contrast to this, the

absorptivity increased when the beam strikes a region with bulk small particles. King et al. [43] also showed that powder with bimodal distribution improved the absorptivity with all metal powder considered. This improvement was relatively different according to the material being process and where the laser strikes on powder layer (Figure 2-8).

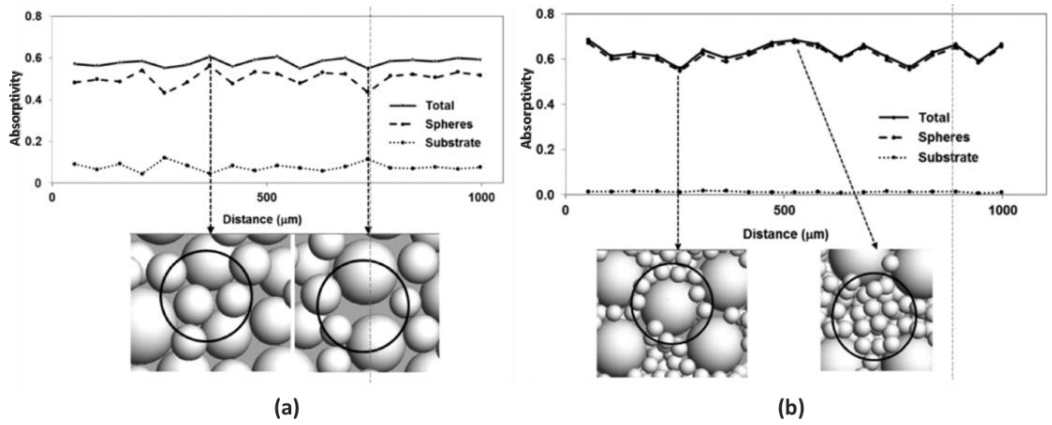

Figure 2-8: Absorptivity measured along laser path for stainless steel powder showing the effect of PSD on absorptivity (a) Gaussian distribution, (b) Bimodal distribution [43]

The morphology of powder particles depends on powder production methods. As spherical shape and a fraction of fine particles are highly preferable, the most common methods to manufacture PBF powder are gas and plasma atomised. Using these processes, the vast majority of the powder particles produced are more spherical in comparison to other methods such as water atomisation, are more productive and cheaper compared to other the plasma rotating electrode process (PREP).

In gas atomisation, molten alloy is introduced from a vacuum induction melting furnace or electrode induction melting gas atomisation and flows through a nozzle where high pressure gas shreds the stream of molten alloy into droplets. These droplets are collected through the bottom collection chamber. The particle size can be vary depending on the gas to melt flow rate [44].

The other common powder production process is plasma atomisation. In this process, a spool of wire or powder feedstock is fed into the atomisation chamber where it is melted and atomised by the plasma torches and gas jets [44]. Figure 2-9 shows the schematic for the both processes.

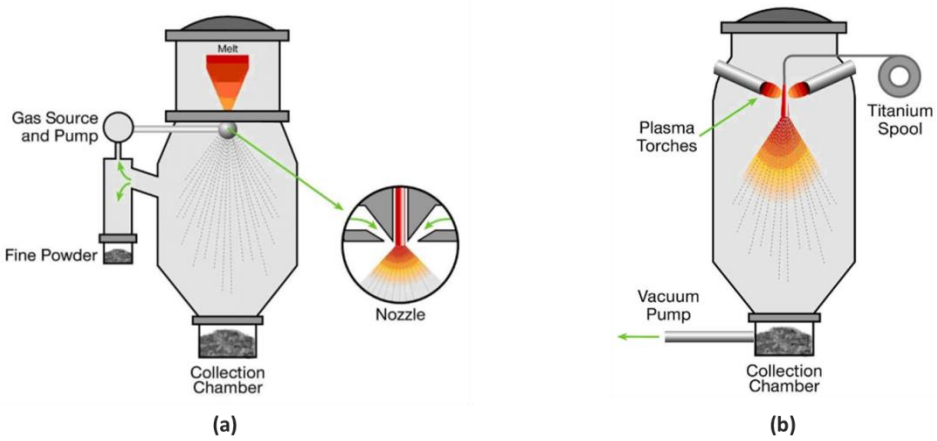

Figure 2-9: Schematics of common powder production processes: (a) gas atomisation process (b) plasma atomisation process [45]

Sutton et al. [41] summarised the main differences between gas and plasma atomisation systems as follows:

- The production rate for the gas atomisation method is higher in comparison to plasma atomisation.
- Both processes produce spherical particles. However, particles of the powder produced by plasma process are extremely spherical.
- The particle size distribution of the powder produced by gas atomisation has a wider range in comparison to plasma, 0-500µm vs 0-200µm respectively.
- The production cost of the plasma atomisation process is high compared to the gas atomisation.

2.3. Main Process Parameters of Laser Powder Bed Fusion

There are numerous processing parameters within the Laser PBF process. Some of these parameters are related to processing a part such as laser power and spot size, scan speed, scan pattern, layer thickness and hatching distance. Li et al. [46] optimised the process

parameters of PBF process for Ti-6Al-4V parts to improve the surface roughness. The main process parameters that were covered in their study were laser power, scan speed and hatching distance. Other parameters are related to the material being processed such as the physical properties and particle size and shape of the powder. The following subsections review some important process parameters which are considered to be the most critical process parameters commonly used to evaluate the energy density.

2.3.1. Laser Power

Laser power (LP) is the main process parameter in the powder bed fusion process. The other process parameters can be tuned according to the laser power and beam characteristics. Other process parameters such as scan speed, hatching distance and layer thickness rely on the characteristics of the laser beam. For instance, scan speed is limited by the availability of laser power (it is possible to increase the scan speed with increased laser power) and hatching distance is limited by the laser beam spot size [47]. Also, layer thickness is restricted by the ability of laser beam to penetrate into the powder bed. Previous studies have investigated the influence of the laser power on part density. Buchbinder et al. [47] investigated the effect of laser power on the part density of AlSi10Mg alloy. They found that increased laser power led to higher density even with a high scan speed. This suggests the increased laser power enhances the build rate (using laser power of 1kW instead of the current power 200-400W increases the build rate by a factor of 4 times, from 5mm^3/s to 21mm^3/s). However, fabricating Aluminium parts requires high laser power for the powder bed fusion process due to the high beam reflection of the material (low powder bed absorption, 9% absorption vs. 91% reflection) therefore, increasing laser power can compensate for the reflection of the beam by the material and increase part density ([48];[49]).

Kamath et al. [50] used prior knowledge of the laser PBF systems, which was limited to less than 225W laser power, and developed a computational model for the process. Then, they conducted single track experiments to determine the process parameter to use with a laser power of 400W that would lead to high density 316L parts. It was concluded that laser power is one of the key process parameters that plays a major role in selecting other parameters and influences part density. Using a high laser power widens the range of potential scan speeds which can be selected [50] and therefore

increases build rate [51]. However, increasing the laser power too much may have a negative impact on the microstructure and/or mechanical properties of the fabricated part. Thus, there is a benefit of increasing the laser power up to a certain point, however, the benefit of increasing the power is not linear within the system.

Pulsed PBF systems give more flexibility to control the volumetric energy density for denser and higher hardness parts compared to continuous wave SLM systems as it was shown with Al-12Si alloys [52]. Moreover, pulsed L-PBF systems improved the surface roughness and are suitable for lattice structures and thin walls ([53]; [54]). Even though the pulsed laser systems deliver lower average power than continuous systems, they result in stronger sintering connection between grains [55].

2.3.1.1. Laser-Powder interaction

As previously discussed the laser scans the powder bed providing sufficient heat to melt the solid powder and form the melt pool. The beam reflection and material absorptivity for a laser beam affects the amount (efficiency) of heat transfer into the material. Generally, the majority of the laser beam reflects during the interaction with metal powder. The laser beam reflection could range from 50% for a material such as Titanium up to 90% for materials such as Aluminium and Copper. The proprieties of the material during the molten phase contribute in heat flow and the melt pool shape. The thermal conductivity of the powder dissipates the heat through the surrounding powder particles, through previous solidified layers below the current layer being built or the build platform (substrate). This process is called conduction. The heat passed through the molten material, convection and radiation, also contribute in heat loss during the process. The inert gas flow increases the heat loss from the exposed part and melt pool surface [56]. Figure 2-10 shows a schematic of the different heat transfer mechanisms which take place during the laser powder interaction.

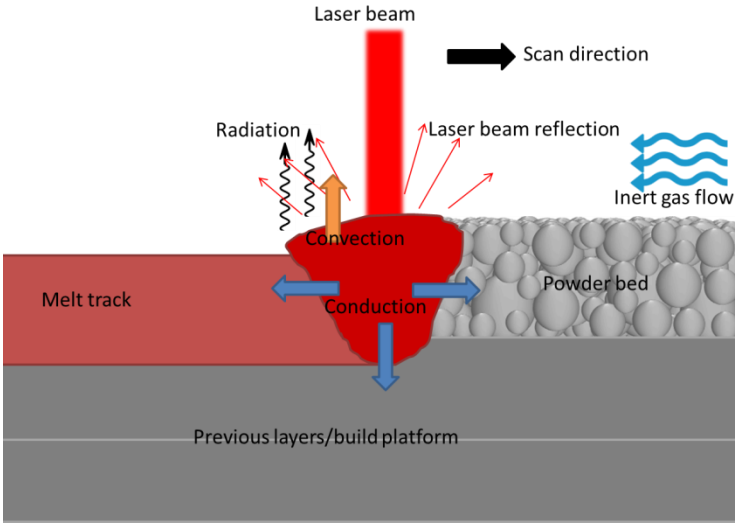

Figure 2-10: A schematic of heat flow of laser-powder interaction during L-PBF process

The amount of heat flow during the powder bed fusion is high which can melt a powder particle before being exposed to the direct laser beam. Scipioni Bertoli et al. [57] observed that the powder particle melts before the interaction with laser beam during initial heating. This means that it is possible that the laser beam interacts with the liquid phase not with the solid material.

Numerous research programmes have been carried out to study the melt pool formation and geometry according to the heat transfer and heat history of sequential layers such as [58]; [59]; [60]; [61]; [62]; [63]; [64]. The shape and geometry of a melt pool is driven by the dynamic of the molten material and physical phenomena such as Marangoni effect and recoil pressure. These effects vary according to the thermal and physical properties of the material. Figure 2-11 shows the main forces identified in the literature that drive the melt flow and contribute to shape the melt pool. The Marangoni effect is the mass transfer from low surface tension to high surface tension zone. The recoil pressure is the force that exerts on surface tension of the melt pool due to the variation of pressure.

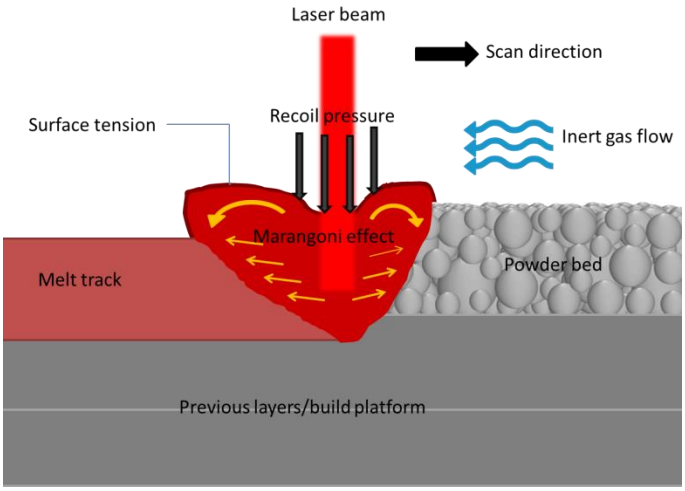

Figure 2-11: A schematic of forces that drive molten material and contribute to shape the melt pool during L-PBF process

The Marangoni effect and recoil pressure are driven by the temperature. Consequently, they occur in conjunction and both contribute to the melt pool dynamic and formation. During their simulation study Heeling et al. [65] found that the recoil pressure had a significant influence in the melt pool dynamics. Khairallah et al. [61] studied the physics of melt flow and the formation of pores, spatter and denudation. When the surface temperature approaches the boiling temperature under the laser beam, the recoil pressure applies an exponential force on the surface on the melt pool and creates a depression causing the molten material to move away from the centre of the melt pool. The molten material moves at a relatively high speed from the centre of the melt pool to the sidewalls and vertically along the sidewalls of the melt pool, which contributes to spatter formation ejecting up from the melt pool region [61]. The majority of spatter was found to be from the front of the melt pool toward the un-molten powder. This was observed in both the modelling [61] and experimental [66] programmes. Gunenthiram et al. [66] found that the spatter trajectory occurred for a wide range of the angles and spatter velocities were in the range 0.3m/s to 0.7m/s. The spatter sizes ranged from small nanoparticles up to 100µm diameter molten droplets. Their size was found to be affected by the laser power used in melting the powder as shown in Figure 2-12 [66]. The figure indicates that using a higher laser power could reduce the amount of spatter that is smaller than 3µm diameter, however, it could increase the amount of the spatter that is larger than 3µm diameter. The high laser power leads to the formation of an increased temperature gradient which could increase the effect of other associated

phenomena that drive the spatter formation such as the Marangoni effect and recoil pressure.

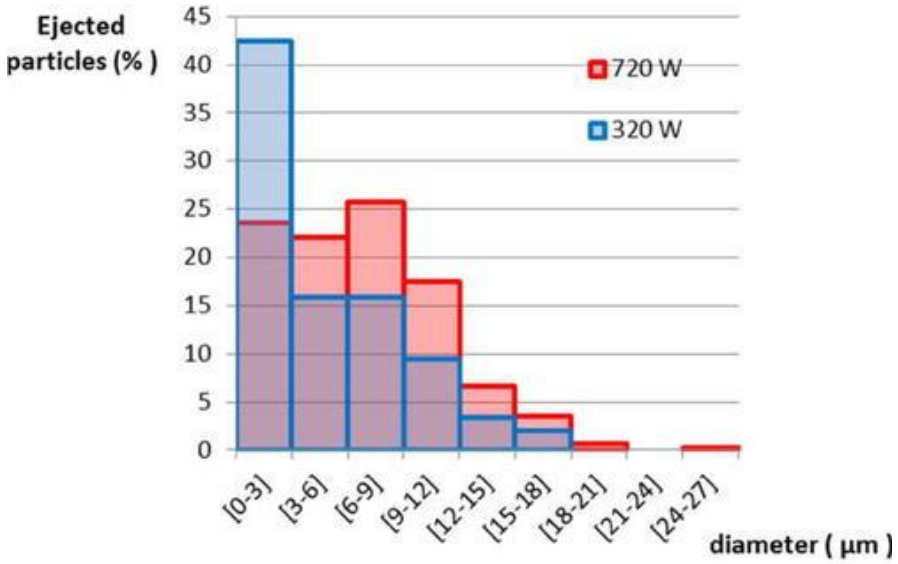

Figure 2-12: Histogram of spatter sizes at different laser power and scan speed of 0.3m/s [66]

Qiu et al. [67] found that the melt flow within a melt pool moved randomly. This could result in an irregular and unpredictable shape for the melt track. The Marangoni effect and recoil pressure in addition to the gas expansion were believed to be the driving forces of forming spatter/splash during the process. They believed that sudden heating of the powder layer led to gas expansion and evaporation which both contribute to spatter development. Applying higher energy was observed to increase thermal gradient and evaporation leading to increased Marangoni force and more instability of the melt flow [67]. The solidification process starts immediately after the heat source (laser) moves away from the melt pool. The melt pool cavity collapses (sidewall depression) with the driving force of the surface tension, rapid decrease in recoil pressure and Marangoni force filling the melt pool cavity to create a melt track. If the cavity of the melt pool is deep, the collapsing melt pool surface may trap gas leading to small circular pores at the bottom of the melt pool. The speed of collapse during the solidification process is quicker than the rate at which the gas can escape into the surrounding atmosphere, causing spatter. The effect of gravity to help fill this deep melt pool during cooling down was found to have a negligible effect [61].

2.3.2. Scan Speed

Scan speed (SS) is another important processing parameter. It indicates the length of time that the laser beam interacts with the powder bed. Numerous research projects have been conducted to investigate the effect of scan speed on the quality of melt track, to identify the optimum conditions for successful fabrication. A slow scan speed means an extended time of interaction between the laser and powder. If the speed is too slow, it is possible that this will result in extreme heating due to the concentration of the laser in a fixed position for an extended duration. This will result in evaporation and material loss. On the other hand, if the scan speed is too fast, this will result in minimal interaction between the laser beam and the powder bed, which may lead to inadequate melting/fusion. The speed of laser beam in powder bed fusion process is driven by the movements of the Galvanometer.

Sun et al. [51] studied the possibility of increasing the build rate while maintaining high density for 316L-SS. They found that the build rate increases linearly by increasing the laser power which allows the scan speed to be increased and speed up the process. The scan speed could be increased by 3.8 times when the laser power was increased from 100W to 380W and still produce high density 316L-SS parts (>99%). However, this is not absolutely correct; Yadroitsev [68] showed that increasing the scan speed has a limit. At a high laser power value, a too high scan speed resulted in discontinuous (droplets) melt track while a low scan speed resulted in distortion and irregularity in the melt track. The margin of the stability zone depends on the laser power and material properties. For instance, and according to the system used (50W laser power), it was possible to successfully fabricate a single melt track for 316L-SS powder using a scan speed range from 80mm/s to 200mm/s. Yet, for CuNi10 alloy, the range of possible scan speed for continuous melt track was limited to between 80mm/s and 140mm/s due to the different material properties of the powder.

In pulsed (modulated) laser systems, scan speed is influenced by the exposure time and point distance. Cherry et al. [5] studied the impact of exposure time and point distance on density and other mechanical properties of 316L-SS parts using the same PBF machine.

2.3.2.1. Point Distance

Point distance (PD) is defined as the distance between two consecutive points. It defines the overlapping rate for fusion points (Figure 2-13). The distance should be in a range where it is not too far therefore discontinues melt track and not exaggerated small that may slow down the build rate or lead to high temperature which may cause evaporation for the material therefore creating keyhole in a fabricated part. The usual value of the PD is smaller than laser spot size, however, it is possible to use a PD value greater than spot size if the resulting molten point size is greater than the spot size and a continuous melt track is achieved [53]. PD has direct impact on the surface roughness as shown by Cherry et al. [5]. They found that increasing PD increased surface roughness when process the 316L-SS powder.

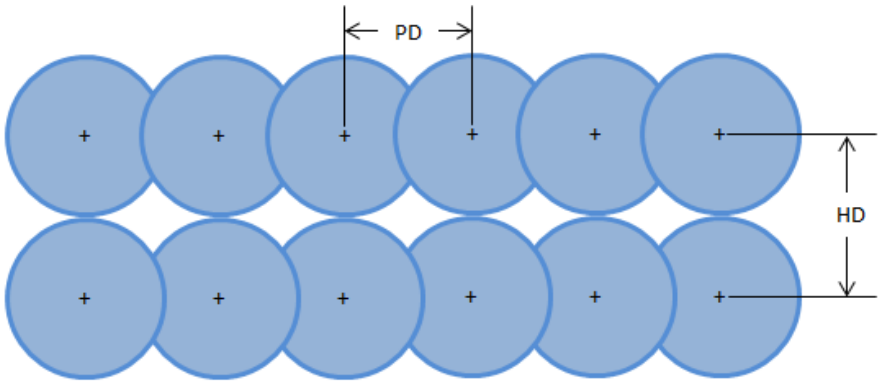

Figure 2-13: Point distance (PD) and hatching distance (HD) illustration for pulsed laser PBF systems

2.3.2.2. Exposure Time

Exposure time (ET), the elapsed time for each laser beam firing or the time that laser remains firing on a point. Demir et al. [53] used a pulsed PBF system to build 18Ni300 Maraging Steel and found that with a fixed energy density, exposure time plays a major role in improving part density by increasing the average power. However, the dimensional accuracy was found to be negatively affected by the increased exposure time. Karimi et al. [69] studied the impact of point distance and exposure time on the fabrication of 718 alloy. Increasing the exposure time at layer thickness of 75µm helped to reduce the porosity caused by the lack of fusion. The negative impact of increasing the exposure time is that it creates more spatter, which may influence the overall part density.

2.3.3. Hatching Distance

Hatching distance (HD) is the offset distance between adjacent melt tracks (Figure 2-13). It has a similar effect to PD because it determines the overlapping rate between melt tracks as the PD is determined by the overlapping between molten points. Density is impacted by HD. Small HD means increased overlapping of the adjacent melt tracks which means complete melting of the powder and uniform distribution of the heat. An extremely small HD could lead to overheating and evaporation of the molten material. Conversely a large HD produces a large offsetting between melt tracks which could lead to lack-of-fusion porosity between adjacent melt tracks.

Kasperovich et al. [4] studied the effect of process parameters of laser powder bed fusion on the porosity of Ti-6Al-4V parts. They found that the HD had less impact on the porosity of fabricated parts compared to other parameters such as the laser power, scan speed and spot size. The value of HD ranged from 40µm to 180µm and the change in the resultant porosity was within the range of 0.25%. The focus value ranged from -4mm to +5mm, but the resultant spot size from these focus values was not mentioned. Therefore, it was not possible to understand reason of the minimal impact of HD by comparing the values of spot size and HD.

A high value of HD is preferable in some applications to create and control pores. Zhang et al. [70] studied the effect of hatching distance on the porosity characterisation and mechanical properties for Ti-6Al-4V implants. The HD in their study was used to control the pore size and shape as the study was focused on fabricating pore structures to match human bones (which are not completely dense), therefore the selected range of HD was used to avoid overlapping between melt tracks. The laser spot size in their system was 150µm and the HD ranged from 200µm to 700µm.

2.3.4. Layer Thickness

Layer thickness (LT) is the measure of the layer height between successive layers for a fabricated part. It is the vertical resolution of the part being fabricated along the Z-axis. Layer thickness is usually selected dependent on the particle size distribution of the powder and on other process parameters such as laser power. A thin layer may not fit all the sizes of powder particle and lead to non-uniform powder spreading. In contrast,

using a thick layer of powder could produce larger voids within the particles or lead to lack-of-fusion porosity. Zhang et al. [71] investigated the effect of porosity on microstructure and fatigue property for 316L-SS parts fabricated using laser powder bed fusion. They developed the porosity by increasing the powder layer thickness (LT) while keeping all other parameters fixed. The LT ranged from 20µm to 80µm in 20µm increments. They found that a large LT had a direct influence in developing large pores that developed into cracks during the fatigue test. The reduction in terms of fatigue life is significant in relation to thick powder layers.

Sufiiarov et al. [72] studied the effect of layer thickness on some mechanical properties for Inconel 718 alloy samples fabricated via the powder bed fusion process using a layer thickness of 30µm and 50µm. They found that samples fabricated at a LT of 30µm had higher strength properties and higher value of impact strength. On the other side, samples fabricated with a LT of 50µm had higher elongation but lower impact strength. They correlated the lower impact strength for the samples built using a LT of 50µm to the presence of lack of fusion and cracks in the 50µm samples.

Wang et al. [73] investigated fabricating 316L-SS samples with LT of 150µm using a 400W powder bed fusion system. They were able to produce 316L-SS samples with a relative density of 99.99% with a layer thickness of 150µm. The build rate was improved by 3 to 10 times compared to previous studies. This successful build was restricted to fine particles with a mean particle size of 18µm. Similar to work done by Sufiiarov et al. [72], Wang et al. [73] found the elongation was higher compared to previous studies that used a thinner powder layer and strength properties was lower for the same comparison. However, due to the different PBF systems used in those studies, the comparison may not be valid.

2.3.5. Effect of Energy Density

Volumetric energy density (VED) is the amount of energy applied to a unit volume of powder. It is the main parameter that is used to study the effect of process parameters on fabricated parts. Energy input is crucial for the high density part fabrication in PBF process. Currently, the VED is the common indicator used with PBF process to determine the optimum zone for successful and high part density builds. Researchers are

using different formula for calculating energy density. Table 2-3 summarises some of the formula used in literature review.

Table 2-3: Examples of the energy density formula found to be used in the literature, with details highlighting the similarities and differences between them

Formula	*Unit*	*Notes*	*References*	*Equation No.*
$ED = \frac{LP}{HD * SS}$	(J/mm^2)	• Energy density for an area without considering layer thickness	[1], [74], [75], [76]	(2-1)
$ED = \frac{LP}{HD * SS * LT}$	(J/mm^3)	• The energy supplied by the laser beam to a volumetric unit of powder material • The overall energy input into the powder-bed during SLM processing • A measure for the averaged applied energy per volume of material during the scanning of a layer • The energy applied to per unit volume of sample • The total energy input per volume of sintered specimen • Volumetric Energy density as scan-speed based • In single track analysis, HD is equal to SP [77]	[3], [35], [77], [78], [79], [80], [81], [82], [83], [84], [85], [86], [87], [88], [89], [90], [91], [92]	(2-2)
$ED = \frac{LP}{SP * SS * LT}$	(J/mm^3)	• SP is the laser beam diameter • Used in single track formation	[77], [93]	(2-3)
$ED = \frac{LP}{SP * SS}$	(J/mm^2)	• Total heat input per unit area • Surface energy density	[42], [94], [95]	(2-4)
$ED = \frac{LP * ET}{LT * HD * PD}$	(J/mm^3)	• Energy input (Renishaw AM250) calculated as exposure-time based • Jump speed is not considered	[5], [69]	(2-5)
$ED = \frac{4 * LP}{\pi * SP^2 * SS}$	(J/mm^3)	• Used in single track formation • The thickness of powder layer is not considered	[96]; [97], [98]	(2-6)

In addition the formula in Table 2-3, Thomas et al. [99] used a normalised formula developed by Ion et al. [100] to show the normalised processing map of the EBM process for a range of materials (2-7). The formula considered the thermo-physical properties of the alloy to be fabricated. It also can be applied to L-PBF systems process when considering the beam characteristics.

$$ED_0^* = \left[\frac{A * LP}{2 * HD * SS * LT}\right]\left[\frac{1}{\rho * C_p(T_m - T_0)}\right] \quad (2\text{-}7)$$

where ED_0^* is defined as normalised equivalent energy density, A is surface absorptivity, ρ is the density, C_p is the specific heat capacity, T_m melting temperature and T_0 is powder bed (initial) temperature.

It has been shown how the density, microstructure and the mechanical properties of PBF parts are directly impacted by the energy applied on the system [90]. Han et al. [90] studied the change of energy density which showed that the grain structure could be tailored to influence the micro hardness of Ti-6Al-4V samples, based on the VED applied. This was a direct result of the heating/cooling pattern which allowed certain grain structures to form. It was also shown that there was an optimum VED, which provided the highest part density and micro hardness, which was in the region of 120 - 190J/mm^3. Values outside this region of VED (both above and below), resulted in lower part densities and microhardness, highlighting that the relationship is not linear and that continually increasing the VED can be at times detrimental. It is possible to obtain a certain measure of part density by varying the energy density input to sinter or melt the metal powder. The work of Bertol et al. [101] shows that using different energy densities can give the same part density. The authors used a laser power of 195W and layer thickness of 50µm on an EOSINT M250X machine to investigate the effects of hatching distance and scan speed on density and hardness. The hatching distance was 50, 75, and 100µm and scan speed was 50 and 100mm/s. A density of around 93% was obtained using different energy densities between 390 and 780J/mm^3, but also different parts densities were obtained at the same energy density (Figure 2-14). The variation in part density may be caused by the build orientation or by the combination of parameters that deliver the energy density. For instance, using hatching distance of 100µm with scan speed of 50mm/s gives the same energy density as using hatching distance 50µm and 100mm/s as scan speed, but the result of part density is slightly different. When the

hatching distance is large, there will be no overlapping between adjacent lines. The melt pool increases when the laser power is high and scan speed is slow, however, the melt pool size will not cover the distance between scan lines if it is larger than melt pool size so that voids (non-melted powder) are created.

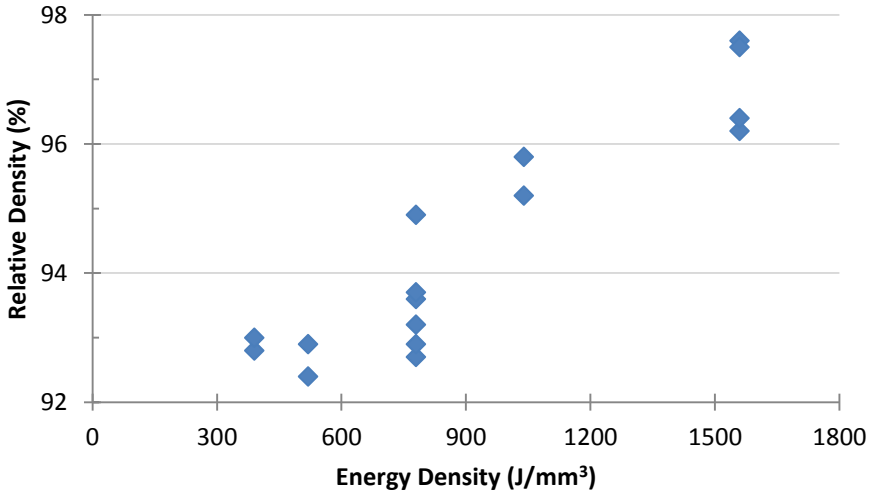

Figure 2-14: The relationship between energy density during the build and relative density of the fabricated parts for Ti-6Al-4V ELI laser sintering [101]. Similar energy densities were achieved even with changing the individual process parameters (e.g. hatching distance and scan speed), resulting in parts with different relative density.

Similarly, Gong et al. in [87] showed that the density of a Ti-6Al-4V fabricated part using AM is affected by the amount of energy density applied to the metal powder for a fixed particle size distribution (Figure 2-15). The relationship between part density and energy density is not linear, however, there are ranges of process parameters that can be used to fabricate near full density parts. According to this study, it is possible to obtain the same energy density using a different combination of parameters, but this does not necessarily give the same part density. For a hatching distance of 0.1mm and layer thickness of 30µm, using a laser power of 160W and scan speed of 1440mm/s or using laser power of 120W and scan speed of 1080mm/s give the same energy density and the relative density of part is almost same in both cases, above 99%. On the other hand, when the laser power is 40W and scan speed is 360mm/s, the energy density is the same but the relative density is about 97%. This work confirms that the value of energy density is not an appropriate indicator of melt energy to obtain defined density parts. All parameters that contribute to the energy density value may need to be considered individually.

It should be mentioned that the large difference in energy density used in [87] and [101] came from using different laser sources. While the latter used fibre laser type, the former used CO_2 laser type which required a slow scan speed to increase the powder absorption.

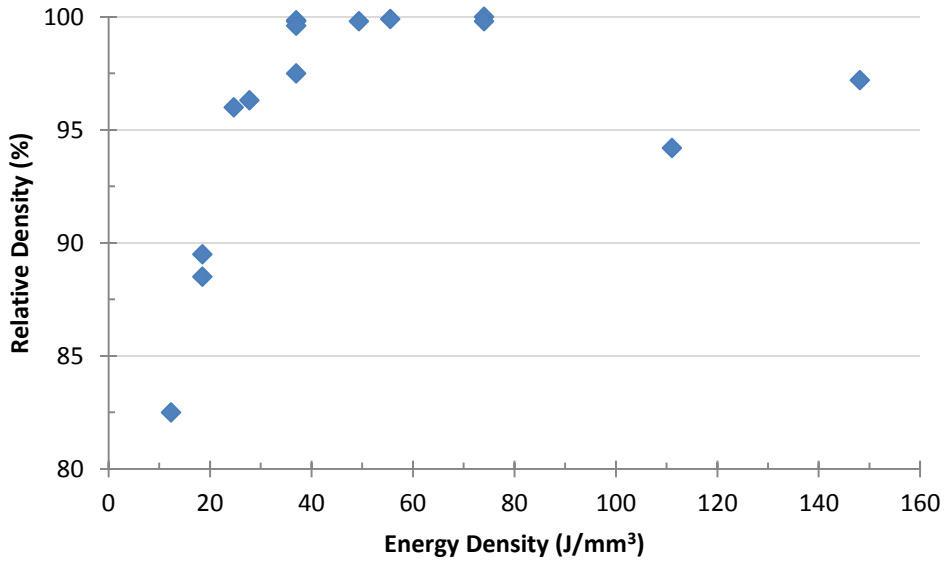

Figure 2-15: The relationship between energy density during the build and relative density of the fabricated parts for Ti-6Al-4V laser melting, with a fixed PSD [87]. Similar energy densities were achieved even with changing the individual process parameters (e.g. hatching distance, layer thickness, laser power and scan speed), resulting in parts with comparable relative density.

For other materials, Figure 2-16 is created from data given in [35]. The figure shows the relative density of different materials versus different energy densities which were obtained by changing laser power and scan rate. The materials were iron-based and steel-based with different particle size distributions. The equipment used was an EOS M250X^{tend} machine with laser beam diameter of 0.4mm. The process parameters were: Laser power of 100-215W, scan speed of 50-600mm/s, layer thickness of 50-200µm and hatching distance of 100-400µm. It is clear from the results that the energy density was not sufficient so that the density was relatively low. Insufficient energy density could be caused by type and the efficiency of the CO_2 laser type, large spot diameter and high layer thickness. In addition, other parameters such as scan speed and hatching distance had an impact on the delivered energy density. The author concluded that as the energy density increases (higher laser power; slower scan speed; lower hatching distance; thinner layer thickness) the part density increases until a saturation level is reached. Beyond that saturation level the density did not improve even with higher

intensive energy. It was concluded that powder properties (particle size distribution; chemistry and shape of the particles), process atmosphere (gas and substrate temperature) and scan strategy also influence the densification process which affects the quality of the parts (e.g. density, geometry and general appearance of parts).

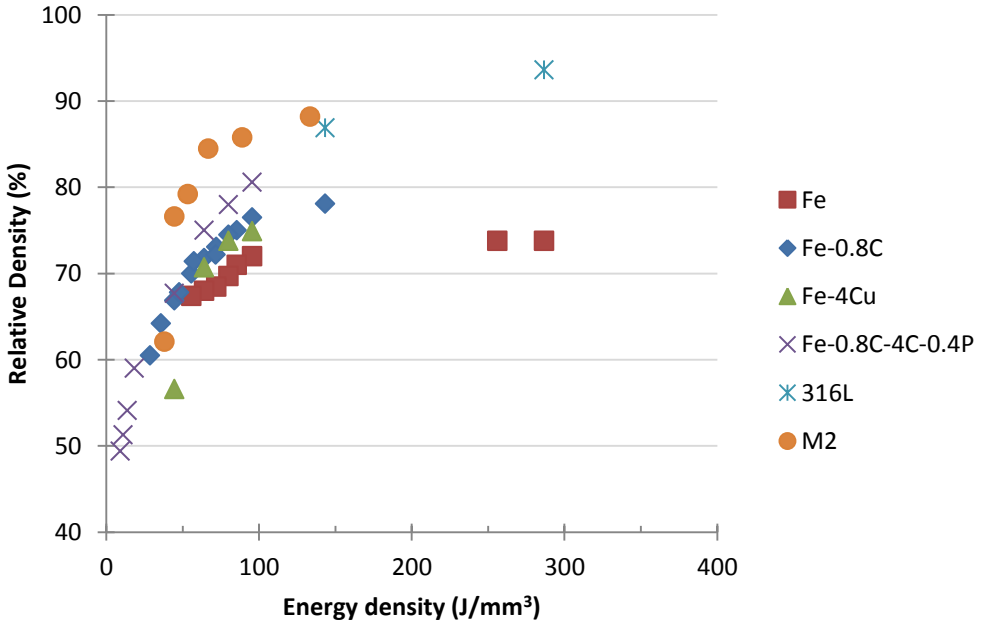

Figure 2-16: The relationship between energy density and relative density of the PBF fabricated parts for different iron-based and steel-based alloys [35]. The different energy densities were achieved with changing the laser power and scan speed.

Cherry et al. [5] and Karimi et al. [69] used exposure-time based formula to calculate the VED. The speed of moving from one point to another (JS) was not considered in this formula. The laser power, layer thickness and hatching distance were all fixed while the point distance and exposure time varied for different VED values. In [69], using a point distance of 59µm and 65µm with exposure time of 190µs and 210µs respectively resulted in the same VED value of 86J/mm^3. However, the porosity value and type (keyhole or lack-of-fusion) were different for the VED of 86J/mm^3.

Furthermore, with changing energy density, scanning strategies may affect the relative density of parts. Thijs et al. [88] used three scanning strategies: unidirectional, zigzag and cross-hatching. Unidirectional scan is the scanning strategy that keeps all scan vectors in the same direction for all layers. In zigzag strategy, the adjacent vector starts from the direction of the end of previous vector while cross-hatching strategy is the same as the zigzag strategy but the scanning direction of the next layer is rotated 90

degrees. Figure 2-17 shows that for exactly the same energy density, the density of parts is influenced by the scanning strategies. The effect of scan strategy was illustrated by using the same parameters (the same energy density) for different scan strategies which led to different part density. For instance, when a combination of parameters was used which gave energy density of 93J/mm^3, the unidirectional, zigzag, and cross-hatching strategies led to relative densities of 99.35, 99.6, and 99.9% respectively. The variation in density may be caused by the cooling rate of the melt pool for the different strategies. Zigzag was better than unidirectional hatching because the continuous hatching in the zigzag strategy slowed down the cooling rate while in the unidirectional strategy the hatching of a new vector starts from a cold point in relation to the previous vector. The cross-hatching strategy resulted in highest relative density because the crossing layer could fill and re-melt the voids in the previous layer.

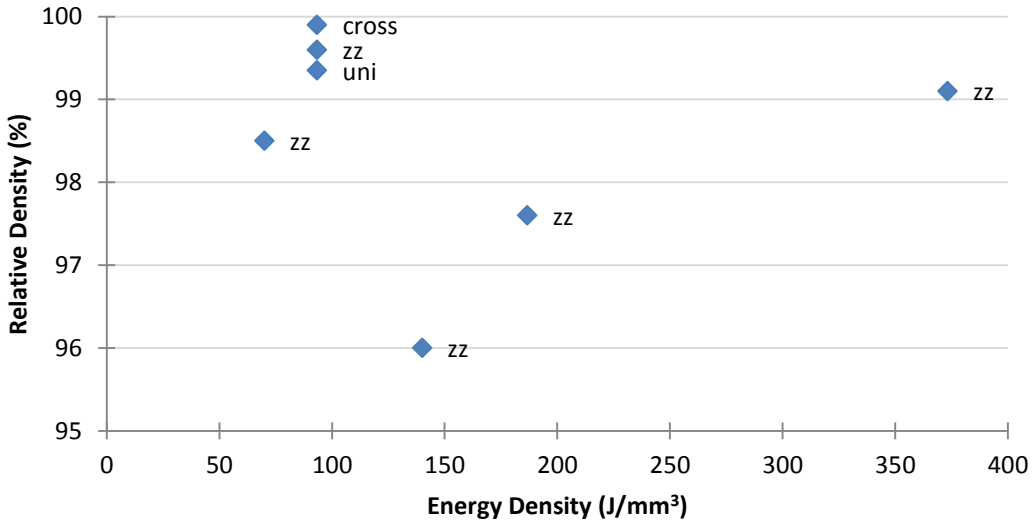

Figure 2-17: The relationship between energy density and relative density of the fabricated parts for Ti-6Al-4V ELI, with a fixed PSD [88]. Different scanning strategies (uni: unidirectional scan; zz: zigzag scan; cross: cross-hatching scan). At energy density of 93J/mm^3, cross scan strategy resulted in relatively higher part density compare to zz and uni strategies.

It is clear that the most common formula to calculate the VED is (2-2). Bertoli et al. [102] investigated the limitation of using the VED as a parameter to determine the optimum energy density required for successful PBF fabrication. They compared a combination of process parameters that delivered the same value of VED and showed that the result could significantly vary. Figure 2-18 is a figure captured from their published work. It shows that at the VED of 242J/mm^3 was obtained from varying the

laser power and scan speed. The resultant melt tracks ranged from regular smooth melt track, irregular, discontinuous to droplets (or balling) tracks.

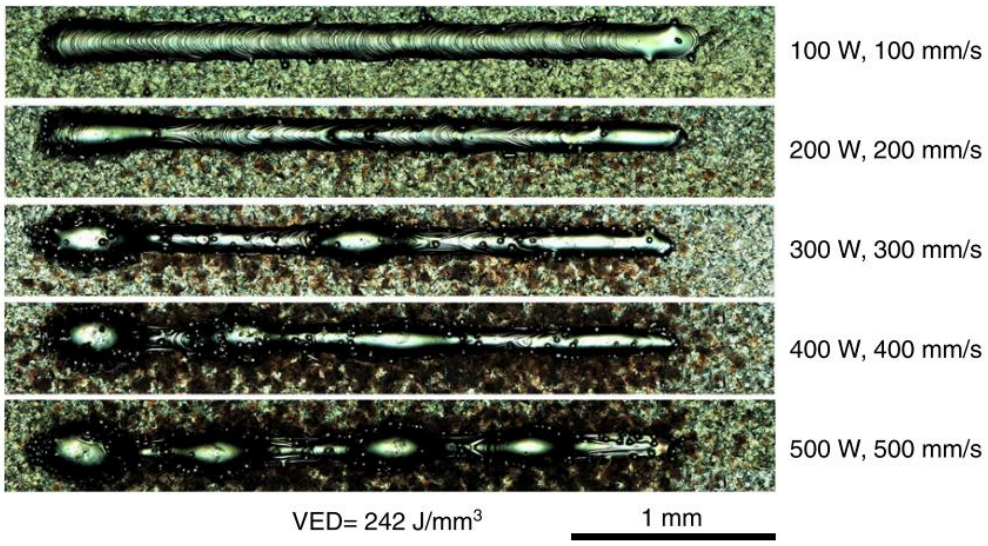

Figure 2-18: The melt pool formations for the same VED obtained by different combinations of power and scan speed [102]. At the VED of 242J/mm^3, the resultant melt tracks ranged from regular smooth melt track, irregular, discontinuous to droplets (or balling) tracks.

The analysis of mechanical properties of fabricated components met the requirements of the targeted application and showed that PBF is a viable manufacturing method for such applications. Porosity of parts, however, prevents using them where high strength and fatigue resistance are required. Gong et al. [87] found that the porosity of PBF parts was affected by the amount of energy density applied to metal powder. Single track formation for a range of process parameters has been used to evaluate the stability of the PBF process experimentally [103] and numerically [104]. Other researchers studied the influence of process parameters on single track, multitrack and multilayer [97] and also with different designs such as overhanging structures [105]. Numerous studies investigated the effect of process parameters on the mechanical properties including [106], [107] and [108]. Improper energy input can create spatter around the melt pool during the laser-powder interaction [96], with irregular melt pools or droplets [109] influencing the density and surface roughness of parts. Other factors inhibiting the manufacture of full density parts are laser scan strategies, build orientation [110] and also chamber pressure ([111]; [112]).

2.4. Porosity in Laser Additive Manufactured Parts

The porosity of powder bed fused parts hinders widening the applications that potentially may use this technology. Porosity has a direct impact on the mechanical properties of the fabricated parts. Zhang et al. [71] studied the influence of porosity on fatigue properties for 316L-SS parts. They found that the larger the pores, the lower the fatigue property. Authors found that when the pores are small, the crack initiation is from the defect of grain boundary. If the pores are large, the cracks would be driven by these pores leading to a reduction in the fatigue life. In addition, when the pores are large and close to each other, they would result in a significant and drastic reduction in fatigue strength. Tammas-Williams et al. [113] used an X-ray CT scan, which allows the identification and visualisation of different pores size and their locations within a part, to correlate the porosity location of additively manufactured parts to the fatigue life of the parts. Pores located close to the surface of a part were found to have a major impact on the fatigue life of that part. The majority of cracks investigated initiated from the pores distributed close to the surface of the part. Although cracks initiated from internal pores, formed deeper from the surface, these cracks were mainly driven by a larger pore size. Their study showed the importance of knowing the porosity distribution/location in AM parts for predicting the fatigue life. The study also emphasised the importance of tuning the process parameters and machining parts post build to enhance the life of AM parts by removing the excessive surface and close-to-surface pores [113].

Porous structures are preferable for some applications such as implants that mimic human bone structure [114], where the mechanical properties of the implants can be controlled to have similar behaviour to that of human bone [115]. Bandyopadhyay et al. [114] additively manufactured Ti-6Al-4V porous structures with porosity of 3%, 11% and 25%. They demonstrated the effect of porosity in biological tissue growth through the pores. This should enhance biological fixation and achieve long-term stability. The amount of Calcium ions (Ca^{++}) concentration within the structure that had a porosity of 25% was higher compared to the structures with a lower porosity. This confirms the importance of porosity in some applications, especially for medical purposes to match human bone density, and the ability of AM technologies to control the porosity. For the same material, Fousová et al. [115] showed the importance of porous structures for

better biological fixation. They fabricated samples with porosity ranging from ~0% to ~79% using a Concept Laser M2 Cusing machine equipped with a 200W laser power. The process parameters were a laser power of 200W, scan speed of 1250mm/s, hatching distance of 80µm and layer thickness of 30µm. The results showed the effect of density on the mechanical properties of the samples and the importance of porosity to mimic the behaviour of human bone. Samples with porosity of 61% were the best match for the Young's modulus of human bone which means the implants with this value would have a limited loosening that caused by the stress shielding effect.

Qiu et al. [67] studied the development of the porosity and surface roughness at different scan speeds (SS) and layer thicknesses (LT). A Concept Laser M2 Cusing system equipped with a laser power of 400W was used to fabricate Ti-6Al-4V samples with scanning speed ranged from 2000mm/s to 4000mm/s and LT of 20µm. Other samples were fabricated at a SS of 2400mm/s and LT of 20µm, 40µm, 60µm, 80µm and 100µm. It was found that increasing SS led to irregular melt track and cave-like pores on the surface which increased the surface roughness and led to increased porosity in the samples. At the fixed SS of 2400mm/s, LT was shown to have a direct impact on developing porosity. The pore size increased continuously with the increase in LT. Above 60µm, the pore size increased rapidly and the shape of the pores became more elongated and irregular. The melt power was consumed to melt new powder particles within the thick powder layer and therefore less power was available to re-melt and weld the previous layer to close the pores.

Other process parameters were investigated by Kasperovich et al. [4]. They studied the effect of process parameters on the porosity of Ti-6Al-4V samples fabricated by the PBF process. Laser power, scan speed, hatching distance and laser focus were the process parameters that were varied to correlate their effect with the porosity, a process parameter each time. Quantitative and qualitative evaluations for the porosity were conducted using 2D and 3D methods. They conclude that the porosity can be significantly reduced by competently optimising the process parameters. They also observed two main types of the porosity that depend on applied energy density: lack-of-fusion porosity (where there was insufficient energy to achieve complete melting process) and keyhole porosity (where there was over melting energy that led to small and spherical pores). Kasperovich et al. conducted a most comprehensive study linking

porosity with great visualisation methods. However, the effects of process parameter interactions were not considered. Studying one process parameter at a time could lead to misleading results, especially when there is a significant effect of the interaction of two or more process parameters. Therefore, a statistical method of the design of experiment that is able to find/estimate the effect of the interaction factors is required and would be a significant addition to knowledge.

Controlling the density of parts helps to control and predict other mechanical properties that are influenced by the amount, shape and distribution of porosity. Similar challenges were observed in the laser welding processes. Madison and Aagesen [116] quantified the porosity that appears in 304L Stainless Steel when process parameters, such as power, beam speed and laser focus, were changed. They found that the value, shape and frequency of porosity vary with changes in process parameters. The porosity resulting from heat transfer of metal alloys welding process was mathematically modelled ([117]; [118]; [119]) where they considered the physical material properties and process parameters. Their models were able to describe the keyhole formation and the influence of some physical phenomena such as recoil pressure, Marangoni affect (the convective flow that is induced from low surface-tension zone to high surface-tension zone) and the dynamic of the weld pool on developing the keyhole porosity. The underlying physics behind welding defects were intensively reviewed by Wei [120]. The interaction between solidification rate and surface tension, the Marangoni effect, the flow of the molten metal, evaporation, hydrodynamic instabilities, etc. were discussed in relation to some of the weld defects noted. Similarly to the welding processes, the PBF processes inherit defects that are driven by the same underlying principles. Marangoni and recoil pressure, for example, contribute to unstable melt tracks in the PBF process ([103]; [121]). Also, insufficient laser-powder interaction can increase balling/droplets or lack-of-fusion in the PBF melt track [122]. In addition, the heat diffusion in gaps among particles is affected by the thermal conductivity of the gas ([123]; [124]; [125]). This means thermal conductivity for bulk material is higher in comparison to powder. However, material as powder has a higher absorption rate than as a molten phase or solid phase due to the multi-reflection of the spheres which increases the absorbability [126]. The next two subsections review some work of the two main types of porosity created during laser PBF process: lack-of-fusion porosity and keyhole porosity.

2.4.1. Lack-of-Fusion Porosity

Lack-of-fusion porosity is defined as incomplete melting of adjacent melt pools or underlying layers (lack of bonding/welding). It is usually caused when the delivered melt energy is insufficient which can be resulted of low power, large hatching distance or point distance and thick powder layer (thick powder layer leads to lack of penetration therefore incomplete layer welding). The lack-of-fusion pores have irregular-elongated shapes, which can be in any direction (x, y or z).

Tang et al. [127] developed a model that can be used to predict the lack-of-fusion porosity. The main source of the lack-of-fusion in their model is insufficient overlapping between adjacent melt pools. The melt pool penetration should be at least as much as the powder layer thickness; otherwise, lack-of-fusion porosity would develop. The model's inputs are the geometry of the cross-sectional area of the melt pool, hatching distance and layer thickness. The melt pool geometries were estimated according to the alloy properties (such as powder absorptivity, melting temperature, density, thermal conductivity... etc.). Data from literature was used to test the model. In some points, the model showed reasonable agreement with experimental result from the literature. Porosity (relative density) obtained from literature is not necessarily caused by the lack of fusion. The different PBF machines and other process parameters and environment might lead to the lack-of-fusion porosity from distinct or unexpected perspectives. For instance, spatter due to the use of a high energy density (low speed) for some materials may hinder or defocus the laser beam making it impossible to achieve complete melt for the targeted point in the powder bed.

2.4.2. Keyhole Porosity

Keyhole porosity is usually caused by applying high melt energy, which leads to material evaporation and a deeper melt pool developing. Then, the collapse of the cavity, which was created by evaporation, traps the gas and develops small circular/spherical pores.

King et al. [128] illustrated the conditions that result in keyhole formation. Using a Concept Laser M2 machine and 316L-SS alloy, single tracks were fabricated for 316L-SS alloy powder. They combined enthalpy value at melting with deposited energy

density (including laser power, scan speed and laser spot size) to study the keyhole mode for 316L-SS alloy. At the conduction mode, the melt pool was controlled by thermal conduction, where the laser beam was absorbed by the powder layer, which melted and, with enough energy, was able to partially melt the previous solid layer creating a well-bonded solid track. A defined threshold for the normalised enthalpy was calculated for the specific material (316L-SS) and at specific processing parameters. Above this threshold the fusion process was observed to transition from conducted mode to the keyhole mode. The keyhole porosity developed above this threshold where the melt pool was seen to be too deep and collapsed leading to porosity. The observed keyhole porosity varied in terms of its presence and size. However, this threshold should change according to the process parameters, material thermal properties and powder characteristics.

The physics behind keyhole formation was illustrated in the work of Khairallah et al. [61]. Physics phenomena such as Marangoni effect and recoil pressure with surface tension are strongly related (because they are all affected by the temperature) and affect the melt pool formation. When the recoil pressure overcomes the surface tension, a deep cavity could form. Then, during the cooling process, the Marangoni effect and surface tension speed up the cavity collapse leading to the formation of pores. This leads to a region in the melt track such as the turning point at the end-start track being exposed to high laser intensity. Intensive laser power leads to narrow and deep depressions which collapse and form pores during solidification. Also, pores were observed at the end of the melt track where the laser was pushed off due to the gas trapped beneath the melt pool surface caused by the sudden shutoff the heat source (laser). A potential solution to avoid this problem was to gradually turnoff the laser progressively as opposed to instantly to prolong the solidification period and allow the entrapped gas to escape.

2.5. Particle Size Distribution vs Layer Thickness

Process parameters are not the only factors that affect the quality of PBF parts. Powder properties such as particle size distribution also influence the density of a part that is obtained for a certain energy density. Figure 2-19 illustrates that for a given layer thickness, using smaller particle size powder gives better density up to a certain limit.

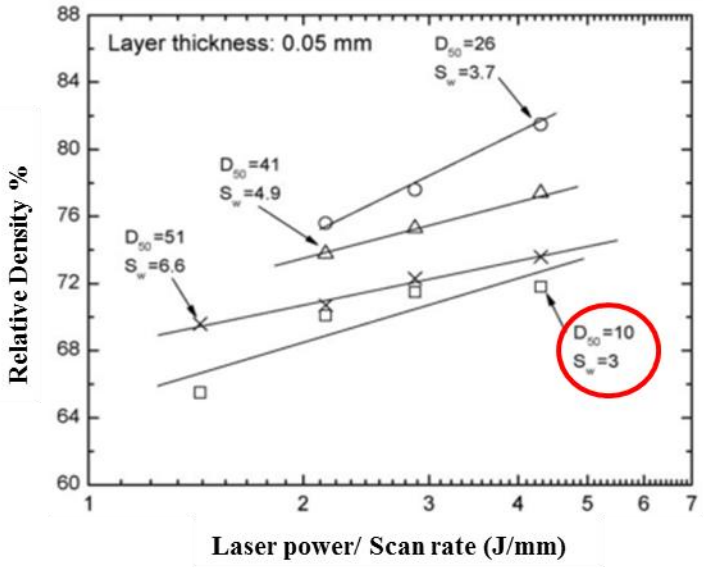

Figure 2-19: The relative density versus energy line for different particle size iron powder using laser sintering [35]. Small particle size distribution improved the relative density. Using too small (fine) particle size distribution, however, affected the relative density negatively.

From Figure 2-19, parts that are manufactured using powder with mean particle diameter of D_{50} =26µm appears to have higher relative density at all values of the energy line when compared with powder of larger particle size, D_{50}=41 and 51µm. Using smaller powder particle above a certain limit can negatively affect the density. The reason could be the amount of powder vs layer thickness. For instance, for a fixed layer thickness (50µm), if the average particle diameter is 26µm, it is possible to double the amount of powder particles for a layer compared to particle diameter of 51µm. Moreover, if D_{50}= 10µm is used, a layer will have approximately 5 times more particles than using D_{50}=51µm. When the line energy is less than 2J/mm, this means less heat transfer to the bottom of the layer so that the density for parts using 10µm was lower than 51µm. Heat transfer from the top layer to the bottom is affected by the number and size of the gaps in addition to powder absorption [129]. When the line energy is higher than 4J/mm, the density of parts using 10µm diameter powder is lower than 51µm. The possible reason for this case can be that the small 10µm particles may get spread away as they are small and high energy can disturb their distribution on the build platform. If the line energy is between 2 and 3J/mm, the density of parts fabricated using particle size of 51µm and 10µm are close to each other. Their density, however, is even lower than the density of parts made from particle size of 41µm and 26µm. The following

section clarifies the importance of raw material selection and its impact on other parameters.

Numerous studies investigated the influence of particle size distribution on process parameter optimization [42] or on surface quality and mechanical properties [130]. Others studied the influence of powder size and shape on processing [131]. Liu et.al. [42] investigated the effect of particle size distribution on processing parameters optimisation. Using a wide range of particle size distributions improves the density and surface finish of parts in comparison to a narrow range of particle size distributions. The wide range of particle size distribution can deliver higher powder bed density by filling the different size of voids between bigger particles with the smaller size particles. On the other hand, powder with a narrow range of particle size distribution can lead to a higher ultimate tensile strength (UTS) and higher hardness. The relationship between particle size distribution and UTS and hardness was not explained in this work. Therefore, further investigation into the effect of particle size distribution on the microstructure of fabricated parts is required. In addition, small particle size powder requires less energy to be melted than larger powder due to the surface area to volume ratio, however, a large amount of fine particles may lock together causing poor flow [42].

Regarding EBM, studies have been carried out to investigate the effect of particle size and layer thickness on manufactured parts. It is expected that using smaller particle size may improve surface finish quality, however, Karlsson et al. [132] noticed that the surface of EBM parts fabricated with a smaller particle size had a greater amount of un-melted particles attached to them and a higher surface roughness. This study was looking to improve the appearance of EBM part by using different particle sizes and layer thicknesses. The authors found no significant difference in hardness and elongation when using different powders and layer thicknesses, however, they expected that using smaller particle size with better development for process parameters could lead to better surface quality.

Spierings et al. [130] studied the effects of particle size distribution of metallic powder (316L-SS) on the density, surface quality and mechanical properties of parts produced by SLM. Three different particle size distributions with two layer thicknesses were

used. They concluded that it was possible to produce parts from all different powder distributions with density above 99% by adjusting the scanning speed accordingly. This means adjusting the energy density with respect to powder grade. It was summarised that smaller particle size helps to produce denser parts with better surface finish and mechanical properties. Using finer particles can deliver higher powder bed density in comparison to coarse particles which helps to produce higher density parts. Fine particles can also be easily melted which influences the final surface finish. On the contrary, larger particles can increase the ductility of parts resulting in increased elongation.

Understanding powder characterisation is essential in get high density parts. Spierings and Levy [86] used the same powder size distributions and layer thicknesses mentioned in previous paragraphs for Stainless Steel 316L. They compared the densities of the parts produced by different layer thicknesses for different powder grades, and they found that the theoretical layer thickness is different from actual layer thickness, discussed as the effective layer thickness (LT_{eff}). They found that the effective layer thickness should be greater by 50% of the diameter of D_{90} particle. The effective layer thickness reaches its stability after about 10 layers.

However, reaching a stable effective layer thickness is not necessarily reached after 10 layers for all powders and is more of a guideline. It depends on the density of the powder layer, density of the solidified layers and layer thickness. The effective layer thickness can be calculated according to the density of layer thickness using the following equation, Eq. (2-8):

$$LT_{eff_x} = LT + LT_{eff_{x-1}}\left(D_m - D_p\right) \tag{2-8}$$

where x is the layer thickness number and $LT_{eff_1} = LT$ when $x = 1$.

After a certain number of layers, Equation (2-9) gives the stability layer thickness that can be obtained along the build.

$$Effective\ Layer\ Thickness\ (LT_{eff}) = \frac{D_m}{D_p} * (LT) \tag{2-9}$$

where D_m is the density after melting, D_p is the density of the powder layer and LT is the theoretical layer thickness. Therefore, the actual layer thickness that is affected by melting energy is the effective layer thickness which should be considered when selecting the process parameters.

Figure 2-20 shows the variability of part density according to energy density for two different powder grades with different layer thicknesses (i.e. 316L-Type1-30µm and 316L-Type2-45µm) is almost similar. This may mean that for a powder grade it is possible to achieve a specific part density at certain energy density by optimising layer thickness with respect to the particle size distribution. However, at a certain level of particle size distribution, other process parameters should be adjusted to obtain high density parts which may negatively affect the productivity [86]. The suitable size ratio between coarse particles and fine ones is 1:10 or above, with about 30% of fine particles [133].

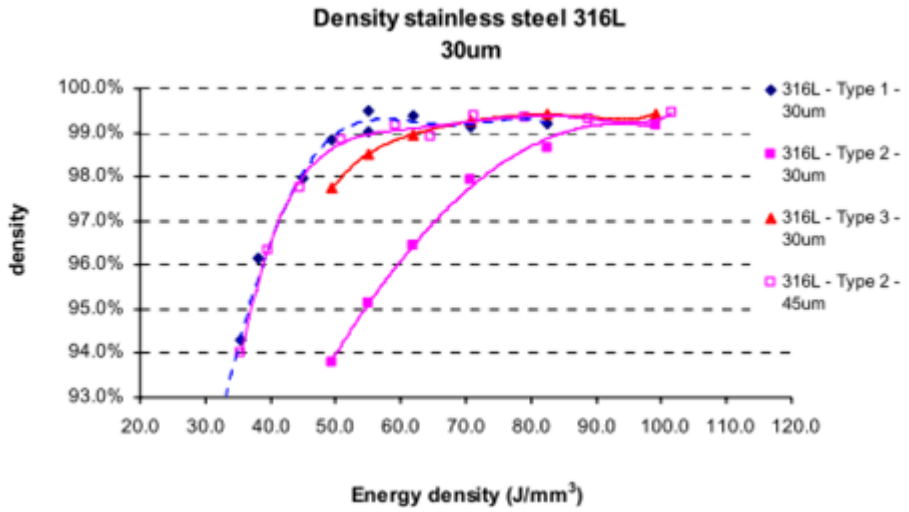

Figure 2-20: The relative density versus the energy density for different grades of 316L-SS powder [86]. Increasing layer thickness could improve the part density for some particle size distributions. For instance, the density of part fabricated by the powder type 2 improved, at lower energy density, when the layer thickness increased from 30µm to 45µm.

2.6. Summary of the Literature Review

In powder-based metal additive manufacturing systems, powder characteristics are critical because they affect the process efficiency and the quality of built parts, therefore it is essential that process parameters are selected accordingly. The spherical shape of powder particles (powder particle morphology) and proper particle size distribution facilitate good packing density and contribute to fabricating parts with good mechanical properties. Large amounts of fine particles will affect the flowability of powder which may lead to an inconsistent powder layer. Insufficient powder can cause voids between powder particles resulting in poor density and uneven surface roughness. The percentage of fine particles to coarser grains should be considered to minimise voids and produce fully or near fully dense parts [86].

Volumetric energy density (VED) is the amount of energy applied to a unit volume of powder. However, variation in part densities may be caused by the combination of parameters that deliver the VED. For instance, using a hatching distance of 100µm with a scan speed of 50mm/s gives the same VED as using a hatching distance of 50µm and a scan speed of 100mm/s but the resulting part density is different. When the hatching distance is large, there will be no overlap between adjacent lines. The melt pool size increases when the laser power is high and scan speed is slow. If the distance between scan lines is larger than the melt pool size, voids (unmolten powder) will be created ([87]; [101]). The relationship between part density and VED is not linear, and there are ranges of process parameters that can be used to fabricate near full density parts. This means that the value of VED should not be used as an appropriate indicator of melt energy for obtaining parts with defined density.

Process parameters are not the only factors that affect the quality of SLM parts. Powder properties such as particle size distribution (PSD) also influence the density of the part produced at a certain VED. Simchi [35] found that for a given layer thickness, using a smaller particle size distribution gives increased density until a specific point is reached. However, they showed that below this point, using smaller powder particle can negatively affect the density. This could be due to the amount of powder vs layer thickness. Heat transfer from the top layer to the bottom is affected by the number and size of the gaps between the particles, together with the thermal conductivity of powder.

Figure 2-21 illustrates the potential differences between the amount and the size of gaps for different particle size distributions for a given layer thickness. Therefore, it is possible that insufficient melt energy reaches the bottom of the layer leaving un-melted powder [129]. Additionally, smaller particles sizes have a greater potential to be disturbed by the high energy of the laser, therefore creating voids in the distributed layer.

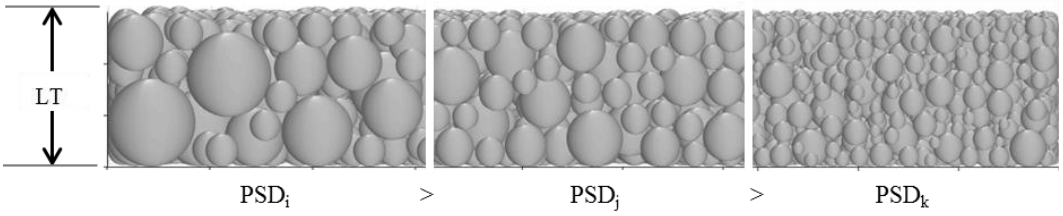

Figure 2-21: Different packing density for different particle size distributions (PSD) vs. fixed layer thickness (LT)

The effect of particle size distribution (PSD) on the SLM process and on the fabricated parts has been studied for 316L ([42]; [130]) and Ti-6Al-4V [134]. The results of these studies can be summarised as follows: metallic powder that has a small PSD (more fine particles [42]) tends to have denser powder bed and higher thermal conductivity. These two characteristics help to fabricate parts with higher density, smoother surfaces and higher mechanical strength compared to parts fabricated by coarse/large particles powder. However, a large proportion of fine particles may lock together causing poor flow. On the other hand, powder with large PSD has better flowability and parts that are fabricated by larger particle size have higher elongation.

2.7. Critical Evaluation of Previous Work and Identification of Gaps in Current Knowledge

A review of previous work suggests that little work has been carried out on the correlation of particle size and layer thickness and their effect on the density of fabricated parts, specifically for pulsed L-PBF systems. This work addresses this gap in existing knowledge and aims to determine the influence of changing powder size and

layer thickness for the same volumetric energy density which is controlled by exposure time.

From the accessed L-PBF work, it is clear that the particular challenge in L-PBF is selecting appropriate process parameter values for defective-free parts [3], finding their correlation with the porosity [4] and predicting mechanical properties [83].

It appears that although many studies have examined the influence of process parameters on build quality none appear to have examined their interaction. This study will be the first systematic attempt to use the response surface methodology (RSM) for the design of experiments (DOE) to investigate the effect of process parameters of the pulsed-laser PBF process on the density of fabricated components.

2.8. Development of Research Questions (or Development of Hypothesis)

As discussed above, it is clear that the effect of particle size distribution on part density has a limit. This limit and its relationship with layer thickness and energy density has not yet been optimized. From the review of literature, minimal work has been carried out on the effect of particle size and layer thickness on the density of fabricated parts, while optimisation of layer thickness for certain particle size distribution has not been investigated in detail. The aim of this work is to find a relationship between particle size distribution and layer thickness for different materials to obtain pre-defined density parts.

3. RESEARCH METHODOLOGIES

This chapter describes the materials, systems and the methodologies used throughout this study. In Section 3.1 the primary metal powder material characteristics are described. Different size primary powders were used to investigate the correlation between layer thickness and particle size distribution. The laser powder bed fusion system is introduced in Section 3.2. The methods used in the design of experiment are discussed in Section 3.3. The procedures of fabricating samples and the selected range of process parameters are described in Section 3.4. Also, the procedure of building samples with a range of layer thickness and particles size distributions are introduced in the same section. Finally, Section 3.5 illustrates the evaluation method for the built samples.

3.1. Materials

The two primary metals powders used in this study were Titanium Ti-6Al-4V ELI (i.e. Extra Low Interstitials) and 316L Stainless Steel. These two metal powders are among the most common powder bed fusion (PBF) materials that have many applications in aerospace, medical and automobile industries. For this study, the following sections (i.e 3.1.1 and 3.1.2) provide the key powder characteristics of the materials, which are among the important properties for the AM powder [135].

The particle size distribution was measured using the Dry Dispersion Unit cell (Aero S) of the Mastersizer 3000 (Malvern, UK). The density of the materials as virgin powder was determined using the AccuPyc II 1340 Pycnometer (MicroMeritics, UK). The apparent density was measured using the Hall Flowmeter Funnel approach, while the tapped density was measured using the 350-Tapped Density Tester (Glasside Technologies, UK).

3.1.1. Powder Characterisation of Ti-6Al-4V ELI

Three types of Titanium alloy Ti-6Al-4V ELI powders with different particle size distributions (PSD) were used in this research. The first type of the powder (T1) was plasma-atomised (Renishaw, UK) while the other two powders (T2 and T3) were gas-atomised (Maher, UK) and they are all nearly spherical in their nature ([44]; [136]). The

particle size distributions (PSD) for the powder types T1, T2 and T3 are shown in Figure 3-1 and their morphologies in Figure 3-2. The main values of PSD (i.e D_{10}, D_{50} and D_{90}) and density are shown in Table 3-1. Table 3-2 shows the nominal chemical composition as quoted by the suppliers for the virgin powder (as received) in percentage weight for all three powders used in this study.

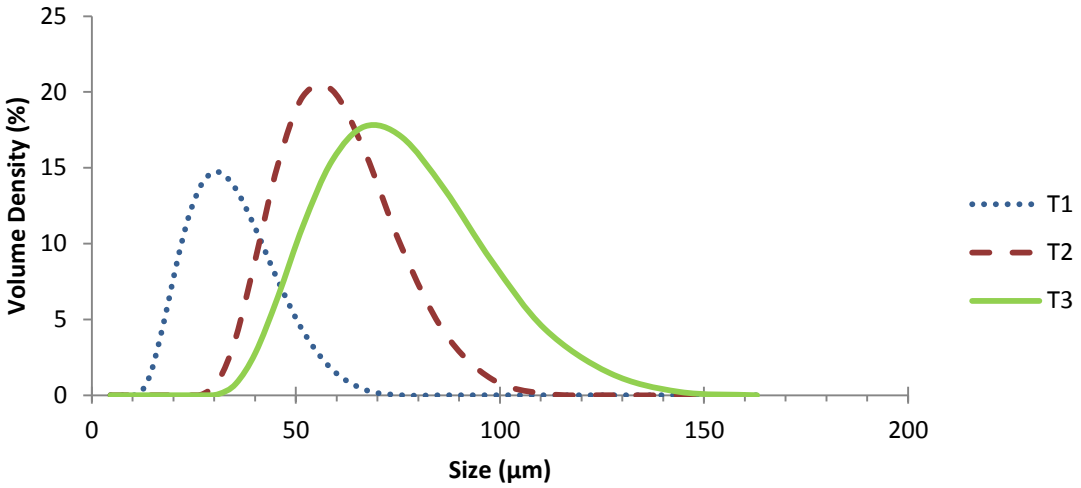

Figure 3-1: The particle size distributions of Ti-6Al-4V ELI powders T1, T2 and T3

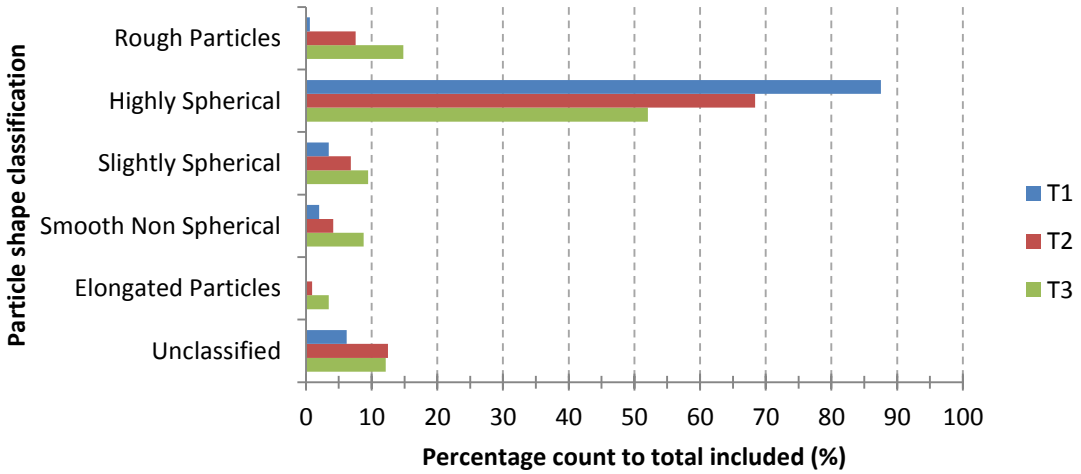

Figure 3-2: The morphology analysis for Ti-6Al-4V ELI powders T1, T2 and T3 showing that the majority of the particles of plasma atomised (T1) is highly spherical.

Table 3-1: Particle size distributions and density of all powder types: T1, T2 and T3 of Ti-6Al-4V ELI

Property	***Ti-6Al-4V ELI Powder Type***		
	T1	T2	T3
D_{10} (µm)	20.6	43.2	51.7
D_{50} (µm)	32	59.3	73.6
D_{90} (µm)	48.6	81.2	105
Powder Density (g/cm^3)	4.42	4.41	4.41
Apparent Density (g/cm^3)	2.58	2.60	2.50
Tapped Density (g/cm^3)	2.86	2.85	2.78
Wrought Material Density of Ti-6Al-4V ELI (g/cm^3)	4.42		

Table 3-2: Percentage weight of the chemical composition of Ti-6Al-4V ELI powders

Powder Type	***Al***	***V***	***O***	***N***	***C***	***H***	***Fe***	***Ti***
T1	6.5	3.9	0.11	0.03	0.01	<0.01	0.2	Bal.
T2	6.14	4.14	0.086	<0.005	0.013	0.0012	0.05	Bal.
T3	6.16	4.17	0.080	<0.005	0.012	0.0012	0.049	Bal.

3.1.2. Powder Characterisation of 316L Stainless Steel

The second material studied was 316L Stainless Steel (316L-SS) alloy. Two different PSD powders of 316L-SS (S1 - Renishaw, UK and S2 - Maher, UK) were used for which the PSDs and morphology analysis are shown in Figure 3-3 and Figure 3-4 respectively, and densities are shown in Table 3-3 and the nominal chemical composition -as quoted by the suppliers- as percentage weight are shown in Table 3-4.

The target was to obtain three PSD powders for the 316L-SS alloy as was the case for the Ti-6Al-4V ELI. Unfortunately this was not possible within the time frame of this research. The critical powder characteristic for the PBF system used is the flowability and the alloy powders available in the market are made for the metal injection moulding (MIM) process. The larger sized powders are suitable for the blown powder system (Direct Energy Deposition). It was impossible to find a third powder with a suitable powder size for 316L-SS within the time frame of the research. The powder samples obtained did not meet the required standard specified by the manufacturer for efficient

processing. Only two 316L-SS powders were found to be combatable with the AM system used in this research.

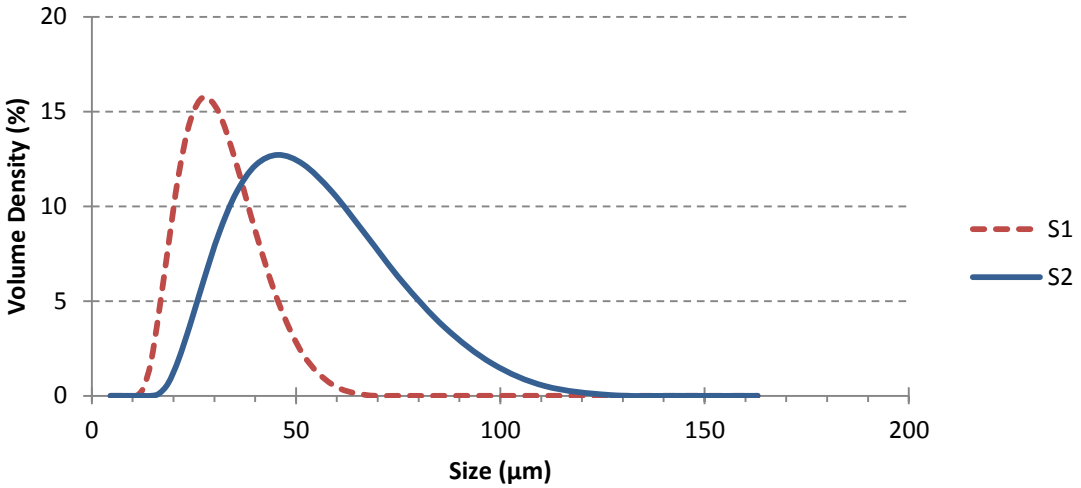

Figure 3-3: The particle size distributions of 316L-SS powder S1 and S2

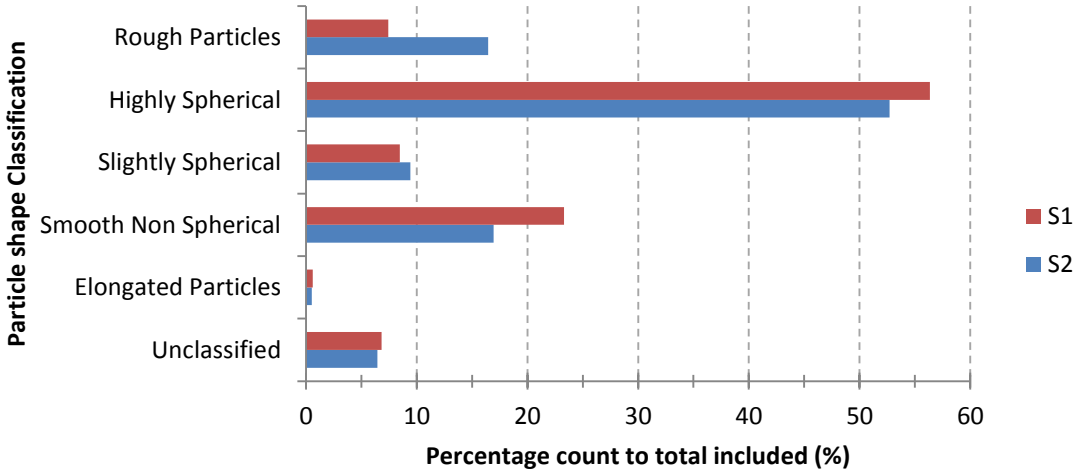

Figure 3-4: The morphology analysis for 316L-SS powders S1 and S2

Table 3-3: 316L-SS Powders characterisation

Property	***316L-SS Powder Type***	
	S1	S2
D_{10} (µm)	19.6	29.5
D_{50} (µm)	29.6	48.5
D_{90} (µm)	44.1	79.1
Powder Density (g/cm^3)	7.94	7.92
Apparent Density (g/cm^3)	4.36	4.55
Tapped Density (g/cm^3)	5.01	5.00
Wrought Material Density of 316L-SS (g/cm^3)	7.99	

Table 3-4: Percentage weight of the chemical composition of 316L-SS powders

Powder Type	***Cr***	***Ni***	***Mo***	***Mn***	***Si***	***Cu***	***N***	***O***	***P***	***C***	***S***	***Fe***
S1	17.50-18.00	12.50-13.00	2.25-2.50	≤2.00	≤0.75	≤0.50	≤0.10	≤0.10	≤0.025	≤0.030	≤0.010	Bal.
S2	16.99	12.75	2.38	1.40	0.65	0	0	0	0.01	0.01	0.005	Bal.

3.2. Laser Powder Bed Fusion System

The laser melting machine used was a Renishaw AM250 (Renishaw, UK), which was equipped with a 200W modulated fibre laser which generates a pulsed laser wave. A schematic of the machine is shown in Figure 2-2. The laser beam has a minimum nominal diameter of 70µm and a wavelength of 1070nm. The machine has a build volume of 250mm x 250mm x 300mm (X x Y x Z). The spot size of the beam was kept at its minimum value for all builds, to provide the maximum energy density, as recommended by the manufacturer. A silicon wiper was used to spread the powder dose across the build platform. The building process was conducted in an inert atmosphere of Argon, to minimise any possibility of oxidisation of the primary powder and to prevent any contamination. The build platform was preheated up to 170°C before all builds, to reduce the temperature difference between melt pools and build platform, which would also reduce the effect of residual stress.

The software Magics (Materialise, UK) was used to design the parts, prepare the layout of the parts on the build platform and to assign the melt strategies which would be used to build the parts. The machine can fabricate parts with a range of process parameters in one build, however, the layer thickness cannot be changed during a build and once a layer thickness is selected for a build, it is constant throughout until build completion. The available melt strategies were Total Fill, Chessboard, Stripes and Meander [137]. The Total Fill strategy is predominantly used for supports structures due to the small cross sectional area, which can be identified as a sequence of offsetting border lines for all the cross section area (Figure 3-5). The scan process in this strategy may start from the inside of a part towards the outside (Inside-Out) or vice-versa (Outside-In).

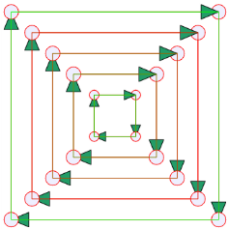

Figure 3-5: Total Fill scan strategy which is defined as offsetting boarders

The other scan strategies are used for fill hatching. The Chessboard strategy divides the cross sectional area into small squares of 5mm x 5mm, and then scans them where the scan direction of each square is rotated 90 degrees from its neighbours. The Stripes and Meander laser strategies are the most commonly used strategies when building a part. While the Stripes strategy scans the area in a manner of stripes, the Meander strategy scans the complete area in parallel vectors and offers a faster build strategy compared with the strategies described. The latter three scan strategies rotate the cross section area by 67° clockwise for each layer, in addition to the scan being against the gas (Argon) flow. Figure 3-6 illustrates the scan of three sequent layers of the scan strategies.

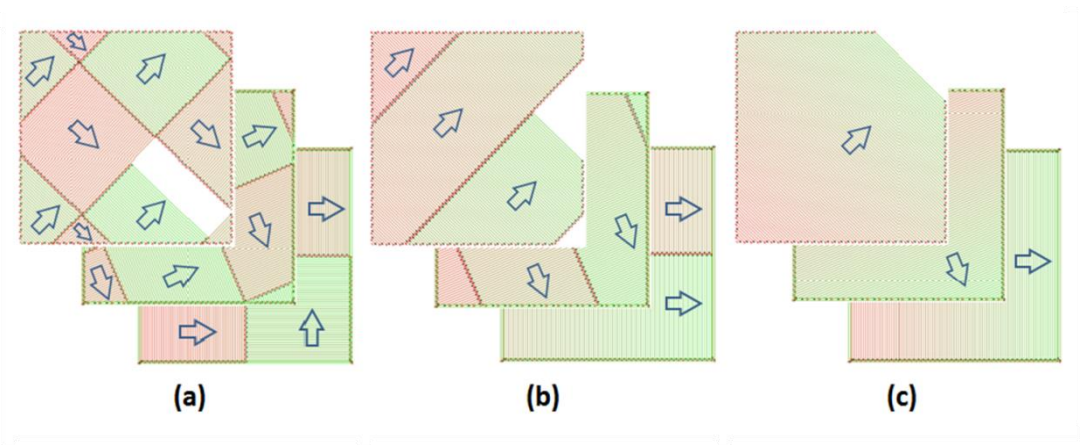

Figure 3-6: Scan strategies: (a) Chessboard, (b) Stripe and (c) Meander. The pattern of the scan strategies was captured by Renishaw SliceViewer

Due to the small cross sectional area for the parts being fabricated, the Meander build strategy was used in this study to fabricate all the parts. The hatching area was rotated 67° clockwise every layer (as recommended by the manufacturer) to avoid repeating the scan line above each other, which can create pores. In this strategy the laser beam always scans the hatching area against the flow of gas. The cross section scanning area was offset from the borders by -60µm for the Ti-6Al-4V ELI and no offset (0µm) for the 316L-SS. The laser beam scans the area in alternative vectors starting from the back-left corner (always against the flow of gas). Then, the laser scans the two border lines inside out. The next cross section scan (layer) is rotated by 67° clockwise and this process is repeated until the build is completed.

3.3. Design of Experiments Methods

Design of Experiments (DOE) is an organised approach that links the inputs of a process to the output. Instead of conducting a series of experiments without a clear structure which requires a vast amount of time and resources, using a DOE results in conducting fewer experiments to provide information in relation to the importance of certain process parameters for the studied process. As soon as these selected experiments are theoretically selected, they can give adequate analysis for the complete considered region of the process. Two techniques of DOE were used in this study: The Taguchi method and the Response Surface Methodology (RSM). Both methods are approved techniques for optimisation of many applications and for the majority of cases can be used interchangeably. For instance, Asghar et al. [138] found that Taguchi and central composite design (CCD), which is a design of RSM models are statistically

significant and are in agreement with each other. However, in terms of ranking the contribution of input factors to the response value, the Taguchi method is a preferable approach for examining operating parameters. Even though the number of experiments given by Taguchi method was significantly fewer than by the CCD, the optimised values obtained by both methods were in good agreement. The authors concluded that Taguchi is a suitable alternative for the CCD in many interest-studied applications. Moreover, Dayanand et al. [139] used RSM and Taguchi methods to optimise and model the factors and response of grinding.. They used L27 instead of L9 for three 3-level factors so that they were able to use Taguchi and RSM interchangeably. The Taguchi method was used to optimise the process parameters and RSM was used to find the interaction between the factors and to obtain a prediction model. They found that the model developed by RSM was able to predict the response in very good agreement with experimental values (adj-$R^2 \approx 0.97$). The Taguchi method is an efficient and systematic method to determine the optimal process parameters, while RSM is a collection of statistical techniques used to model the interaction between factors and their response. It has been reported that the RSM predicts the response better than the Taguchi method [140]. The Taguchi method gives the optimal combinations at the specified levels, while RSM can give the optimal values within or beyond the range of the given levels. The authors mentioned that the prediction model obtained from RSM is more accurate than the model obtained by Taguchi. Other similar integrations were carried out for different applications. Taguchi was used to find the most significant influencing factors and their levels, then RSM was utilised to verify that the optimal parameters and to model the process parameters with the response for future prediction. All these studies and others from different disciplines, showed a good performance of the Taguchi method for optimisation and identification of the significant influencing factors, as well as showing the advantage of the response surfaces methodology in prediction/developing an empirical model ([141]; [142]; [143]; [144]; [145]). In short, both of the methods can be utilised for efficiently optimising and for predicting an empirical model that represents a process. However, models obtained by RSM are generally more accurate due to the fewer discrepancies between the predicted results and actual results [146].

Due to the number of the selected process parameters for the optimisation of the Ti-6Al-4V ELI, the Taguchi method was ideally suited for this. For the 316L-SS process

parameters optimisation, the number of considered process parameters was reduced to allow the RSM method to be used.

3.3.1. Taguchi Method

The Taguchi approach is one of the most powerful and reliable evaluating methods used in multi-factor experiments. It allows the main effects of design parameters to be investigated by conducting the fewest number of experiments [147]. The method has previously been used to optimise process parameters in SLM [148] and in Laser Engineering Net Shaping [149]. In principle, Taguchi's design of experiments is used to obtain information about the main effects of the input factors. The objectives of the Taguchi approach for parameter design is to identify the best combination of design parameters, in addition to reducing the variation of the response. Signal-to-Noise (S/N) ratio is the analysis characteristic that the Taguchi method depends on. There are three different types of S/N calculation: smaller-the-better (Eq. (3-1)) when the objective of the optimisation is minimisation, nominal-the-best (Eq. (3-2)) when there is a target value for the optimisation, and larger-the-better (Eq. (3-3)) when the objective function is to maximise the output. The main aim for these experiments is to optimise the laser process parameters to obtain the greatest possible part density, therefore the larger-is-better (Eq. (3-3)) characteristic was chosen for this analysis.

$$S/N = -10\,Log_{10}\left(\sum_{1}^{n} y^2\right) \tag{3-1}$$

$$S/N = 10\,Log_{10}\left(\frac{\bar{y}^2}{s^2}\right) \tag{3-2}$$

$$S/N = -10\,Log_{10}\left(\sum_{1}^{n} \frac{1}{y^2}\right) \tag{3-3}$$

where y is the observed data, $\bar{y}$ is the data mean, s is the standard deviation of the data, and n is the number of observations.

The Taguchi approach is mainly used in design for discrete systems. Therefore, the return value of optimisation is a value of one of the selected levels for each factor. This is considered as a limitation of the Taguchi approach when it is used for optimising continuous systems. There is the possibility for a better or optimum value at a point in a location between the selected levels. Another limitation is the lack of representation of

the interaction between factors which may lead to confound factors. As a result of these limitations, verification experiments are required to validate the results of this approach.

3.3.2. Response Surface Methodology (RSM)

The Response Surface Methodology (RSM) is a method of designing experiments to study the relationship between input variables (factors) and the outputs (responses). It has been used to optimise process parameters [150] and to develop the predictive model [83] of PBF processes. Central Composite Designs (CCD) and Box-Behnken Designs (BBD) are two of the major response surface designs. The response of the design is expressed as function of the input factors as Equation (3-4).

$$Y = f(x_1, x_2, \dots, x_k) + \varepsilon \quad (3\text{-}4)$$

where k is the number of the factors and ε is the response error.

The CCD has two major designs: Axial design where the axial points are shifted out of the box that is defined by the corner points, and Cube design where the axial points are located on the midpoints of the cube edges. The shifted distance is defined by the value of γ which can be customised. When the value of γ is 1, the design is Cube. The number of corner points is 4*K and the number of axial points are 2*K, where K is the number of the factors. Figure 3-7 shows the design points of each type of these CC designs: (a) is the axial design and (b) is cube design.

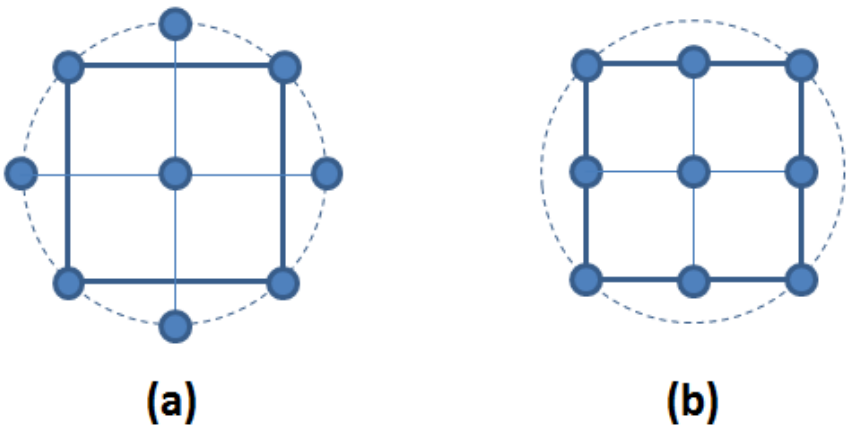

Figure 3-7: The graphical representation of two factors design using RSM: (a) Axial design and (b) Cube design

The BBD is the other major RSM design. The main difference in comparison to CCD is that the BBD has a no extreme points (corner points), as can be seen in Figure 3-8. There are the centre points and axial points as midpoints of the edge of the region of the experiments. Factor levels using BBD are three compared to five in CCD.

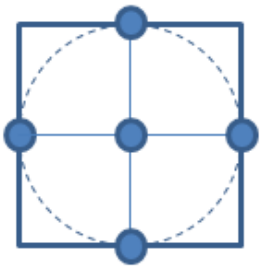

Figure 3-8: The simplified graphical representation of BBD

3.4. Fabricating L-PBF Samples

The samples selected were $10 * 10 * 10\ mm^3$ cubes with 3mm supports. Each sample was labelled with a unique identification number. There were four cubes for each set of process parameter combination for all experimental builds, arranged on the platform alternately to mitigate the effect of particles rejected from the melt pool during the process of neighbouring cubes (see Figure 3-9). The cubes from each set were distributed throughout the build platform, to enable the effect of the build location on the part density to be investigated. This ensured that cubes from the same set of process parameter were not located in the same region of the build platform. The four cubes were randomly located either in the right, middle, left, front and/or back of the build platform.

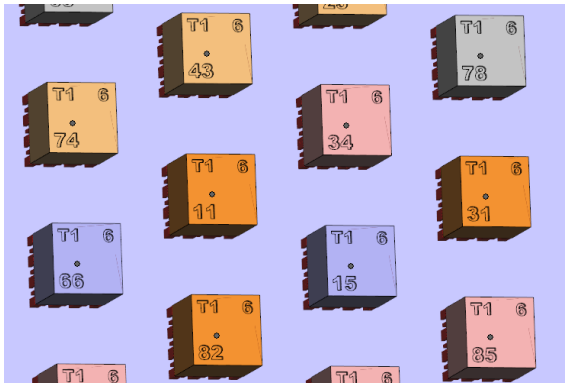

Figure 3-9: Samples labelling and arrangement on the build platform

The build platform was pre-heated up to 170°C in line with the standard build procedure recommended by the manufacturer [151], and all builds were fabricated under Argon atmosphere. The builds only began once the oxygen level in the chamber was below 0.1%. The scan strategy of Meander was used, with the scan direction rotating 67° clockwise from the previous layer.

3.4.1. Process Parameters Optimisation

L-PBF has numerous process parameters that contribute to the quality of fabricated parts. The focus of this work, however, is on the critical process parameters that have a direct impact on the melt pool formation. These parameters will therefore have the major influence on the part density.

3.4.1.1. Ti-6Al-4V ELI

Process parameter optimisation was carried out using powder type 1 (T1). Layer thickness (LT), laser power (LP), scan speed (SS) and hatching distance (HD) were considered to be the most critical parameters because their effects on the delivered melt energy. In pulsed L-PBF systems, the laser does not fire continuously but rather in a discrete manner. In this case the scan speed is calculated according to point distance (PD, the distance between two consecutive points), as can be seen in Figure 3-10, exposure time (ET, the elapsed time for each laser beam firing), and jump speed (JS, the speed of galvanometer mirror when moving from point to point). Equation (3-5) was used to calculate the scan speed.

$$Scan\ Speed\ (SS) = \frac{PD}{ET + \frac{PD}{JS}} \tag{3-5}$$

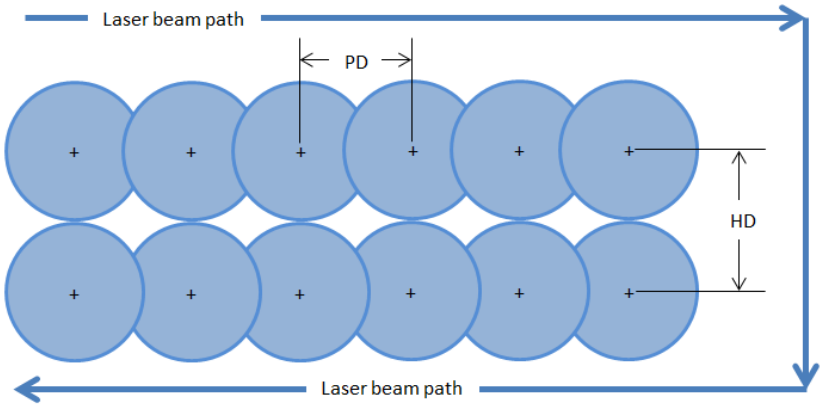

Figure 3-10: Point distance and hatching distance illustration for pulsed laser PBF systems

In this study the jump speed was kept constant at 5000mm/s for all builds as recommended by the equipment manufacturer, while the PD and ET were considered as variables in this study and were considered as optimisation parameters. The parameters and their selected levels are shown in Table 3-5. In pulsed L-PBF, however, it is not accurate to study the effect of scan speed as a single parameter on part quality. The scan speed can be obtained by different parameter combinations, but not all are suitable for use even when the combined values are identical. For instance, using a combination of a PD of 50µm and an ET of 50µs will lead to the same scan speed as a PD of 200µm and an ET of 200µs. Even though the value of scan speed is exactly the same, the latter combination may not be suitable for full density builds, as the size of the melt pool will not cover the distance between consecutive points (PD) even with the prolonged firing time (ET). Therefore, it is of paramount importance that each individual parameter is carefully selected. Thus, the scan speed value should only be used as a guideline, with further consideration given to the components which make up the scan speed value.

Table 3-5: Process parameters and their levels used in the experiments

Parameter	***Levels***				
	1	2	3	4	5
Layer Thickness, LT - (µm)	20	30	50	70	100
Laser Power, LP - (W)	90	120	150	180	200
Point Distance, PD - (µm)	35	45	55	70	100
Exposure Time, ET - (µs)	50	70	100	150	200
Hatching Distance, HD - (µm)	50	60	70	85	100

The five process parameters (Table 3-5) were considered as control factors while the rest of process parameters were considered as to create a range of noise conditions. Thus, for a five, five-level factors there are a total of 3125 (5^5) different combinations that should be considered for a full factorial design. Using other fractional design such as Central Composite Design (CCD) and Box-Behnken Design (BBD) leads to 52-104 and 46-60 combinations (experiments) respectively. The range of the number of experiments of CCD and BBD depends on the number of factors that are considered as continuous or categorical factors. However, using the Taguchi approach for designing the experiments, the number of experiments required can be reduced drastically to save time and resources, and the approach still yields results in good agreement with other methods [138]. According to the Taguchi approach, the samples can be organised into only 25 groups. An orthogonal array of L25 was used for 5 parameters and 5 levels. Each run was repeated four times. Minitab17 was used to build and analyse the experimental design.

The optimisation experiments (runs) and their process parameters were generated using the Taguchi methods (Table 3-6). Each run was repeated 4 times so that at the end of the experiment, there were 100 fabricated samples. For the same layer thickness, the machine is able to fabricate samples with different process parameters. As a result, the runs were grouped according to the LT. The parts were fabricated in five builds with varying layer thicknesses from 20µm to 100µm.

Table 3-6: Experimental runs generated by the Taguchi method for Ti-6Al-4V ELI and their process parameters

Run#	***LT*** *(µm)*	***LP*** *(W)*	***PD*** *(µm)*	***ET*** *(µs)*	***HD*** *(µm)*
1	20	90	35	50	50
2	20	120	45	70	60
3	20	150	55	100	70
4	20	180	70	150	85
5	20	200	100	200	100
6	30	90	45	100	85
7	30	120	55	150	100
8	30	150	70	200	50
9	30	180	100	50	60
10	30	200	35	70	70
11	50	90	55	200	60
12	50	120	70	50	70
13	50	150	100	70	85
14	50	180	35	100	100
15	50	200	45	150	50
16	70	90	70	70	100
17	70	120	100	100	50
18	70	150	35	150	60
19	70	180	45	200	70
20	70	200	55	50	85
21	100	90	100	150	70
22	100	120	35	200	85
23	100	150	45	50	100
24	100	180	55	70	50
25	100	200	70	100	60

3.4.1.2. 316L-SS

For 316L-SS process parameters optimisation, the same process parameters were considered except the LP was kept fixed at the highest possible value. Using high laser power, however, widens the process window for other process parameters and provides

greater flexibility in investigating a wider range of process parameters on additively manufactured 316L-SS parts [50]. In addition, the result of optimising the process parameters for the Ti-6Al-4V ELI showed that using the LP with its maximum possible value improves the part density and can increase the system throughput. Therefore, the laser power in this study was used at its maximum value of 200W. The process parameters and their selected ranges are shown in Table 3-7.

Table 3-7: Range of the process parameters used in the experiments for 316L-SS

Parameter	***Range***	
	min	max
Layer Thickness, LT - (µm)	50	100
Point Distance, PD - (µm)	40	80
Exposure Time, ET - (µs)	50	150
Hatching Distance, HD - (µm)	50	120

The axial-points CCD of RSM was used to design the experiments for fabricating 316L-SS parts. For the four selected process parameters, the RSM suggested 31 runs in total (Table 3-8) which are classified as 16 cube points, 8 axial points and 7 centre points. The levels of the factors (process parameters) were selected as axial points. The design was replicated 4 times. Minitab17 was used to design and analyse the experiments.

Table 3-8: Suggested runs by the RSM for 316L-SS

Run#	***LT*** *(µm)*	***PD*** *(µm)*	***ET*** *(µs)*	***HD*** *(µm)*
1	50	60	100	85
2	65	50	75	68
3	65	70	75	68
4	65	50	125	68
5	65	70	125	68
6	65	50	75	103
7	65	70	75	103
8	65	50	125	103
9	65	70	125	103
10	75	40	100	85
11	75	80	100	85
12	75	60	50	85
13	75	60	150	85
14	75	60	100	50
15	75	60	100	120
16	75	60	100	85
17	75	60	100	85
18	75	60	100	85
19	75	60	100	85
20	75	60	100	85
21	75	60	100	85
22	75	60	100	85
23	90	50	75	68
24	90	70	75	68
25	90	50	125	68
26	90	70	125	68
27	90	50	75	103
28	90	70	75	103
29	90	50	125	103
30	90	70	125	103
31	100	60	100	85

3.4.2. Layer Thickness vs. Particle Size Distribution Samples

From the results obtained during the optimisation stage, the optimum process parameters of LP, PD, and HD were used to investigate the effect of changing the layer thickness and the powder size distribution on the density of parts at different exposure times. The exposure time (ET) variable was used to keep the volumetric energy density

(VED) constant and study its effect on the density of samples when LT and PSD were changed. Three powder types of Ti-6Al-4V ELI and two powder types of 316L-SS were used to build 10x10x10mm^3 cubes with different layer thicknesses. The exposure time was varied at each layer thickness build for obtaining a range of energy densities. Each powder type was used to build parts with different layer thicknesses. The exposure time was varied in increments of 10µs to study its effect on layer thickness for a particular PSD. Table 3-9 shows the layer thicknesses (LT) and exposure time (ET) values for Ti-6Al-4V ELI and Table 3-10 for 316L-SS.

Table 3-9: Exposure time range and number of samples for each layer thickness for Ti-6Al-4V ELI

LT (µm)	T1	30	-	60	80	100
	T2	-	40	60	80	100
	T3	-	-	60	80	100
ET range (µs)		20-120	20-160	40-250	60-330	70-420
Number of samples		11	15	22	28	36
Repeat		4	4	4	4	4
Total number of samples		44	60	88	112	144
Total		1136				

Table 3-10: Exposure time range and number of samples for each layer thickness for 316L-SS

LT (µm)	S1	30	-	60	80	100
	S2	-	40	60	80	100
ET range (µs)		40-140	50-160	90-240	130-330	160-420
Number of samples		11	12	16	21	27
Repeat		4	4	4	4	4
Total number of samples		44	48	128	168	216
Total		604				

The range of volumetric energy density (Eq. (3-6)) was approximately the same for all layer thicknesses. The total number of samples that were produced was 1136 samples for the Ti-6Al-4V ELI and 604 samples for 316L-SS.

$$Volumetric\ Enegy\ Density\ (VED)\ = \frac{LP}{SS * HD * LT} \quad (3\text{-}6)$$

It is possible to obtain the same value of VED by adjusting the process parameter combinations. However, certain combinations may not be suitable for a successful build for reasons which will be elaborated on in the result chapters.

3.5. Porosity Evaluation

The density of the samples was measured using the Archimedes principle which is considered by Spierings et al. [152] to be a reliable and fast method. The authors [152] aimed to set a standard for measuring the density of AM parts, comparing the accuracy of three density measurement methods: microscopic analysis of cross section, X-ray computed tomography (CT) scanning and the Archimedes principle. They concluded that the microscopic analysis of a cross section can be used to find the size and distribution of the porosity, however, as the porosity increases in a part, the variation of measurement increases. Also, as this is a destructive approach, the sample is destroyed after measurement due to sectioning. The advantage of X-ray CT scanning is that it is a non-destructive technique and allows the 3D visualisation of the porosity distribution throughout the part, however, due to resolution limitations of the machine, relatively small pores may not be detected, thus giving a density reading which is higher than the true density and the process is extremely time consuming. Despite the long history of use and development of X-ray CT scanning it still has some challenges [153]. The two most relevant challenges are resolution and beam hardening. Resolution is the ability of the imaging system to capture small features (pores in this study). The scanner cannot capture a pore that is smaller in size than the spatial resolution of the system. The other challenge is “beam hardening”. Beam hardening is one of the most common weaknesses of polychromatic X-ray CT scanning systems. As the beam passes through the object, the lower-energy photons are absorbed. The high-energy photons pass through the object resulting in a non-linear attenuation for the different thickness areas of the object. This produces a dishing effect in the 2D image and shading effect in the 3D reconstructed volume. There are two simple methods to deal with the beam hardening: using an algorithm to linearise the projection data using a calibration curve and adding a metal filter in the path of the beam to absorb the low-energy photons. Finally, the

Archimedes method which is relatively easy and quick to conduct delivers more reliable results as the whole part is used for measurement.

The following steps were taken to evaluate the density of the samples:

1. As the supports were processed using a different melt strategy from the selected melt parameters, the samples were ground to remove any residual supports ensuring that the samples evaluated were purely built by the selected build strategy being investigated.

2. After the removal of supports, the samples were ultrasonically washed using Ultraclean SA solution with water (5:100 ml) for 15 minutes at 45^0C to remove any residual powder.

3. The samples were then dried in the atmosphere and allowed to cool to room temperature before evaluation.

4. Weighing scale accurate to 3-decimal places was used to calculate the density.

5. Each sample was measured three times in air and three times in distilled water. Then the values were expressed using the mean value.

6. The measurements were taken at a room temperature between 19.5^0C and 21.5^0C, with the density of distilled water taken as 0.998 g/cm^3.

7. The density was calculated using equation (3-7).

$$Density = \left(\frac{weight\ in\ air - weight\ in\ liquid}{weight\ in\ air}\right) * density\ of\ liquid \qquad (3\text{-}7)$$

8. The densities of the parts were analysed using Minitab17 to establish the significant factors that affect the density of L-PBF fabricated samples and therefore determine the best combination of parameters to produce the highest density for the built part.

Some samples were CT scanned to visualise the porosity distribution using Nikon CTH225 LC model (X-TEK SYSTEM LTD, UK). The scan was performed at a

180kV voltage, a 74µA current and a molybdenum reflection target. The resolution (voxel size) was 13.5µm and a 0.25mm Cu beam filter was used to reduce beam hardening artefacts.

EXPERIMENTAL RESULTS

The following chapters display the results for the experimental work conducted along with the discussion in relation to the analysis of the results. The obtained results for the process parameters' optimisation are discussed in Chapter 4, followed by Chapter 5 which discusses the results of developing the regression models and investigating the correlation between LT and PSD. The build location effect is discussed in Chapter 6.

4. PROCESS PARAMETER DETERMINATION

The process reliability depends critically on the correct establishment of the process parameters. To achieve this within this study, optimum process windows were determined depending on the optimisation phases that were conducted for each material. The key objective of the process parameters optimisation stage was to achieve the maximum part density for the parts built. The range of investigated process parameters and the generated process parameter combinations were discussed in Chapter 3. The results of the process parameters optimisation and the experimental findings are presented in this chapter. Section 4.1 details the results related to Ti-6Al-4V ELI, and Section 4.2 details the results associated with 316L-SS.

4.1. Process Parameters Optimisation for L-PBF of Ti-6Al-4V ELI

The experimental runs that were generated by the DOE (Chapter 3.4.1.1) were conducted to investigate and identify the optimum combination of process parameters which give the highest part density. The Taguchi method was used to optimise the process parameters of the Ti-6Al-4V ELI. The experimental results are illustrated in Table 4-1 and in Figure 4-1, where it can be seen that the maximum average relative density (RD) recorded is 99.97%, which was for run number 6. The average RD measurement is the result of three separate readings for each of the four cubes built in each run. The accuracy of measurements of the selected method depends on the surface roughness of all sides of the sample and the surface tension of the liquid (distilled water). When the surface is smooth, the variation of the measurements is small and vice versa.

Table 4-1: Average relative density (RD) resulted from the experimental runs of Ti-6Al-4V ELI

Run No.	*Cube No.*	*Avg. RD %*	*Run No.*	*Cube No.*	*Avg. RD %*	*Run No.*	*Cube No.*	*Avg. RD %*
1	1-4	99.09	**10**	37-40	99.56	**19**	73-76	98.39
2	5-8	99.92	**11**	41-44	99.51	**20**	77-80	99.16
3	9-12	99.62	**12**	45-48	94.60	**21**	81-84	94.34
4	13-16	98.86	**13**	49-52	97.98	**22**	85-88	97.00
5	17-20	99.00	**14**	53-56	97.07	**23**	89-92	95.61
6	21-24	99.97	**15**	57-60	96.48	**24**	93-96	98.86
7	25-28	99.64	**16**	61-64	91.23	**25**	97-100	99.34
8	29-32	98.22	**17**	65-68	97.11			
9	33-36	99.13	**18**	69-72	97.84			

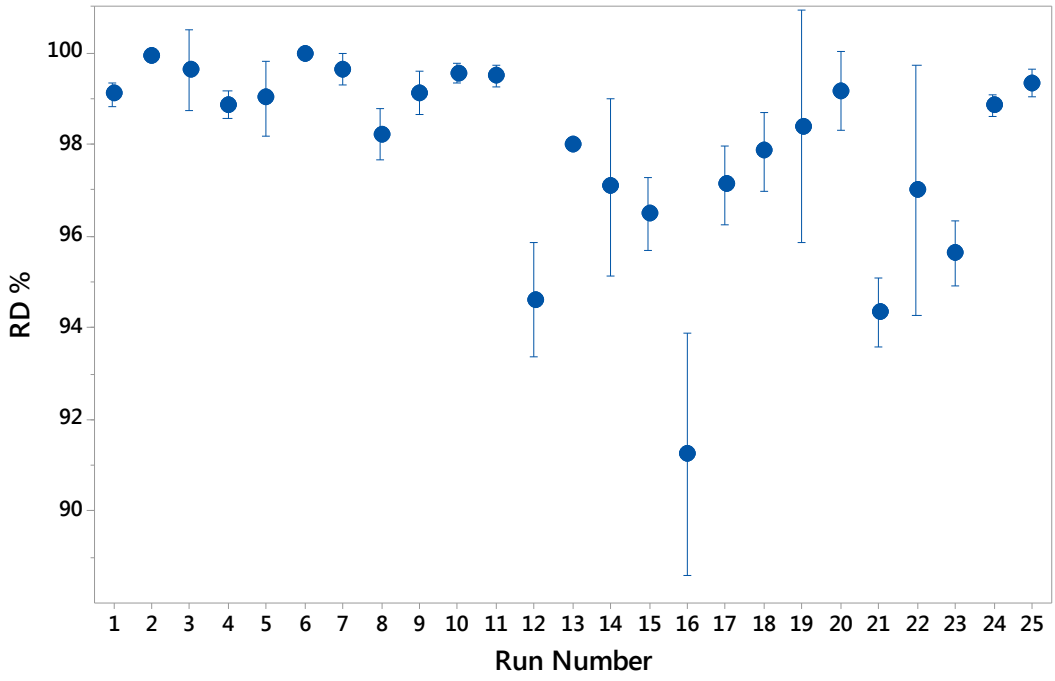

Figure 4-1: Relative density of the Ti-6Al-4V ELI cubes for each run, indicating measurement accuracy

The porosity was visualised by using X-ray computed tomography (CT) using CTH225 LC model (X-TEK SYSTEM LTD, UK). Figure 4-2 shows samples of CT scanned cubes. The selected cubes represent the maximum and minimum relative density, cube 21 from run 6 and cube 61 from run 16 respectively (Figure 4-2 (a) and (c)). The other scanned cubes (b and d) were selected according to the average high and average low

RD. The majority of porosity distribution was located in the centre of the samples. In cube number 27, however, the porosity was more concentrated to the right-hand side of the cube. This could be caused by the machine architecture along with the process parameters (i.e. the gas flow direction is from the right to the left). The calculated RD value via the CT scan was slightly higher than that calculated by the Archimedes' principle. The calculated RD of the CT scanned cubes 21, 27, 61 and 95 was 99.99%, 99.90%, 93.24% and 98.94% respectively while the calculated RD using Archimedes' principle was 99.96%, 99.46%, 88.87% and 98.92% respectively. This variation is believed to be due to the incapability of the CT scan to detect small pores, due to resolution limitations of the machine.

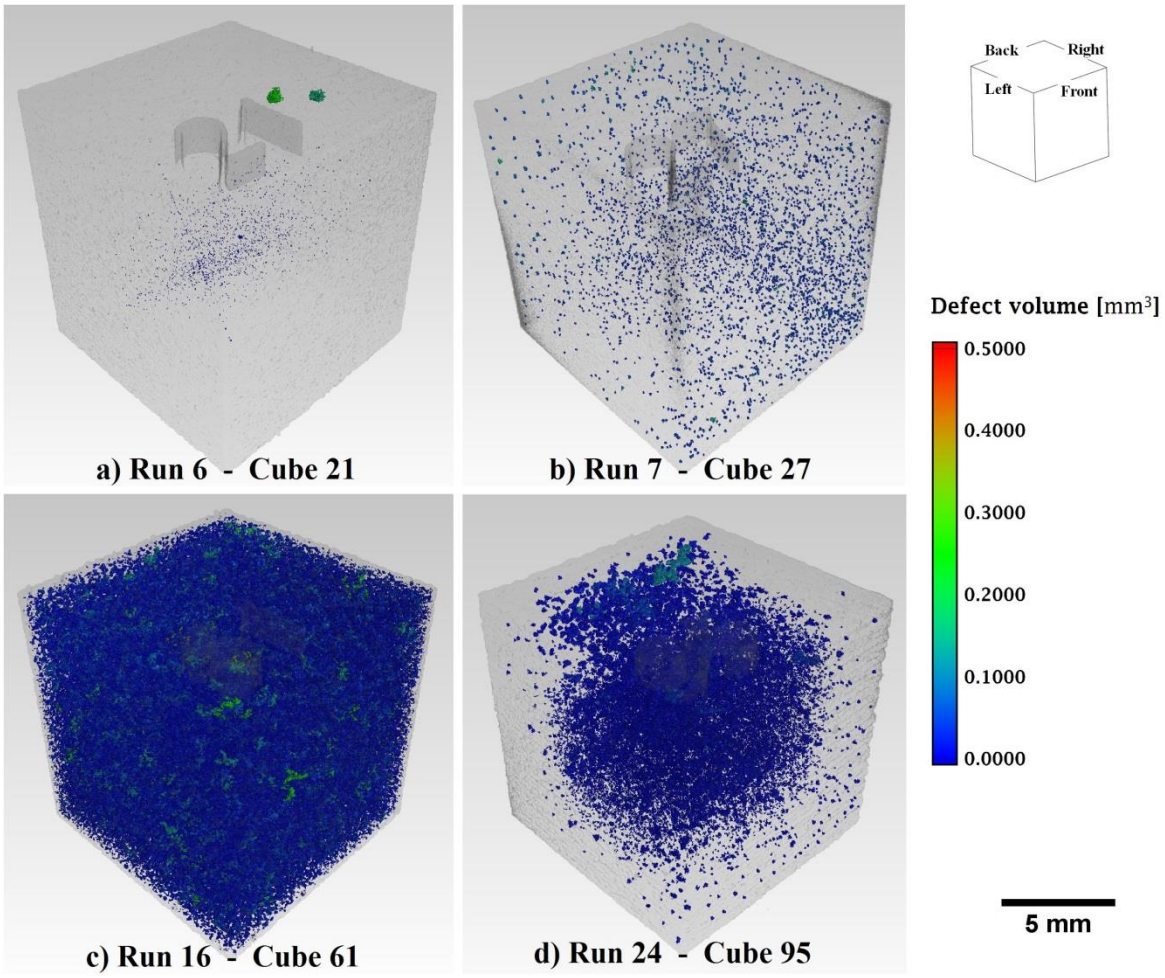

Figure 4-2: CT scanning of the internal porosity accumulation of samples 21, 27, 61 and 95 from Run number 6, 7, 16 and 24 respectively identified by colour according to pore size

For the most effective process parameters, the Signal-to-Noise ratio S/N ratio was analysed and summarised in Table 4-2. The Delta value represents the difference between maximum and minimum S/N ratio for the levels of each factor. The value of

Delta represents the significance of a factor, with a higher Delta value indicating a greater significance of that factor.

Table 4-2: Response Table for Signal to Noise Ratios (Larger is better) for resultant density

	S/N for factor:				
Level	**LT**	**LP**	**PD**	**ET**	**HD**
1	12.87	12.64	12.76	12.71	12.75
2	12.87	12.72	12.76	12.7	12.85
3	12.67	12.74	12.87	12.81	12.69
4	12.64	12.79	12.61	12.7	12.8
5	12.66	12.81	12.71	12.79	12.61
Delta	0.23	0.17	0.26	0.11	0.24
Rank	3	4	1	5	2

The highest values for the S/N ratio of the factors identify the ideal level in terms of the control factor settings, which minimizes the effects of the noise factors. The factors are ranked according to their effectiveness. As shown in Table 4-2 and Figure 4-3, point distance (PD) and hatch distance (HD) are the most significant factors (Rank 1 and Rank 2 respectively). Layer thickness (LT) is the third most influential factor on the process, followed by laser power (LP) and finally, exposure time (ET).

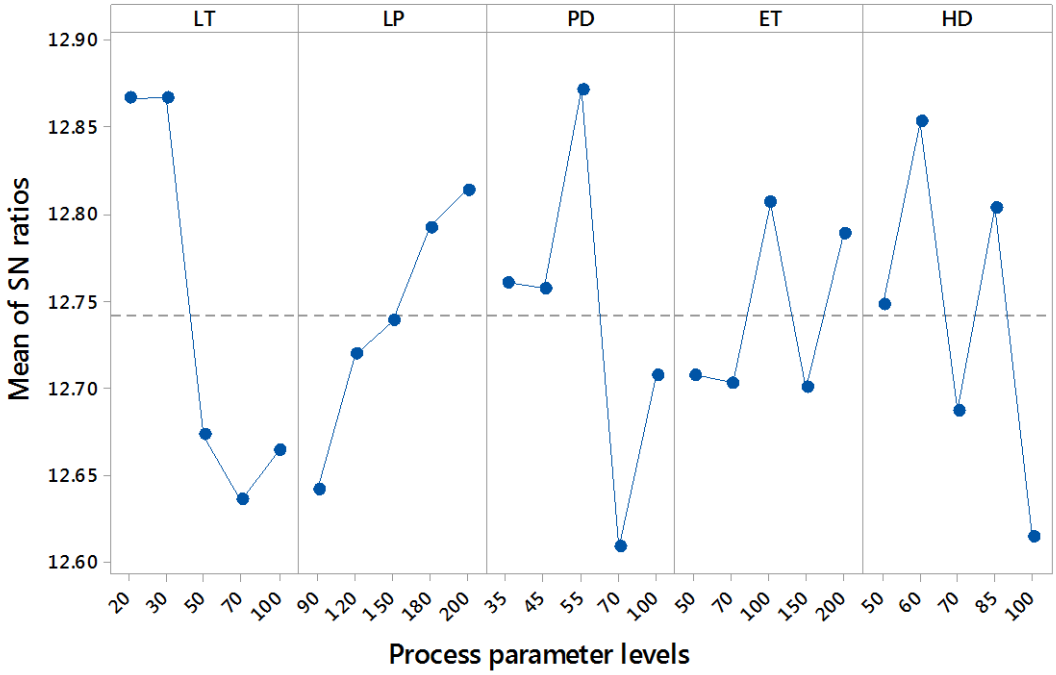

Figure 4-3: Main effects plot for S/N ratios (larger is better) for the resultant density

The optimal parameter combination from the selected experimental design identified is: layer thickness of 30µm, laser power of 200W (maximum power gives greater flexibility in choosing other parameter ranges [50]), point distance of 55µm, exposure time of 100µs, and hatching distance of 60µm.

Validation experiments were carried out using the same materials and equipment as previously described. The levels of factors were selected around the best combination of parameters that were established by the Taguchi method. Layer thickness and laser power were fixed at 30µm and 200W respectively. The experiments were based on a full factorial experiment (Table 4-3).

Table 4-3: Validation process parameters levels

#	*Parameter*	*Levels*			
1	Layer Thickness - (µm)	30			
2	Laser Power - (W)	200			
3	Point Distance - (µm)	50	55	60	65
4	Exposure Time - (µs)	50		100	
5	Hatching Distance - (µm)	55	60	65	

The results from the validation experiments show that there are additional combinations of point distance and hatching distance that produce higher density parts (Figure 4-4). Two other combinations of process parameters were obtained: the first where the PD is 50µm, ET is 50µs, and HD is 65µm and the second where the PD, ET, and HD are 65µm, 50µs, and 65µm respectively.

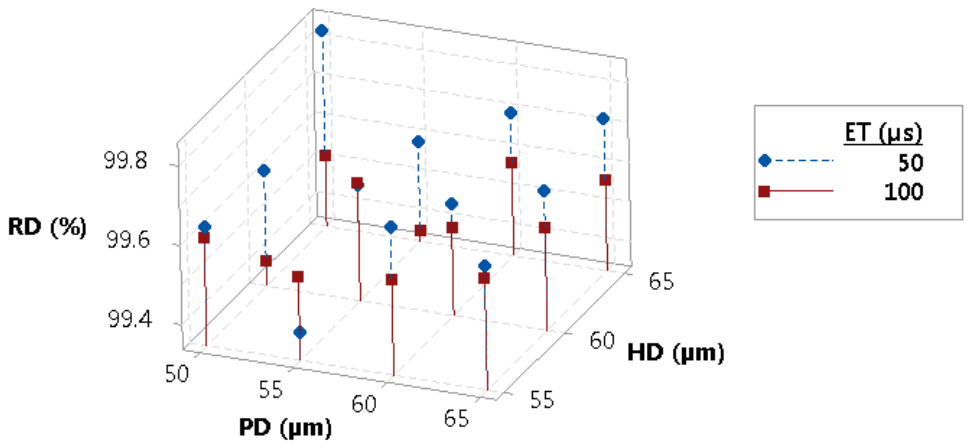

Figure 4-4: Results of validation experiments comparing the relative density with respect to the point distance and hatching distance at exposure time of 50µs and 100µs.

From Table 4-4, the density of the Ti-6Al-4V ELI parts fabricated using the new parameters combinations, identified via the validation experiments, was higher in comparison to the density of the parts obtained by either the Taguchi method or the manufacturer's recommended profile. Using the exposure time suggested by the Taguchi method (ET of 100µs) preserves the robustness of the process and ensures the system is less sensitive to any slight changes in other parameters such as the PD and the HD. The relative density percentage given in Table 4-4 is in comparison to the theoretical density of titanium alloy (4.43g/cm^3 [154]).

Table 4-4: Comparison of results of the process parameter combinations found by Taguchi and validation experiments against the manufacturer's profile for Ti-6Al-4V ELI

Parameter	*Taguchi*	*Valid. Process 1*	*Valid. Process 2*	*Manufacturer's profile*
Layer Thickness - (µm)	30	30	30	30
Laser Power - (W)	200	200	200	200
Point Distance - (µm)	55	50	65	75
Exposure Time - (µs)	100	50	50	50
Hatching Distance - (µm)	60	65	65	65
Relative Density – (%)	99.62	99.83	99.72	99.53

Figure 4-5 shows the relationship between volumetric energy density (VED) and relative density for the different layer thicknesses. The results indicate that it is possible

to fabricate parts with a larger layer thickness and still obtain high density parts. The effect of changing the layer thickness is comprehensively investigated in the next chapter, in addition to changing the particle size distribution of the primary powder.

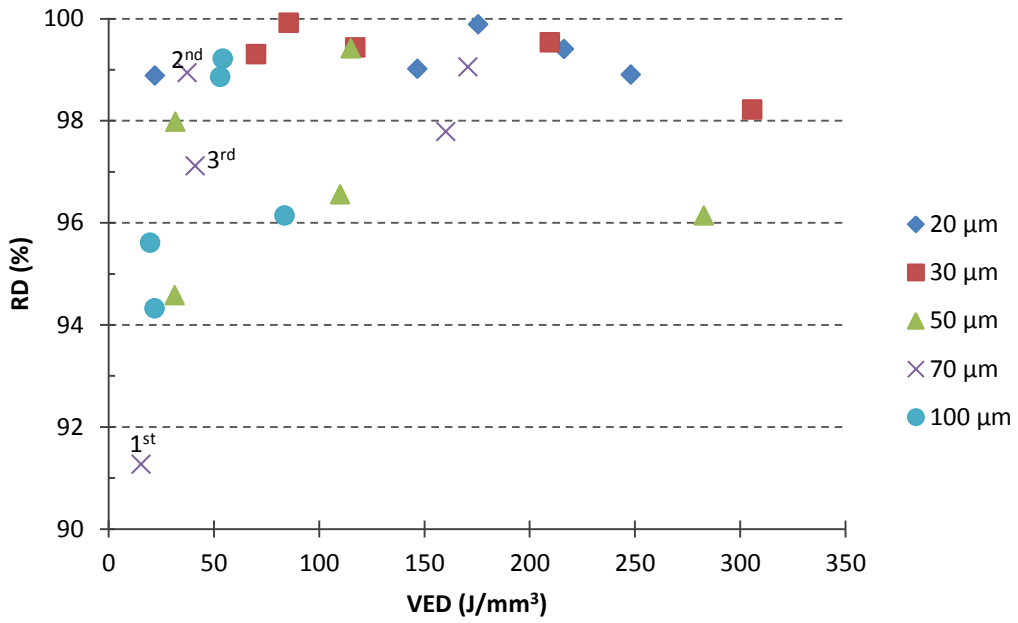

Figure 4-5: The relative density of Ti-6Al-4V ELI parts versus VED for each layer thickness obtained from optimisation phase

Using a layer thickness of 30µm gives the highest relative density. It is, however, possible to use thicker layers with an adjusted VEDs in the optimal parameter window, to fabricate high density parts, as with all layer thicknesses investigated it was possible to achieve a relative density of approximately 99%.

The noticeable variation in density for a single layer thickness might be caused by a combination of parameters, not solely by the overall value of VED. For the second (2^{nd}) and third (3^{rd}) points of the 70µm layer thickness in Figure 4-5, it can be noted that the combination of process parameters led to similar VED values, however, the part densities varied significantly. The main effect in this case was the point distance (PD). The third point had almost double the point distance of the second point, 100 vs 55µm respectively and the density of the third point is 97% while the second point has a density of 99%. It is clear from above that the value for the VED alone is not appropriate to achieve a successful build, and that it is of paramount importance to understand the individual components which in combination deliver a specific value of VED. Therefore, the values of process parameters should be carefully selected to

establish certain values of scan speed or VED. Figure 4-6 shows that there is a linear relationship between LT and RD, and also LP and RD but the other three factors exhibit a non-linear relationship with respect to RD. Using a small PD, high ET or small HD results in a high energy density which contributed and resulted in evaporation and the development of keyhole porosity. In contrast, high PD, small ET or high HD causes a lack of fusion due to insufficient energy density being applied to fully melt the powder. Therefore the relation of these three factors to the relative density was non-linear. Moreover, it is expected that the LP also has a non-linear relation with RD which would be if an excessive LP was used, however, due to limitations of the current system used in this study, the maximum LP achievable was 200W, up to which the relation appeared linear.

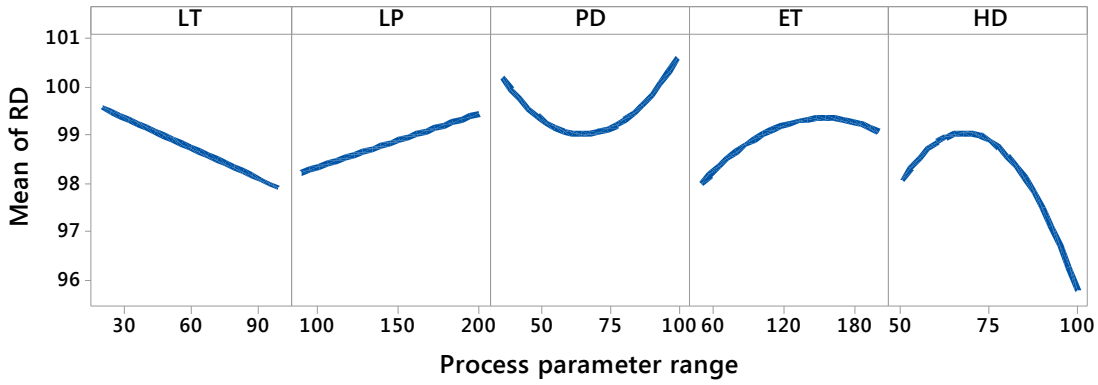

Figure 4-6: Main effects plot for RD of Ti-6Al-4V ELI parts and its relationship with each parameter

Table 4-5 shows the optimum process parameters that were used in the investigation of particle size distribution and layer thickness in the next chapter.

Table 4-5: Optimum process parameters of L-PBF for Ti-6Al-4V ELI

Parameter	***Value***
Layer Thickness - (µm)	30
Laser Power - (W)	200
Point Distance - (µm)	50
Exposure Time - (µs)	50
Hatching Distance - (µm)	65

4.2. Process Parameters Optimisation for L-PBF of 316L-SS

Experiments were carried out to establish the factors that have the greatest effect on the density of metal parts fabricated by PBF technology and to determine the best combination of process parameters. The RSM was used to design and analyse the experiments for 316L-SS alloy. The results for the relative density measurements are shown in Table 4-6. The measured values ranged from 93% to above 99%, compared to the standard density of 316L-SS of 7.99g/cm^3 [155].

Table 4-6: Experimental results of the RD of 316L-SS for all runs selected by the RSM design

Run No.	***RD %***	***Run No.***	***RD %***	***Run No.***	***RD %***	***Run No.***	***RD %***
1	99.05	**9**	98.94	**17**	98.67	**25**	96.23
2	98.74	**10**	96.55	**18**	98.64	**26**	96.97
3	98.92	**11**	98.85	**19**	98.70	**27**	98.13
4	96.56	**12**	93.35	**20**	98.77	**28**	93.26
5	98.44	**13**	96.74	**21**	98.76	**29**	96.27
6	98.96	**14**	97.81	**22**	98.80	**30**	98.79
7	97.79	**15**	98.96	**23**	97.04	**31**	96.92
8	97.48	**16**	98.67	**24**	97.91		

The analysis of variance (ANOVA) was used to identify the significant factors and their interactions with each other (Table 4-7). The significance of the terms was calculated by conducting the F-test. The test compares the ratio of the mean square of a term to the error mean square. The P-value is then found from the F distribution. If the P-value is less than a threshold (set to 5%), the null hypothesis should be rejected and the term is statistically significant. The null hypothesis in this case was the term is not significant to explain the change in the response (density) when process parameters are changed. According to the P-value of the F-test, all process parameters have a significant effect on the response (density), in the selected ranges. Based on the ANOVA analysis it can be concluded that most of the linear, quadratic and two-way interaction terms have significant effects on the density of additively fabricated parts. The factors LT^2, HD^2, LT*PD, and LT*HD were found to be insignificant.

Table 4-7: ANOVA analysis for the selected factors and their interactions

Source	*DF*	*Adj Sum of Square*	*Adj Mean Square*	*F-Value*	*P-Value*
Model	14	1.33232	0.095166	23.71	0
Linear	4	0.37436	0.09359	23.32	0
LT	1	0.02773	0.027734	6.91	0.01
PD	1	0.02190	0.021897	5.46	0.021
ET	1	0.26668	0.266680	66.45	0
HD	1	0.04568	0.045679	11.38	0.001
Square	4	0.57613	0.144033	35.89	0
LT*LT	1	0.01448	0.014482	3.61	0.06
PD*PD	1	0.0329	0.0329	8.2	0.005
ET*ET	1	0.56138	0.561382	139.88	0
HD*HD	1	0.00125	0.001251	0.31	0.578
2-Way Interaction	6	0.42371	0.070618	17.6	0
LT*PD	1	0.01512	0.015122	3.77	0.055
LT*ET	1	0.03826	0.038262	9.53	0.003
LT*HD	1	0.00783	0.007834	1.95	0.165
PD*ET	1	0.21438	0.214378	53.42	0
PD*HD	1	0.05248	0.052485	13.08	0
ET*HD	1	0.09562	0.095624	23.83	0
Error	109	0.43746	0.004013		
Total	123	1.76978			

To find the optimal values of the selected factors, the RSM response optimiser was used to analyse the results of the density measurements. Figure 4-7 shows the optimal parameter combination for high density parts from the selected experimental design. The optimal value of parameters were identified as: point distance (PD) of approximately 70µm, exposure time (ET) of 120µs, hatching distance (HD) of 120µm and layer thickness (LT) of 50µm.

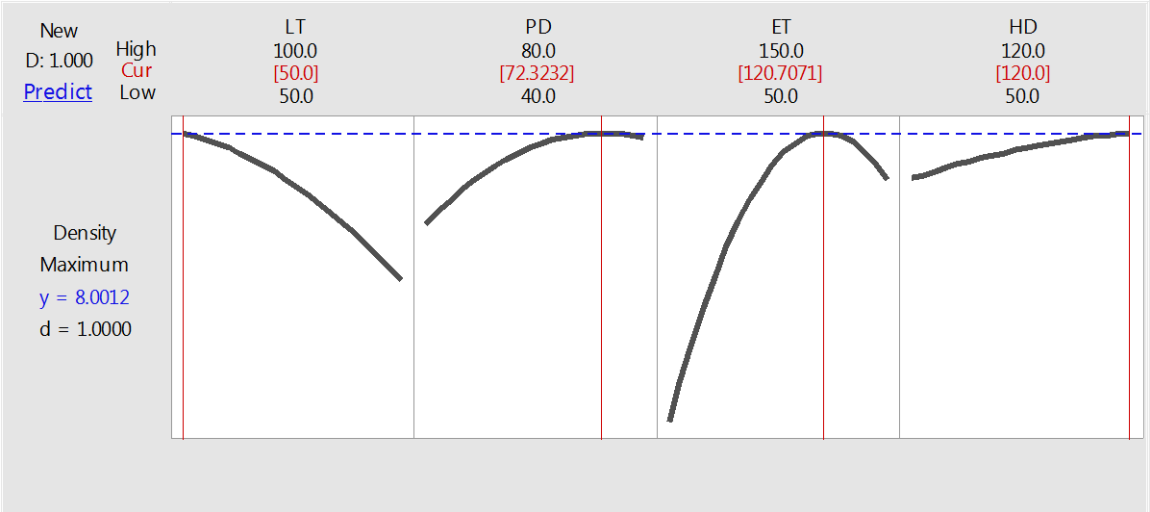

Figure 4-7: Process parameters optimisation shows the optimal parameter combination for high density from the selected experimental design for 316L-SS.

The optimal process parameters identified should result in the highest possible density of the fabricated part according to the selected process parameter ranges. Validation experiments were then selected to validate the findings and investigate any other possible parameter combinations that could produce high density parts. The parameters' values were maintained at the point determined by the previous optimisation with the exception of the exposure time, which was changed to obtain different energy densities (runs 1-8 and 9-11). Further runs were selected using the Minitab 17 optimiser and contour figures to find additional combinations of parameters that would give high part density (runs 12-16). Table 4-8 shows the values of the parameters of validation experiments and the results of their relative density.

Table 4-8: Process parameter combinations that were used in validation builds and their resultant relative density for 316L-SS parts

Run #	*LT (µm)*	*PD (µm)*	*ET (µs)*	*HD (µm)*	*RD (%)*
1	50	72	70	120	96.00
2	50	72	80	120	97.85
3	50	72	90	120	98.84
4	50	72	100	120	99.02
5	50	72	110	120	98.94
6	50	72	120	120	99.18
7	50	72	130	120	99.02
8	50	72	140	120	99.08
9	50	70	100	120	99.08
10	50	70	110	120	99.02
11	50	70	120	120	99.19
12	50	50	60	60	98.85
13	50	80	102	50	98.92
14	50	100	125	70	99.05
15	50	75	95	50	99.00
16	50	80	110	85	99.00

The results of the validation experiments demonstrate that the process parameters found in the optimisation stage (runs 6 and 11) provide the highest density parts. There are other combinations of parameters that can give relative density of approximately 99%, e.g. runs 12-16. The lowest obtained porosity was 0.8% which may be inherited from internal porosity of the raw powder. The optimum process parameters identified for 316L-SS powder are shown in the Table 4-9.

Table 4-9: Optimum process parameters of L-PBF for 316L-SS

Parameter	*Value*
Layer Thickness - (µm)	50
Laser Power - (W)	200
Point Distance - (µm)	70
Exposure Time - (µs)	120
Hatching Distance - (µm)	120

4.3. Micro-Level Density Analysis for 316L-SS Parts

The results presented in Sections 4.1 and 4.2 indicate that 316L-SS is more sensitive to process parameter changes and tends to have greater porosity than Ti-6Al-4V ELI under the respective optimal process parameters identified. Therefore, it is beneficial to investigate the location of the porosity at micro level. The parts porosity/density was studied using a technique of image processing via a MATLAB code adapted from Rabbani et al. [156] and available in Appendix A. The result obtained by the image processing code showed a good agreement with results obtained by the Archimedes method with the average and standard variation of 0.90% and 0.54% respectively (0.90 ± 0.54%). The samples were sectioned along the XZ plane as shown in Figure 4-8 .Optical images from the build-direction cross-sectional area were converted to black and white binary images, where the black pixels corresponded to pores/air. The ratio of black pixels to the total number of pixels was calculated to estimate the porosity. The influence of the process parameters of layer thickness, point distance, exposure time and hatching distance on developing different shapes, sizes and locations of porosity was investigated. The correlation between each process parameter and the porosity is discussed in the subsequent sections.

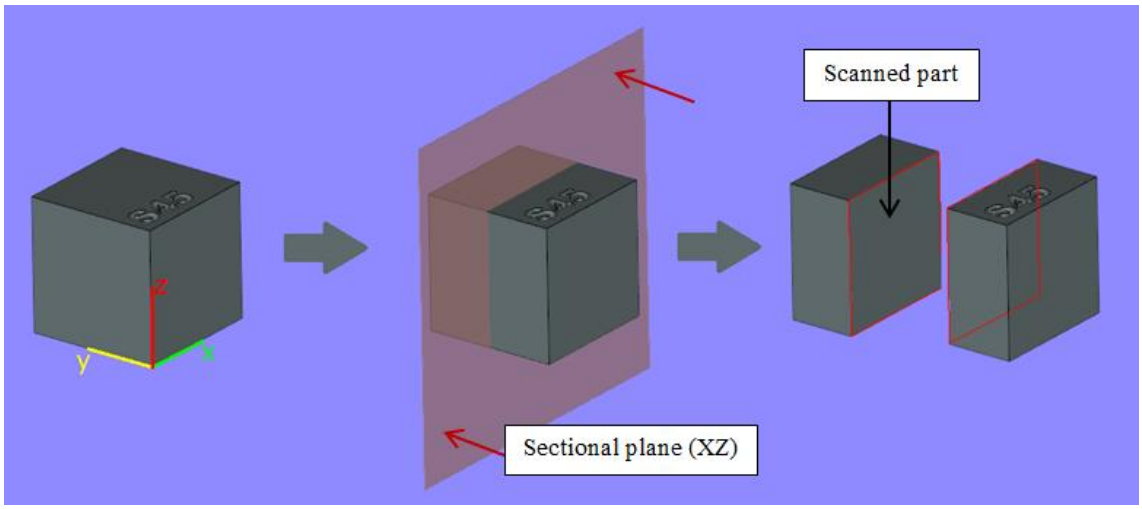

Figure 4-8: A schematic diagram shows the sectional (xz) plane where z is the build direction. The section was approximately in the middle of the y dimension and xz-plane is the scanned face.

Figure 4-9 to Figure 4-14 show the polished cross sections in the build direction for different cubes fabricated with a range of processing parameters together with a histogram analysis plot of each section. Every two adjacent plots (in the same row) are

for cubes that were fabricated by the same process parameters except for the process parameter under focus, to show the direct effect of this parameter.

4.3.1. Point Distance (PD)

Using a short distance between consecutive points in the melt track increases denudation and evaporation due to the increased energy being applied in a small area. Consequently, voids and pores were created. This was valid for all LTs. Small values of PD increase the VED which causes more evaporation and leads to a higher number of small pores. This is known as keyhole mode, when the fusion process passes the thermal conduction mode to keyhole mode. Increasing the PD by 20µm decreased the amount of pores dramatically. For instance, the estimated number of pores in Figure 4-9-(a) was 2339 with a largest pore radius of 68µm, while in Figure 4-9-(b) the number of pores reduced to 399 with a largest pore radius of 43µm. This dramatic reduction in the total number of pores was achieved by increasing the PD by 20µm (50µm to 70µm). Similarly for Figure 4-9 (c) and (d), the number of pores was reduced from 2404 for (c) to 821 for (d) by increasing PD by 20µm. While the mean pore size was 13.45 and 9.21 for (c) and (d) respectively, the largest pore size was 157.8µm for (c) and 42.1µm for (d) which shows a wide span in the pore size.

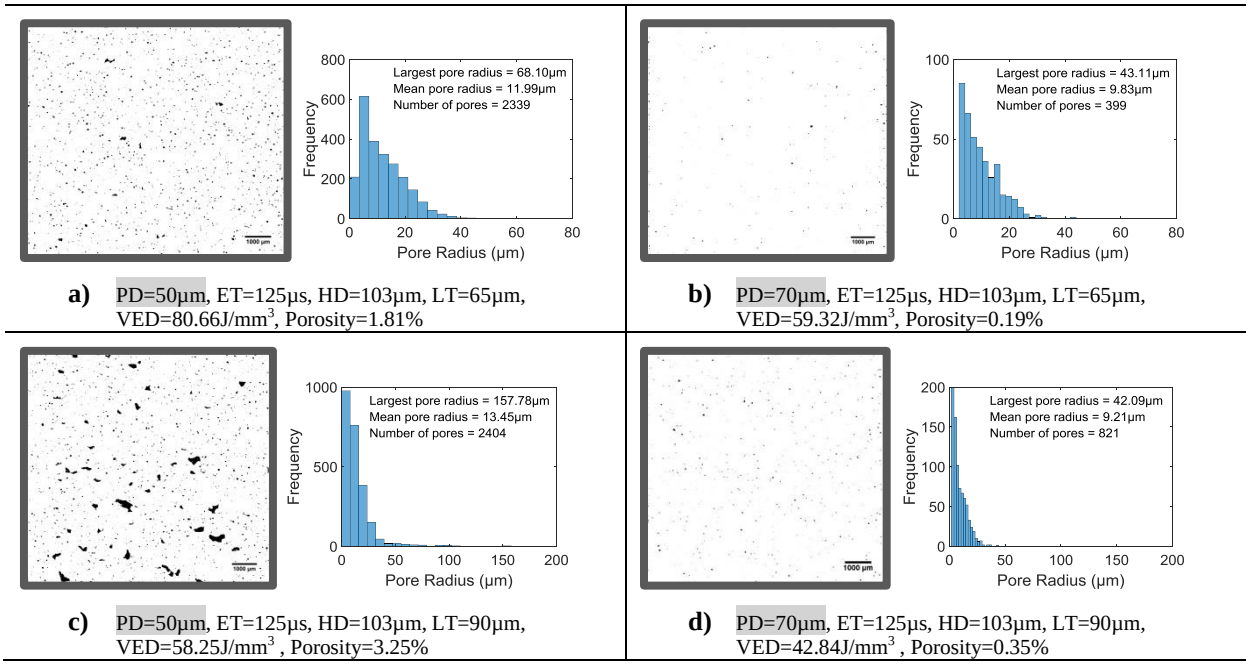

a) PD=50µm, ET=125µs, HD=103µm, LT=65µm, VED=80.66J/mm^3, Porosity=1.81%

b) PD=70µm, ET=125µs, HD=103µm, LT=65µm, VED=59.32J/mm^3, Porosity=0.19%

c) PD=50µm, ET=125µs, HD=103µm, LT=90µm, VED=58.25J/mm^3 , Porosity=3.25%

d) PD=70µm, ET=125µs, HD=103µm, LT=90µm, VED=42.84J/mm^3 , Porosity=0.35%

Figure 4-9: Optical micrographs and histogram analysis of polished build-direction sections of parts fabricated using ET of 100µs and HD of 103µm showing the effects of PD on the amount and size of pores at different LTs. All the scale bars are 1000µm.

4.3.2. Exposure Time (ET)

Exposure time (ET) has a twofold impact on porosity. It can increase the porosity if the PD is small, however, it can also reduce the porosity if the appropriate value of PD is used at all selected layer thicknesses. This means that the interaction between ET and PD has a significant influence. According to the cross-sectional area, the majority of pore shapes at a layer thickness of 65µm are spherical and small in size, compared to the pores of other layer thicknesses which are more irregularly shaped and larger in size. This is believed to be due to the lack of fusion when welding the different layers together (Figure 4-10). This indicates that when the VED is high, it results in evaporation and thus leads to small-circular pores. For instance, Figure 4-11 (a) vs (b) and (c) vs (d) show that by increasing the VED by increasing ET, dramatically affect the number of pores as well as reducing the RD. In (e) vs (f), where the LT was 90µm, the number of pores was not significantly affected, but the size of pores and the RD were negatively impacted.

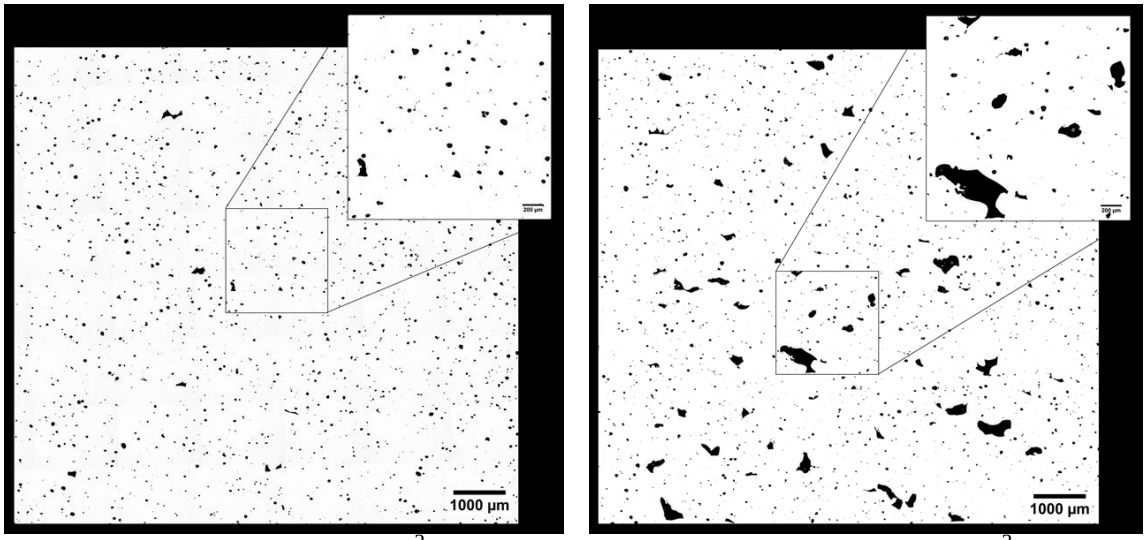

a) LT=65µm, VED=83.22J/mm^3 **b)** LT=90µm, VED=59.58J/mm^3

Figure 4-10: Shape of pores at process parameters of PD=50µm, ET=125µs, HD=103µm and (a) LT of 65µm and (b) LT of 90µm. Part (b) shows irregular shape due to lack of fusion to join the layer properly.

At larger PD (60 and 70µm), increasing the ET improved the fusing of subsequent layers on top of one another, leading to a dramatic improvement in the RD, pores size and number of pores. For example, the porosity was reduced by 8-9% and the number

of pores reduced by more than 85% when the ET was increased (Figure 4-11 (g) vs (h) and (i) vs (j)).

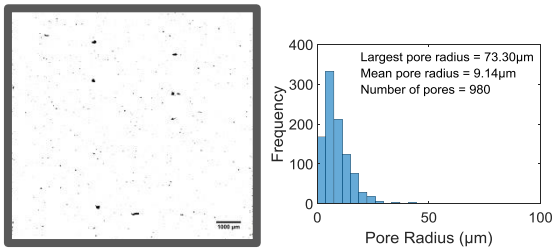

a) PD=50µm, ET=75µs, HD=68µm, LT=65µm, VED=76.92J/mm^3 , Porosity=0.46%

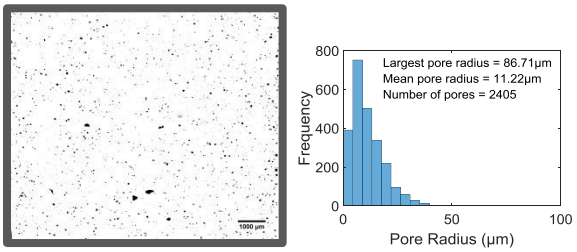

b) PD=50µm, ET=125µs, HD=68µm, LT=65µm, VED=122.17J/mm^3 , Porosity=1.78%

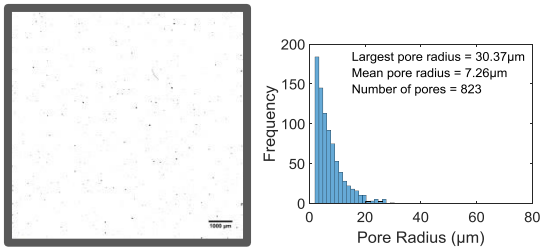

c) PD=50µm, ET=75µs, HD=103µm, LT=65µm, VED=50.78J/mm^3 , Porosity=0.21%

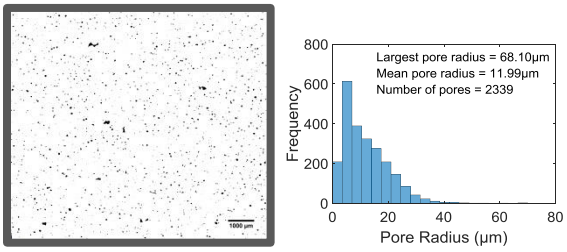

d) PD=50µm, ET=125µs, HD=103µm, LT=65µm, VED=80.66J/mm^3 , Porosity=1.81%

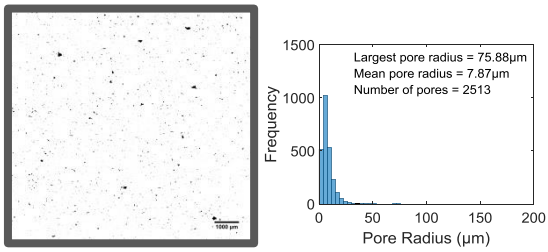

e) PD=50µm, ET=75µs, HD=103µm, LT=90µm, VED=36.68J/mm3 , Porosity=0.82%

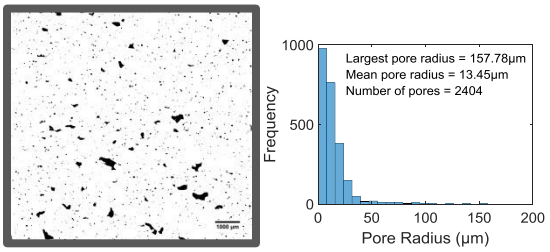

f) PD=50µm, ET=125µs, HD=103µm, LT=90µm, VED=58.25J/mm3 , Porosity=3.25%

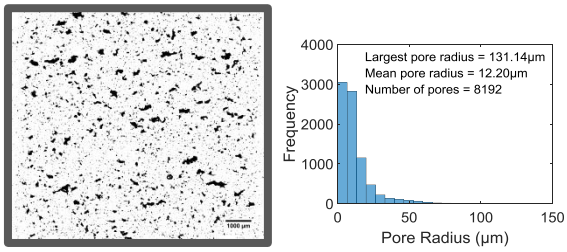

g) PD=60µm, ET=50µs, HD=85µm, LT=75µm, VED=32.42J/mm^3 , Porosity=8.78%

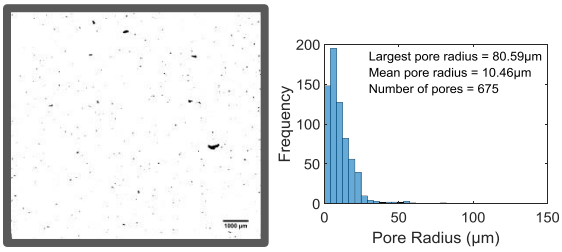

h) PD=60µm, ET=100µs, HD=85µm, LT=75µm, VED=58.56J/mm^3 , Porosity=0.44%

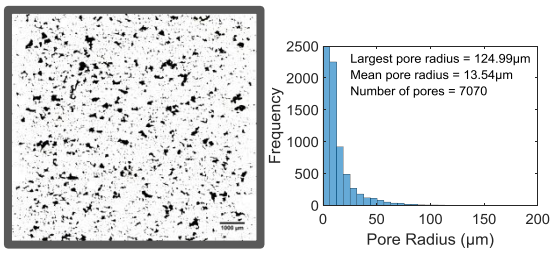

i) PD=70µm, ET=75µs, HD=103µm, LT=90µm, VED=27.43J/mm^3 , Porosity=9.58%

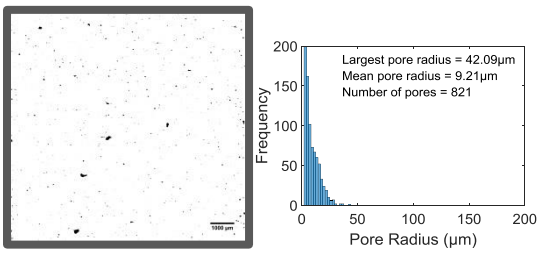

j) PD=70µm, ET=125µs, HD=103µm, LT=90µm, VED=42.84J/mm^3 , Porosity=0.35%

Figure 4-11: Optical micrographs and histogram analysis showing the effects of ET on the amount and size of pores at different process parameters. All the scale bars are 1000µm.

4.3.3. Hatching Distance (HD)

The effect of HD on the porosity was minimal when a LT of 65µm was used in conjunction with a PD of 50µm (Figure 4-12 (a) vs (b) and (c) vs (d)) or when the value of the ET was high (125µs) as shown in Figure 4-12 (e) vs (f). The change in the RD, pore size and the number of pores was not significant. Also, when the value of the parameters for the LT, PD, ET was at their midpoint of their selected range 75µm, 60µm, 100µs respectively, the effect of HD was insignificant (Figure 4-12 (g) vs (h)).

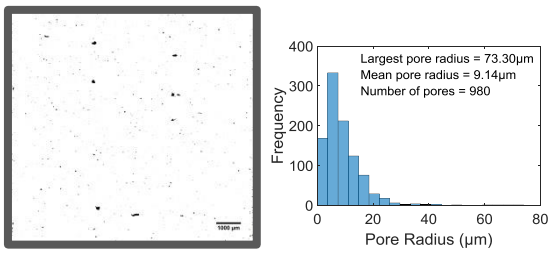

a) PD=50µm, ET=75µs, HD=68µm, LT=65µm, VED=76.92J/mm^3 , Porosity=0.46%

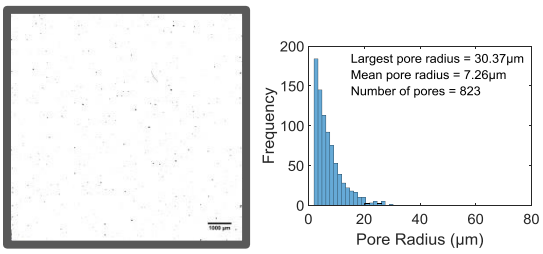

b) PD=50µm, ET=75µs, HD=103µm, LT=65µm, VED=50.78J/mm^3 , Porosity=0.21%

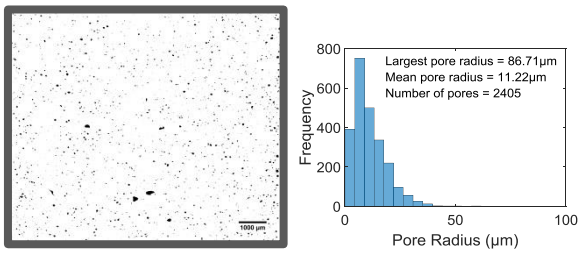

c) PD=50µm, ET=125µs, HD=68µm, LT=65µm, VED=122.17J/mm^3 , Porosity=1.78%

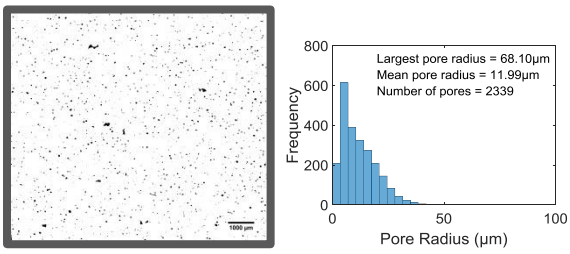

d) PD=50µm, ET=125µs, HD=103µm, LT=65µm, VED=80.66J/mm^3 , Porosity=1.81%

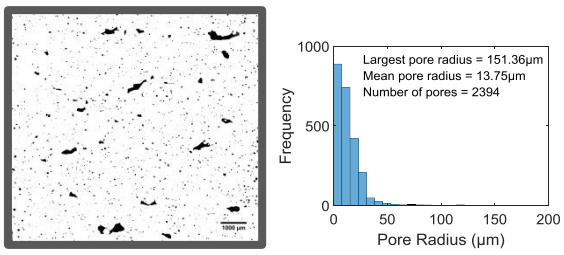

e) PD=50µm, ET=125µs, HD=68µm, LT=90µm, VED=88.24J/mm^3 , Porosity=3.34%

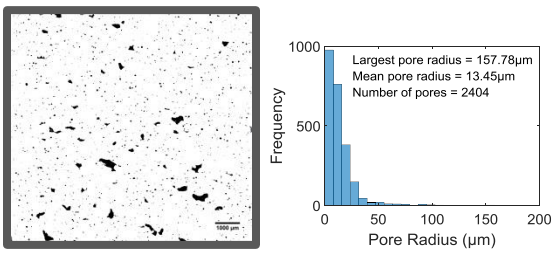

f) PD=50µm, ET=125µs, HD=103µm, LT=90µm, VED=58.25J/mm^3 , Porosity=3.25%

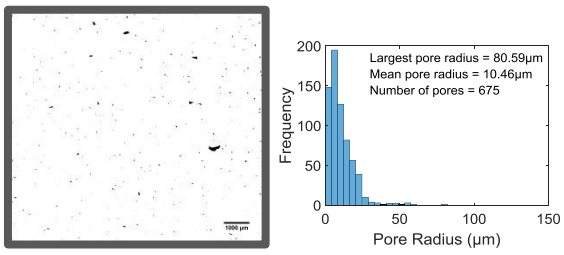

g) PD=60µm, ET=100µs, HD=85µm, LT=75µm, VED=58.56J/mm^3 , Porosity=0.44%

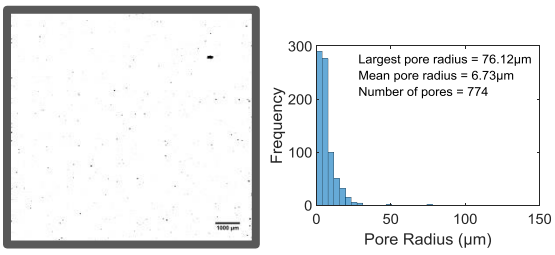

h) PD=60µm, ET=100µs, HD=120µm, LT=75µm, VED=41.48J/mm^3 , Porosity=0.21%

Figure 4-12: Optical micrographs and histogram analysis showing the effects of HD (PD of 50µm and 60µm) on the amount and size of pores when other process parameters are fixed. All the scale bars are 1000µm.

At a PD of 70µm, the porosity improved by changing HD if it is associated with changing the ET at any LT. For instance, using a HD of 68µm increases the porosity if the ET is high (125µs) while it can reduce the porosity if the ET is low (75µs). Similarly, if the HD is 103µm, it requires the ET to be 125µs to reduce the porosity. This relation is shown in Figure 4-13 (a) vs (b) and (c) vs (d) for a LT of 90µm and in Figure 4-13 (e) vs (f) for a LT of 65µm. From this observation, it is possible to conclude that using a small value for the HD (short distance) and a long ET resulted in a high

energy input (high VED) which increased the evaporation of powder, leading to higher porosity. For a high ET such as (a) vs (b), increasing the HD from 68µm to 103µm helped reduce the largest pore radius and mean pore radius by approximately 78% and 45% respectively. At ET of 75µs (Figure 4-13 (c) vs (d)) and for the same change in the HD, the porosity increased from 0.88% to 9.58% and the number of pores and pore radius were increased significantly. The impact of increasing the HD on the porosity and mean pore radius at a LT of 65µm (Figure 4-13 (e) vs (f)) was less in comparison to that observed at a LT of 90µm. However, the number of pores, increased by 5 times in (e) vs (f) while it was approximately 2.8 times in (c) vs (d).

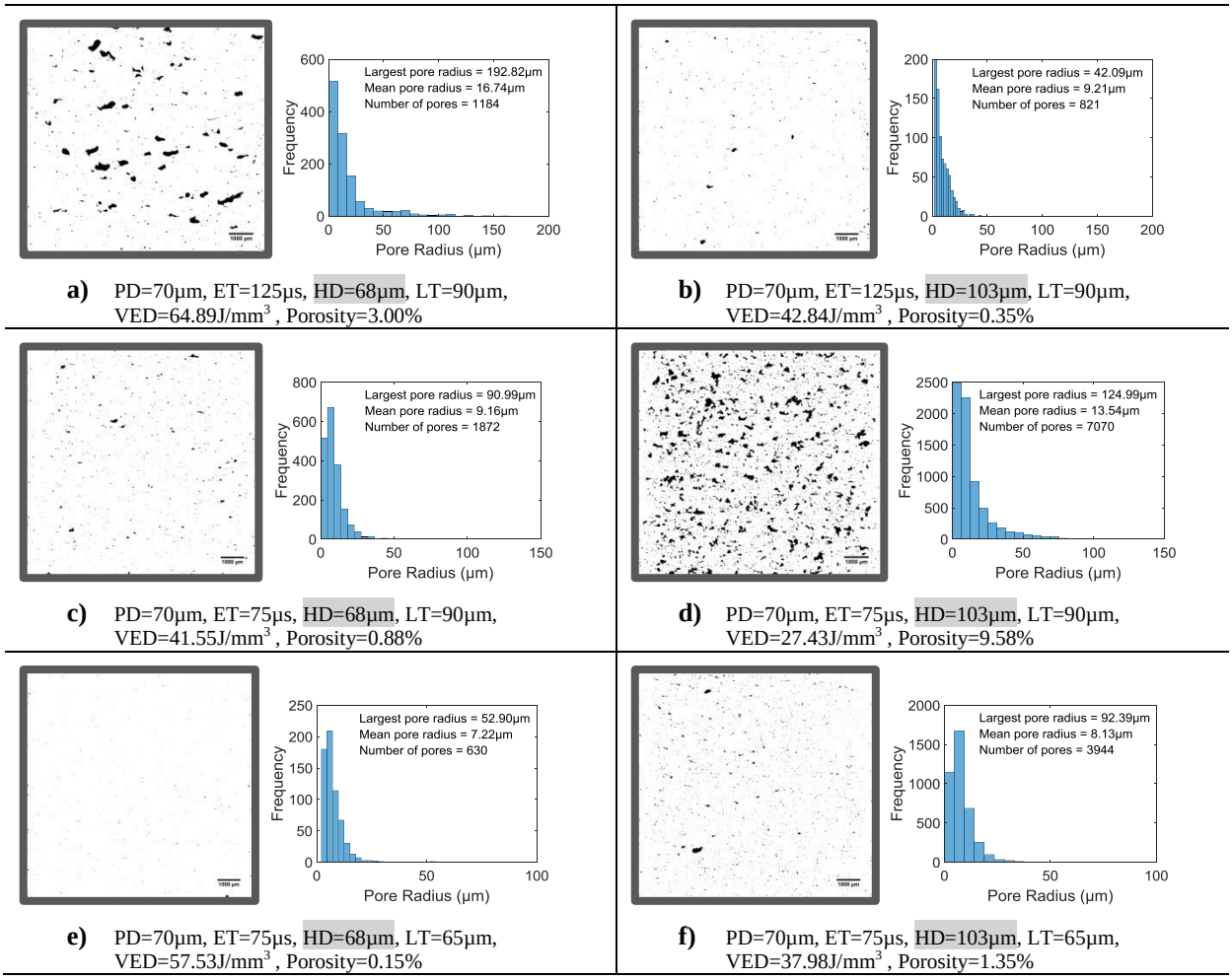

a) PD=70µm, ET=125µs, HD=68µm, LT=90µm, VED=64.89J/mm^3 , Porosity=3.00%

b) PD=70µm, ET=125µs, HD=103µm, LT=90µm, VED=42.84J/mm^3 , Porosity=0.35%

c) PD=70µm, ET=75µs, HD=68µm, LT=90µm, VED=41.55J/mm^3 , Porosity=0.88%

d) PD=70µm, ET=75µs, HD=103µm, LT=90µm, VED=27.43J/mm^3 , Porosity=9.58%

e) PD=70µm, ET=75µs, HD=68µm, LT=65µm, VED=57.53J/mm^3 , Porosity=0.15%

f) PD=70µm, ET=75µs, HD=103µm, LT=65µm, VED=37.98J/mm^3 , Porosity=1.35%

Figure 4-13: Optical micrographs and histogram analysis showing the effects of HD (PD of 70µm) on the amount and size of pores when other process parameters are fixed. All the scale bars are 1000µm.

Generally, the influence of HD can be controlled by appropriate selection of other process parameters, which indicates that the HD is not a key significant factor in

fabricating steel alloy using PBF process. The result from this study agrees with similar studies in the literature ([106]; [107]).

4.3.4. Layer Thickness (LT)

Even though using a thicker powder layer improves production time if all other parameters are fixed, it may affect the part density. If the change in layer thickness (LT) is not significant, the effect of LT would not be clear [106]. According to the selected range of the LT in the current study, the effect of LT was significant. Using a thick LT contributes to creating additional and larger pores in comparison to when a thin layer is used. The shape of the vast majority of pores caused by increasing the LT is irregular, which was considered to be as a result of the lack of fusion/joining of layers. The effect of the LT can be relatively mitigated by tuning the other parameters accordingly. As shown in Figure 4-14, increasing the LT increases the number of pores and also creates larger pore sizes (Figure 4-14 plot (a) - (f)). The largest pore radius increases from 68µm to 158µm in Figure 4-14 plot (a) and (b) respectively. Similarly, the pore radius increased in (c) vs (d) which can be seen in the change of the mean pore radius. These large pores were considered to be due to the lack of fusion (poor connectivity/welding between layers), where the laser power was insufficient to penetrate into the powder layer to the pre-existing layers, due to the effect of thermal conduction in the material and thermal loss in contactless particles and voids. The change in porosity, pore radius (the largest and the mean) in plot (g) vs (h) was not significant. This was a result of the appropriate combination of the other process parameters.

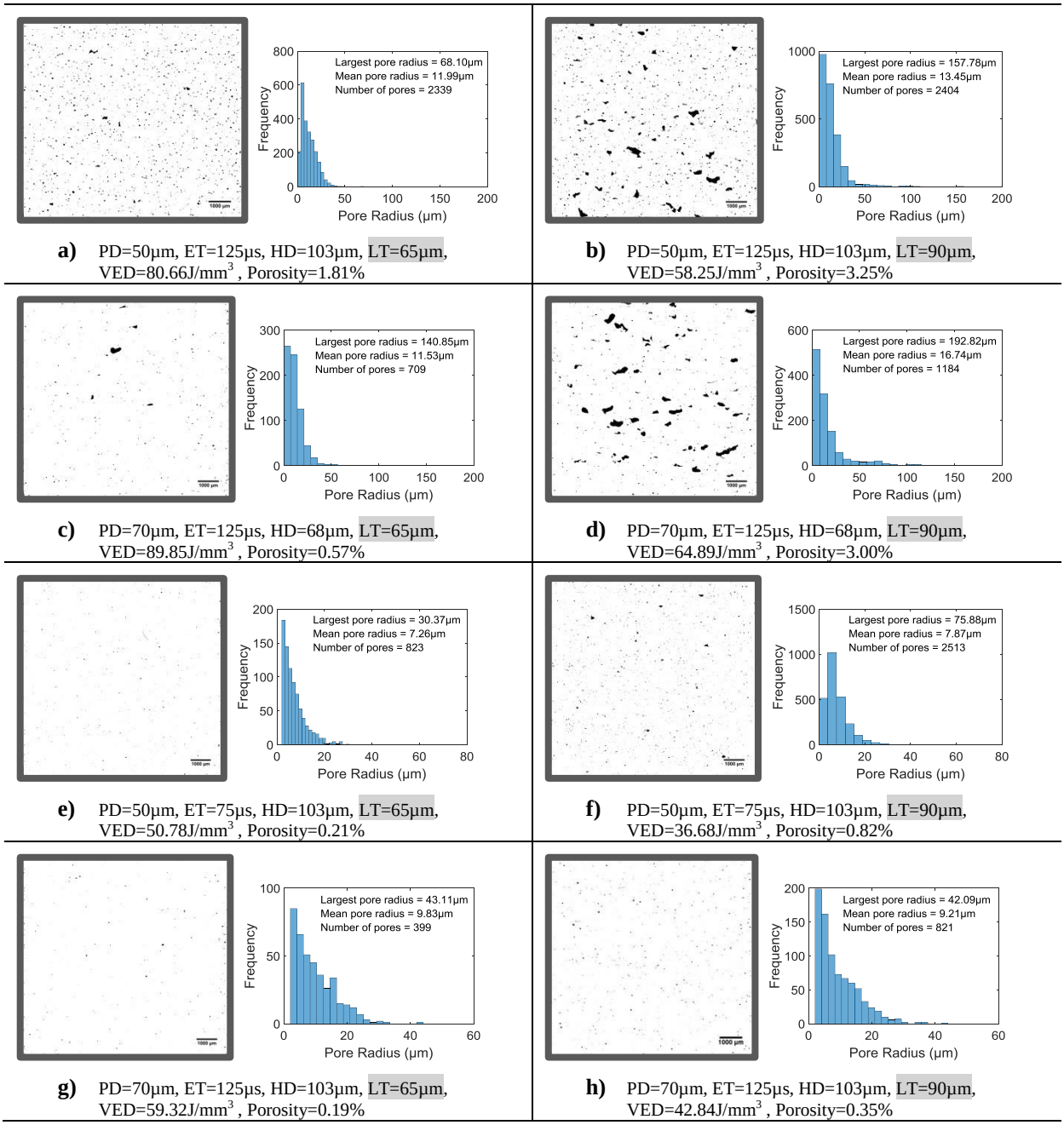

a) PD=50µm, ET=125µs, HD=103µm, LT=65µm, VED=80.66J/mm^3 , Porosity=1.81%

b) PD=50µm, ET=125µs, HD=103µm, LT=90µm, VED=58.25J/mm^3 , Porosity=3.25%

c) PD=70µm, ET=125µs, HD=68µm, LT=65µm, VED=89.85J/mm^3 , Porosity=0.57%

d) PD=70µm, ET=125µs, HD=68µm, LT=90µm, VED=64.89J/mm^3 , Porosity=3.00%

e) PD=50µm, ET=75µs, HD=103µm, LT=65µm, VED=50.78J/mm^3 , Porosity=0.21%

f) PD=50µm, ET=75µs, HD=103µm, LT=90µm, VED=36.68J/mm^3 , Porosity=0.82%

g) PD=70µm, ET=125µs, HD=103µm, LT=65µm, VED=59.32J/mm^3 , Porosity=0.19%

h) PD=70µm, ET=125µs, HD=103µm, LT=90µm, VED=42.84J/mm^3 , Porosity=0.35%

Figure 4-14: Optical micrographs and histogram analysis showing the effects of LT on the amount and size of pores. All the scale bars are 1000µm.

This section showed optically the effect of process parameters on the amount, size and shape of the porosity. It was found that the ET was the most significant parameter, not solely as an individual parameter, but also its interaction with the other process parameters.

The results of studying the effect of process parameters individually were in agreement with the majority of studies in the literature. However, considering the interaction between process parameters led to different conclusions. For instance, the HD is not an effective parameter but its effect becomes clear when associated with other process parameters. This strongly supports the observation that the interaction between process parameters must be considered, which is a novel contribution of this chapter. This has not been found in any previous papers in the literature.

The review of previous research indicated that previous studies have optimised process parameters individually and without considering their interaction during the optimisation process. Additionally, a thicker LT is known to lead to a lack-of-fusion porosity but adjusting the process parameters appropriately can help mitigate its effect.

4.4. Discussion

It was found that different combinations of process parameters can be used to fabricate near fully dense parts. Due to the different material properties of the materials considered, it is expected that the process parameters required for this would vary. Material thermal properties and beam absorption rate of the metal powder are some of the important properties that affect the melt pool formation [157], and therefore the overall complete 3D build. Even though the melt range and powder absorption of the laser beam are approximately similar for both materials studied (Ti-6Al-4V ELI and 316L-SS), the thermal conductivity is dramatically different which leads to distinct behaviours (Table 4-10).

Table 4-10: Generic data wrought material Ti-6Al-4V ELI and 316L-SS

Characteristic	***Ti-6Al-4V ELI***	***316L-SS***
Thermal conductivity (W/mK) at 20 ºC	6.7 [154]	16.2 [155]
Melting range (°C)	1604-1660 [154]	1371-1399 [155]
Measured powder absorbability	0.36-0.44 ([49]; [158]; [43])	0.3-0.4 ([49]; [111]; [128]; [159]; [65])

The width of the melt pool for Ti-6Al-4V ELI is 63% greater in comparison to the width of 316L-SS melt pool, for the same exposure time of 220µs and at a LT of 60µm. The variation of the melt pool width between Ti-6Al-4V ELI and 316L-SS was approximately 28% at a low exposure time of 70µs and 80µs respectively. However, when the exposure time was increased to 220µs for both materials while maintaining the same LT, the variation between the two increased by 35% to 63% (Figure 4-15). From the investigation of the melt pool formation, it was noticed that the melt pool geometry of the Ti-6Al-4V ELI and 316L-SS was formed differently for the same energy density.

The thermal conductivity of a material plays a major role in the geometry of the melt pool formed. A metal with a low thermal conductivity tends to retain the heat in a limited area for longer while a metal with a high thermal conductivity dissipates the heat away from the melt pool more rapidly. The size of the melt pool for Ti-6Al-4V increased more with increased energy density as it has lower thermal conductivity compared to 316L-SS). In addition the thermal conductivity of the inert gas was found to affect the process as it can increase the thermal conductivity of a material powder [125]. A gas such as Helium can increase the thermal conductivity of the powder by as much as 300% compared to Argon and Nitrogen. This was not considered to be a reason for different melt pool size in this study as both materials were processed under the same inert gas (Argon). Laser beam absorption was not considered as a factor in producing a different melt pool size. Both alloys (Ti-6Al-4V and 316L-SS) were found to have similar range of measured powder absorbability.

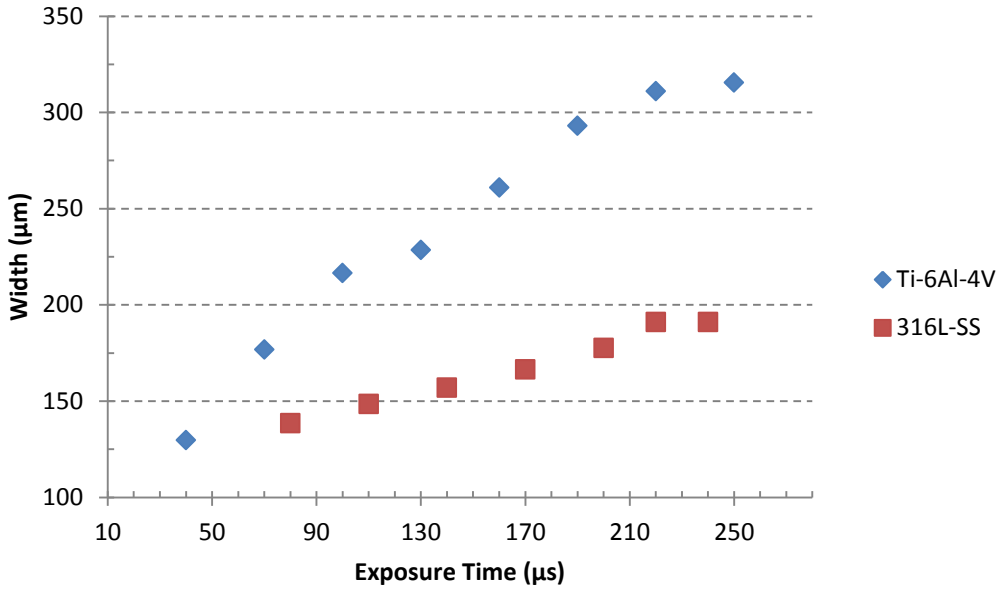

Figure 4-15: Change in melt pool width vs the ET for Ti-6Al-4V ELI and 316L-SS at LT of 60µm

In general, there are two main mechanisms that lead to the development of pores.

a) Lack-of-fusion; which may be caused when the overlapping distance of individual points or melt tracks is insufficient [127], when the applied energy is inadequate to melt the powder, or when the powder layer is too thick for all the material to be melted during the set exposure time. In pulse laser PBF systems, PD can play a role in creating voids when the distance between two consecutive points is greater than the optimum distance.

b) When the applied energy is excessive in comparison to the required energy. This results in evaporation or keyholing [128]. This is when the fusion process passes the thermal conduction region and enters into the keyhole region. Exaggerated overlapping in HD or/and PD, long ET and high laser power can contribute to the development of keyholes in PBF parts.

It is clear that using the value of the VED to calculate the proper applied energy for a certain level of density/porosity, is not universally correct. The VED should be used more as a guideline for indication purposes to narrow down into the region of desired operating conditions, with then finer tuning of the operating parameters for the identification of optimal conditions. The value of VED and SS do not provide enough information to describe the effect of process parameters, therefore individual process

parameters should be carefully selected for a specific combination value of VED or SS. However, the VED can be used to restrict the delivered energy to be within acceptable levels. Going below or above a specific VED value can impact the build quality. In this study, a VED below 40J/mm^3 or above 60J/mm^3 was found to be unsuitable for the selected particle size of 316L-SS alloy.

The distribution of the pores is generally uniform in all the samples investigated regardless of the frequency observed. However, the frequency of pores around the edge of the samples was observed to be generally constant and appeared to be independent of the pores distribution in the bulk area. Because the value of melt parameters along the borders of the samples was fixed for all fabricated parts, the shape and size of the pores at the edges were the same for all samples. The porosity at the edge can be caused by high temperature due to the turning point of the melt tracks, particularly at the joining point between the border and scan area of the layer.

The work described in this chapter provides foundation for the next chapter, which develops process models. It also provides an important contribution towards the consideration of process parameters optimisation. The work emphasises the importance and necessity of taking into account the relationships between process parameters. These relationships significantly influence the stability of the process by providing an important understanding of the interaction between how and how much a process parameter will behave in conjunction with other process parameters.

5. REGRESSION ANALYSIS AND CORRELATION MODELS

5.1. Introduction

Regression analysis is "*a quantitative research method which is used when the study involves modelling and analysing several variables, where the relationship includes a dependent variable and one or more independent variables*" [160]. It is a beneficial tool that represents the relationships in a process and predicts future results, according to the experimental data that was used to develop the regression model. It provides an improved understanding of how a predictor response is connected to the considered effective factors. The aim of this chapter is to assess the relationships between the various process parameters and the RD for each material. By determining these relationships the two, time and cost of further experimental work for enhanced investigations would be reduced or eliminated. The overall goal is to identify and establish these relationships, which can be used to predict the RD. As a result of this analysis, the regression models of the powder bed fusion (PBF) process for the studied materials were developed and validated for the standard powders of Ti-6Al-4V ELI and 316L-SS, which are commonly used with the PBF system (Section 5.2). In Section 5.3, the relationships between process parameter combination as a function of the VED term and the RD according to the material, PSD and LT were assessed. The obtained models for each PSD and LT were compared, to establish the effect of changing PSD and LT on the RD of built parts.

The data collected from the experimental work was used for correlation and regression analysis to establish the relationships. The Minitab software (version 17), was used throughout the analysis.

5.2. Regression Analysis

Regression analysis is a statistical process which is used to identify which of the input variables (independent variables) impact the response outputs (dependent variable). It can assess the relationships between process parameters and the response of a system, determine which independent variables matter most and how the factors interact with each other. Regression analysis is also used for prediction and forecasting for future events, in a similar situation to the used data for developing a regression model.

Analysis of variance (ANOVA) is the most common tool that used with the regression analysis to determine the impact of inputs factor on the response. In this work, process parameters are the input factors and the RD the response. ANOVA describes the relationships between process parameters as inputs and the RD as output. It shows the amount of variation and the significance of the process parameters terms. Statistical terms are used to evaluate the regression model developed. For instance, the sum of squares, mean square, F-value and P-value are generally the main terms found in the ANOVA table for analysing the model. The sum of squares, measures the differences produced by a model. It is classified into different sum of squares according to the source of the variations: sum of squares of a regression model or a term, which is the calculated variations of the model explained by the regression relationship; sum of squares of the error, which is the variations that are not explained by the model; total sum of squares, which is the total variations of the response from the mean. The total sum of squares is the sum of squares of the error plus the sum of squares of the regression. When the sum of squares is used to calculate the increase in the sum of squares of the regression by a term compared to the sum of squares for the regression for the other terms, it is called the adjusted sum of squares. Equations (5-1) to (5-3) are the formula used to calculate the sum of squares [161].

$$Sum\ of\ Square_{Regression} = \sum(\hat{y}_i - \bar{y})^2 \tag{5-1}$$

$$Sum\ of\ Square_{Error} = \sum(y_i - \hat{y}_i)^2 \tag{5-2}$$

$$Sum\ of\ Square_{Total} = \sum(y_i - \bar{y})^2 \tag{5-3}$$

where y_i is the ith observation (process response), $\hat{y}_i$ is the ith fitted value and $\bar{y}$ is the mean value of the observations.

Mean square is calculated by dividing the sum of squares by the degree of freedom as shown in equations (5-4) to (5-6). It determines how much variation a model or a term explains.

$$Mean\ Square_{Regression} = \frac{\sum(\hat{y}_i - \bar{y})^2}{p} \tag{5-4}$$

$$Mean\ Square_{Error} = \frac{\sum(y_i - \hat{y}_i)^2}{n - p - 1} \tag{5-5}$$

$$Mean\ Square_{Total} = \frac{\sum(y_i - \bar{y})^2}{n - 1} \tag{5-6}$$

where n is the number of observations and p is the number of terms in the model.

The significance of a model is calculated from the F-test. The test compares the ratio of the mean square of a regression model to the error mean square. The P-value is then found from the F distribution. If the P-value is less than a threshold (set to 5%), the null hypothesis should be rejected and the regression model is statistically significant. The null hypothesis in this case was the model is not significant in explaining the change in the response (density) when process parameters change.

$$F_{value} = \frac{Mean\ Square_{Regression}}{Mean\ Square_{Error}} \tag{5-7}$$

Then, the P-value is calculated using the F-test table for the $F_{\alpha,\lambda_1,\lambda_2}$ where α is the risk value (set to 0.05), λ_1 is the degree of freedom (DF) of the regression and λ_2 is the degree of freedom of the error. The obtained P-value from the F-test is used to assess the statistical significance of the model. Using the hypothesis testing, if the P-value is smaller than the critical risk value (<0.05), the null hypothesis should be rejected. In this case, the null hypothesis is that the regression model (fitted line) is not significant.

S values, which is known as standard error of the regression (or standard error of the estimate), represent the standard deviation of distance that observations fall from the regression line. The smaller the S value, the closer the values are for the observations in relation to the regression line. It also can be used as an indicator for the precision of the model. Equation (5-8) shows the formula used to calculate the S value. Another statistical important indicator is the R-square (Equation (5-9)). The numerator of the second part of the equation is the sum of square errors, which represents the adding up all the square values of the distance from an observation to the fitted line. The denominator is the sum of square total, which is calculated by adding up all square variation between an observation and the mean value of the observations. This means

that the R-square compares the errors of the regression model to errors if the mean value of the observation would be used to model the data.

$$S = \sqrt{(Mean\ Square_{Error})} = \sqrt{\frac{\sum(y_i - \hat{y}_i)^2}{n - p - 1}} \tag{5-8}$$

$$R^2 = 1 - \frac{\sum(y_i - \hat{y}_i)^2}{\sum(y_i - \bar{y})^2} \tag{5-9}$$

A model with numerous terms (predictors) may have a high value of the R-square. R-square improves with adding terms to the model. In this case, adjusted R-square should be used for studying the improvement in a model (Equation (5-10)). Adjusted R-square only improves the model when the added terms to the model clearly improve the model. It always has a value less than R-square value. Predicted R-square measures the accuracy of a model to predict an observation after systematically being removed from a studied data set. It was calculated using equation (5-11).

$$R^2_{Adjusted} = 1 - \left(\frac{\sum(y_i - \hat{y}_i)^2}{\sum(y_i - \bar{y})^2}\right)\left(\frac{n - 1}{n - p - 1}\right) \tag{5-10}$$

$$R^2_{Predicted} = 1 - \frac{\sum\left(\frac{e_i}{1 - h_i}\right)^2}{\sum(y_i - \bar{y})^2} \tag{5-11}$$

where e_i is the i^{th} error (residual) and h_i is the i^{th} diagonal element of $(X'X)^{-1}X'$ (Hat Matrix). X is the design matrix of input factors (independent variables/predictors).

The aforementioned statistical terms were used to interpret the regression models and fitted line plots. The next step is to assess the statistical significance of the model using the analysis of variance (ANOVA).

5.2.1. Ti-6Al-4V ELI Regression Analysis

The data obtained from the design of experiments for the Ti-6Al-4V ELI was used to find the best fit regression model to accurately predict the density according to the values of the process parameters. There were 100 readings for the experiments. The readings were divided into two groups: 65 readings for training the model and 35 readings to validate the model. The backward elimination method was used to find the

regression model. It eliminates the highest p-value term starting with the high order terms. As shown in the summary of the model in ANOVA analysis Table 5-1, the model can describe above 85% of the process variation with insignificant Lack-of-Fit.

Table 5-1: ANOVA analysis and summary for the regression model for all selected factors and their interactions for Ti-6Al-4V ELI

Source	*DF*	*Adj SS*	*Adj MS*	*F-Value*	*P-Value*
Regression	12	0.452078	0.037673	33.61	0
LT	1	0.055197	0.055197	49.25	0
ET	1	0.082282	0.082282	73.42	0
HD	1	0.004766	0.004766	4.25	0.044
LT^2	1	0.018857	0.018857	16.83	0
LP^2	1	0.01152	0.01152	10.28	0.002
PD^2	1	0.034797	0.034797	31.05	0
HD^2	1	0.005201	0.005201	4.64	0.036
LT*LP	1	0.109901	0.109901	98.06	0
LT*PD	1	0.027902	0.027902	24.9	0
LP*PD	1	0.02843	0.02843	25.37	0
LP*ET	1	0.059341	0.059341	52.95	0
LT^3	1	0.01257	0.01257	11.22	0.002
Error	52	0.058279	0.001121		
Lack-of-Fit	11	0.014636	0.001331	1.25	0.287
Pure Error	41	0.043642	0.001064		
Total	64	0.510357			
Model Summary					
	S	**R-sq**	**R-sq(adj)**	**R-sq(pred)**	
	0.0334776	88.58%	85.95%	81.99%	

The regression model equation (5-12) was tested by the validation data. It was able to predict the density with good accuracy, (Figure 5-1). At some points, however, there is slight variation on the behaviour of the predicted RD compared to the actual value from the experimental results. This variation may be as a result from the process instability. Also, variations were found in the relative density of parts built in different locations. This is discussed in the next chapter.

$$\begin{aligned} Density = {} & 4.543 - 0.03262\,LT + 0.003577\,ET + 0.00594\,HD \\ & + 0.000336\,LT^2 + 0.000004\,LP^2 + 0.000077\,PD^2 \\ & - 0.000040\,HD^2 + 0.000077\,LT*LP - 0.000052\,LT \\ & *PD - 0.000045\,LP*PD - 0.000020\,LP*ET \\ & - 0.000002\,LT^3 \end{aligned} \tag{5-12}$$

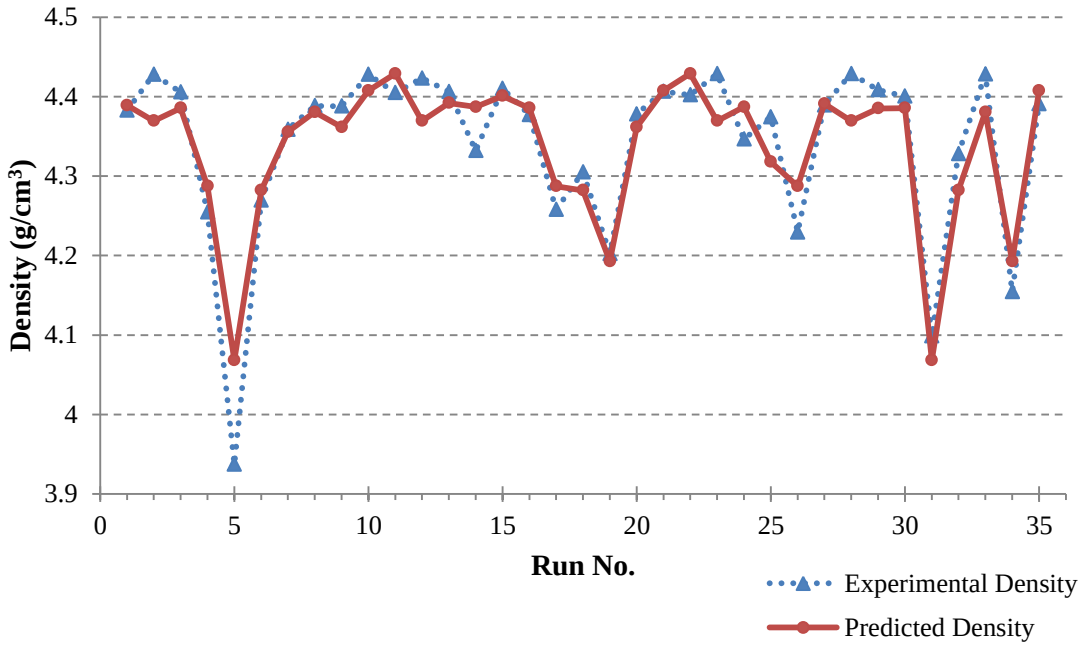

Figure 5-1: Actual density vs. predicted density using the developed regression model forTi-6Al-4V ELI

5.2.2. 316L-SS Regression Analysis

The data obtained from the first experiment runs and the validation runs were combined and randomly divided into two groups: two thirds of the data was used to obtain a regression model and one third was used to validate the model. The regression model covered all possible levels of interactions among the factors. It was obtained by using a backward elimination method. All terms that were insignificant (p-value ≥ 5%) were removed. Table 5-2 shows the ANOVA analysis and model summary of regression model. The Lack-of-Fit is shown as insignificant. The regression model obtained can describe 98% of the variation in the data and has an accuracy of 95% when predicting the density. The density can be predicted using Equation (5-13). The Error term should represent the variation between the actual and predicted density. Figure 5-2 shows the comparison between the actual and predicted density, which are in good agreement.

$$\text{Density} = \text{Constant} + \sum(\text{Term} * \text{RegressionCoeff.}) + Error \qquad (5\text{-}13)$$

Table 5-2: ANOVA analysis and summary for the regression model for all selected factors and their interactions for 316L-SS

Term	*Regression Coeff.*	*DF*	*Adj SS*	*Adj MS*	*F-Value*	*P-Value*
Regression	-	32	1.03574	0.032367	153.76	0
PD	-4.127	1	0.00938	0.009384	44.58	0
ET	-1.423	1	0.00947	0.009465	44.97	0
HD	-4.86	1	0.00906	0.009062	43.05	0
LT	0.852	1	0.00512	0.005117	24.31	0
PD^2	0.02884	1	0.00806	0.008057	38.27	0
ET^2	0.01102	1	0.00697	0.006967	33.1	0
HD^2	0.02882	1	0.00835	0.008349	39.66	0
PD*ET	0.007731	1	0.01937	0.019367	92	0
PD*HD	-0.02081	1	0.00604	0.006036	28.67	0
PD*LT	0.0838	1	0.00921	0.009209	43.75	0
ET*HD	0.06168	1	0.0089	0.008896	42.26	0
ET*LT	-0.0655	1	0.00787	0.007867	37.37	0
HD*LT	0.00371	1	0.03634	0.036339	172.63	0
PD^3	-0.0001	1	0.00808	0.00808	38.38	0
ET^3	0.000009	1	0.0093	0.009299	44.18	0
HD^3	-0.000037	1	0.00851	0.008507	40.41	0
LT^3	-0.000144	1	0.00867	0.008668	41.18	0
PD^2*HD	-0.000007	1	0.00216	0.002158	10.25	0.002
PD^2*LT	-0.000139	1	0.00777	0.007765	36.89	0
PD*ET^2	-0.000024	1	0.01118	0.01118	53.11	0
PD*ET*HD	-0.000036	1	0.02617	0.026165	124.3	0
PD*ET*LT	-0.000047	1	0.03356	0.033562	159.44	0
PD*HD^2	0.000151	1	0.00835	0.008351	39.67	0
PD*HD*LT	-0.000068	1	0.04603	0.046029	218.66	0
PD*LT^2	-0.000413	1	0.00845	0.008453	40.16	0
ET^2*HD	-0.000056	1	0.0091	0.009102	43.24	0
ET^2*LT	-0.000088	1	0.00919	0.009187	43.64	0
ET* HD^2	-0.000285	1	0.0083	0.008303	39.44	0
ET*HD*LT	-0.000033	1	0.03203	0.032029	152.15	0
ET* LT^2	0.000572	1	0.00856	0.008557	40.65	0
ET^4	< -0.000001	1	0.00488	0.00488	23.18	0
PD*ET*HD*LT	0.000001	1	0.04079	0.040789	193.77	0
Constant	238.2	-	-	-	-	0
Error	-	87	0.01831	0.000211		
Lack-of-Fit	-	8	0.00125	0.000157	0.72	0.669
Pure Error	-	79	0.01706	0.000216		
Total	-	119	1.05406			

Model Summary			
S	**R-sq**	**R-sq(adj)**	**R-sq(pred)**
0.0145087	98.26%	98%	95.54%

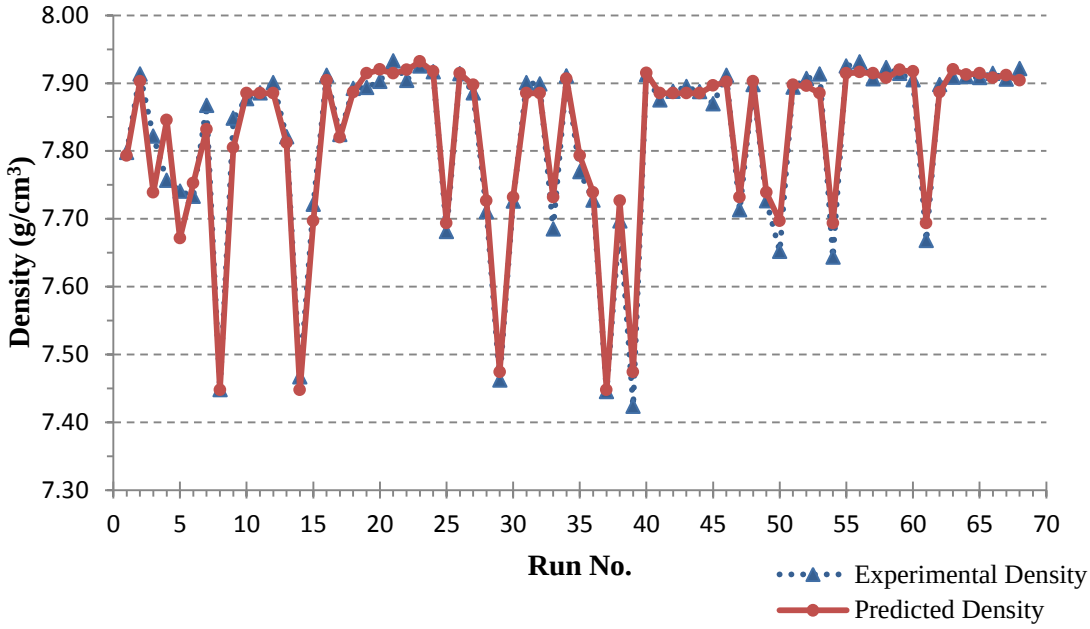

Figure 5-2: Actual density vs. predicted density using the developed regression model for 316L-SS

To summarise this section, regression models were developed and validated for the powder bed fusion process to predict the density of Ti-6Al-4V ELI and 316-SS fabricated parts. Both models (Ti-6Al-4V ELI and 316L-SS) were in excellent agreement with experimental results. The regression model of 316L-SS showed a better ability to predict the part density with high accuracy compared to the Ti-6Al-4V ELI model. The differences between the two models are discussed at the end of this chapter.

5.3. Correlation Models for each LT and PSD vs VED

5.3.1. Ti-6Al-4V ELI

The optimal values of LP, PD and HD for Ti-6Al-4V ELI shown in Table 4-5 were used to investigate the effect of changing layer thickness and powder size distribution on the density of parts at different volumetric energy density (VED) by changing only the exposure times (ET). Three powder types of Ti-6Al-4V ELI (T1, T2 and T3) were used to build 10x10x10mm^3 cubes for varying layer thicknesses as shown in Table 3-9. The exposure time was varied according to the layer thickness to keep the VED comparable throughout the all LTs. Tables in Appendix B show the calculated values of the SS and

VED according to the changes in ET and LT for all powder types using Equation (3-5) for SS and Equation (3-6) for VED. The other process parameters used were based on their optimal values found in the optimisation phase: LP of 200W, PD of 50µm and HD of 65µm.

The regression models of all powder types and layer thicknesses were developed. An example of one PSD-LT investigation was selected to be presented here to demonstrate the relationship. The selected example was chosen because it has a wide variation in density measurements (the variation between the smallest and the largest values of RD was the greatest). Table 5-3 is an example of the builds for the goal of this chapter. It shows the process parameters and the resultant RD for the Ti-6Al-4V ELI type 3 (T3) powder for a layer thickness of 60µm. The data for all powder types and layer thicknesses is provided at the Appendix B.

Table 5-3: Process parameters and the resultant RD for the builds that were used to study the effect of changing PSD and LT for T3 and LT of 60µm for the material Ti-6Al-4V ELI

Run#	***LT*** *(mm)*	***LP*** *(W)*	***PD*** *(mm)*	***ET*** *(s)*	***HD*** *(mm)*	***SS*** *(mm/s)*	***VED*** *(J/mm^3)*	***RD*** *(%)*
1	0.06	200	0.05	0.00004	0.065	1000.00	51.28	93.69
2	0.06	200	0.05	0.00005	0.065	833.33	61.54	95.78
3	0.06	200	0.05	0.00006	0.065	714.29	71.79	97.42
4	0.06	200	0.05	0.00007	0.065	625.00	82.05	98.25
5	0.06	200	0.05	0.00008	0.065	555.56	92.31	98.56
6	0.06	200	0.05	0.00009	0.065	500.00	102.56	98.85
7	0.06	200	0.05	0.0001	0.065	454.55	112.82	99.01
8	0.06	200	0.05	0.00011	0.065	416.67	123.08	98.82
9	0.06	200	0.05	0.00012	0.065	384.62	133.33	98.98
10	0.06	200	0.05	0.00013	0.065	357.14	143.59	98.84
11	0.06	200	0.05	0.00014	0.065	333.33	153.85	98.99
12	0.06	200	0.05	0.00015	0.065	312.50	164.10	98.87
13	0.06	200	0.05	0.00016	0.065	294.12	174.36	99.02
14	0.06	200	0.05	0.00017	0.065	277.78	184.62	98.94
15	0.06	200	0.05	0.00018	0.065	263.16	194.87	98.71
16	0.06	200	0.05	0.00019	0.065	250.00	205.13	98.42
17	0.06	200	0.05	0.0002	0.065	238.10	215.38	98.53
18	0.06	200	0.05	0.00021	0.065	227.27	225.64	98.66
19	0.06	200	0.05	0.00022	0.065	217.39	235.90	98.70
20	0.06	200	0.05	0.00023	0.065	208.33	246.15	98.63
21	0.06	200	0.05	0.00024	0.065	200.00	256.41	98.89
22	0.06	200	0.05	0.00025	0.065	192.31	266.67	98.94

As recommended by practitioners and software developer the best approach is to find the simplest representative model that best correlates with experimental data, the relationship between applied energy and RD was studied, firstly, as linear relation.

The linear fitted line for the powder T3 and LT of 60µm shown in Figure 5-3 has an R-square value of 31.5%. This means that the model could explain 31.5% of the variation of the process response. The accuracy of the regression model was displayed graphically as the confidence interval (CI) and prediction interval (PI). The main response range of the RD for a given VED should fall within the confidence interval

limits with a confidence level of 95%. Moreover, prediction accuracy of the regression model would be within the prediction limits with a confidence level of 95%.

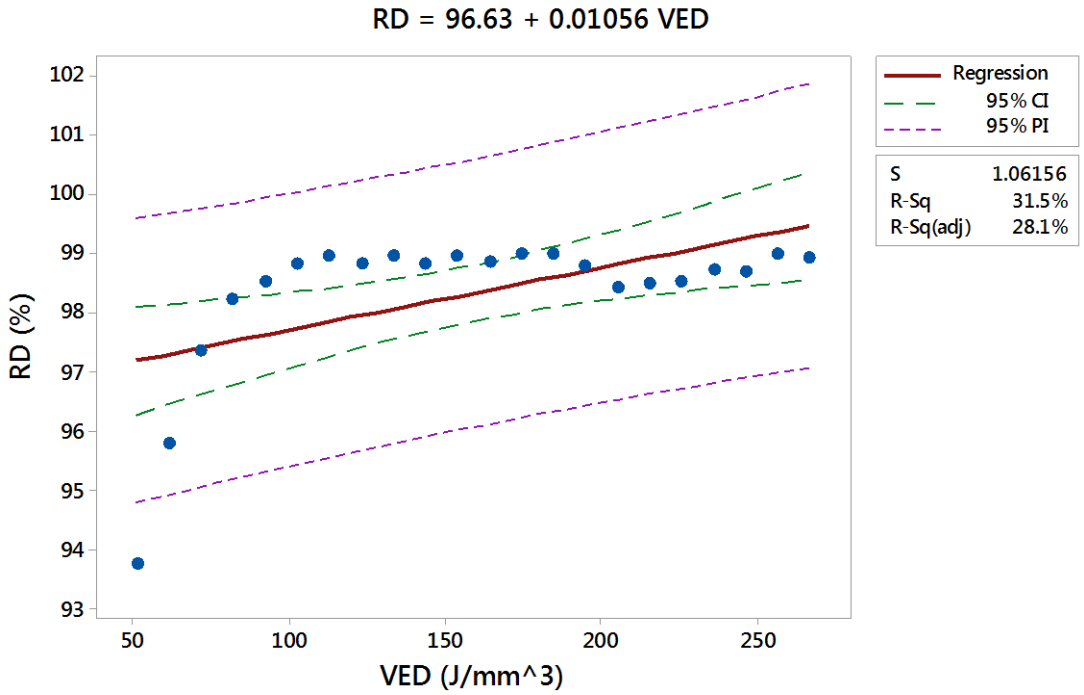

Figure 5-3: Fitted line plot of the linear relationship of the RD versus VED for the powder type of T3 and LT of 60µm

The next step is to check the ANOVA table to assess the significance of the model and evaluate the hypothesis test. P-value in the ANOVA table (Table 5-4) is below 0.05 which suggested that the null hypothesis was rejected with 95% confidence that the RD was influenced by the VED.

Table 5-4: ANOVA table for the linear regression model of the RD versus VED for the powder type of T3 and LT of 60µm

Source	***DF***	***Sum of Square***	***Mean Square***	***F-Value***	***P-Value***
Regression	1	10.3816	10.3816	9.21	0.007
Error	20	22.5383	1.1269		
Total	21	32.9198			
Summary	**S** = 1.06156	**R-Sq** = 31.5%	**R-Sq(adj)** = 28.1%		

Even though the R-square was small and the model was considered not accurate enough, the null hypothesis must be rejected because the p-value was below 5%. The decision of rejecting the null hypothesis via the data provided by the ANOVA table is

not always enough to assess the accuracy of the regression model. Residual analysis should be used to support the decision. It was conducted and shown in Figure 5-4. The residual showed a lack of normality and the histogram was compressed and focused predominantly to the right. For the accurate regression model, it is expected that the histogram of the residual values would be distributed symmetrically around zero. It was not, however, the case in the current linear regression model. Also, the residual had a pattern compared to the fitted value or observation order. The curvature of the residual versus fitted value revealed that there is a polynomial relationship. As a result a second order polynomial model was tested.

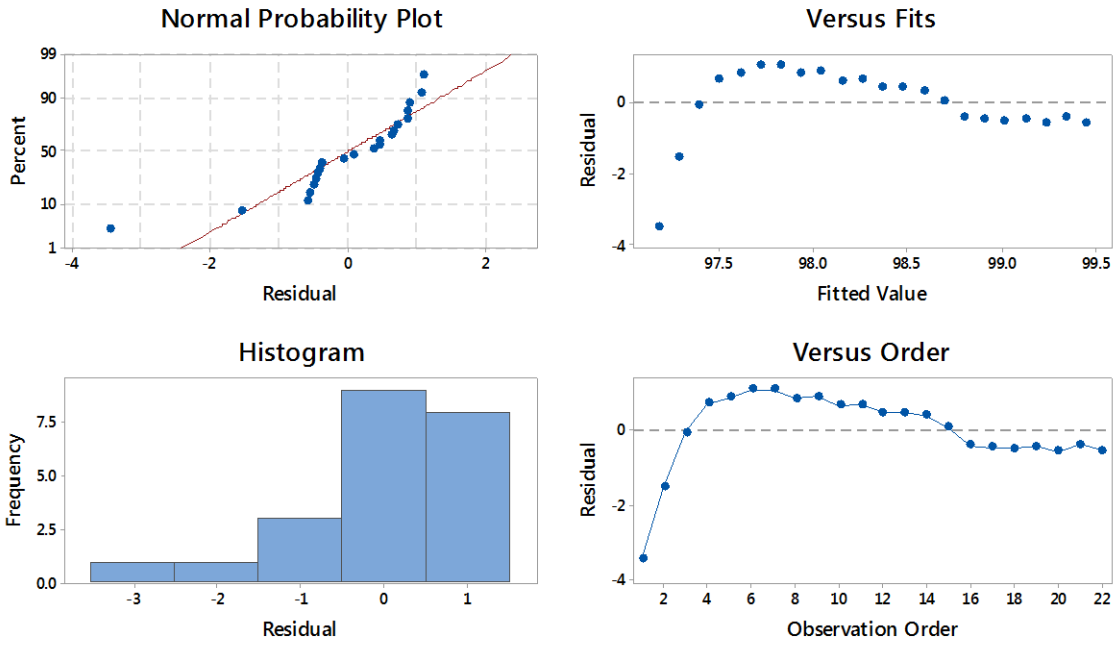

Figure 5-4: Residual plots of the linear regression model of RD versus VED of the powder type of T3 and LT of 60µm

The linear regression model showed poor fit according to the residual analysis. In addition, the residual versus fitted values illustrated that the relationship of RD versus the VED appears non-linear. Consequently, a polynomial regression model with second order (quadratic) or third order (cubic) should provide more accurate regression model. A quadratic regression model was tested and analysed then compared with the previous linear regression model. Figure 5-5 shows the quadratic fitted line of the RD versus VED for the same powder type and LT (T3-60). The model showed an improvement in its accuracy indices. S value, R-square became 0.76% and 66.3% respectively compared to 1.06% and 31.5% respectively for the linear regression model. Also, the adjusted R-

square confirmed that adding a term to the model led to a more enhanced accuracy (62.7% versus 28.1%).

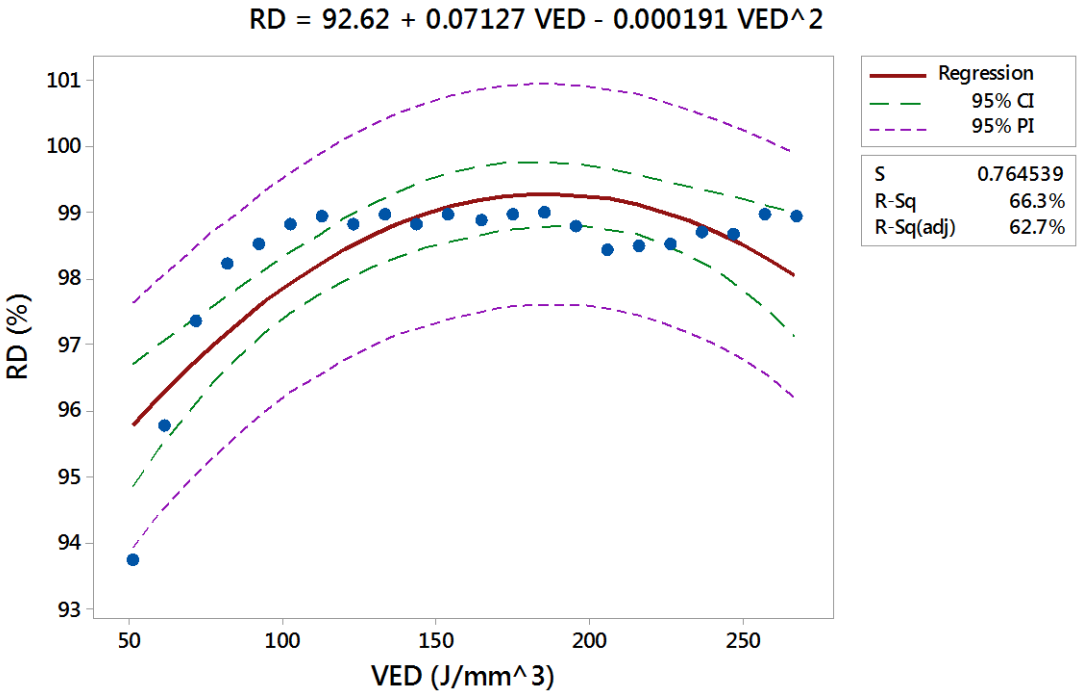

Figure 5-5: Fitted line plot of the quadratic relationship of the RD versus VED for the powder type of T3 and LT of 60µm

The F critical value from the ANOVA table (Table 5-5) led to a p-value far below 0.05 (actual value 0.000033). This implies that the null hypothesis must be rejected with 95% confidence and that the response RD is influenced by the VED, and the quadratic model can describe 66% of the variation of the response values.

Table 5-5: ANOVA table for the quadratic regression model of the RD versus VED for the powder type of T3 and LT of 60µm

Source	***DF***	***Sum of Square***	***Mean Square***	***F-Value***	***P-Value***
Regression	2	21.8140	10.9070	18.66	0.000
Error	19	11.1059	0.5845		
Total	21	32.9198			
Summary	**S** = 0.764539		**R-Sq** = 66.3%	**R-Sq (adj)** = 62.7%	

The residual analysis in Figure 5-6 showed improvements for all plots when the quadratic regression model was used. However, the normality test and histogram plot, showed a lack of normality, which in some cases was believed to be due to the reduced number of collected observations. The residual versus fitted value and the residual versus observation order plots also showed that the residual trend continues to follow a

pattern which could mean that the suggested regression model was not accurate to represent the relationship between the inputs and outputs (VED and RD in this case). Therefore, a cubic regression model was tested.

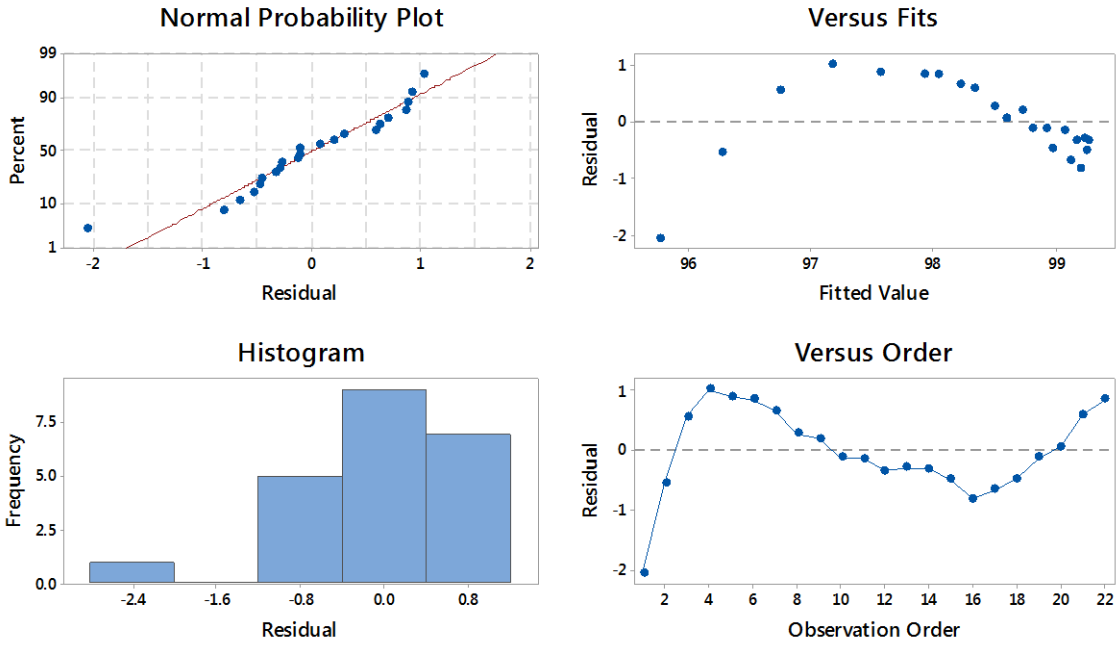

Figure 5-6: Residual plots of the quadratic regression model of RD versus VED of the powder type of T3 and LT of 60µm

The regression analysis process was repeated for the cubic regression model test. Figure 5-7 shows the fitted line, in which the S value was reduced to 0.365% compared to 0.764 and 1.061 for the quadratic and linear regression models respectively. The cubic regression model could describe 92.7% of the response variations. Also, the null hypothesis could be rejected with the confidence of 95% as concluded from the p-value in Table 5-6.

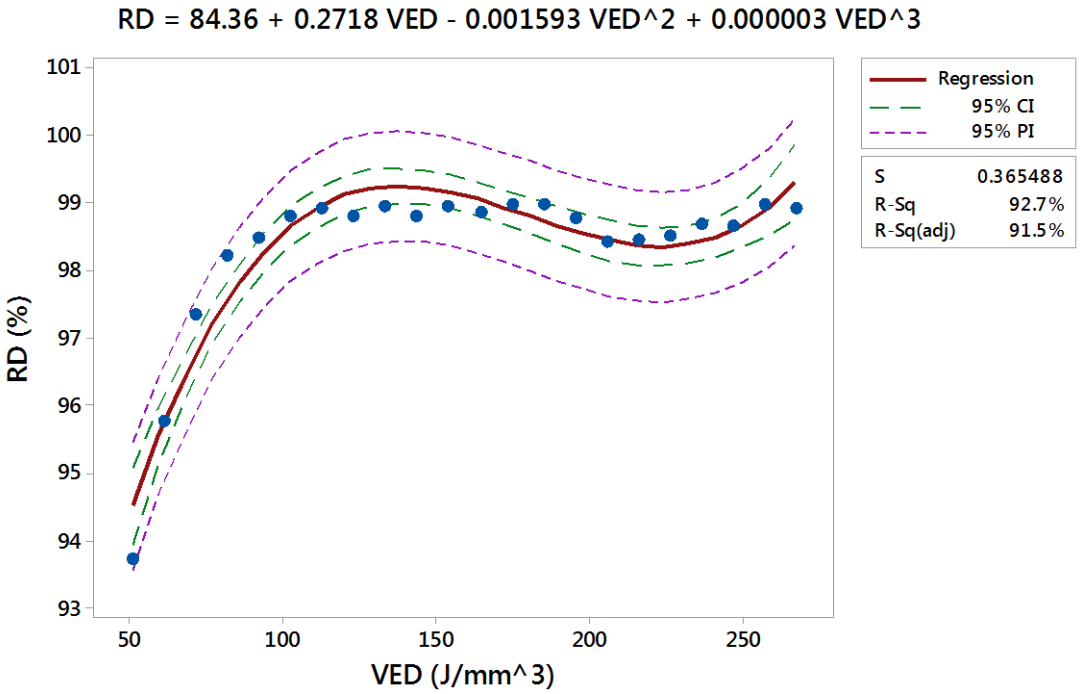

Figure 5-7: Fitted line plot of the cubic relationship of the RD versus VED for the powder type of T3 and LT of 60µm

Table 5-6: ANOVA table for the cubic regression model of the RD versus VED for the powder type of T3 and LT of 60µm

Source	*DF*	*Sum of Square*	*Mean Square*	*F-Value*	*P-Value*
Regression	3	30.5154	10.1718	76.15	0.000
Error	18	2.4045	0.1336		
Total	21	32.9198			
Summary		**S** = 0.365488	**R-Sq** = 92.7%	**R-Sq(adj)** = 91.5%	

The residual analysis shown in Figure 5-8 revealed that there was a significant improvement in the normality plot as well as the histogram. The residual data points were predominantly located symmetrically around the mean of zero with a slight tendency to the left-hand side. Similarly, residual versus fitted value and observation order showed clear improvements too.

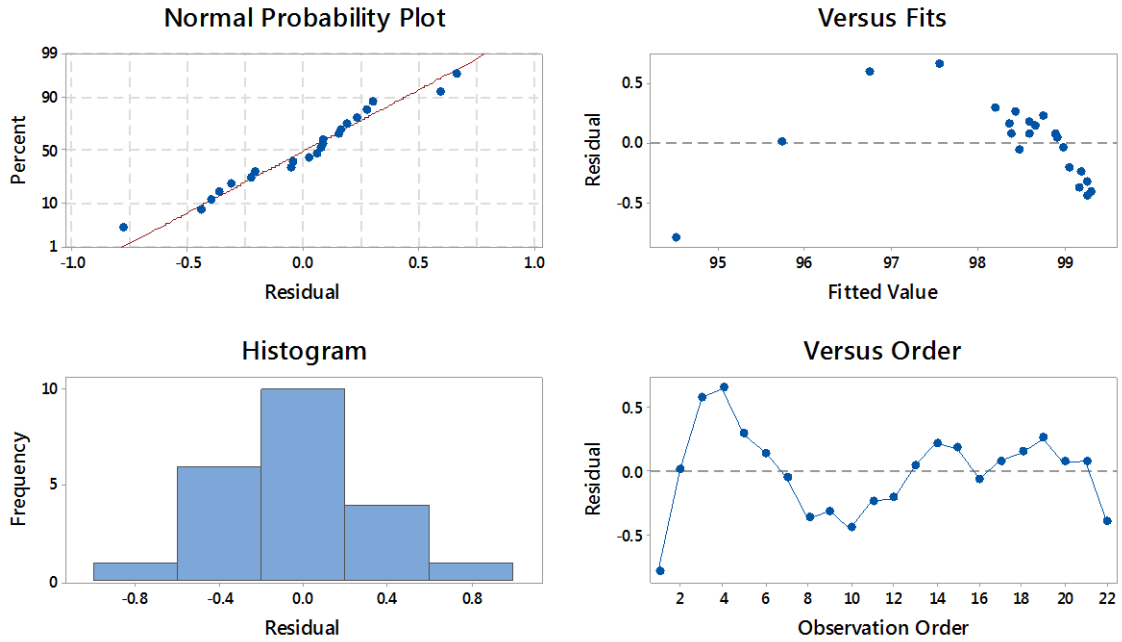

Figure 5-8: Residual plots of the cubic regression model of RD versus VED of the powder type of T3 and LT of 60µm

The shape of the curve appears to have a Logarithmic function as a parent function therefore in Figure 5-9, a Logarithmic relationship was tested. The resultant regression model from this improved and the histogram became symmetrical at the residual mean of zero. Also, Figure 5-9 shows a dramatic improvement in the regression model in terms of the S value, R-square, CI and PI. According to the F-value and the values of the degree of freedom of the regression and error, the P-value is drastically below the selected threshold of 0.05 (Table 5-7). Furthermore, the residual analysis did not reveal any abnormality. The residual in the histogram distributed perfectly around zero (Figure 5-10).

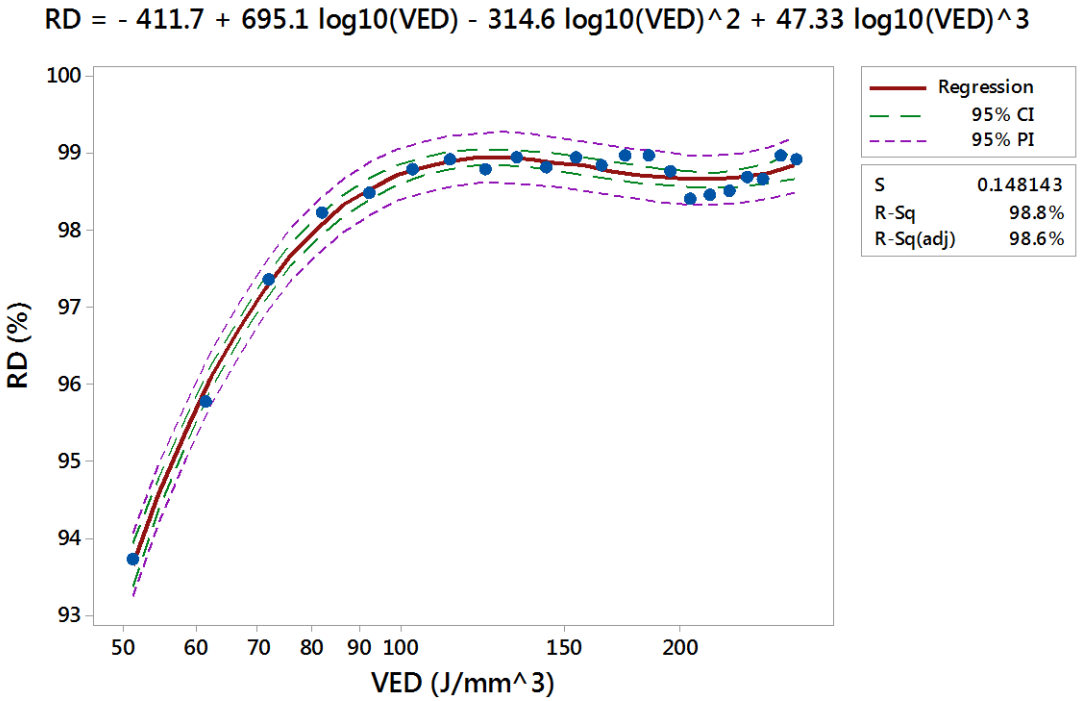

Figure 5-9: Fitted line plot of the cubic relationship of the RD versus $\log_{10}$ (VED) for the powder type of T3 and LT of 60µm

Table 5-7: ANOVA table for the cubic regression model of the RD versus $\log_{10}$ (VED) for the powder type of T3 and LT of 60µm

Source	***DF***	***Sum of Square***	***Mean Square***	***F-Value***	***P-Value***
Regression	3	32.5248	10.8416	494.00	0.000
Error	18	0.3950	0.0219		
Total	21	32.9198			
Summary		**S** = 0.148143	**R-Sq** = 98.8%	**R-Sq(adj)** = 98.6%	

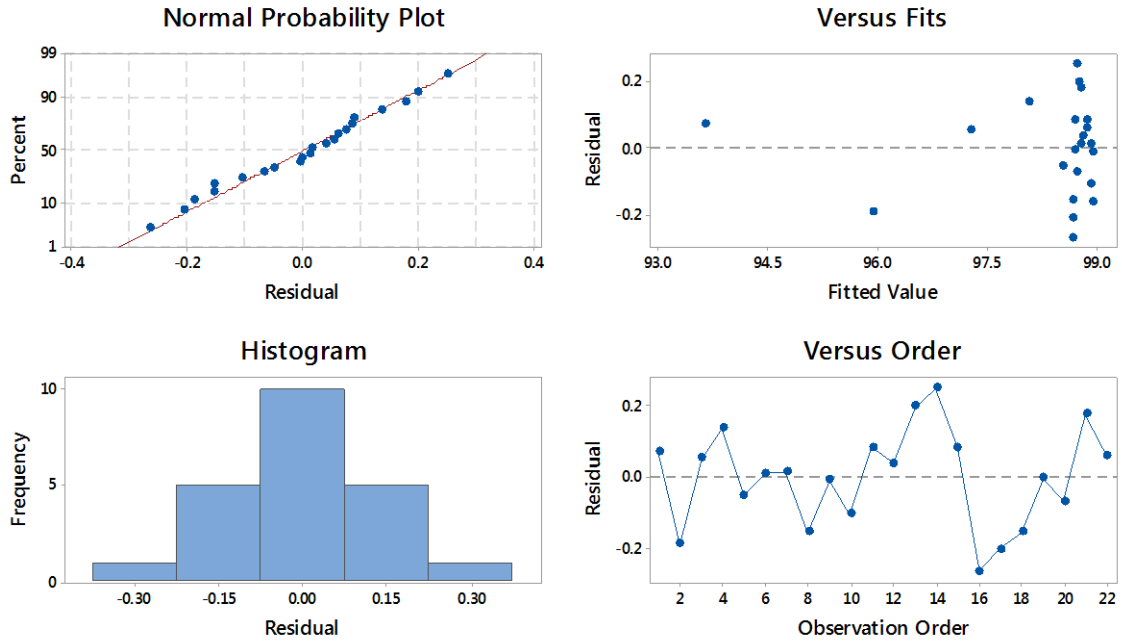

Figure 5-10: Residual plots of the cubic regression model of RD versus $\log_{10}$ (VED) of the powder type of T3 and LT of 60µm

Similar regression models for the all powder types and LTs were developed. However, it was not possible to develop the regression model when the change in the response is not significant enough to identify any clear trend or relationship. For instance, the regression model of the powder type T1 and LT of 80µm was not representative (Figure 5-11). The R-square value was minimal. Using the minimum VED of 53.85J/mm^3, which was the result of using an ET of 60µs, which is near the optimum value (ET of 50µs) led to the highest possible density for the fabricated part from the beginning for this operating condition. Thus, any further increase in the ET/VED did not improve the density of the fabricated part. As a result the fitted line was virtually straight throughout, with no noticeable positive or negative relationship. All other possible regression models for the T1-80 were investigated and none of them could be identified as optimal. The regression model shown in Figure 5-11 was chosen here to keep the consistency with other regression models, for the other powder types and layer thickness of Ti-6Al-4V ELI.

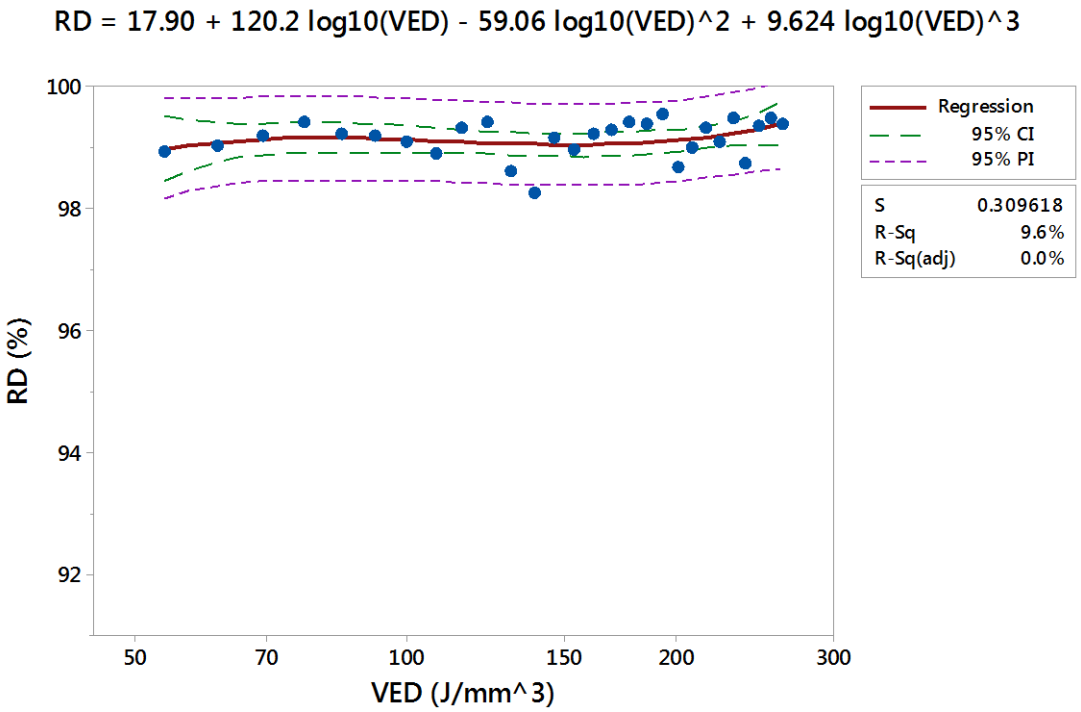

Figure 5-11: Fitted line plot of the cubic relationship of the RD versus $\log_{10}$ (VED) for the powder type of T1 and LT of 80µm

5.3.2. Effect of Changing PSD and LT on RD for Ti-6Al-4V ELI Parts

The effect of changing the PSD and LT of the powder feed on RD was studied intensely for all PSDs and LTs. The relationships identified are compared and discussed in this section. Figure 5-12 shows the correlation between VED and relative density for each powder type and layer thickness builds. Generally, using large particles or thicker powder layers results in a decrease in the fabricated part density, although, it is possible to obtain 99% relative density using any of these powder types. As the ET is increased (VED increases), the part density also increases until a specific level is reached. At this level, the density of the fabricated part does not increase any further, even with further increasing the exposure time.

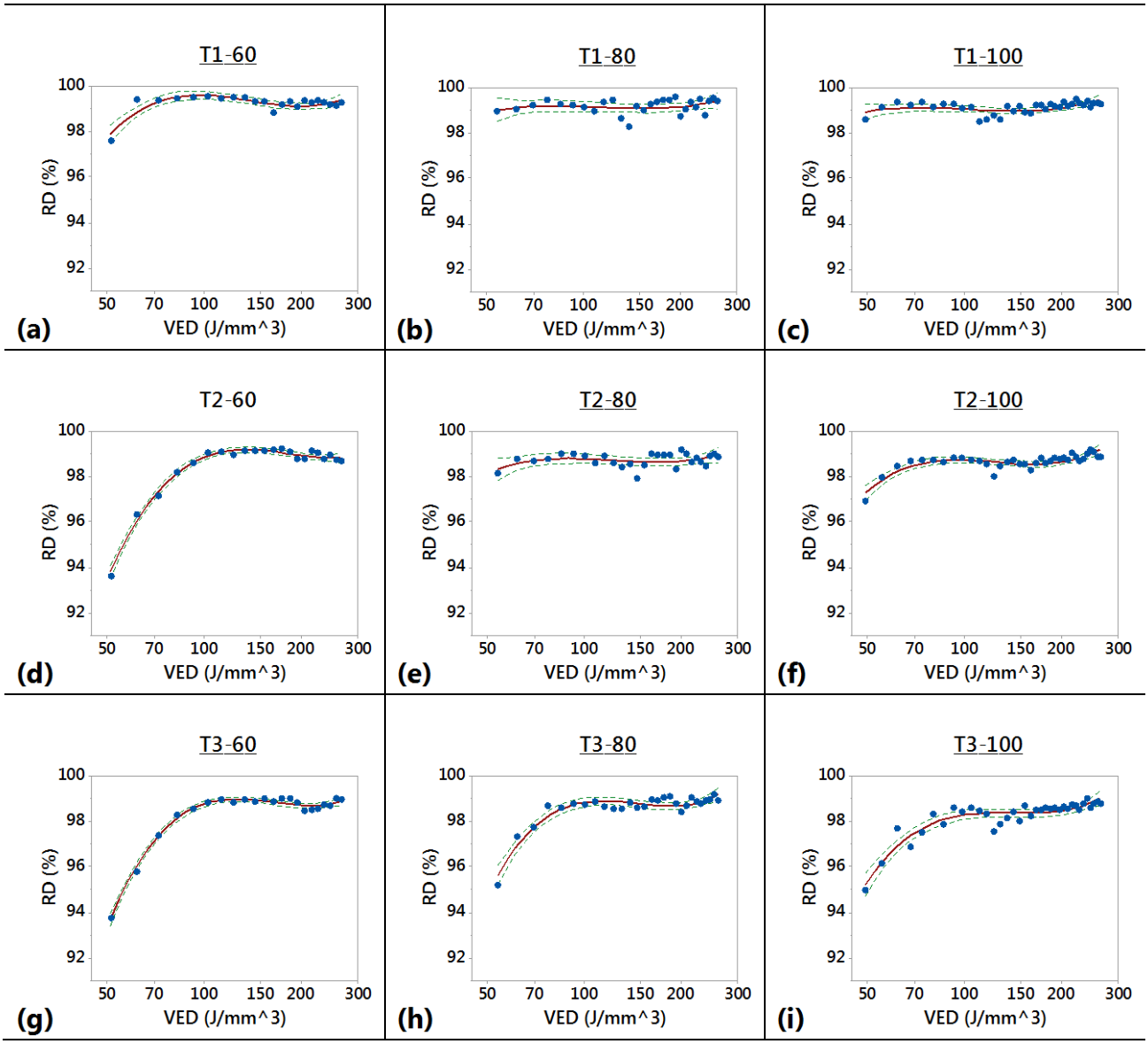

Figure 5-12: Fitted lines of the RD versus VED for all powder types: T1; T2; T3 and layer thicknesses (LT): 60; 80; 100µm. The green dashed line represents the confidence interval.

In Figure 5-12, plots (a-c) are for powder type T1, plots (d-f) are for powder type T2 and plots (g-i) are for powder type T3. Each plot is identified by the powder type and its layer thickness (e.g. T2-80 is the plot of powder type T2 and layer thickness 80µm). The VED in plot a, b and c conducted at exposure time of 40, 60 and 70 respectively, are almost the same. However, this VED led to varying relative densities of the parts, with approximately 97% for T1-60, 99% for T1-80 and 98.5% for T1-100.

For plots (d) and (g), they appear similar due to the particle size distribution of the powder which fits into their layer thicknesses is almost identical. By assuming that the powder layer density was between the apparent density and the tapped density ([162];

[163]), a value of 60% was used. This means the effective layer thickness for a LT of 60µm would be approximately 100µm (according to Equation (2-9)). The actual smallest and largest detected particle size for powder type T2 were 27.4µm and 111µm respectively and for powder type T3 were 31.1 and 144µm respectively. Thus, the particles for both powder types T2 and T3 are able to pack and arrange themselves and fit into layers of 100µm based on the lower limit of the measured particle size. Thus, as a result, it is expected that these ranges of powder particles which are fairly similar, would lead to the comparable results.

Even though the exposure time of 40µs and a layer thickness of 60µm provides a higher VED than an ET of 70µs and an LT of 100µm, the RD of the latter was higher (above 98.5%). This highlights that the VED alone is not an accurate indicator to select a suitable energy for fully melting powder; each factor needs be taken into consideration, especially for pulsed laser PBF. The VED could be used as a guideline to narrow the range down into a potential region, however, the factors which compose the VED need to be isolated to better understand the effect of each individual factor on the overall build.

Generally, the results showed that density of Ti-6Al-4V ELI parts increased in conjunction as the VED was increased up to a certain level. After the RD of the part reached a certain level, it remained relatively constant even with further increases in the VED. This relationship was identified for all PSDs and LTs studied.

5.3.3. 316L-SS

The optimal values of LP, PD and HD shown in Table 4-9 for 316L-SS, were used to investigate the effect of changing layer thickness and powder size distribution on the density of parts at different VED (by varying the exposure time, ET). Two types of 316L-SS (S1 and S2) were used to build 10x10x10mm^3 cubes for different layer thicknesses as shown in Table 3-10. The exposure time was varied according to layer thickness to keep the VED comparable throughout the all LTs. Tables in Appendix B show the calculated values of the SS and VED according to the changes in ET and LT for all powder types, based on Equation (3-5) for SS and Equation (3-6) for VED. The other process parameters were used based on their optimal values found in the optimisation phase: LP of 200W, PD of 70µm and HD of 120µm. Table 5-8 shows an

example of the process parameters and resultant SS, VED and RD for powder type S2 and LT of 40µm.

Table 5-8: Process parameters and the resultant RD for the builds that were used to study the effect of changing PSD and LT for S2 and LT of 40µm for the material 316L-SS

Run#	*LT* (mm)	*LP* (W)	*PD* (mm)	*ET* (s)	*HD* (mm)	*SS* (mm/s)	*VED* (J/mm^3)	*RD* (%)
1	0.04	200	0.07	0.00005	0.12	1093.75	38.10	91.76
2	0.04	200	0.07	0.00006	0.12	945.95	44.05	94.82
3	0.04	200	0.07	0.00007	0.12	833.33	50.00	97.17
4	0.04	200	0.07	0.00008	0.12	744.68	55.95	98.30
5	0.04	200	0.07	0.00009	0.12	673.08	61.90	98.84
6	0.04	200	0.07	0.0001	0.12	614.04	67.86	98.82
7	0.04	200	0.07	0.00011	0.12	564.52	73.81	98.83
8	0.04	200	0.07	0.00012	0.12	522.39	79.76	98.90
9	0.04	200	0.07	0.00013	0.12	486.11	85.71	98.67
10	0.04	200	0.07	0.00014	0.12	454.55	91.67	98.81
11	0.04	200	0.07	0.00015	0.12	426.83	97.62	98.51
12	0.04	200	0.07	0.00016	0.12	402.30	103.57	98.58

Similar to the steps of developing the regression models for the Ti-6Al-4V ELI powder types and layer thicknesses, the regression model were established. The main noticeable different from Ti-6Al-4V ELI powder, was that when developing the regression models for the 316L-SS powders for the layer thicknesses of 60, 80 and 100µm, at high VED the RD decreased. Unlike the Ti-6Al-4V ELI powders, 316L-SS did not maintain it density once a peak value was reached. The effect of changing PSD and LT on part density is discussed in the next section.

5.3.4. Effect of Changing PSD and LT on RD for 316L-SS Parts

This section shows the effect of changing the PSD and LT on the density of the built parts. Powder type of S1 was used to build samples with layer thicknesses of 30, 60, 80 and 100µm. The other powder type, S2, was used to build samples with a layer thickness of 40, 60, 80 and 100µm. Figure 5-13 shows the scatter plots with fitted lines of all powder types and layer thicknesses. The plots are labelled according to the powder type (S1 and S2) and the build LTs.

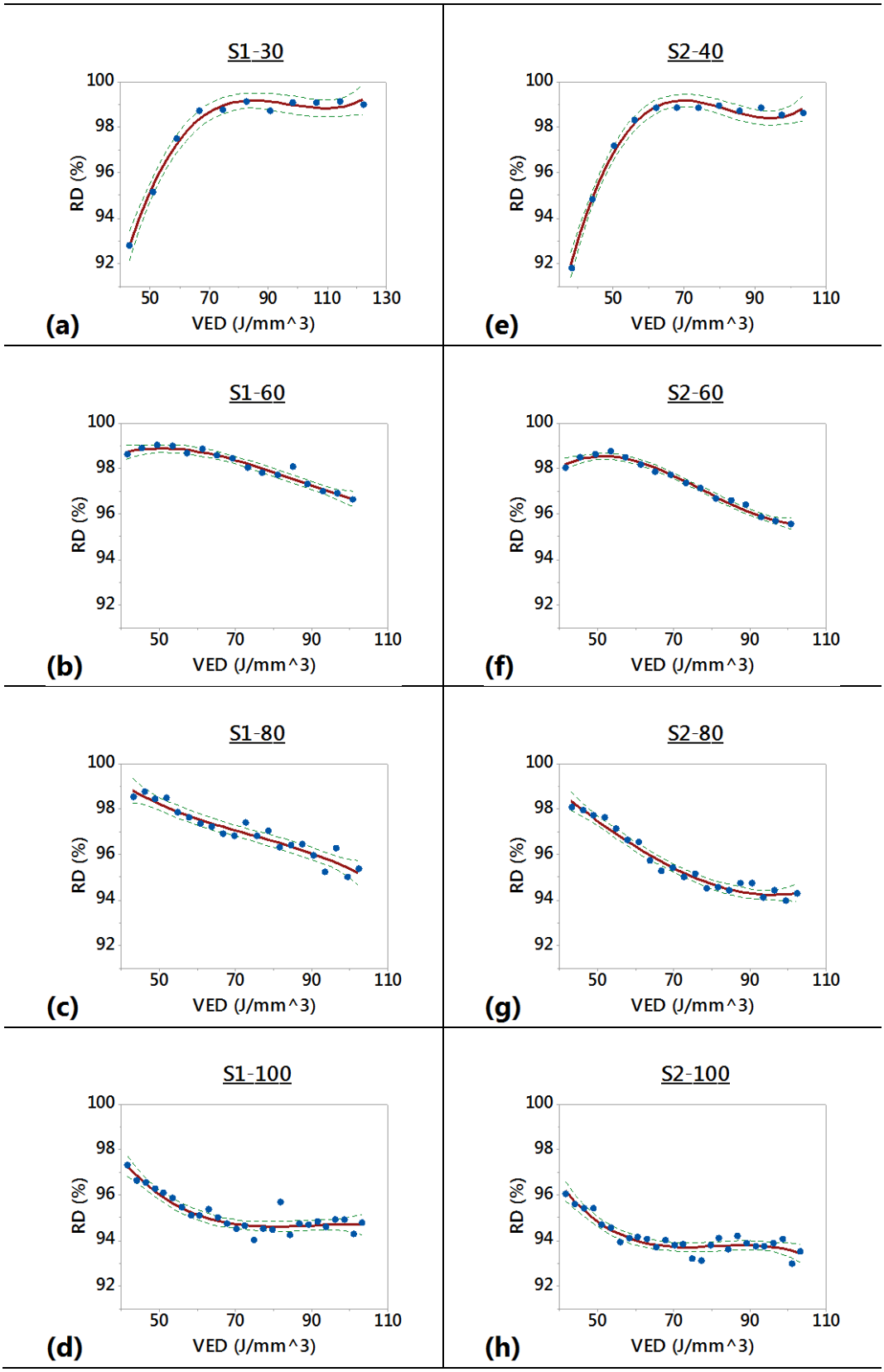

Figure 5-13: Fitted lines of the RD versus VED for all powder types: S1; S2 and layer thicknesses (LT) of: 30; 60; 80; 100µm for S1 and 40; 60; 80; 100µm for S2. The green dashed line represents the confidence interval.

In Figure 5-13, plots (a-d) are for the S1 powder type and layer thickness of 30, 60, 80, 100µm respectively, and the plots of (e-h) are for the S2 powder type and layer thickness of 40, 60, 80, 100µm respectively. Because the mean of the particle size for S2 powder has higher mean than S1 powder, the initial investigated layer thickness was slightly higher.

For the thin powder layer thicknesses (S1-30 and S2-40), the part density increased as the VED was increased. The VED ranged from 42.86J/mm^3 for an ET of 40µs up to 122.22J/mm^3 for an ET of 140µs for the powder type S1, and from 38.1J/mm^3 for an ET of 50µs up to 103.57J/mm^3 for an ET of 160µs. The two plots for the RD against VED appear similar; however, there is a slight difference. The RD of the small PSD powder type of S1, started at a point higher than the S2 powder type. This is believed to be due to the higher surface area to volume ratio for the small PSD powder, where a larger number of the particles are affected by heat and melt faster in comparison to larger powder which will have a smaller surface area to volume ratio. The heat transfer from the outside of the powder to the centre of the powder will be more rapid when the distance travelled (diameter of powder) is smaller.

The relative density of larger layer thicknesses was found to decrease with increasing VED, as shown in plots for the LT 60, 80 and 100µm in Figure 5-13 for both powder types. The deterioration on the RD stopped at a value of approximately between 93.5 and 94.5% for LT of 100µm. The rate of decrease in the RD as the VED was increased depended upon both the PSD and LT; as the larger the PSD or LT, the faster the RD decrease. In other words, a slow scan speed (SS), which resulted in a longer ET, decreased the RD of parts fabricated in 316L-SS. For instance, at the VED of 60J/mm^3 for the S2 powder type, the SS was approximately 673, 454, 343 and 275mm/s for the LT of 40, 60, 80 and 100µm respectively and the ET was 90, 140, 190 and 240µs respectively. Therefore, the VED of 60J/mm^3 at LT of 100µm was a result of using ET at 240µs. This extended period of ET may have contributed in further denudation, spatters and evaporation of the melt pool which resulted in a reduction in the RD of the part.

Comparing the plots of S1-30 and S2-40 to other thicker layer plots, indicated that there was a lack of observations for these two thin layer plots. The highest ET values were

140 and 160µs while for the next LT (60µm) for both PSD, the highest ET used for these was 240µs, which showed the direction of the curve with an increased ET. This implies that potentially the two plots for the smallest layer thickness (S1-30 and S2-40) did not show the complete behaviour of the RD while increasing the VED. If the ET was increased further for the smallest layer thickness, it is believed the trend of the plots would be similar to those seen for the 60µm, in terms of a decrease in the RD as the VED is increased further.

5.4. Discussion

The regression models developed were able to predict the density in good agreement with the actual experimental data obtained. The regression model of Ti-6Al-4V ELI was adequate to describe the variation of the process. It was not, however, as good as the model developed for 316L-SS. The reason for this is believed to be due to the training and validation data used to create and test the model for Ti-6Al-4V ELI, which was obtained from the DOE using the Taguchi method. Even though the Taguchi method is valid to be used in such a process, it is primarily designed for use in discrete events. In addition, the method is not sensitive enough to describe the interactions between the process factors. This means that compared to the RSM method, the Taguchi method is less capable of producing an excellent regression model. For the current study, the advantage of the Taguchi method is that the regression model obtained is simpler and has fewer terms compared to that produced by the RSM method for the 316L-SS data. The regression model of the 316L-SS was accurate enough to describe as much as 98% of the variation of the process. The interaction between factors can be captured by using the RSM method. This increases the complexity of the model. In this study, the number of significant factors is high. Any elimination of any of these significant factors causes the model to deteriorate dramatically. For instance, deleting the term that has the smallest coefficient value (ET^4) results in a model which has p-value where the Lack-of-Fit term is ≤ 0.0001, which means significant Lack-of-Fit. The models developed, however, may only be valid for the range of parameters and the materials investigated.

To produce a more robust model for the PBF process, material properties (such as particle size distribution, powder absorptivity for the melt energy and heat conductivity)

and process parameters (such as including other parameters, different ranges of process parameter) should be included in the model equations.

Correlation models for different PSD and LT showed that small PSD powders gave higher part density at all LTs and thin powder layer (small LT) gave higher part density within the same PSD powder. This was the same for both materials (Ti-6Al-4V ELI and 316L-SS). The use of a small PSD powder results in a higher packing density and higher laser beam absorbability/absorption. Therefore, the small PSD produces a higher density part even when the number of particles is higher in a fixed LT. This was in agreement with similar results found by King et al. [43]. They illustrated that the laser beam absorption increases when the beam hits an area with small particles. The multiple beam reflection by particles improves the powder absorption rate compared to larger powder particles. Building near fully dense parts by using courser particles, however, is still possible. Thermal conductivity for steel contributes to rapid cooling before a melt pool collapses completely, which leads to keyhole porosity and deterioration in the relative density. With Ti-6Al-4V ELI parts the relative density maintained the highest value reached even with further increase in the volumetric energy density (VED). In the case of 316L-SS parts the relative density decreased with further increases in the VED and then maintained its level. A collection of the all plots supports the conclusion that the curve shape for 316L-SS material could be as shown in Figure 5-14. The minimum RD would be the RD of the powder before fusion and the highest RD would differ according to the PSD and LT.

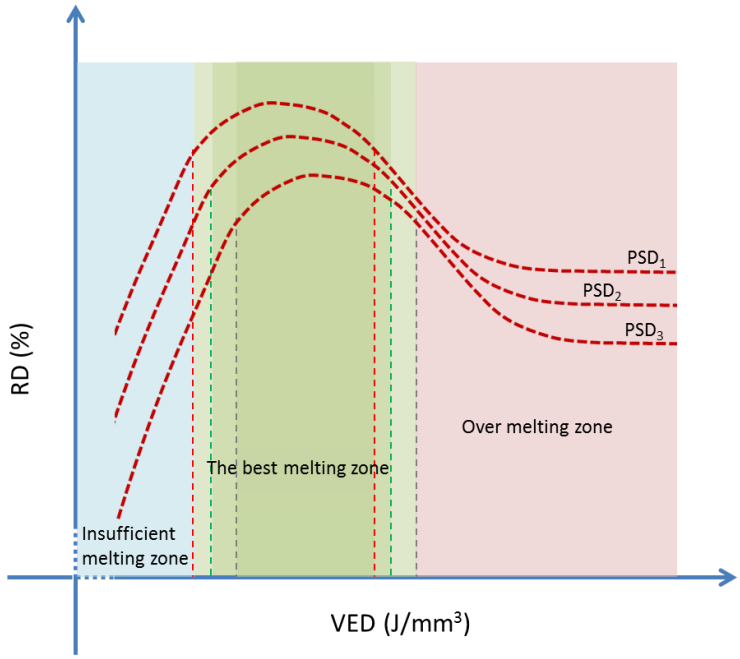

Figure 5-14: Predicted shape of the relationship between VED and RD for additively manufactured 316L-SS parts using any different particle size distributions (PSD), where $PSD_1 < PSD_2 < PSD_3$.

Moreover, it was noticed that 316L-SS powder created more spatter on the build area during the melt process compared to the Ti-6Al-4V ELI powder. Figure 5-15 shows the amount of spatter for the Ti-6Al-4V ELI and 316L-SS powders. Figure 5-15 (a) is for the Ti-6Al-4V ELI powder with a LT of 100µm and the ET ranging from 60µs to 330µs. For 316L-SS, the LT was 80µm and the ET ranged from 130µs to 330µs, Figure 5-15 (b). The PSDs of both materials was almost the same (T1 vs S1).

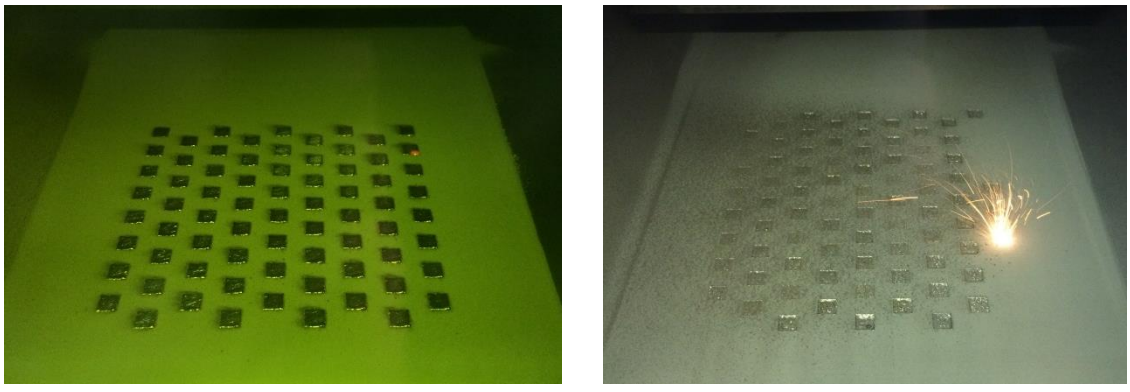

(a) **(b)**

Figure 5-15: Examples of the amount of spatter for (a) Ti-6Al-4V ELI and (b) 316L-SS during PBF process.

Two scenarios are believed to contribute in the spatter issue. Firstly, it is observed that 316L-SS generated more spatter than Ti-6Al-4V. The thermal properties of the 316L-SS could be a cause for generating more spatter. For instance, the melting temperature of 316L-SS is lower than the melting temperature of Ti-6Al-4V. Consequently, at the same energy density, 316L-SS powder will melt faster than Ti-6Al-4V and potentially boil and bubble. This will eject some molten material from the melt pool as droplets of spatter, which is driven by high recoil pressure.

As the low melting temperature of 316L-SS is lower, that means it is possible that small particles ejected will condense and coalesce with each other while flying in air and solidify as larger spatter material that cannot be blown off the build platform by the gas flow [164]. As the cooling rate of 316L-SS is faster than Ti-6Al-4V, it is possible to produce more condensed spatter during processing 316L-SS. A further possible reason is due to the different physical properties, particularly the density of the material. The weight of a particle of Ti-6Al-4V ELI is approximately 55% of that of an equivalent particle of 316L-SS. Therefore, spatter of the lighter Ti-6Al-4V ELI may be easily blown away from the build area while for the denser 316L-SS, the spatter has a greater chance of landing back on the scan cross section area. Consequently, the spatter will impact the next layer negatively, leading to parts being fabricated with a reduced RD. The impact of the spatter is believed to be more prevalent on parts built furthest from the argon gas, and least on the parts built closest to the argon gas though further work is needed to verify this.

This study is believed to be the first systematic attempt to use RSM for the design of experiments (DOE) to investigate the effect of process parameters of the pulsed-laser PBF process on the density of fabricated components.

The study demonstrated a clear correlation between the number and shape of pores and the process parameters was identified. Point distance, exposure time and layer thickness were found to significantly affect part density. The interaction between these parameters also critically affected the development of porosity. Finally, a regression model was developed and verified experimentally which can be used to accurately predict part

density. The results of this work were published in the Rapid Prototype Journal[1] in 2019.

[1] A. Y. Alfaify, J. Hughes, and K. Ridgway, "Controlling the Porosity of 316L Stainless Steel Parts Manufactured via the Powder Bed Fusion Process," Rapid Prototyping Journal, vol. 25 (1), pp. 162-175, 2019.

6. BUILD LOCATION EFFECTS

6.1. Introduction

The majority of the research conducted on powder bed fusion (PBF) processes, has focused primarily on the process parameters and/or powder characterisation and material properties of the alloys being fabricated. During the study of previous research, no study was been identified that looked into the effects of machine architecture on the quality of fabricated parts. In the current study, it was observed that there was a variation in the density of cubes built using identical process parameters during the same build. Even though the variation was sometime minimal, it was detectable. It was believed this variation in density could be correlated to the build location on the platform. It was an interesting observation and motivation to re-analyse the fabricated samples according to the build location. The aim of this chapter is to investigate the effect of build location on the platform upon the density of the part being fabricated, to determine the optimum build location on the platform that gives the highest part density. Also, the chapter aims to investigate the possible reasons that lead to this variation and ways to mitigate or eliminate this variation to make the process more reproducible.

6.2. Location Analysis

For 25 builds (from in excess of 1500 samples) of Ti-6Al-4V ELI and 316L-SS, the part location on the platform was analysed to investigate the effect of build location on the platform and establish the optimum location on the build platform for the highest part density. Each set of samples contained four cubes, which were built using the same process parameters. They were arranged on the build platform to cover different locations on the build area. Figure 6-1 shows a sample of the arrangement of the cubes on the platform.

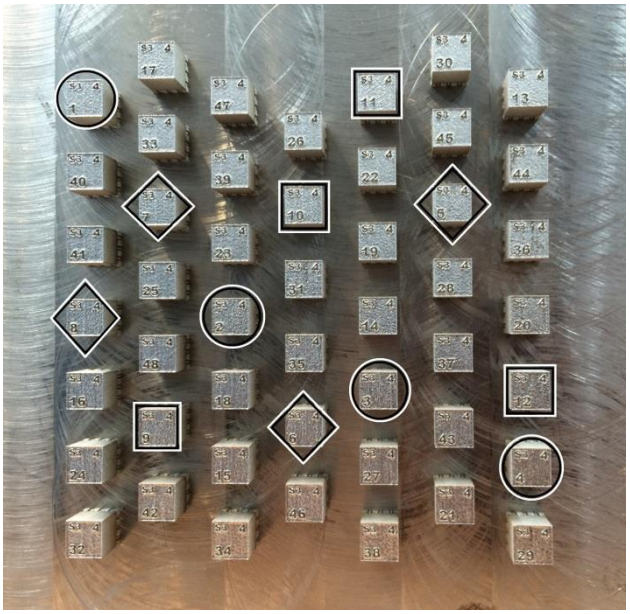

Figure 6-1: Cubes' arrangement on the built platform. Three sets are highlighted to illustrate their arrangements: cubes 1-4 (marked by circles) are for the first set, cubes 5-8 (marked by diamonds) for the second set and cubes 9-12 (marked by squares) are for the third set.

For each set of cubes that were fabricated by the same process parameter, the density variation was labelled as minor and negligible if it was less than 0.1%, medium if the density variation was greater than 0.1% and less than 0.5%. If the variation was greater than 0.5%, it was considered major (Table 6-1).

Table 6-1: Density variation categorisation

Density Variation, DV (%)	***Label***
DV < 0.1	Minor/negligible
0.1 < DV < 0.5	Medium
DV > 0.5	Major

The variation was coded according to the main RGB colours, with Blue corresponding to zero and indicating minor variation, medium variation was coded Green and major variation indicated by the Red colour. The complete platform size is approximately 250 x 250mm^2, and build area was 200 x 200mm^2 which represents the area on which parts could be fabricated. The actual build area on the platform was divided into 25 squares, which were 40 x 40mm^2 each (Figure 6-2).

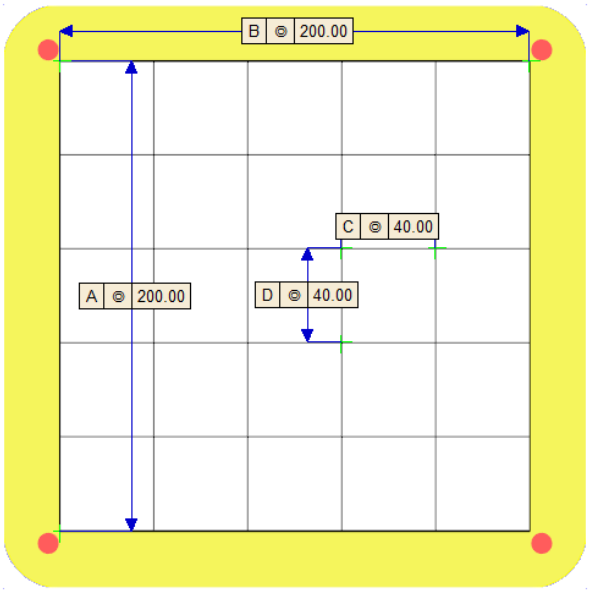

Figure 6-2: Selected area of 200mm x 200mm on the build platform divided into 25 squares, 40mm x 40mm.

The samples that were built in each square were put into a group according to their variation from the best cube in their set. Then, the number was converted into a percentage value according to the total number of cubes that were built in the square and called C_{ijk}. The percentage of each colour on the X-Y location (coded (ij)) on the build platform is represented as the following matrix:

$$C_{ijk} = \begin{bmatrix} \begin{bmatrix} c_k \\ c_k \\ c_k \end{bmatrix}_{ij} & \begin{bmatrix} c_k \\ c_k \\ c_k \end{bmatrix}_{ij} & \begin{bmatrix} c_k \\ c_k \\ c_k \end{bmatrix}_{ij} & \begin{bmatrix} c_k \\ c_k \\ c_k \end{bmatrix}_{ij} & \begin{bmatrix} c_k \\ c_k \\ c_k \end{bmatrix}_{ij} \\ \begin{bmatrix} c_k \\ c_k \\ c_k \end{bmatrix}_{ij} & \begin{bmatrix} c_k \\ c_k \\ c_k \end{bmatrix}_{ij} & \begin{bmatrix} c_k \\ c_k \\ c_k \end{bmatrix}_{ij} & \begin{bmatrix} c_k \\ c_k \\ c_k \end{bmatrix}_{ij} & \begin{bmatrix} c_k \\ c_k \\ c_k \end{bmatrix}_{ij} \\ \begin{bmatrix} c_k \\ c_k \\ c_k \end{bmatrix}_{ij} & \begin{bmatrix} c_k \\ c_k \\ c_k \end{bmatrix}_{ij} & \begin{bmatrix} c_k \\ c_k \\ c_k \end{bmatrix}_{ij} & \begin{bmatrix} c_k \\ c_k \\ c_k \end{bmatrix}_{ij} & \begin{bmatrix} c_k \\ c_k \\ c_k \end{bmatrix}_{ij} \\ \begin{bmatrix} c_k \\ c_k \\ c_k \end{bmatrix}_{ij} & \begin{bmatrix} c_k \\ c_k \\ c_k \end{bmatrix}_{ij} & \begin{bmatrix} c_k \\ c_k \\ c_k \end{bmatrix}_{ij} & \begin{bmatrix} c_k \\ c_k \\ c_k \end{bmatrix}_{ij} & \begin{bmatrix} c_k \\ c_k \\ c_k \end{bmatrix}_{ij} \\ \begin{bmatrix} c_k \\ c_k \\ c_k \end{bmatrix}_{ij} & \begin{bmatrix} c_k \\ c_k \\ c_k \end{bmatrix}_{ij} & \begin{bmatrix} c_k \\ c_k \\ c_k \end{bmatrix}_{ij} & \begin{bmatrix} c_k \\ c_k \\ c_k \end{bmatrix}_{ij} & \begin{bmatrix} c_k \\ c_k \\ c_k \end{bmatrix}_{ij} \end{bmatrix}$$

A MATLAB code was developed to generate a colour map that represents the optimum location on the build platform, which produces the lowest density variations compared to the highest possible density for the same process parameters built on any location on

the build platform. The RGB colour analysis for any colour depends on the mixed value of the main three colours: red, green and blue.

$$colour = \begin{bmatrix} Red \\ Green \\ Blue \end{bmatrix}$$

The value is between 0 and 255 for each of the three colours. For instance, the black colour is a result of mixing zero values of red, green and blue, while the white colour is a result of mixing 255, 255, and 255 of red, green and blue respectively. For the main colours, the RGB combination is represented by:

$$Red = \begin{bmatrix} 255 \\ 0 \\ 0 \end{bmatrix}, Green = \begin{bmatrix} 0 \\ 255 \\ 0 \end{bmatrix}, \text{and } Blue = \begin{bmatrix} 0 \\ 0 \\ 255 \end{bmatrix}$$

These three colours were used to design the weighting matrix which was used to convert the colours obtained from classifying the cube density according to their variation colour. The weighting matrix is as follows:

$$W_{kl} = \begin{matrix} Red \rightarrow \\ Green \rightarrow \\ Blue \rightarrow \end{matrix} \begin{bmatrix} w_{11} & w_{12} & w_{13} \\ w_{21} & w_{22} & w_{23} \\ w_{31} & w_{31} & w_{33} \end{bmatrix} = \begin{bmatrix} 255 & 0 & 0 \\ 0 & 255 & 0 \\ 0 & 0 & 255 \end{bmatrix}$$

The total weighted colour value, V_{ij}, for a location is given by the following equation, Equation (6-1):

$$V_{ij} = \sum_{k} \left(C_{ijk} * \left(\sum_{l=1}^{l} (W_{kl})^{l} \right) \right) \tag{6-1}$$

where V_{ij} is the summation of multiplying a colour code in C_{ijk} by the summation of the colour code weight at the same row of W_{kl}.

Then, the value of all V_{ij} was normalised between 0 and 100 as follows, Equation (6-2):

$$Normalised\ value = \left(\frac{V_{ij} - \min(V_{ij})}{\max(V_{ij}) - \min(V_{ij})} \right) * 100 \tag{6-2}$$

The colour map of the value of $(1 - Normalised\ value)$, which is the porosity, was generated so that the highest value represents the worst location on build platform for the fabricated part to be located and the lowest value represents the ideal location on the build platform for the fabricated part to be located.

For colour presentation, RGB colour analysis was conducted using MTLAB (R2016b), Appendix C, where Red represents major variation, Green represents the medium variation and the Blue represents the mild variation. As it was possible for a build to be located on the boundaries of the squares created by dividing the build platform (Figure 6-2), smooth transitions of colours between squares were coded. The colour map for Ti-6Al-4V ELI in Figure 6-3 (a) shows that the parts built in the top right of the platform have the potential for higher densities compared with those built elsewhere on the platform when using the same process parameters. Figure 6-3 (b) for 316L-SS reveals that the right-hand side of the platform gives higher density parts compared to the left-hand side. The analysis results of Ti-6Al-4V ELI, Figure 6-3 (a), and 316L-SS, Figure 6-3 (b), show that 316L-SS has a greater sensitivity to the build location in comparison to Ti-6Al-4V ELI for the process parameters studied. Consequently, the difference between the right hand side and the left hand side of platform is high. Even though the top-right location of platform is considered to be the best build location for both materials, the discrepancy of the build locations is also influenced by the primary powder material.

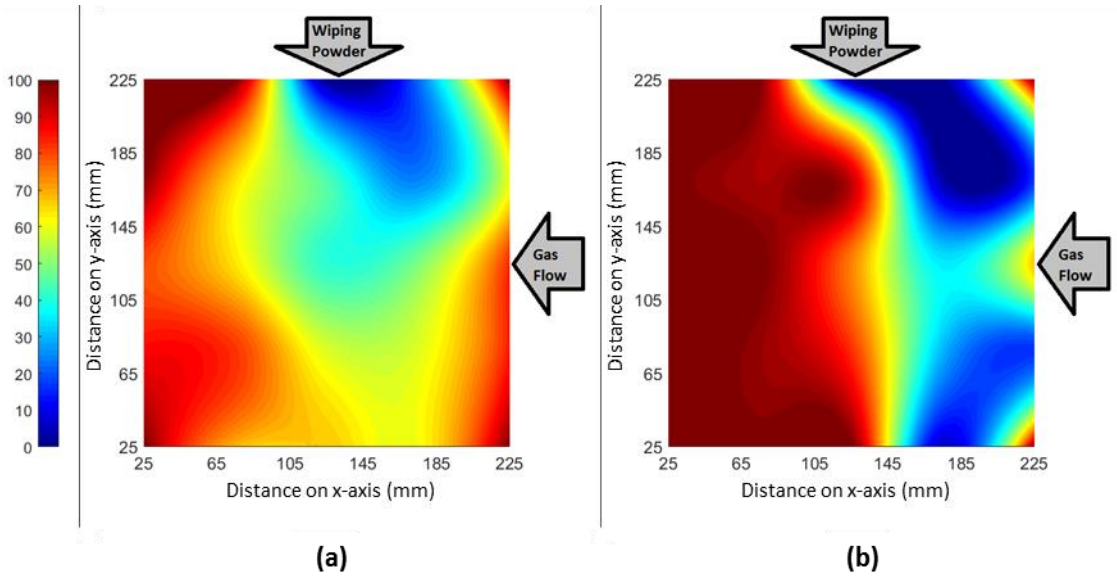

Figure 6-3: Colour map of the build location analysis on the platform for the area of 200mm x 200mm of (a) Ti-6Al-4V ELI and (b) 316L-SS.

The illustration bar in Figure 6-3 represents the normalised porosity variation. They can be considered as indicators of the probability of obtaining lower density builds when compared to other locations on the platform. It is assumed that the origin of the platform is located in the bottom left corner, in accordance with the machine coordinate system as defined in the ASTM standard [6]. The X-axis and Y-axis values are the distance from the origin. Figure 6-3 shows that the analysis of part location covered a 200 x 200mm^2 area starting 25mm from the origin on X and Y for (a) Ti-6Al-4V ELI and (b) 316L-SS.

The areas on the build platform that have the highest variation, higher than 80 on the colour bar, were quantified by 19.03% from the build platform area for the Ti-6Al-4V ELI and by 48.69% for 316L-SS. However, 316L-SS had a greater percentage for the area with lowest variation, less than 20 on the colour bar and 14.92% for 316L-SS compared to 4.18% for Ti-6Al-4V ELI. The acceptable level of variation depends on the quality needed for any application. However, the area represented by the range from above 20 to 80 on the colour bar for Ti-6Al-4V ELI is double the area for 316L-SS, 76.7% versus 36.39% respectively. Table 6-2 shows the percentage of each colour range of the analysed area on the build platform. Table 6-2 is a summary of the colour analysis presentation shown in Figure 6-4.

Table 6-2: Colour area as a percentage out of 200mm x 200mm according to the colour range shown on the colour bar in Figure 6-3

Range	***Material***	
	Ti-6Al-4V ELI	316L-SS
> 0 to 10	1.01	8.11
> 10 to 20	3.17	6.81
> 20 to 30	5.03	8.35
> 30 to 40	8.37	8.03
> 40 to 50	11.57	6.53
> 50 to 60	14.87	4.37
> 60 to 70	21.99	3.99
> 70 to 80	14.87	5.12
> 80 to 90	13.62	6.04
> 90 to 100	5.41	42.65

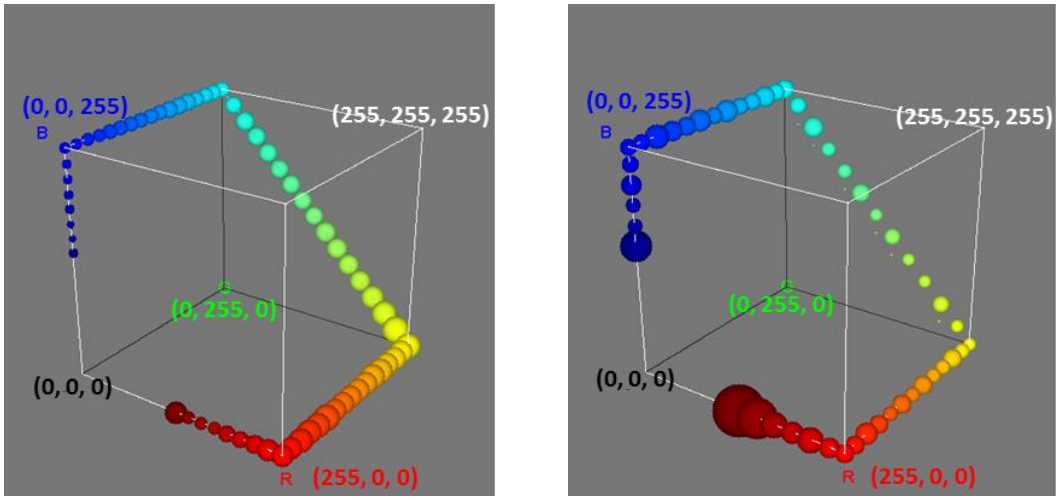

Figure 6-4: A presentation of the percentage area of each colour for the considered 200 x 200mm^2 build area on the build platform for (a) Ti-6Al-4V ELI and (b) 316L-SS. Ti-6Al-4V ELI build plat form had a larger area that may result in minor variation in part density. 316L-SS build platform had a larger area that could lead to major variation in the resultant part density (Red in (b)). However, it had a larger area that can be used where the variation in the resultant part density was negligible.

As the majority of the builds were fabricated in the middle of the platform, another location analysis was conducted for the most commonly used area on the platform to trace the variation on the reduced build area. The covered area was of 150mm x 150mm, starting 50mm from the origin on X and Y. It was divided into 9 squares and each square was 50mm in length (Figure 6-5).

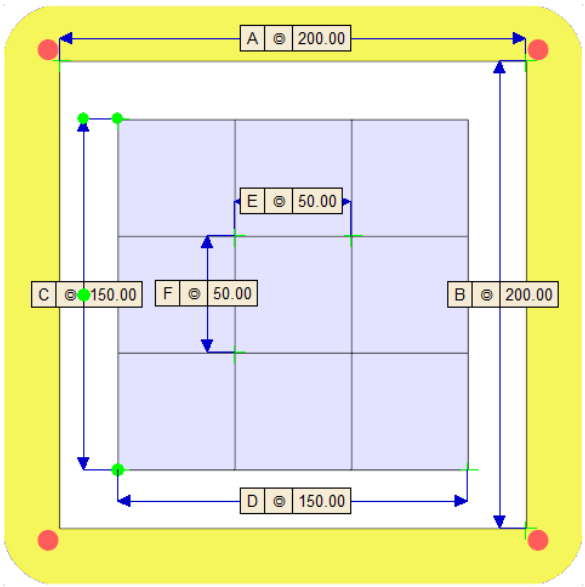

Figure 6-5: Reduced build area, 150mm x 150mm, on the build platform divided into 9 squares, 50mm x 50mm.

Generally, from Figure 6-6, it was confirmed that the right-hand side of the build platform was better than the left-hand side. However, Ti-6Al-4V ELI builds appeared to be less sensitive in the reduced area considered, with minimal variation in terms of location. The 316L-SS builds still had a greater variation in terms of build location, when compared to Ti-6Al-4V ELI. This confirms that the build location is also material-dependent, and therefore other materials may be more or less sensitive to the location in which they are fabricated on the substrate.

These findings highlight the importance of considering the positioning of the sample being fabricated on the build platform and how the location may need to be fixed for multiple builds to achieve acceptable reproducibility. This also highlights the importance of part orientation on a build, as a part fabricated in one region initially for the first layers, for example the lower left region, and then as the layer are built up in the Z-height, the part shifts towards the upper right, this will result in density variation within the part. Thus, care must be taken to understand the effect of part orientation not solely on optimising and reducing build time, but the influence this will have on the part density.

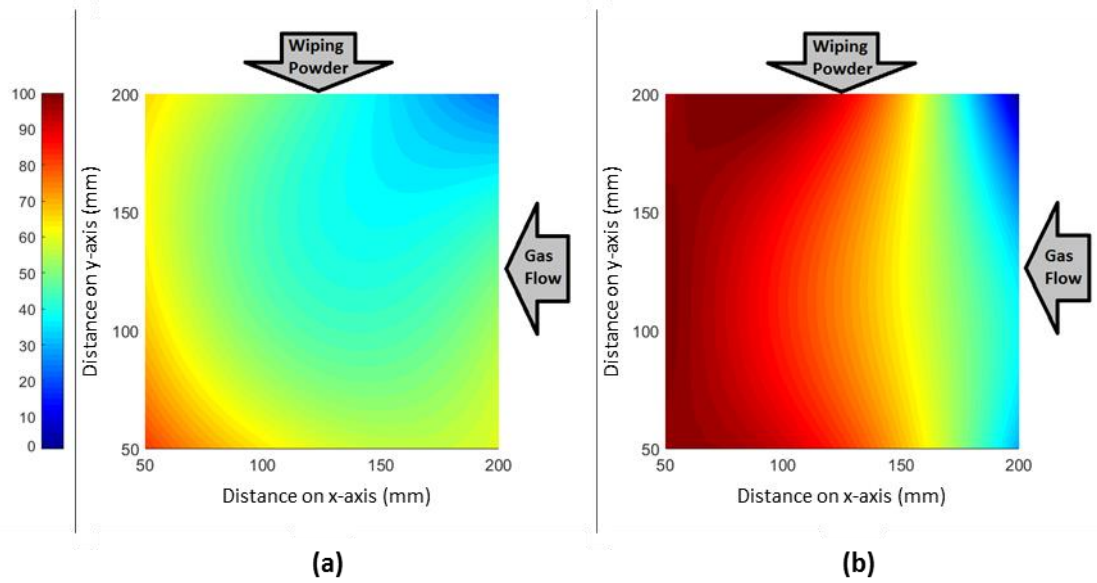

Figure 6-6: Colour map of the build location analysis on the platform for the area of 150mm x 150mm of (a) Ti-6Al-4V ELI and (b) 316L-SS, where the blue colour represents the location where the potential porosity variation is minimal.

The result from the Table 6-3 and Figure 6-7 indicated that 99.95% of the 150mm x150mm area on the build platform is located on a range from above 20 to 80 on colour

bar for Ti-6Al-4V ELI. The same range for 316L-SS, however, covered only 52.58% of the considered build area while 46.45% is above the value 80 on colour bar.

Table 6-3: Colour area as a percentage out of 150mm x 150mm according to the colour range shown on the colour bar in Figure 6-6

Range	*Material*	
	Ti-6Al-4V ELI	316L-SS
> 0 to 10	0	0.16
> 10 to 20	0	0.79
> 20 to 30	1.52	1.6
> 30 to 40	24.09	6.62
> 40 to 50	33.84	9.03
> 50 to 60	28.53	9.8
> 60 to 70	10.19	12.81
> 70 to 80	1.78	12.72
> 80 to 90	0.03	18.54
> 90 to 100	0	27.91

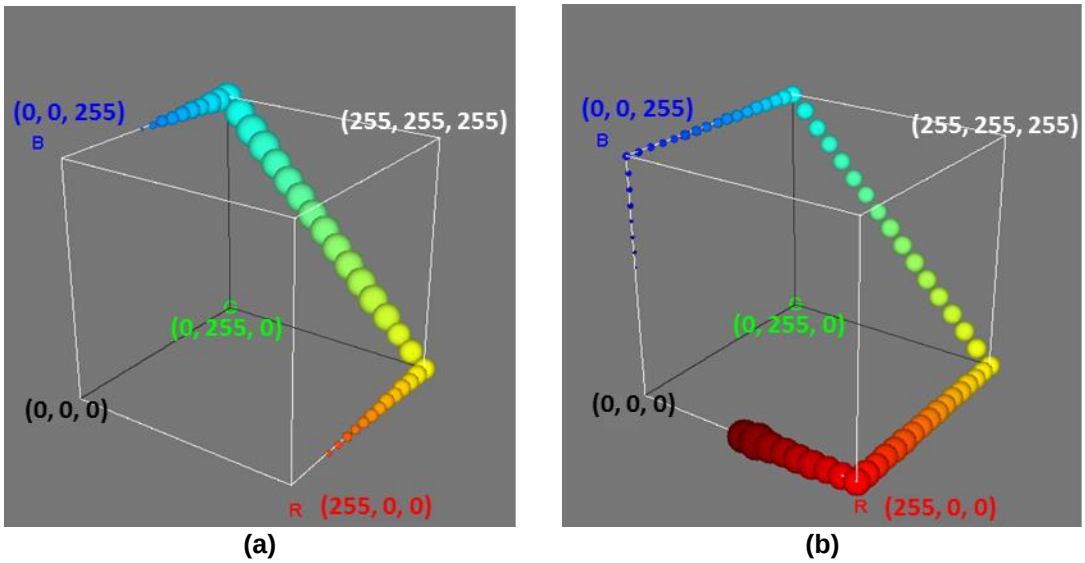

Figure 6-7: A presentation of the percentage area of each colour for the considered 150mm x 150mm build area on the build platform for (a) Ti-6Al-4V ELI and (b) 316L-SS. For Ti-6Al-4V ELI reduced build area, 99.95% of the platform resulted in the minor variation in the part density while there was 52.58% for 316L-SS. Area with negligible variation (<20% on the colour bar) was 0.03% for Ti-6Al-4V ELI and 46.45% for the 316L-SS.

The following figures show the actual measured values of the porosity of parts built using the same process parameters (in the same group) yet, in different locations on the platform. Figure 6-8 is for Ti-6Al-4V ELI parts and Figure 6-9 is for 316L-SS parts. Both figures are for standard powders with a layer thickness of 60µm.

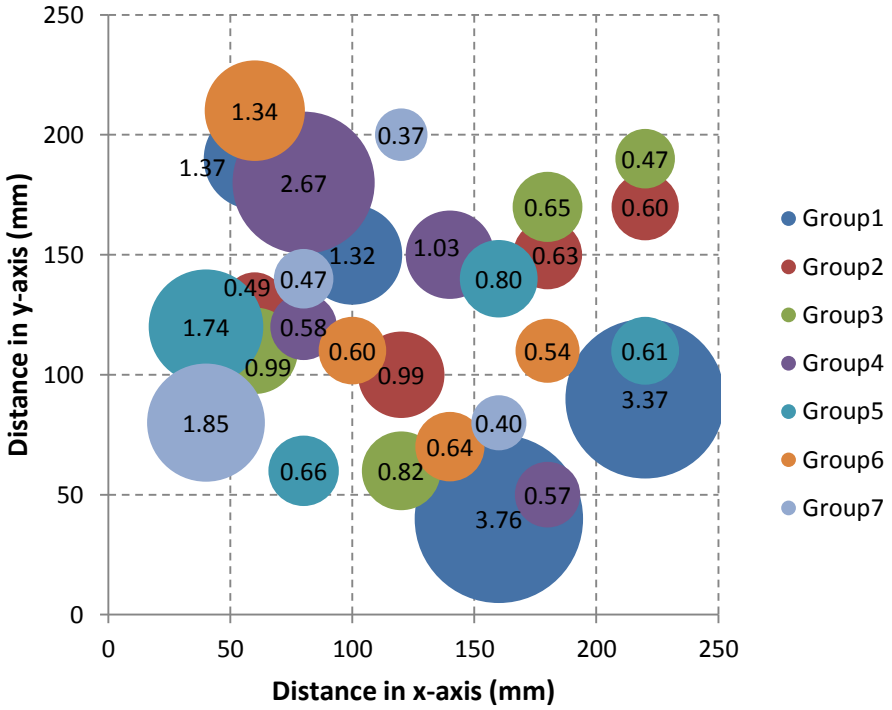

Figure 6-8: Porosity as percentage (%) values for samples of Ti-6Al-4V ELI parts fabricated by standard powder (T1) and LT of 60µm at different distances from the origin of the build platform.

When the process parameters are not suitable for high part density, the variation on the density for the four cubes in the same set is higher. For instance, Group 1 in Figure 6-8 has an average relative density of 97.5%. The porosity ranged from 1.32% to 3.76%. In contrast, when the process parameters are suitable to fabricate parts with high density, the porosity range between fabricated cubes was smaller (0.37-1.85% for Group 7 as an example). Therefore, the obtained relative density for Group 1 ranges from 96.24% to 98.68% and for Group 7 ranges from 98.15% to 99.63%. This overlapping in relative density values between Group 1 and Group 7 could mislead process parameter selection. Using process parameters of Group 7 to fabricate Ti-6Al-4V ELI parts with a relative density higher than 99% is not always guaranteed, as the incorrect choice of build location has the potential to result in a density of 98%.

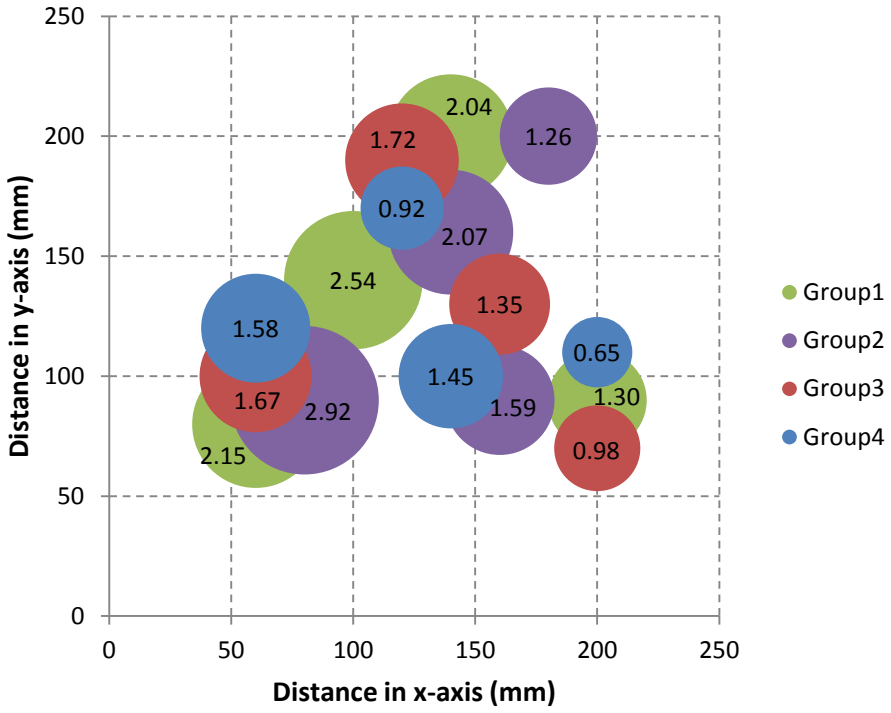

Figure 6-9: Porosity as percentage (%) values for samples of 316L-SS parts fabricated by standard powder (T1) and LT of 60µm at different distances from the origin of the build platform.

The higher variation in the density of fabricated Ti-6Al-4V ELI parts was dominantly located on the left side of the build platform. There were some groups of parts which tended to have a higher variation at the right side of the platform, however, that was found to be minimal and the majority was to the left. The number of groups for 316L-SS shown in Figure 6-9 is only four to avoid overlapping and for more clarity. It was found that the density value of 316L-SS parts was more sensitive to build location than Ti-6Al-4V ELI parts. In Figure 6-9, the variation in the relative density of Group 3 was small, less than 0.75% with relative density ranges from 98.28% to 99.02% while in the variation in Group 2 was between 0.85% and 1.66% (Relative density 97.08% - 98.74%). Again, this overlapping could lead to a wrong selection for the process parameters.

6.3. Discussion

There are many possible reasons that may cause the variation in density when building in different locations such as:

- Wiping powder direction: as the wiper moves from the back of the platform to the front of the build platform (for the Renishaw AM250) to spread the powder, the majority of small particles in the powder being spread can fit easily in the first locations from the back. As a result, the furthest parts from the back of the platform (extreme front parts) would have larger particles as the majority of smaller particles would have been spread already. Whiting and Fox [165] showed that the D_{90} for the particles located close to the powder dispenser was smaller than particles located on the other side along the wiping direction. Even though the variation was small, the difference was detectable. As some larger particles can settle in the valleys between the melt track of previous melt layers as seen by Whiting and Fox [165], the majority of them are pushed towards the end of or outside the build platform as observed by Slotwinski et al. [166]. Consequently, the powder bed porosity could be found to increase along the wiping direction (farthest from the powder dispenser) [167]. In addition to this, the spatter from previous scanned layer would be dragged towards the front of the build platform as the new layer of powder is being spread. These will contribute to additional porosity in parts located in the front of the build platform. The direction of the wiping powder had more impact on the Ti-6Al-4V ELI parts than the 316L-SS parts.

- Ejected powder particles from melt pool ([112]; [164]; [168]; [169]): spatter (ejected particles) from the melt pool would be blown away by the gas flow to the left of the build platform. Consequently, the parts located on the left-hand side of the platform have a greater possibility to be affected by this spatter, which could be partially molten, oxidised and deformed in shape (non-spherical). When builds were removed from the machine, the loose powder on left-hand side of the build was clearly affected by the spatter as shown in Figure 6-10. The impact of the spatter is believed to be more prevalent on parts built furthest from the gas flow, and least on the parts built closest to the gas flow, although further work is needed to verify this and to see the extent to which the gas flow and spatter affects the fabricated parts.

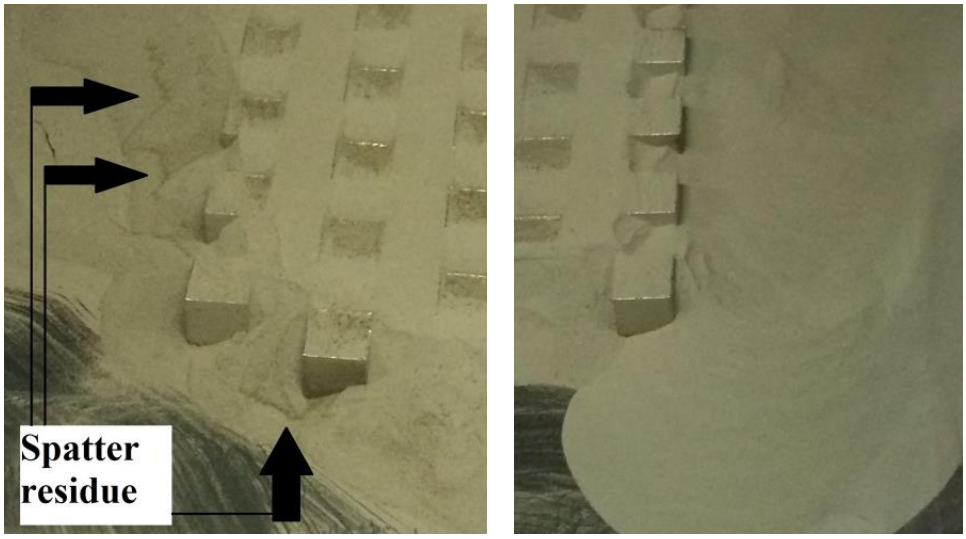

Figure 6-10: Images of the left and right sides of the build platform for the same build shows spatter residue mixed with powder in the left side of the build platform (a) while the powder in the right side (b) was clean.

- Defocused laser beam by fine spatter: spatter creates a cloud of nanoparticles which could disturb the laser beam. The amount and the density of this nanoparticles' dust has the potential to magnify the loss of beam density/focus. This may lead to localised lack of fusion.

The two latter points are caused by spatter. It could be possible to mitigate or eliminate the spatter by better understanding and optimising the gas flow. Also, the location and the level of inlet and outlet of the gas inside the build chamber relative to the fusion cross sectional area can be studied and redesigned to reduce the effect of the spatters. An affective gas flow that can carry the small (nanoscale) and large spatters out of the building area is an essential requirement and offers a potential solution to this problem.

- Laser beam deformation (focus): when the beam is at an extreme angle, it is possible that the lens does not keep a spherical beam when the build location is far from the central region of the build platform. Therefore, the defocused beam results in a lower energy density being applied and thus leading to different melting material results. This issue has been resolved by the manufacturer (Renishaw) in the latest machine model, which is equipped with a new dynamic optical system to focus the laser dynamically and continuously as the laser beam angle changes [170].

- Gas pressure flow direction ([112]; [164]; [171]): gas flow contributes to transfer spatter from a melt pool to the another location away from the melt pool and in the direction of the gas flow. This location would be the left-hand side of the build platform in the AM system studied. Small particles are usually blown out of the build platform, however, the heavier particles could land on other parts of the build platform. Also, powder of a material that has a higher density would be influenced greater by the rejected powder because the powder particles would be heavier and therefore cannot be blown outside the build platform. This was clearly visible when comparing the result of build location analysis of the Ti-6Al-4V ELI with 316L-SS (Figure 5-15). Stainless Steel powder was more sensitive to build location. Controlling the gas flow rate could mitigate its impact on the part density.

- Number of parts on the platform: more samples on the same build platform results in greater variation. This can be attributed to the effect of rejected particles, which is greater due to more parts being built. Increasing the space between parts on the platform or reducing the number of parts being built on the platform during a build could help reduce the variation of the part density. The optimum space between parts should be determined after studying the travelling distance of the spatters which changes according to the process parameters.

The density/porosity variation on the fabricated parts in terms of location was also found to be material dependent. The material properties contribute to this problem. It was clear that 316L-SS is more sensitive in comparison to Ti-6Al-4V ELI for the process parameters investigated. It is possible that the higher ductility of 316L-SS contributed to creating larger spatters, which are heavy and landed back on the build cross section area as opposed to being blow away from the build platform. As the Ti-6Al-4V ELI alloy is more brittle and the spatter particles created were smaller and lighter, therefore more likely to be blown outside of the build cross sectional area. Figure 6-11 shows the amount of spatter during fabricating samples of Ti-6Al-4V ELI and 316L-SS. It is believed that the spatter impacted greatly on the density of parts built in different locations on the build platform.

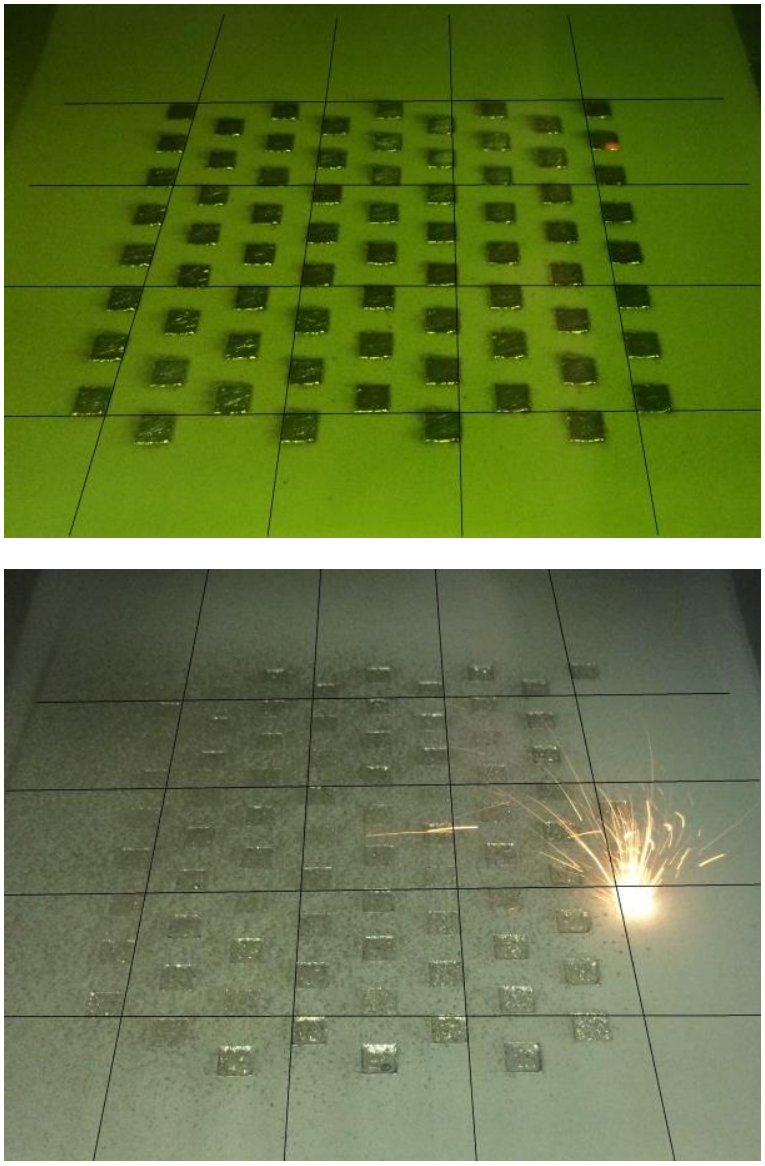

(a)

(b)

Figure 6-11: Amount of spatters during fabricating samples of (a) Ti-6Al-4V ELI and (b) 316L-SS. The black grid was added to the images to show the approximate build locations.

To show the concentration of the spatter on 316L-SS build, the image in Figure 6-11 (b) was further analysed. It was assumed that the brightness/darkness of the colour was caused by the spatter, analysing the Grey level (white to black) was used to confirm that the spatter greatly influenced the parts built on the left-hand side of the build platform. Four selected areas (1-4) shown in Figure 6-12 was analysed and compared. The length of the areas was approximately 150mm on y-axis. Area 1 started from 50mm on x axis and then the following areas started after 30mm in x-axis. All areas have a width of less than or equal to 8mm to avoid touching the built parts. The Grey colour scale range from 0 to 255, where 0 is white and 255 is black.

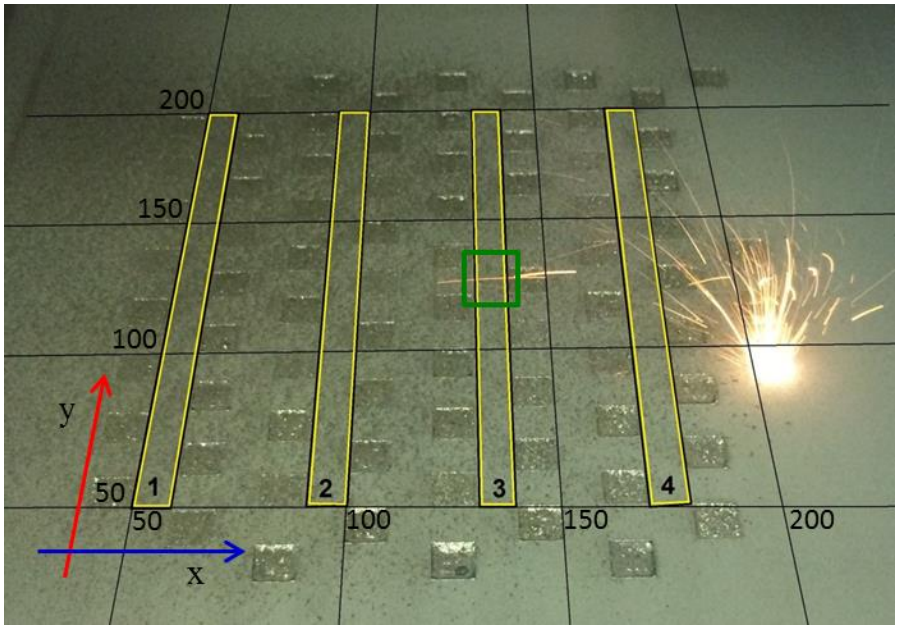

Figure 6-12: Selected areas from Area 1 to Area 4 are highlighted. They have the same distance on y-axis (approximately 150mm) and were selected on different distance on x-axis.

The result of the Grey colour analysis is shown in Figure 6-13. This shows that the brightness of the Grey colour decreased along the y-axis within an area. But, the brightness increased along the x-axis when moving from Area 1 to Area 4 (left to right on the build platform). Area 1 contains a lower Grey value and is influenced more by spatter compared to Area 4, which is believed to be due to the direction of the gas flow, which directs spatter towards the left region of the build platform.

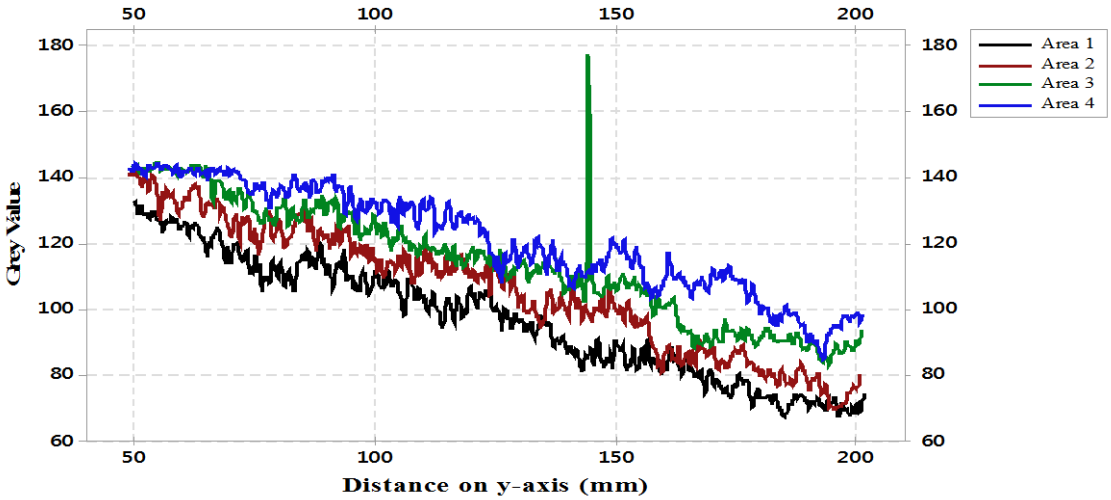

Figure 6-13: Result of Grey colour analysis; it shows that the Area 1 (left of the build platform) is the most affected zone by the spatter as the spatter was considered the major reason of the darkness.

Points in Area 3 showed a very bright colour compared to the trend of Grey colour across the build platform area. The reason was shiny spatter from the fired point crossing Area 3 (shown in Green square in Figure 6-12) so that the analysis of that area showed a brighter Grey value.

As a result of this study, part orientation should be considered not only for faster build, but also for consistent density throughout the part. Building at an angle to the xy-plane may result in a part that has varying density. Fabricating a part could start from a good build location and end at a poorer location and vice versa. The results suggest that part location can have negative influence on part quality for the current generation of machine designs. However, it is secondary compared to the influence of process parameter selection.

The study also introduced a visual method of comparing PBF equipment. Using a unique colour coding system it was possible to generate heat maps showing areas of varying part density.

The results of this work were published in Additive Manufacturing[2] in 2018.

[2] A.Y. Alfaify, J. Hughes, and K. Ridgway, "Critical evaluation of the pulsed selective laser melting process when fabricating Ti64 parts using a range of particle size distributions," Additive Manufacturing, vol. 19, pp. 197–204, 2018.

7. CONCLUSION

In this study, the effect of particle size distribution and layer thickness on part density fabricated by pulsed-laser powder bed fusion (L-PBF) process was studied. Two material alloys were investigated: Ti-6Al-4V ELI and 316L-SS. Three particle size distributions of Ti-6Al-4V ELI powder and two particle size distributions of 316L-SS powder were considered in this research. To evaluate the effect of changing powder size and layer thickness on part density, Design of Experiment (DOE) approaches were used to identify the best process parameter combinations which should be used. The objective of the work was to identify the correlation between applied energy during the build and the resulting density of the fabricated parts when changing the particle size distribution and powder layer thickness. As the Archimedes' principle was considered in the literature to be the most suitable method to evaluate the part density, it was used throughout this work to ensure that whole part porosity was measured. In addition to this, X-ray CT-scanning and optical micrography of cross sectional areas were used for further porosity measurements and additional validation.

- Standard Ti-6Al-4V ELI alloy powder was used to optimise the process parameters and identify the optimum combination for high part density fabrication. It was found that the density of parts is not only affected by the applied VED, but by the parameters that deliver the VED. In other words, the same VED value can be obtained by different configurations of parameters, but, the results may be completely different. The Taguchi approach for design of experiments was used for the optimisation. The most significant factors that affect the process are distance between points (PD) and hatching distance (HD), which control melt overlapping. The best combination of parameters for high density parts was found to be a PD of 50µm, HD of 65µm, LT of 30µm, LP of 200W, and ET of 50µs. This combination of parameters resulted in 100% relative density and sample properties that compared well with wrought material properties.

- The density of the fabricated parts for 316L-SS as found to be extremely sensitive to the process parameters. The statistical design of experiments approach of RSM was used to vary what were believed to be the most important

parameters. Density/porosity of the fabricated parts was chosen as the response. As the 316L-SS behaved differently from Ti-6Al-4V ELI, micro-level investigation was carried out to confirm the impact of changing process parameters on the amount and shape of porosity. The micrographic images were analysed for each parameter and its interactions with other parameters. It was found that point distance (PD), exposure time (ET) and layer thickness (LT) significantly affected the density of fabricated parts. Using a low value for the PD led to an increased number of small size pores, mostly circular in shape, due to evaporation caused by the high energy applied to the powder surface. A high value of LT was found to result in a lack of fusion and poor bonding between the layers, leading to large pores which were irregular in shape. Hatching distance (HD) was found to be the least effective parameter. The interaction between factors were found to be very critical, especially the interaction between ET and other factors.

- The volumetric energy density (VED) has been used as a control variable to study the effect of PBF parameters on part density in many previous studies ([3]; [4]; [35]; [78]; [79]; [80]; [81]; [82]; [83]; [84]; [85]; [86]; [87]; [88]; [89]). However, controlling density should not be investigated according to the overall VED value as a comprehensive indicator. The effect of each parameter within the VED and its interactions with other parameters should be considered. As soon as the value of VED is within acceptable levels, the size and shape of the pores can be controlled by careful tuning the parameters.

- Empirical models were developed for both Ti-6Al-4V ELI and 316L-SS materials to predict/estimate the density of fabricated parts. It was shown that part density could be predicted using statistical regression models to within an adequately acceptable level of accuracy. The models presented are valid for the range of parameters of materials investigated. To produce a more robust model of the PBF process, material properties (such as particle size distribution, powder absorptivity for the melt energy and heat conductivity) and process parameters (including other parameters, different ranges of process parameter) need to be incorporated into the model equations to allow universal use for a range of powders (e.g. Aluminium, Copper, etc.). Such a model will allow

industry to operate of optimal conditions relatively quickly, with minimal development/optimisation work. This is a novel contribution to the field of PBF. This study is believed to be the first systematic attempt to use RSM for the design of experiments (DOE) to investigate the effect of process parameters of the pulsed-laser PBF process on the density of the 316L-SS alloy components.

- A clear correlation between the number and shape of pores and the process parameters was identified. Point distance, exposure time and layer thickness were found to significantly affect part density. The interaction between these parameters also critically affected the development of porosity. Finally, a regression model was developed and verified experimentally and used to accurately predict part density. The results were published in the Journal of Rapid Prototyping[3].

- The optimum process parameters identified in the optimisation phase were used extensively to fabricate parts with different particle size distributions and layer thicknesses. Layer thickness ranged from 30µm to 100µm. It was found that it is possible to produce a near fully dense part with thicker build layers by selecting a suitable VED. A density of approximately 99% was obtained for all layer thicknesses. However, using a thinner layer leads to higher density at lower VED than using a thicker layer. Similarly, using small powder particles helps achieve higher density in a considerably shorter production time. From all types of powder and layer thicknesses, it was observed that exposure time in this pulsed L-PBF system should not be lower than 50µs even for small powder particles and thin powder layers for Ti-6Al-4V ELI powder. Using PSD and LT outside the ranges for those found in the literature showed a very different behaviour. The density was influenced negatively by increasing the VED. This was not the case for lower LT. This demonstrates that the present findings in the literature are limited to the LT investigated and it is not universal for all layer thicknesses.

[3] A. Y. Alfaify, J. Hughes, and K. Ridgway, "Controlling the Porosity of 316L Stainless Steel Parts Manufactured via the Powder Bed Fusion Process," Rapid Prototyping Journal, vol. 25 (1), pp. 162-175, 2019

- As larger particle size distribution powders are usually cheaper to produce, it was found that it is feasible to use these low-cost powders in the laser powder bed fusion processes. The large particle size powders can also cut down the cost of fabricating parts which are not required to be 100% dense. The main concern is tuning the process parameters for optimal fusion of the component desired. This demonstrates that it is possible to adapt operating conditions for economical reasons without compromising on fabricated part quality (density) which is ideal for industrial applications.

- 316L-SS density for different PSDs and LTs contradicted with literature which state that the density maintains the highest level reached. The research showed that the density of 316L-SS decreased from its highest point and then maintained its level with increased energy density. Showing that taking an approach of increasing energy density, ET (VED in general), can in some cases be detrimental, and therefore highlighting the importance of identifying the optimal value of process parameters. As the current works shows the optimal window may be within a narrow range for a combination of process parameters.

- All built parts were used to assess the effect of building parts on different locations on the build platform. As all build samples was replicated four times for different build locations on the platform, it was reasonable to conduct this study. A MATLAB code was adapted to analyse the density of samples built with identical process parameters but in different location. The code output was coloured maps of the best build location on the platform that produces the highest density or minimal density variation compared to the highest possible density. Build location on the platform leads to a slight different part density due to machine architecture and process behaviour. Possible reasons that contributed in this variation were wiping powder direction, spatter, gas flow and laser focus. The factor found to have the greatest influence was believed to be spatter. Melting 316L-SS created more spatter than Ti-6Al-4V ELI powder. An intensive study of this point is recommended. This would provide a greater understanding of the poor repeatability achieved when fabricating parts using the PBF process.

- This ‘first of its kind’ visual method of identifying build density at different locations could be a useful tool for comparing the performance of different PBF machines and is a further novel addition to current knowledge. The results of this study were published in the Additive Manufacturing Journal[4].

[4] A. Y. Alfaify, J. Hughes, and K. Ridgway, “Critical evaluation of the pulsed selective laser melting process when fabricating Ti64 parts using a range of particle size distributions,” Additive Manufacturing, vol. 19, pp. 197–204, 2018.

8. RECOMMENDATIONS FOR FUTURE WORK

This research investigated the effect of changing the primary powder particle size distributions and layer thicknesses on part density. It also presented regression models for the process, which allowed the prediction for the density of fabricated parts. The research also conducted the first build location study, which assessed the influence of building in different locations on the build platform on the part density. However, not all related aspects have been considered in this research as they are out of the scope of this research. Other processing parameters need to be included in future work.

The database and the findings of this work would be highly beneficial for the practitioners. Repeating the work for other materials would definitely increase the understanding of the process and result in a greater understanding of the laser-material interaction and comparison studies. Moreover, for an enhanced understanding of process parameter and their interactions, it would be better to conduct the same study using a continuous laser beam. A continuous beam would be beneficial as it would allow certain parameters to be studied in isolation, to further understand their interactions on final fabricated parts. For instance, the point distance factor will no longer be applicable, as the laser would fire continuously. The combination of point distance, exposure time and jump speed as scan speed will be replaced by one parameter, solely scan speed which is the speed of Golva. Furthermore, the effects of ignition and intermittently stopping the laser beam will be mitigated as the number of times the laser is turned on and off will be reduced.

One of the main reasons for process instability from one material to another is the powder absorptivity of the heat source. Further research using a superior heat source such as a laser beam with different wavelength should help increasing the use and adaptation of powder bed fusion process into manufacturing and would allow the inclusion of additional materials, which could be used in fabricating part using PBF processes.

The volumetric energy density (VED) has been used to evaluate the ideal input energy zone for fabricating a material. As shown during this research, using VED alone as a single parameter to determine and compare the applied energy is not appropriate. The combination of process parameters that deliver the value of VED must be considered

individually, to ensure a comprehensive understanding. As future work, another energy indicator factor needs to be found or at least a modification for the current VED should be established, which is more representative and applicable to be used. Spot size, overlapping rate and penetration depth (welding layers) are factors that need to be included in an applied energy indicator, especially if it is known that each material behaves differently. Small spot size penetrates vertically into the layers but does not cover a wider region horizontally for adequate overlapping between adjacent melt pools, and vice versa. The rate of overlapping controls the melting area and depends on the applied energy. The overlapping between adjacent melt pools is determined by the value of hatching distance and resulting melt pool width. For a pulsed laser system, the overlapping between points in a melt track is determined by the point distance. The spot size influences both values while it is not included in the common formula that is used to calculate the VED.

Spatter, which is ejected particles during laser beam scanning and melt-pool formation, has a huge impact on quality of fabricated parts. It is a complex phenomenon that has not been comprehensively studied yet. An intensive study that investigates spatters associated with different materials and process parameters is a must. During the current study, it was observed that spatter is material dependent. Titanium alloy (Ti-6Al-4V ELI) produces fewer spatters in comparison to Stainless Steel (316L-SS) for similar VED and PSD. The amount and size of 316L-SS spatter is more and larger, which is more challenging. This means that the phenomenon is material dependent and requires a deeper investigation to understand what affects the spatter and how to control/minimise spatter. It is believed that the direction of gas flow inside the chamber and flow rate must be optimised for the best spatter control. They should be adjustable according to the material being process and fusion process parameters. In short, machine design is critical to control spatter. Ejected particles do not only impact the quality of fabricated parts but also increase the cost of the process; the more the spatter, the more the waste powder. The quantity of waste powder would be huge in mass production systems of AM. A dynamic optical system that has been embedded in Renishaw's new machine may improve the part quality and allow for more reproducibility in any location on the build platform. In addition, the speed of the ejected particles for different material needs to be studied.

To achieve a robust and comprehensive prediction model for the laser powder bed fusion process, more process parameters, material properties, powder characterisation and the physical phenomena associated with the process need to be considered. As the models developed in the current study included the process parameters and their interaction, including power-powder interaction and physical properties for a material should increase the accuracy of the model. The model may be linked with simulation for the purpose of validation. Also, an intelligent software that is able to reduce the build time and improve the productivity would be highly beneficial. For example, software that enables slicing in different layer thicknesses can help increase productivity. The different slicing can be done according to the importance of a part section. Supports for instance, are not necessarily to be melt with every layer. If a part is sliced to have a layer thickness of 30µm, supports can be fused every other layer (i.e. at layer thickness of 60µm). Another example, when a part has a section that is not required to be full dense with other sections of the part that need to be full dense, a faster melting energy/scan can be calculated and suggested by software to speed up the build process in this section. Moreover, the software should be smart enough to identify any instability in the process, distinguish the cause and correct the process parameters accordingly in a closed loop system. There are a variety of sensors are available which can be used to modify current machines (especially laser machines), such as thermal imaging, spectrometers, optical imaging, etc., to detect process instabilities. Nowadays, there are some machines in the market with in-process monitoring capabilities. However, the difficulty would be capturing a high volume of data and processing it in short time to correct the process automatically.

9. REFERENCES

[1] I. Gibson, D. W. Rosen, and B. Stucker, *Additive Manufacturing Technologies*, 1st ed. Springer New York Heidelberg Dordrecht London, 2010.

[2] W. S. W. Harun, M. S. I. N. Kamariah, N. Muhamad, S. A. C. Ghani, F. Ahmad, and Z. Mohamed, "A review of powder additive manufacturing processes for metallic biomaterials," *Powder Technol.*, vol. 327, pp. 128–151, 2018.

[3] H. Gong, K. Rafi, H. Gu, T. Starr, and B. Stucker, "Analysis of defect generation in Ti-6Al-4V parts made using powder bed fusion additive manufacturing processes," *Addit. Manuf.*, vol. 1, pp. 87–98, 2014.

[4] G. Kasperovich, J. Haubrich, J. Gussone, and G. Requena, "Correlation between porosity and processing parameters in TiAl6V4 produced by selective laser melting," *Mater. Des.*, vol. 105, pp. 160–170, 2016.

[5] J. A. Cherry, H. M. Davies, S. Mehmood, N. P. Lavery, S. G. R. Brown, and J. Sienz, "Investigation into the effect of process parameters on microstructural and physical properties of 316L stainless steel parts by selective laser melting," *Int. J. Adv. Manuf. Technol.*, vol. 76, no. 5–8, pp. 869–879, 2014.

[6] ISO/ASTM 52900:2015(E), "Standard Terminology for Additive Manufacturing – General Principles – Terminology," *ISO/ASTM 52900*, vol. ISO/ASTM 5, pp. 1–9, 2015.

[7] K. V. Wong and A. Hernandez, "A review of additive manufacturing," *ISRN Mech. Eng.*, vol. 2012, pp. 1–10, 2012.

[8] R. F. Housholder, "Molding process," 4247508, 1981.

[9] L. Yang, K. Hsu, B. Baughman, D. Godfrey, F. Medina, M. Menon, and S. Wiener, *Additive Manufacturing of Metals: The Technology, Materials, Design and Production*. Springer International Publishing AG, 2017.

[10] C. R. Deckard, "Method and apparatus for producing parts by selective

sintering," 4863538, 1989.

[11] C. R. Deckard, "Method and apparatus for producing parts by selective sintering," 4937420, 1990.

[12] W. E. Frazier, "Metal additive manufacturing: a review," *J. Mater. Eng. Perform.*, vol. 23, no. 6, pp. 1917–1928, Apr. 2014.

[13] E. Herderick, "Additive manufacturing of metals: a review," *Mater. Sci. Technol. Conf. Exhib. 2011, MS T'11*, vol. 2, no. 176252, pp. 1413–1425, 2011.

[14] X. Gong, T. Anderson, and K. Chou, "Review on powder-based electron beam additive manufacturing technology," *Manuf. Rev.*, vol. 1, p. 2, 2014.

[15] H. Lee, C. H. J. Lim, M. J. Low, N. Tham, V. M. Murukeshan, and Y. J. Kim, "Lasers in additive manufacturing: A review," *Int. J. Precis. Eng. Manuf. - Green Technol.*, vol. 4, no. 3, pp. 307–322, 2017.

[16] V. Bhavar, P. Kattire, V. Patil, S. Khot, K. Gujar, and R. Singh, "A review on powder bed fusion technology of metal additive manufacturing," *4th Int. Conf. Exhib. Addit. Manuf. Technol.*, pp. 1–2, 2014.

[17] J. F. Isaza and C. Aumund-Kopp, "Additive manufacturing with metal powders: design for manufacture evolves into design for function," *Powder Metallurgy Review*, vol. 3, no. 2, pp. 41–50, 2014.

[18] A. Russell, "The Rev. William Gregor (1761-1817) Discoverer of Titanium," *Thr Mineral. Mag. J. Mineral. Soc.*, vol. 30, no. 229, pp. 617–624, 1955.

[19] M. J. Donachie, "Introduction to Selection of Titanium Alloys," in *Titanium: A Technical Guide*, 2nd Editio., vol. 180, Ohio, USA: ASM International., 2000, pp. 5–11.

[20] C. Leyens and M. Peters, *Titanium and Titanium Alloys: Fundamentals and Applications*. Germany: WILEY-VCH Verlag GmbH & Co. KGaA, Weinheim, 2003.

[21] C. Veiga, J. P. Devim, and A. J. R. Loureiro, "Properties and applications of

titanium alloys: a brief review," *Rev. Adv. Mater. Sci.*, vol. 32, no. 2, pp. 133–148, 2012.

[22] J. R. P. Jorge, V. A. Barão, J. A. Delben, L. P. Faverani, T. P. Queiroz, and W. G. Assunção, "Titanium in dentistry: historical development, state of the art and future perspectives," *J. Indian Prosthodont. Soc.*, vol. 13, no. 2, pp. 71–77, 2013.

[23] G. Lütjering and J. C. Williams, *Titanium, Engineering Materials and Processes*, 2nd ed. Springer-Verlag Berlin Heidelberg, 2007.

[24] S. Liu and Y. C. Shin, "Additive manufacturing of Ti6Al4V alloy : A review," *Mater. Des.*, vol. 164, p. 107552, 2019.

[25] D. Gu, Y. C. Hagedorn, W. Meiners, G. Meng, R. J. S. Batista, K. Wissenbach, and R. Poprawe, "Densification behavior, microstructure evolution, and wear performance of selective laser melting processed commercially pure titanium," *Acta Mater.*, vol. 60, no. 9, pp. 3849–3860, 2012.

[26] M. Simonelli, Y. Tse, and C. Tuck, "Further Understanding of Ti6Al4V Selective Laser Melting Using Texture Analysis," *Proc. 23rd Annu. ...*, pp. 480–491, 2012.

[27] J. R. Davis, "Alloy Digest Sourcebook: Stainless Steels," Ohio, USA: ASM International:, 2000, p. 577.

[28] Atlas Steels, *the Atlas Steel Technical Handbook of Stainless Steels*, no. August. Atlas Steels Technical Department, 2013.

[29] Outokumpu, *Handbook of Stainless Steel*. Espoo, Finland: Outokumpu Oyj, 2013.

[30] J. R. Davis, *ASM Speciality Handbook: Stainless Steels*. Ohio, USA: ASM International, 1994.

[31] "Statista," 2018. [Online]. Available: https://www.statista.com.

[32] H. M. Cobb, *The History of Stainless Steel*. Ohio, USA: ASM International, 2010.

[33] B. Leffler, “Stainless steels and their properties,” *AvestaPolarit AB*, pp. 1–45, 1996.

[34] K. H. Lo, C. H. Shek, and J. K. L. Lai, “Recent developments in stainless steels,” *Mater. Sci. Eng. R Reports*, vol. 65, no. 4–6, pp. 39–104, 2009.

[35] A. Simchi, “Direct laser sintering of metal powders: mechanism, kinetics and microstructural features,” *Mater. Sci. Eng. A*, vol. 428, no. 1–2, pp. 148–158, Jul. 2006.

[36] Y. Zhong, L. Liu, S. Wikman, D. Cui, and Z. Shen, “Intragranular cellular segregation network structure strengthening 316L stainless steel prepared by selective laser melting,” *J. Nucl. Mater.*, vol. 470, pp. 170–178, 2016.

[37] T. Sourmail and H. K. D. H. Bhadeshia, “Stainless Steels,” *University of Cambridge*, 2005. [Online]. Available: http://www.phase-trans.msm.cam.ac.uk/2005/Stainless_steels/stainless.html.

[38] E. Liverani, S. Toschi, L. Ceschini, and A. Fortunato, “Effect of selective laser melting (SLM) process parameters on microstructure and mechanical properties of 316L austenitic stainless steel,” *J. Mater. Process. Technol.*, vol. 249, no. November 2016, pp. 255–263, 2017.

[39] K. Saeidi, X. Gao, Y. Zhong, and Z. J. Shen, “Hardened austenite steel with columnar sub-grain structure formed by laser melting,” *Mater. Sci. Eng. A*, vol. 625, pp. 221–229, 2015.

[40] S. Vock, B. Klöden, A. Kirchner, T. Weißgärber, and B. Kieback, “Powders for powder bed fusion: a review,” *Prog. Addit. Manuf.*, vol. 0, no. 0, p. 0, 2019.

[41] A. T. Sutton, C. S. Kriewall, M. C. Leu, and J. W. Newkirk, “Powder characterisation techniques and effects of powder characteristics on part properties in powder-bed fusion processes,” *Virtual Phys. Prototyp.*, vol. 12, no. 1, pp. 3–29, 2017.

[42] B. Liu, R. Wildman, C. Tuck, I. Ashcroft, and R. Hague, “Investigation the effect of particle size distribution on processing parameters optimisation in selective

laser melting process," *Sff*, no. mm, pp. 227–238, 2011.

[43] W. E. King, A. T. Anderson, R. M. Ferencz, N. E. Hodge, C. Kamath, S. A. Khairallah, and A. M. Rubenchik, "Laser powder bed fusion additive manufacturing of metals: physics, computational, and materials challenges," *Appl. Phys. Rev.*, vol. 2, no. 4, p. 041304, 2015.

[44] J. Dawes, R. Bowerman, and R. Trepleton, "Introduction to the additive manufacturing powder metallurgy supply chain," *Johnson Matthey Technol. Rev.*, vol. 59, no. 3, pp. 243–256, 2015.

[45] LPW Technology, "Powder production," 2019. [Online]. Available: https://www.lpwtechnology.com/technical-library/powder-production/.

[46] Z. Li, I. Kucukkoc, D. Z. Zhang, and F. Liu, "Optimising the process parameters of selective laser melting for the fabrication of Ti6Al4V alloy," *Rapid Prototyp. J.*, pp. 00–00, 2017.

[47] D. Buchbinder, H. Schleifenbaum, S. Heidrich, W. Meiners, and J. Bültmann, "High power selective laser melting (HP SLM) of Aluminum parts," *Phys. Procedia*, vol. 12, pp. 271–278, Jan. 2011.

[48] S. Bland and N. T. Aboulkhair, "Reducing porosity in additive manufacturing," *Met. Powder Rep.*, vol. 70, no. 2, pp. 2–4, 2015.

[49] N. T. Aboulkhair, N. M. Everitt, I. Ashcroft, and C. Tuck, "Reducing porosity in AlSi10Mg parts processed by selective laser melting," *Addit. Manuf.*, vol. 1–4, pp. 77–86, 2014.

[50] C. Kamath, B. El-dasher, G. F. Gallegos, W. E. King, and A. Sisto, "Density of additively-manufactured, 316L SS parts using laser powder-bed fusion at powers up to 400 W," *Int. J. Adv. Manuf. Technol.*, pp. 65–78, 2014.

[51] Z. Sun, X. Tan, S. B. Tor, and W. Y. Yeong, "Selective laser melting of stainless steel 316L with low porosity and high build rates," *Mater. Des.*, vol. 104, pp. 197–204, 2016.

[52] R. Chou, J. Milligan, M. Paliwal, and M. Brochu, “Additive Manufacturing of Al-12Si Alloy Via Pulsed Selective Laser Melting,” *Jom*, vol. 67, no. 3, pp. 590–596, 2015.

[53] A. G. Demir, P. Colombo, and B. Previtali, “From pulsed to continuous wave emission in SLM with contemporary fiber laser sources: effect of temporal and spatial pulse overlap in part quality,” *Int. J. Adv. Manuf. Technol.*, vol. 91, no. 5–8, pp. 2701–2714, 2017.

[54] K. a. Mumtaz and N. Hopkinson, “Selective laser melting of thin wall parts using pulse shaping,” *J. Mater. Process. Technol.*, vol. 210, no. 2, pp. 279–287, Jan. 2010.

[55] P. Fischer, V. Romano, H. P. Weber, and S. Kolossov, “Pulsed laser sintering of metallic powders,” *Thin Solid Films*, vol. 453–454, pp. 139–144, 2004.

[56] C. Li, M. F. Gouge, E. R. Denlinger, J. E. Irwin, and P. Michaleris, “Estimation of Part-to-Powder Heat Losses as Surface Convection in Laser Powder Bed Fusion,” *Addit. Manuf.*, 2019.

[57] U. Scipioni Bertoli, G. Guss, S. Wu, M. J. Matthews, and J. M. Schoenung, “In-situ characterization of laser-powder interaction and cooling rates through high-speed imaging of powder bed fusion additive manufacturing,” *Mater. Des.*, vol. 135, pp. 385–396, 2017.

[58] J.-P. Kruth, G. Levy, F. Klocke, and T. H. C. Childs, “Consolidation phenomena in laser and powder-bed based layered manufacturing,” *CIRP Ann. - Manuf. Technol.*, vol. 56, no. 2, pp. 730–759, Jan. 2007.

[59] A. V. Gusarov, I. Yadroitsev, P. Bertrand, and I. Smurov, “Model of Radiation and Heat Transfer in Laser-Powder Interaction Zone at Selective Laser Melting,” *J. Heat Transfer*, vol. 131, no. 7, p. 072101, 2009.

[60] A. V. Gusarov and I. Smurov, “Modeling the interaction of laser radiation with powder bed at selective laser melting,” *Phys. Procedia*, vol. 5, no. PART 2, pp. 381–394, 2010.

[61] S. A. Khairallah, A. T. Anderson, A. Rubenchik, and W. E. King, “Laser powder-bed fusion additive manufacturing: physics of complex melt flow and formation mechanisms of pores, spatter, and denudation zones,” *Acta Mater.*, vol. 108, pp. 36–45, 2016.

[62] M. Xia, D. Gu, G. Yu, D. Dai, H. Chen, and Q. Shi, “Porosity evolution and its thermodynamic mechanism of randomly packed powder-bed during selective laser melting of Inconel 718 alloy,” *Int. J. Mach. Tools Manuf.*, vol. 116, no. November 2016, pp. 96–106, 2017.

[63] Y. Li, K. Zhou, S. B. Tor, C. K. Chua, and K. F. Leong, “Heat transfer and phase transition in the selective laser melting process,” *Int. J. Heat Mass Transf.*, vol. 108, pp. 2408–2416, 2017.

[64] J. R. Zhuang, Y. T. Lee, W. H. Hsieh, and A. S. Yang, “Determination of melt pool dimensions using DOE-FEM and RSM with process window during SLM of Ti6Al4V powder,” *Opt. Laser Technol.*, vol. 103, pp. 59–76, 2018.

[65] T. Heeling, M. Cloots, and K. Wegener, “Melt pool simulation for the evaluation of process parameters in selective laser melting,” *Addit. Manuf.*, vol. 14, pp. 116–125, 2017.

[66] V. Gunenthiram, P. Peyre, M. Schneider, M. Dal, F. Coste, and R. Fabbro, “Analysis of laser–melt pool–powder bed interaction during the selective laser melting of a stainless steel,” *J. Laser Appl.*, vol. 29, no. 2, p. 022303.1-022303.8, 2017.

[67] C. Qiu, C. Panwisawas, M. Ward, H. C. Basoalto, J. W. Brooks, and M. M. Attallah, “On the role of melt flow into the surface structure and porosity development during selective laser melting,” *Acta Mater.*, vol. 96, pp. 72–79, 2015.

[68] I. Yadroitsev, *Selective Laser Melting: Direct Manufacturing of 3D-objects by Selective Laser Melting of Metal Powders*. saarbrücken, Germany: LAP LAMBERT Academic Publishing AG & Co. KG, 2009.

[69] P. Karimi, T. Raza, J. Andersson, and L. E. Svensson, “Influence of laser exposure time and point distance on 75-µm-thick layer of selective laser melted alloy 718,” *Int. J. Adv. Manuf. Technol.*, pp. 1–9, 2017.

[70] S. Zhang, Q. Wei, L. Cheng, S. Li, and Y. Shi, “Effects of scan line spacing on pore characteristics and mechanical properties of porous Ti6Al4V implants fabricated by selective laser melting,” *Mater. Des.*, vol. 63, pp. 185–193, 2014.

[71] M. Zhang, C. Sun, X. Zhang, P. C. Goh, J. Wei, H. Li, and D. Hardacre, “Competing influence of porosity and microstructure on the fatigue property of laser powder bed fusion Stainless Steel 316L,” *Solid Free. Fabr. Symp.*, pp. 365–376, 2017.

[72] V. S. Sufiiarov, A. A. Popovich, E. V. Borisov, I. A. Polozov, D. V. Masaylo, and A. V. Orlov, “The effect of layer thickness at selective laser melting,” *Procedia Eng.*, vol. 174, pp. 126–134, 2017.

[73] S. Wang, Y. Liu, W. Shi, B. Qi, J. Yang, F. Zhang, D. Han, and Y. Ma, “Research on high layer thickness fabricated of 316L by selective laser melting,” *Materials (Basel).*, vol. 10, no. 9, p. 1055, 2017.

[74] J. D. Williams and C. R. Deckard, “Advances in modeling the effects of selected parameters on the SLS process,” *Rapid Prototyp. J.*, vol. 4, no. 2, pp. 90–100, 1998.

[75] K. Maeda and T. H. . Childs, “Laser sintering (SLS) of hard metal powders for abrasion resistant coatings,” *J. Mater. Process. Technol.*, vol. 149, no. 1–3, pp. 609–615, Jun. 2004.

[76] E. O. Olakanmi, R. F. Cochrane, and K. W. Dalgarno, “A review on selective laser sintering/melting (SLS/SLM) of aluminium alloy powders: Processing, microstructure, and properties,” *Prog. Mater. Sci.*, 2015.

[77] J. Ciurana, L. Hernandez, and J. Delgado, “Energy density analysis on single tracks formed by selective laser melting with CoCrMo powder material,” *Int. J. Adv. Manuf. Technol.*, vol. 68, no. 5–8, pp. 1103–1110, 2013.

[78] T. Gustmann, A. Neves, U. Kühn, P. Gargarella, C. S. Kiminami, C. Bolfarini, J. Eckert, and S. Pauly, "Influence of processing parameters on the fabrication of a Cu-Al-Ni-Mn shape-memory alloy by selective laser melting," *Addit. Manuf.*, vol. 11, pp. 23–31, 2016.

[79] B. Vandenbroucke and J.-P. Kruth, "Selective laser melting of biocompatible metals for rapid manufacturing of medical parts," *Rapid Prototyp. J.*, vol. 13, no. 4, pp. 196–203, 2007.

[80] I. A. Aziz, "Microstructure and mechanical properties of Ti-6Al-4V produced by selective laser sintering of pre-alloyed powders," The University of Waikato, 2010.

[81] T. Bormann, R. Schumacher, B. Müller, M. Mertmann, and M. Wild, "Tailoring selective laser melting process parameters for NiTi implants," *J. Mater. Eng. Perform.*, vol. 21, no. 12, pp. 2519–2524, 2012.

[82] H. Meier and C. Haberland, "Experimental studies on selective laser melting of metallic parts," *Materwiss. Werksttech.*, vol. 39, no. 9, pp. 665–670, 2008.

[83] G. Miranda, S. Faria, F. Bartolomeu, E. Pinto, S. Madeira, a. Mateus, P. Carreira, N. Alves, F. S. Silva, and O. Carvalho, "Predictive models for physical and mechanical properties of 316L stainless steel produced by selective laser melting," *Mater. Sci. Eng. A*, vol. 657, pp. 43–56, 2016.

[84] M. Tang, P. C. Pistorius, and J. Beuth, "Prediction of lack-of-fusion porosity for powder bed fusion," *Addit. Manuf.*, p. under review, 2016.

[85] T. Kimura and T. Nakamoto, "Microstructures and mechanical properties of A356 (AlSi7Mg0.3) aluminum alloy fabricated by selective laser melting," *Mater. Des.*, vol. 89, pp. 1294–1301, 2016.

[86] A. B. Spierings and G. Levy, "Comparison of density of stainless steel 316L parts produced with selective laser melting using different powder grades," in *The Annual International Solid Freeform Fabrication Symposium, The University of Texas*, 2009, p. 20.

[87] H. Gong, K. Rafi, T. Starr, and B. Stucker, “The effects of processing parameters on defect regularity in Ti-6Al-4V parts fabricated by selective laser melting and electron beam melting,” in *24th Annual International Solid Freeform Fabrication Symposium*, 2013, pp. 424–439.

[88] L. Thijs, F. Verhaeghe, T. Craeghs, J. Van Humbeeck, and J.-P. Kruth, “A study of the microstructural evolution during selective laser melting of Ti–6Al–4V,” *Acta Mater.*, vol. 58, no. 9, pp. 3303–3312, May 2010.

[89] W. Xu, M. Brandt, S. Sun, J. Elambasseril, Q. Liu, K. Latham, K. Xia, and M. Qian, “Additive manufacturing of strong and ductile Ti–6Al–4V by selective laser melting via in situ martensite decomposition,” *Acta Mater.*, vol. 85, pp. 74–84, 2015.

[90] J. Han, J. Yang, H. Yu, J. Yin, M. Gao, Z. Wang, and X. Zeng, “Microstructure and mechanical property of selective laser melted Ti6Al4V dependence on laser energy density,” *Rapid Prototyp. J.*, vol. 23, no. 2, pp. 217–226, 2017.

[91] F. H. Kim, S. P. Moylan, E. J. Garboczi, and J. A. Slotwinski, “Investigation of pore structure in cobalt chrome additively manufactured parts using X-ray computed tomography and three-dimensional image analysis,” *Addit. Manuf.*, vol. 17, pp. 23–38, 2017.

[92] H. S. Park and D. S. Nguyen, “Study on flaking behavior in selective laser melting process,” *Procedia CIRP*, vol. 63, pp. 569–572, 2017.

[93] T. T. Roehling, S. S. Q. Wu, S. A. Khairallah, J. D. Roehling, S. S. Soezeri, M. F. Crumb, and M. J. Matthews, “Modulating laser intensity profile ellipticity for microstructural control during metal additive manufacturing,” *Acta Mater.*, vol. 128, pp. 197–206, 2017.

[94] M. Das, S. Bysakh, D. Basu, T. S. Sampath Kumar, V. K. Balla, S. Bose, and A. Bandyopadhyay, “Microstructure, mechanical and wear properties of laser processed SiC particle reinforced coatings on titanium,” *Surf. Coatings Technol.*, vol. 205, no. 19, pp. 4366–4373, 2011.

[95] L. N. Carter, X. Wang, N. Read, R. Khan, M. Aristizabal, K. Essa, and M. M. Attallah, “Process optimisation of selective laser melting using energy density model for nickel based superalloys,” *Mater. Sci. Technol.*, vol. 0836, no. October 2017, pp. 1–5, 2016.

[96] Y. Liu, Y. Yang, S. Mai, D. Wang, and C. Song, “Investigation into spatter behavior during selective laser melting of AISI 316L stainless steel powder,” *Mater. Des.*, vol. 87, pp. 797–806, 2015.

[97] W. Di, Y. Yongqiang, S. Xubin, and C. Yonghua, “Study on energy input and its influences on single-track, multi-track, and multi-layer in SLM,” *Int. J. Adv. Manuf. Technol.*, vol. 58, no. 9–12, pp. 1189–1199, 2012.

[98] V. Gunenthiram, P. Peyre, M. Schneider, M. Dal, F. Coste, I. Koutiri, and R. Fabbro, “Experimental analysis of spatter generation and melt-pool behavior during the powder bed laser beam melting process,” *J. Mater. Process. Technol.*, vol. 251, no. August 2017, pp. 376–386, 2018.

[99] M. Thomas, G. J. Baxter, and I. Todd, “Normalised model-based processing diagrams for additive layer manufacture of engineering alloys,” *Acta Mater.*, vol. 108, pp. 26–35, 2016.

[100] J. C. Ion, H. R. Shercliff, and M. F. Ashby, “Diagrams for laser materials processing,” *Acta Metall. Mater.*, vol. 40, no. 7, pp. 1539–1551, 1992.

[101] L. S. Bertol, W. K. Júnior, F. P. Da Silva, and C. Aumund-Kopp, “Medical design: direct metal laser sintering of Ti–6Al–4V,” *Mater. Des.*, vol. 31, no. 8, pp. 3982–3988, Sep. 2010.

[102] U. Scipioni Bertoli, A. J. Wolfer, M. J. Matthews, J. P. R. Delplanque, and J. M. Schoenung, “On the limitations of volumetric energy density as a design parameter for selective laser melting,” *Mater. Des.*, vol. 113, pp. 331–340, 2017.

[103] I. Yadroitsev, A. Gusarov, I. Yadroitsava, and I. Smurov, “Single track formation in selective laser melting of metal powders,” *J. Mater. Process. Technol.*, vol. 210, no. 12, pp. 1624–1631, Sep. 2010.

[104] K. Antony, N. Arivazhagan, and K. Senthilkumaran, “Numerical and experimental investigations on laser melting of stainless steel 316L metal powders,” *J. Manuf. Process.*, vol. 16, no. 3, pp. 345–355, 2014.

[105] D. Wang, Y. Yang, Z. Yi, and X. Su, “Research on the fabricating quality optimization of the overhanging surface in SLM process,” *Int. J. Adv. Manuf. Technol.*, vol. 65, no. 9–12, pp. 1471–1484, 2013.

[106] K. Guan, Z. Wang, M. Gao, X. Li, and X. Zeng, “Effects of processing parameters on tensile properties of selective laser melted 304 stainless steel,” *Mater. Des.*, vol. 50, pp. 581–586, 2013.

[107] P. Hanzl, M. Zetek, T. Bakša, and T. Kroupa, “The influence of processing parameters on the mechanical properties of SLM parts,” *Procedia Eng.*, vol. 100, no. January, pp. 1405–1413, 2015.

[108] W. Shifeng, L. Shuai, W. Qingsong, C. Yan, Z. Sheng, and S. Yusheng, “Effect of molten pool boundaries on the mechanical properties of selective laser melting parts,” *J. Mater. Process. Technol.*, vol. 214, no. 11, pp. 2660–2667, 2014.

[109] I. Yadroitsev and I. Smurov, “Selective laser melting technology: from the single laser melted track stability to 3D parts of complex shape,” *Phys. Procedia*, vol. 5, no. PART 2, pp. 551–560, 2010.

[110] I. Tolosa, F. Garciandía, F. Zubiri, F. Zapirain, and A. Esnaola, “Study of mechanical properties of AISI 316 stainless steel processed by ‘selective laser melting’, following different manufacturing strategies,” *Int. J. Adv. Manuf. Technol.*, vol. 51, no. 5–8, pp. 639–647, 2010.

[111] A. Masmoudi, R. Bolot, and C. Coddet, “Investigation of the laser–powder–atmosphere interaction zone during the selective laser melting process,” *J. Mater. Process. Technol.*, vol. 225, pp. 122–132, 2015.

[112] M. J. Matthews, G. Guss, S. A. Khairallah, A. M. Rubenchik, P. J. Depond, and W. E. King, “Denudation of metal powder layers in laser powder bed fusion processes,” *Acta Mater.*, vol. 114, pp. 33–42, 2016.

[113] S. Tammas-Williams, P. J. Withers, I. Todd, and P. B. Prangnell, "The Influence of Porosity on Fatigue Crack Initiation in Additively Manufactured Titanium Components," *Sci. Rep.*, vol. 7, no. 1, pp. 1–13, 2017.

[114] A. Bandyopadhyay, F. Espana, V. K. Balla, S. Bose, Y. Ohgami, and N. M. Davies, "Influence of porosity on mechanical properties and in vivo response of Ti6Al4V implants," *Acta Biomater.*, vol. 6, no. 4, pp. 1640–1648, 2010.

[115] M. Fousová, D. Vojtěch, J. Kubásek, E. Jablonská, and J. Fojt, "Promising characteristics of gradient porosity Ti-6Al-4V alloy prepared by SLM process," *J. Mech. Behav. Biomed. Mater.*, vol. 69, no. January, pp. 368–376, 2017.

[116] J. D. Madison and L. K. Aagesen, "Quantitative characterization of porosity in laser welds of stainless steel," *Scr. Mater.*, vol. 67, no. 9, pp. 783–786, 2012.

[117] J. Zhou, H.-L. Tsai, and P.-C. Wang, "Transport phenomena and keyhole dynamics during pulsed laser welding," *J. Heat Transfer*, vol. 128, no. 7, p. 680, 2006.

[118] R. Rai, J. W. Elmer, T. A. Palmer, and T. Debroy, "Heat transfer and fluid flow during keyhole mode laser welding of tantalum, Ti-6Al-4V, 304L stainless steel and vanadium," *J. Phys. D. Appl. Phys.*, vol. 40, no. 18, pp. 5753–5766, 2007.

[119] H. Zhao, W. Niu, B. Zhang, Y. Lei, M. Kodama, and T. Ishide, "Modelling of keyhole dynamics and porosity formation considering the adaptive keyhole shape and three-phase coupling during deep-penetration laser welding," *J. Phys. D. Appl. Phys.*, vol. 44, no. 48, p. 485302, 2011.

[120] P. S. Wei, "Thermal science of weld bead defects: a review," *J. Heat Transfer*, vol. 133, no. 3, p. 031005, 2011.

[121] M. Rombouts, J. P. Kruth, L. Froyen, and P. Mercelis, "Fundamentals of selective laser melting of alloyed steel powders," *CIRP Ann. - Manuf. Technol.*, vol. 55, no. 1, pp. 187–192, 2006.

[122] D. Gu and Y. Shen, "Balling phenomena in direct laser sintering of stainless steel powder: metallurgical mechanisms and control methods," *Mater. Des.*, vol. 30,

no. 8, pp. 2903–2910, 2009.

[123] M. Rombouts, L. Froyen, A. V. Gusarov, E. H. Bentefour, and C. Glorieux, "Light extinction in metallic powder beds: correlation with powder structure," *J. Appl. Phys.*, vol. 98, no. 1, 2005.

[124] A. V. Gusarov, T. Laoui, L. Froyen, and V. I. Titov, "Contact thermal conductivity of a powder bed in selective laser sintering," *Int. J. Heat Mass Transf.*, vol. 46, no. 6, pp. 1103–1109, 2003.

[125] L. C. Wei, L. E. Ehrlich, M. J. Powell-Palm, C. Montgomery, J. Beuth, and J. A. Malen, "Thermal conductivity of metal powders for powder bed additive manufacturing," *Addit. Manuf.*, vol. 21, pp. 201–208, 2018.

[126] A. V. Gusarov and I. Smurov, "Two-dimensional numerical modelling of radiation transfer in powder beds at selective laser melting," *Appl. Surf. Sci.*, vol. 255, no. 10, pp. 5595–5599, 2009.

[127] M. Tang, P. C. Pistorius, and J. L. Beuth, "Prediction of lack-of-fusion porosity for powder bed fusion," *Addit. Manuf.*, vol. 14, pp. 39–48, 2017.

[128] W. E. King, H. D. Barth, V. M. Castillo, G. F. Gallegos, J. W. Gibbs, D. E. Hahn, C. Kamath, and A. M. Rubenchik, "Observation of keyhole-mode laser melting in laser powder-bed fusion additive manufacturing," *J. Mater. Process. Technol.*, vol. 214, no. 12, pp. 2915–2925, 2014.

[129] C. Boley, S. Khairallah, and A. M. Rubenchik, "Modeling of powder absorption in additive manufacturing," in *25th Annual International Solid Freeform Fabrication Symposium*, 2014, p. AM1L.5.

[130] A. B. Spierings, N. Herres, and G. Levy, "Influence of the particle size distribution on surface quality and mechanical properties in AM steel parts," *Rapid Prototyp. J.*, vol. 17, no. 3, pp. 195–202, 2011.

[131] a. Strondl, O. Lyckfeldt, H. Brodin, and U. Ackelid, "Characterization and control of powder properties for additive manufacturing," *Jom*, vol. 67, no. 3, pp. 549–554, 2015.

[132] J. Karlsson, A. Snis, H. Engqvist, and J. Lausmaa, “Characterization and comparison of materials produced by Electron Beam Melting (EBM) of two different Ti–6Al–4V powder fractions,” *J. Mater. Process. Technol.*, vol. 213, no. 12, pp. 2109–2118, Dec. 2013.

[133] N. Karapatis and G. Egger, “Optimization of powder layer density in selective laser sintering,” *Proc. 9th Solid …*, pp. 255–264, 1999.

[134] A. Hicks, H. Doak, and B. Stucker, “Effects of powder variation on the microstructure and tensile strength of Ti6Al4V parts fabricated by selective laser melting,” *Solid Free. Fabr. Symp.*, pp. 470–483, 2014.

[135] A. Cooke and J. Slotwinski, “Properties of metal powders for additive manufacturing: a review of the state of the art of metal powder property testing,” *Natl. Inst. Stand. Technol.*, vol. IR 7873, p. 22, 2012.

[136] P. C. Angelo and R. Subramanian, *Powder Metallurgy: Science, Technology and Applications*, Second. New Delhi: PHI Learning Private Limited, 2009.

[137] Renishaw plc, “Magics training : material profile editing,” 2015.

[138] A. Asghar, A. A. Abdul Raman, and W. M. A. W. Daud, “A comparison of central composite design and Taguchi method for optimizing Fenton process.,” *ScientificWorldJournal.*, vol. 2014, p. 869120, 2014.

[139] P. Dayanand, R. Shrikantha, and S. Raviraj, “Application of Taguchi and Response Surface methodologies for metal removal rate and surface roughness in grinding of DRAC’s,” *Int. J. Eng. Manag. Sci.*, vol. 3, no. 1, pp. 1–8, 2012.

[140] D. P. Raykundaliya and A. Shanubhogue, “Comparison study: Taguchi methodology vis.-a-vis. Response Surface methodology through a case study of accelerated failure in spin-on-filter,” *Iarjset*, vol. 2, no. 3, pp. 1–5, 2015.

[141] V. K. Sharma, Q. Murtaza, and S. K. Garg, “Response Surface methodology & Taguchi techquines to optimization of C.N.C. turning process,” *Int. J. Prod. Technol.*, vol. 1, no. 1, pp. 13–31, 2010.

[142] K. S. Wang, J. H. Chen, Y. H. Huang, and S. L. Huang, "Integrated Taguchi method and Response Surface methodology to confirm hydrogen production by anaerobic fermentation of cow manure," *Int. J. Hydrogen Energy*, vol. 38, no. 1, pp. 45–53, 2013.

[143] Y.-T. Jou, W.-T. Lin, W.-C. Lee, and T.-M. Yeh, "Integrating the Taguchi method and Response Surface methodology for process parameter optimization of the injection molding," *Appl. Math. Inf. Sci.*, vol. 8, no. 3, pp. 1277–1285, 2014.

[144] M. Sarıkaya and A. Güllü, "Taguchi design and Response Surface methodology based analysis of machining parameters in CNC turning under MQL," *J. Clean. Prod.*, vol. 65, pp. 604–616, 2014.

[145] R. Narayan Dash, H. Mohammed, and T. Humaira, "An integrated Taguchi and response surface methodological approach for the optimization of an HPLC method to determine glimepiride in a supersaturatable self-nanoemulsifying formulation," *Saudi Pharm. J.*, vol. 24, no. 1, pp. 92–103, 2016.

[146] Sivaraos, K. R. Milkey, A. R. Samsudin, A. K. Dubey, and P. Kidd, "Comparison between Taguchi method and Response Surface Methodology (RSM) in modelling CO2 laser machining," *Jordan J. Mech. Ind. Eng.*, vol. 8, no. 1, pp. 35–42, 2014.

[147] Phillip J. Ross, *Taguchi Ttechniques for Quality Engineering*, 2nd ed. NewYork: McGraw Hill Professional, 1996.

[148] J. Sun, Y. Yang, and D. Wang, "Parametric optimization of selective laser melting for forming Ti6Al4V samples by Taguchi method," *Opt. Laser Technol.*, vol. 49, pp. 118–124, 2013.

[149] C. P. Paul, P. Ganesh, S. K. Mishra, P. Bhargava, J. Negi, and A. K. Nath, "Investigating laser rapid manufacturing for Inconel-625 components," *Opt. Laser Technol.*, vol. 39, no. 4, pp. 800–805, Jun. 2007.

[150] A. Safdar, H. Z. He, L.-Y. Wei, A. Snis, and L. E. C. De Paz, "Effect of process

parameters settings and thickness on surface roughness of EBM produced Ti-6Al-4V," *Rapid Prototyp. J.*, vol. 18, no. 5, pp. 401–408, 2012.

[151] Renishaw plc, "Renishaw additive manufacturing system AM250 user guide," 2013.

[152] A. B. Spierings, M. Schneider, and R. Eggenberger, "Comparison of density measurement techniques for additive manufactured metallic parts," *Rapid Prototyp. J.*, vol. 17, no. 5, pp. 380–386, 2011.

[153] G. R. Davis and J. C. Elliott, "Artefacts in X-ray microtomography of materials," *Mater. Sci. Technol.*, vol. 22, no. 9, pp. 1011–1018, 2006.

[154] MatWeb, "Titanium Alloy (Ti-6Al-4V ELI; ASTM Grade 23)," 2018. .

[155] Renishaw plc, "SS 316L-0407 powder for additive manufacturing," 2018.

[156] A. Rabbani, S. Jamshidi, and S. Salehi, "An automated simple algorithm for realistic pore network extraction from micro-tomography images," *J. Pet. Sci. Eng.*, vol. 123, pp. 164–171, 2014.

[157] J. Beuth, J. Fox, J. Gockel, C. Montgomery, R. Yang, H. Qiao, E. Soylemez, P. Peeseewatt, A. Anvari, S. Narra, and N. Klingbeil, "Process mapping for qaulification across multiple direct metal additive manufacturing processes," *Proc. SFF Symp. Austin, TX*, vol. 1, no. 9, pp. 655–665, 2013.

[158] F. Verhaeghe, T. Craeghs, J. Heulens, and L. Pandelaers, "A pragmatic model for selective laser melting with evaporation," *Acta Mater.*, vol. 57, no. 20, pp. 6006–6012, 2009.

[159] S. A. Khairallah and A. Anderson, "Mesoscopic simulation model of selective laser melting of stainless steel powder," *J. Mater. Process. Technol.*, vol. 214, no. 11, pp. 2627–2636, 2014.

[160] Research Methodology.net, "Regression Analysis." [Online]. Available: https://research-methodology.net/research-methods/quantitative-research/regression-analysis/.

[161] “Minitab 17 Statistical Software, Minitab, Inc.” Minitab, Inc., State College, PA, 2016.

[162] Y. Bai, G. Wagner, and C. B. Williams, “Effect of bimodal powder mixture on powder packing density and sintered density in binder jetting of metals,” *2015 Annu. Int. Solid Free. Fabr. Symp.*, p. 62, 2015.

[163] E. O. Olakanmi, “Selective laser sintering/melting (SLS/SLM) of pure Al, Al-Mg, and Al-Si powders: effect of processing conditions and powder properties,” *J. Mater. Process. Technol.*, vol. 213, no. 8, pp. 1387–1405, 2013.

[164] A. Ladewig, G. Schlick, M. Fisser, V. Schulze, and U. Glatzel, “Influence of the shielding gas flow on the removal of process by-products in the selective laser melting process,” *Addit. Manuf.*, vol. 10, pp. 1–9, 2016.

[165] J. Whiting and J. Fox, “Characterization of feedstock in the powder bed fusion process: sources of variationin particle size distribution and the factors that influence them,” *Solid Free. Fabr. 2016*, vol. Proceeding, pp. 1057–1068, 2016.

[166] J. A. Slotwinski, E. J. Garboczi, P. E. Stutzman, C. F. Ferraris, S. S. Watson, and M. A. Peltz, “Characterization of metal powders used for additive manufacturing,” *J. Res. Natl. Inst. Stand. Technol.*, vol. 119, pp. 460–493, 2014.

[167] E. B. Herbold, O. Walton, and M. A. Homel, “Simulation of powder layer deposition in additive manufacturing processes using the discrete element method,” *Llnl-Tr-678550*, 2015.

[168] A. N. D. Gasper, B. Szost, X. Wang, D. Johns, S. Sharma, A. T. Clare, and I. A. Ashcroft, “Spatter and oxide formation in laser powder bed fusion of Inconel 718,” *Addit. Manuf.*, vol. 24, no. June, pp. 446–456, 2018.

[169] D. Wang, S. Wu, F. Fu, S. Mai, Y. Yang, Y. Liu, and C. Song, “Mechanisms and characteristics of spatter generation in SLM processing and its effect on the properties,” *Mater. Des.*, vol. 117, pp. 121–130, 2017.

[170] Renishaw, “Unlock your additive manufacturing possibilities with multi-laser productivity,” 2018.

[171] B. Ferrar, L. Mullen, E. Jones, R. Stamp, and C. J. Sutcliffe, “Gas flow effects on selective laser melting (SLM) manufacturing performance,” *J. Mater. Process. Technol.*, vol. 212, no. 2, pp. 355–364, 2012.

10. APPENDICES

A. MATLAB Code to Calculate the Relative Density from Micrographic Images

```
% MATLAB code was adapted from: Rabbani et al. [156]:
A. Rabbani, S. Jamshidi, S. Salehi, An automated simple
algorithm for realistic pore network extraction from micro-
tomography images, J. Pet. Sci. Eng. 123 (2014) 164-171.
doi:10.1016/j.petrol.2014.08.020.

clc;clear; close all;
% INPUTS
Input=imread('S3_AsPolished_Overview.JPG');
Resolution=1.28; % micron/pixel, (1000um/782pixel=1.28)
Number_of_categories=20;

% CALCULATIONS
FinalImage=im2bw(Input,graythresh(Input));
Conn=8; % number of connected neighbors
[s1,s2]=size(FinalImage);
FinalImage=bwmorph(FinalImage,'majority',20);
Porosity=sum(sum(~FinalImage))/(s1*s2);
D=-bwdist(FinalImage,'cityblock');
B=medfilt2(D,[3 3]);
B=watershed(B,Conn);
Pr=zeros(s1,s2);

for I=1:s1
    for J=1:s2
        if FinalImage(I,J)==0 && B(I,J)~=0
            Pr(I,J)=1;
        end
    end
end
Pr=bwareaopen(Pr,9,Conn);
[Pr_L,Pr_n]=bwlabel(Pr,Conn);
V=zeros(Pr_n,1);
for I=1:s1
    for J=1:s2
        if Pr_L(I,J)~=0
            V(Pr_L(I,J))=V(Pr_L(I,J))+1;
        end
    end
end
R=Resolution.*(V./pi).^.5; % Pore radius

%Outputs
MAX_pore_radius_micron=max(R);
MIN_pore_radius_micron=min(R);
Average_pore_radius_micron=mean(R);
```

```
Standard_deviation_of_pore_radius_micron=std(R);
Relative_Density=(1-Porosity)*100;

histogram(R,Number_of_categories);
xlabel('Pore Radius (µm)','FontSize',20);
ylabel('Frequency','FontSize',20);
set(gca,'fontsize',20);
```

B. Process Parameters and the Resultant RD for the Builds that were Used to Study the Effect of Changing PSD and LT

B.1. Ti-6Al-4V ELI

The tables in the following subsections show the process parameters, scan speed (SS), volumetric energy density (VED) and the resultant relative density (RD) for the builds that were used to study the effect of changing PSD and LT for Ti-6Al-4V ELI.

B.1.1. Powder Type 1 (T1)

Table B-1 to Table B-4 are for the Layer Thickness (LT) of 30, 60, 80, and 100µm respectively.

Table B-1: Process parameters and the resultant RD for the builds that were used to study the effect of changing PSD and LT for T1 and LT of 30µm for the material Ti-6Al-4V ELI

Run#	*LT (mm)*	*LP (W)*	*PD (mm)*	*ET (s)*	*HD (mm)*	*SS (mm/s)*	*VED (J/mm^3)*	*RD (%)*
1	0.03	200	0.05	0.00002	0.065	1666.67	61.54	93.51
2	0.03	200	0.05	0.00003	0.065	1250.00	82.05	99.40
3	0.03	200	0.05	0.00004	0.065	1000.00	102.56	99.46
4	0.03	200	0.05	0.00005	0.065	833.33	123.08	99.50
5	0.03	200	0.05	0.00006	0.065	714.29	143.59	99.65
6	0.03	200	0.05	0.00007	0.065	625.00	164.10	99.59
7	0.03	200	0.05	0.00008	0.065	555.56	184.62	99.60
8	0.03	200	0.05	0.00009	0.065	500.00	205.13	99.56
9	0.03	200	0.05	0.0001	0.065	454.55	225.64	99.55
10	0.03	200	0.05	0.00011	0.065	416.67	246.15	99.19
11	0.03	200	0.05	0.00012	0.065	384.62	266.67	99.34

Table B-2: Process parameters and the resultant RD for the builds that were used to study the effect of changing PSD and LT for T1 and LT of 60µm for the material Ti-6Al-4V ELI

Run#	*LT (mm)*	*LP (W)*	*PD (mm)*	*ET (s)*	*HD (mm)*	*SS (mm/s)*	*VED (J/mm^3)*	*RD (%)*
1	0.06	200	0.05	0.00004	0.065	1000.00	51.28	97.54
2	0.06	200	0.05	0.00005	0.065	833.33	61.54	99.36
3	0.06	200	0.05	0.00006	0.065	714.29	71.79	99.32
4	0.06	200	0.05	0.00007	0.065	625.00	82.05	99.43
5	0.06	200	0.05	0.00008	0.065	555.56	92.31	99.45
6	0.06	200	0.05	0.00009	0.065	500.00	102.56	99.50
7	0.06	200	0.05	0.0001	0.065	454.55	112.82	99.42
8	0.06	200	0.05	0.00011	0.065	416.67	123.08	99.44
9	0.06	200	0.05	0.00012	0.065	384.62	133.33	99.44
10	0.06	200	0.05	0.00013	0.065	357.14	143.59	99.27
11	0.06	200	0.05	0.00014	0.065	333.33	153.85	99.27
12	0.06	200	0.05	0.00015	0.065	312.50	164.10	98.79
13	0.06	200	0.05	0.00016	0.065	294.12	174.36	99.13
14	0.06	200	0.05	0.00017	0.065	277.78	184.62	99.26
15	0.06	200	0.05	0.00018	0.065	263.16	194.87	99.05
16	0.06	200	0.05	0.00019	0.065	250.00	205.13	99.31
17	0.06	200	0.05	0.0002	0.065	238.10	215.38	99.25
18	0.06	200	0.05	0.00021	0.065	227.27	225.64	99.33
19	0.06	200	0.05	0.00022	0.065	217.39	235.90	99.22
20	0.06	200	0.05	0.00023	0.065	208.33	246.15	99.15
21	0.06	200	0.05	0.00024	0.065	200.00	256.41	99.10
22	0.06	200	0.05	0.00025	0.065	192.31	266.67	99.23

Table B-3: Process parameters and the resultant RD for the builds that were used to study the effect of changing PSD and LT for T1 and LT of 80µm for the material Ti-6Al-4V ELI

Run#	*LT (mm)*	*LP (W)*	*PD (mm)*	*ET (s)*	*HD (mm)*	*SS (mm/s)*	*VED (J/mm^3)*	*RD (%)*
1	0.08	200	0.05	0.00006	0.065	714.29	53.85	98.93
2	0.08	200	0.05	0.00007	0.065	625.00	61.54	99.02
3	0.08	200	0.05	0.00008	0.065	555.56	69.23	99.19
4	0.08	200	0.05	0.00009	0.065	500.00	76.92	99.42
5	0.08	200	0.05	0.0001	0.065	454.55	84.62	99.23
6	0.08	200	0.05	0.00011	0.065	416.67	92.31	99.20
7	0.08	200	0.05	0.00012	0.065	384.62	100.00	99.10
8	0.08	200	0.05	0.00013	0.065	357.14	107.69	98.90
9	0.08	200	0.05	0.00014	0.065	333.33	115.38	99.32
10	0.08	200	0.05	0.00015	0.065	312.50	123.08	99.41
11	0.08	200	0.05	0.00016	0.065	294.12	130.77	98.60
12	0.08	200	0.05	0.00017	0.065	277.78	138.46	98.24
13	0.08	200	0.05	0.00018	0.065	263.16	146.15	99.14
14	0.08	200	0.05	0.00019	0.065	250.00	153.85	98.96
15	0.08	200	0.05	0.0002	0.065	238.10	161.54	99.24
16	0.08	200	0.05	0.00021	0.065	227.27	169.23	99.30
17	0.08	200	0.05	0.00022	0.065	217.39	176.92	99.41
18	0.08	200	0.05	0.00023	0.065	208.33	184.62	99.39
19	0.08	200	0.05	0.00024	0.065	200.00	192.31	99.53
20	0.08	200	0.05	0.00025	0.065	192.31	200.00	98.68
21	0.08	200	0.05	0.00026	0.065	185.19	207.69	98.99
22	0.08	200	0.05	0.00027	0.065	178.57	215.38	99.34
23	0.08	200	0.05	0.00028	0.065	172.41	223.08	99.10
24	0.08	200	0.05	0.00029	0.065	166.67	230.77	99.48
25	0.08	200	0.05	0.0003	0.065	161.29	238.46	98.74
26	0.08	200	0.05	0.00031	0.065	156.25	246.15	99.36
27	0.08	200	0.05	0.00032	0.065	151.52	253.85	99.48
28	0.08	200	0.05	0.00033	0.065	147.06	261.54	99.38

Table B-4: Process parameters and the resultant RD for the builds that were used to study the effect of changing PSD and LT for T1 and LT of 100µm for the material Ti-6Al-4V ELI

Run#	*LT (mm)*	*LP (W)*	*PD (mm)*	*ET (s)*	*HD (mm)*	*SS (mm/s)*	*VED (J/mm^3)*	*RD (%)*
1	0.1	200	0.05	0.00007	0.065	625.00	49.23	98.54
2	0.1	200	0.05	0.00008	0.065	555.56	55.38	99.09
3	0.1	200	0.05	0.00009	0.065	500.00	61.54	99.31
4	0.1	200	0.05	0.0001	0.065	454.55	67.69	99.21
5	0.1	200	0.05	0.00011	0.065	416.67	73.85	99.33
6	0.1	200	0.05	0.00012	0.065	384.62	80.00	99.12
7	0.1	200	0.05	0.00013	0.065	357.14	86.15	99.22
8	0.1	200	0.05	0.00014	0.065	333.33	92.31	99.22
9	0.1	200	0.05	0.00015	0.065	312.50	98.46	99.06
10	0.1	200	0.05	0.00016	0.065	294.12	104.62	99.11
11	0.1	200	0.05	0.00017	0.065	277.78	110.77	98.47
12	0.1	200	0.05	0.00018	0.065	263.16	116.92	98.56
13	0.1	200	0.05	0.00019	0.065	250.00	123.08	98.74
14	0.1	200	0.05	0.0002	0.065	238.10	129.23	98.54
15	0.1	200	0.05	0.00021	0.065	227.27	135.38	99.13
16	0.1	200	0.05	0.00022	0.065	217.39	141.54	98.90
17	0.1	200	0.05	0.00023	0.065	208.33	147.69	99.12
18	0.1	200	0.05	0.00024	0.065	200.00	153.85	98.86
19	0.1	200	0.05	0.00025	0.065	192.31	160.00	98.81
20	0.1	200	0.05	0.00026	0.065	185.19	166.15	99.20
21	0.1	200	0.05	0.00027	0.065	178.57	172.31	99.20
22	0.1	200	0.05	0.00028	0.065	172.41	178.46	98.99
23	0.1	200	0.05	0.00029	0.065	166.67	184.62	99.22
24	0.1	200	0.05	0.0003	0.065	161.29	190.77	99.13
25	0.1	200	0.05	0.00031	0.065	156.25	196.92	99.11
26	0.1	200	0.05	0.00032	0.065	151.52	203.08	99.33
27	0.1	200	0.05	0.00033	0.065	147.06	209.23	99.14
28	0.1	200	0.05	0.00034	0.065	142.86	215.38	99.23
29	0.1	200	0.05	0.00035	0.065	138.89	221.54	99.48
30	0.1	200	0.05	0.00036	0.065	135.14	227.69	99.28
31	0.1	200	0.05	0.00037	0.065	131.58	233.85	99.19
32	0.1	200	0.05	0.00038	0.065	128.21	240.00	99.35
33	0.1	200	0.05	0.00039	0.065	125.00	246.15	99.11
34	0.1	200	0.05	0.0004	0.065	121.95	252.31	99.29
35	0.1	200	0.05	0.00041	0.065	119.05	258.46	99.28
36	0.1	200	0.05	0.00042	0.065	116.28	264.62	99.25

B.1.2. Powder Type 2 (T2)

Table B-5 to Table B-8 are for the Layer Thickness (LT) of 40, 60, 80, and 100µm respectively.

Table B-5: Process parameters and the resultant RD for the builds that were used to study the effect of changing PSD and LT for T2 and LT of 40µm for the material Ti-6Al-4V ELI

Run#	*LT (mm)*	*LP (W)*	*PD (mm)*	*ET (s)*	*HD (mm)*	*SS (mm/s)*	*VED (J/mm^3)*	*RD (%)*
1	0.04	200	0.05	0.00002	0.065	1666.67	46.15	94.27
2	0.04	200	0.05	0.00003	0.065	1250.00	61.54	93.86
3	0.04	200	0.05	0.00004	0.065	1000.00	76.92	95.51
4	0.04	200	0.05	0.00005	0.065	833.33	92.31	96.05
5	0.04	200	0.05	0.00006	0.065	714.29	107.69	96.78
6	0.04	200	0.05	0.00007	0.065	625.00	123.08	97.97
7	0.04	200	0.05	0.00008	0.065	555.56	138.46	99.31
8	0.04	200	0.05	0.00009	0.065	500.00	153.85	99.11
9	0.04	200	0.05	0.0001	0.065	454.55	169.23	99.45
10	0.04	200	0.05	0.00011	0.065	416.67	184.62	99.10
11	0.04	200	0.05	0.00012	0.065	384.62	200.00	99.52
12	0.04	200	0.05	0.00013	0.065	357.14	215.38	99.60
13	0.04	200	0.05	0.00014	0.065	333.33	230.77	98.93
14	0.04	200	0.05	0.00015	0.065	312.50	246.15	99.49
15	0.04	200	0.05	0.00016	0.065	294.12	261.54	99.34

Table B-6: Process parameters and the resultant RD for the builds that were used to study the effect of changing PSD and LT for T2 and LT of 60µm for the material Ti-6Al-4V ELI

Run#	*LT (mm)*	*LP (W)*	*PD (mm)*	*ET (s)*	*HD (mm)*	*SS (mm/s)*	*VED (J/mm^3)*	*RD (%)*
1	0.06	200	0.05	0.00004	0.065	1000.00	51.28	93.73
2	0.06	200	0.05	0.00005	0.065	833.33	61.54	96.46
3	0.06	200	0.05	0.00006	0.065	714.29	71.79	97.38
4	0.06	200	0.05	0.00007	0.065	625.00	82.05	98.45
5	0.06	200	0.05	0.00008	0.065	555.56	92.31	98.69
6	0.06	200	0.05	0.00009	0.065	500.00	102.56	99.18
7	0.06	200	0.05	0.0001	0.065	454.55	112.82	99.29
8	0.06	200	0.05	0.00011	0.065	416.67	123.08	99.10
9	0.06	200	0.05	0.00012	0.065	384.62	133.33	99.27
10	0.06	200	0.05	0.00013	0.065	357.14	143.59	99.26
11	0.06	200	0.05	0.00014	0.065	333.33	153.85	99.26
12	0.06	200	0.05	0.00015	0.065	312.50	164.10	99.21
13	0.06	200	0.05	0.00016	0.065	294.12	174.36	99.44
14	0.06	200	0.05	0.00017	0.065	277.78	184.62	99.19
15	0.06	200	0.05	0.00018	0.065	263.16	194.87	98.88
16	0.06	200	0.05	0.00019	0.065	250.00	205.13	99.00
17	0.06	200	0.05	0.0002	0.065	238.10	215.38	99.32
18	0.06	200	0.05	0.00021	0.065	227.27	225.64	99.25
19	0.06	200	0.05	0.00022	0.065	217.39	235.90	99.03
20	0.06	200	0.05	0.00023	0.065	208.33	246.15	99.17
21	0.06	200	0.05	0.00024	0.065	200.00	256.41	98.91
22	0.06	200	0.05	0.00025	0.065	192.31	266.67	98.94

Table B-7: Process parameters and the resultant RD for the builds that were used to study the effect of changing PSD and LT for T2 and LT of 80µm for the material Ti-6Al-4V ELI

Run#	*LT (mm)*	*LP (W)*	*PD (mm)*	*ET (s)*	*HD (mm)*	*SS (mm/s)*	*VED (J/mm^3)*	*RD (%)*
1	0.08	200	0.05	0.00006	0.065	714.29	53.85	98.37
2	0.08	200	0.05	0.00007	0.065	625.00	61.54	98.86
3	0.08	200	0.05	0.00008	0.065	555.56	69.23	98.96
4	0.08	200	0.05	0.00009	0.065	500.00	76.92	99.04
5	0.08	200	0.05	0.0001	0.065	454.55	84.62	99.12
6	0.08	200	0.05	0.00011	0.065	416.67	92.31	99.16
7	0.08	200	0.05	0.00012	0.065	384.62	100.00	99.04
8	0.08	200	0.05	0.00013	0.065	357.14	107.69	98.70
9	0.08	200	0.05	0.00014	0.065	333.33	115.38	99.04
10	0.08	200	0.05	0.00015	0.065	312.50	123.08	98.69
11	0.08	200	0.05	0.00016	0.065	294.12	130.77	98.53
12	0.08	200	0.05	0.00017	0.065	277.78	138.46	98.61
13	0.08	200	0.05	0.00018	0.065	263.16	146.15	98.05
14	0.08	200	0.05	0.00019	0.065	250.00	153.85	98.64
15	0.08	200	0.05	0.0002	0.065	238.10	161.54	99.07
16	0.08	200	0.05	0.00021	0.065	227.27	169.23	99.05
17	0.08	200	0.05	0.00022	0.065	217.39	176.92	99.08
18	0.08	200	0.05	0.00023	0.065	208.33	184.62	99.16
19	0.08	200	0.05	0.00024	0.065	200.00	192.31	98.44
20	0.08	200	0.05	0.00025	0.065	192.31	200.00	99.20
21	0.08	200	0.05	0.00026	0.065	185.19	207.69	99.11
22	0.08	200	0.05	0.00027	0.065	178.57	215.38	98.68
23	0.08	200	0.05	0.00028	0.065	172.41	223.08	98.93
24	0.08	200	0.05	0.00029	0.065	166.67	230.77	98.79
25	0.08	200	0.05	0.0003	0.065	161.29	238.46	98.59
26	0.08	200	0.05	0.00031	0.065	156.25	246.15	98.89
27	0.08	200	0.05	0.00032	0.065	151.52	253.85	99.14
28	0.08	200	0.05	0.00033	0.065	147.06	261.54	99.07

Table B-8: Process parameters and the resultant RD for the builds that were used to study the effect of changing PSD and LT for T2 and LT of 100µm for the material Ti-6Al-4V ELI

Run#	*LT (mm)*	*LP (W)*	*PD (mm)*	*ET (s)*	*HD (mm)*	*SS (mm/s)*	*VED (J/mm^3)*	*RD (%)*
1	0.1	200	0.05	0.00007	0.065	625.00	49.23	97.21
2	0.1	200	0.05	0.00008	0.065	555.56	55.38	98.19
3	0.1	200	0.05	0.00009	0.065	500.00	61.54	98.73
4	0.1	200	0.05	0.0001	0.065	454.55	67.69	98.77
5	0.1	200	0.05	0.00011	0.065	416.67	73.85	98.88
6	0.1	200	0.05	0.00012	0.065	384.62	80.00	98.90
7	0.1	200	0.05	0.00013	0.065	357.14	86.15	98.84
8	0.1	200	0.05	0.00014	0.065	333.33	92.31	98.97
9	0.1	200	0.05	0.00015	0.065	312.50	98.46	99.02
10	0.1	200	0.05	0.00016	0.065	294.12	104.62	98.91
11	0.1	200	0.05	0.00017	0.065	277.78	110.77	98.98
12	0.1	200	0.05	0.00018	0.065	263.16	116.92	98.84
13	0.1	200	0.05	0.00019	0.065	250.00	123.08	98.18
14	0.1	200	0.05	0.0002	0.065	238.10	129.23	98.59
15	0.1	200	0.05	0.00021	0.065	227.27	135.38	98.96
16	0.1	200	0.05	0.00022	0.065	217.39	141.54	99.01
17	0.1	200	0.05	0.00023	0.065	208.33	147.69	98.62
18	0.1	200	0.05	0.00024	0.065	200.00	153.85	98.78
19	0.1	200	0.05	0.00025	0.065	192.31	160.00	98.46
20	0.1	200	0.05	0.00026	0.065	185.19	166.15	98.88
21	0.1	200	0.05	0.00027	0.065	178.57	172.31	98.92
22	0.1	200	0.05	0.00028	0.065	172.41	178.46	98.77
23	0.1	200	0.05	0.00029	0.065	166.67	184.62	98.86
24	0.1	200	0.05	0.0003	0.065	161.29	190.77	99.05
25	0.1	200	0.05	0.00031	0.065	156.25	196.92	98.92
26	0.1	200	0.05	0.00032	0.065	151.52	203.08	99.02
27	0.1	200	0.05	0.00033	0.065	147.06	209.23	98.87
28	0.1	200	0.05	0.00034	0.065	142.86	215.38	99.09
29	0.1	200	0.05	0.00035	0.065	138.89	221.54	99.12
30	0.1	200	0.05	0.00036	0.065	135.14	227.69	98.87
31	0.1	200	0.05	0.00037	0.065	131.58	233.85	99.05
32	0.1	200	0.05	0.00038	0.065	128.21	240.00	99.18
33	0.1	200	0.05	0.00039	0.065	125.00	246.15	99.21
34	0.1	200	0.05	0.0004	0.065	121.95	252.31	99.26
35	0.1	200	0.05	0.00041	0.065	119.05	258.46	99.09
36	0.1	200	0.05	0.00042	0.065	116.28	264.62	99.13

B.1.3. Powder Type 3 (T3)

Table B-9 to Table B-11 are for the Layer Thickness (LT) of 60, 80, and 100µm respectively.

Table B-9: Process parameters and the resultant RD for the builds that were used to study the effect of changing PSD and LT for T3 and LT of 60µm for the material Ti-6Al-4V ELI

Run#	*LT (mm)*	*LP (W)*	*PD (mm)*	*ET (s)*	*HD (mm)*	*SS (mm/s)*	*VED (J/mm^3)*	*RD (%)*
1	0.06	200	0.05	0.00004	0.065	1000.00	51.28	93.72
2	0.06	200	0.05	0.00005	0.065	833.33	61.54	95.76
3	0.06	200	0.05	0.00006	0.065	714.29	71.79	97.34
4	0.06	200	0.05	0.00007	0.065	625.00	82.05	98.22
5	0.06	200	0.05	0.00008	0.065	555.56	92.31	98.49
6	0.06	200	0.05	0.00009	0.065	500.00	102.56	98.80
7	0.06	200	0.05	0.0001	0.065	454.55	112.82	98.92
8	0.06	200	0.05	0.00011	0.065	416.67	123.08	98.79
9	0.06	200	0.05	0.00012	0.065	384.62	133.33	98.93
10	0.06	200	0.05	0.00013	0.065	357.14	143.59	98.80
11	0.06	200	0.05	0.00014	0.065	333.33	153.85	98.94
12	0.06	200	0.05	0.00015	0.065	312.50	164.10	98.85
13	0.06	200	0.05	0.00016	0.065	294.12	174.36	98.96
14	0.06	200	0.05	0.00017	0.065	277.78	184.62	98.97
15	0.06	200	0.05	0.00018	0.065	263.16	194.87	98.77
16	0.06	200	0.05	0.00019	0.065	250.00	205.13	98.40
17	0.06	200	0.05	0.0002	0.065	238.10	215.38	98.46
18	0.06	200	0.05	0.00021	0.065	227.27	225.64	98.52
19	0.06	200	0.05	0.00022	0.065	217.39	235.90	98.69
20	0.06	200	0.05	0.00023	0.065	208.33	246.15	98.66
21	0.06	200	0.05	0.00024	0.065	200.00	256.41	98.96
22	0.06	200	0.05	0.00025	0.065	192.31	266.67	98.91

Table B-10: Process parameters and the resultant RD for the builds that were used to study the effect of changing PSD and LT for T3 and LT of 80µm for the material Ti-6Al-4V ELI

Run#	*LT (mm)*	*LP (W)*	*PD (mm)*	*ET (s)*	*HD (mm)*	*SS (mm/s)*	*VED (J/mm^3)*	*RD (%)*
1	0.08	200	0.05	0.00006	0.065	714.29	53.85	95.15
2	0.08	200	0.05	0.00007	0.065	625.00	61.54	97.30
3	0.08	200	0.05	0.00008	0.065	555.56	69.23	97.70
4	0.08	200	0.05	0.00009	0.065	500.00	76.92	98.63
5	0.08	200	0.05	0.0001	0.065	454.55	84.62	98.57
6	0.08	200	0.05	0.00011	0.065	416.67	92.31	98.73
7	0.08	200	0.05	0.00012	0.065	384.62	100.00	98.68
8	0.08	200	0.05	0.00013	0.065	357.14	107.69	98.81
9	0.08	200	0.05	0.00014	0.065	333.33	115.38	98.58
10	0.08	200	0.05	0.00015	0.065	312.50	123.08	98.49
11	0.08	200	0.05	0.00016	0.065	294.12	130.77	98.52
12	0.08	200	0.05	0.00017	0.065	277.78	138.46	98.78
13	0.08	200	0.05	0.00018	0.065	263.16	146.15	98.56
14	0.08	200	0.05	0.00019	0.065	250.00	153.85	98.62
15	0.08	200	0.05	0.0002	0.065	238.10	161.54	98.91
16	0.08	200	0.05	0.00021	0.065	227.27	169.23	98.85
17	0.08	200	0.05	0.00022	0.065	217.39	176.92	99.00
18	0.08	200	0.05	0.00023	0.065	208.33	184.62	99.03
19	0.08	200	0.05	0.00024	0.065	200.00	192.31	98.75
20	0.08	200	0.05	0.00025	0.065	192.31	200.00	98.39
21	0.08	200	0.05	0.00026	0.065	185.19	207.69	98.65
22	0.08	200	0.05	0.00027	0.065	178.57	215.38	99.01
23	0.08	200	0.05	0.00028	0.065	172.41	223.08	98.84
24	0.08	200	0.05	0.00029	0.065	166.67	230.77	98.73
25	0.08	200	0.05	0.0003	0.065	161.29	238.46	98.86
26	0.08	200	0.05	0.00031	0.065	156.25	246.15	98.90
27	0.08	200	0.05	0.00032	0.065	151.52	253.85	99.14
28	0.08	200	0.05	0.00033	0.065	147.06	261.54	98.86

Table B-11: Process parameters and the resultant RD for the builds that were used to study the effect of changing PSD and LT for T3 and LT of 100µm for the material Ti-6Al-4V ELI

Run#	*LT (mm)*	*LP (W)*	*PD (mm)*	*ET (s)*	*HD (mm)*	*SS (mm/s)*	*VED (J/mm^3)*	*RD (%)*
1	0.1	200	0.05	0.00007	0.065	625.00	49.23	94.92
2	0.1	200	0.05	0.00008	0.065	555.56	55.38	96.10
3	0.1	200	0.05	0.00009	0.065	500.00	61.54	97.65
4	0.1	200	0.05	0.0001	0.065	454.55	67.69	96.83
5	0.1	200	0.05	0.00011	0.065	416.67	73.85	97.46
6	0.1	200	0.05	0.00012	0.065	384.62	80.00	98.30
7	0.1	200	0.05	0.00013	0.065	357.14	86.15	97.84
8	0.1	200	0.05	0.00014	0.065	333.33	92.31	98.56
9	0.1	200	0.05	0.00015	0.065	312.50	98.46	98.37
10	0.1	200	0.05	0.00016	0.065	294.12	104.62	98.57
11	0.1	200	0.05	0.00017	0.065	277.78	110.77	98.42
12	0.1	200	0.05	0.00018	0.065	263.16	116.92	98.30
13	0.1	200	0.05	0.00019	0.065	250.00	123.08	97.50
14	0.1	200	0.05	0.0002	0.065	238.10	129.23	97.82
15	0.1	200	0.05	0.00021	0.065	227.27	135.38	98.11
16	0.1	200	0.05	0.00022	0.065	217.39	141.54	98.37
17	0.1	200	0.05	0.00023	0.065	208.33	147.69	97.95
18	0.1	200	0.05	0.00024	0.065	200.00	153.85	98.62
19	0.1	200	0.05	0.00025	0.065	192.31	160.00	98.20
20	0.1	200	0.05	0.00026	0.065	185.19	166.15	98.47
21	0.1	200	0.05	0.00027	0.065	178.57	172.31	98.47
22	0.1	200	0.05	0.00028	0.065	172.41	178.46	98.56
23	0.1	200	0.05	0.00029	0.065	166.67	184.62	98.53
24	0.1	200	0.05	0.0003	0.065	161.29	190.77	98.57
25	0.1	200	0.05	0.00031	0.065	156.25	196.92	98.44
26	0.1	200	0.05	0.00032	0.065	151.52	203.08	98.59
27	0.1	200	0.05	0.00033	0.065	147.06	209.23	98.53
28	0.1	200	0.05	0.00034	0.065	142.86	215.38	98.70
29	0.1	200	0.05	0.00035	0.065	138.89	221.54	98.63
30	0.1	200	0.05	0.00036	0.065	135.14	227.69	98.48
31	0.1	200	0.05	0.00037	0.065	131.58	233.85	98.71
32	0.1	200	0.05	0.00038	0.065	128.21	240.00	98.96
33	0.1	200	0.05	0.00039	0.065	125.00	246.15	98.57
34	0.1	200	0.05	0.0004	0.065	121.95	252.31	98.73
35	0.1	200	0.05	0.00041	0.065	119.05	258.46	98.82
36	0.1	200	0.05	0.00042	0.065	116.28	264.62	98.72

B.2. 316L-SS

The tables in the following subsections show the process parameters, scan speed (SS), volumetric energy density (VED) and the resultant relative density (RD) for the builds that were used to study the effect of changing PSD and LT for 316L-SS.

B.2.1. Powder Type 1 (S1)

Table B-12 to Table B-15 are for the Layer Thickness (LT) of 30, 60, 80, and 100µm respectively.

Table B-12: Process parameters and the resultant RD for the builds that were used to study the effect of changing PSD and LT for S1 and LT of 30µm for the material 316l-SS

Run#	*LT (mm)*	*LP (W)*	*PD (mm)*	*ET (s)*	*HD (mm)*	*SS (mm/s)*	*VED (J/mm^3)*	*RD (%)*
1	0.03	200	0.07	0.00004	0.12	1296.30	42.86	92.76
2	0.03	200	0.07	0.00005	0.12	1093.75	50.79	95.13
3	0.03	200	0.07	0.00006	0.12	945.95	58.73	97.46
4	0.03	200	0.07	0.00007	0.12	833.33	66.67	98.67
5	0.03	200	0.07	0.00008	0.12	744.68	74.60	98.71
6	0.03	200	0.07	0.00009	0.12	673.08	82.54	99.10
7	0.03	200	0.07	0.0001	0.12	614.04	90.48	98.69
8	0.03	200	0.07	0.00011	0.12	564.52	98.41	99.07
9	0.03	200	0.07	0.00012	0.12	522.39	106.35	99.04
10	0.03	200	0.07	0.00013	0.12	486.11	114.29	99.11
11	0.03	200	0.07	0.00014	0.12	454.55	122.22	98.97

Table B-13: Process parameters and the resultant RD for the builds that were used to study the effect of changing PSD and LT for S1 and LT of 60µm for the material 316l-SS

Run#	*LT (mm)*	*LP (W)*	*PD (mm)*	*ET (s)*	*HD (mm)*	*SS (mm/s)*	*VED (J/mm^3)*	*RD (%)*
1	0.06	200	0.07	0.00009	0.12	673.08	41.27	98.59
2	0.06	200	0.07	0.0001	0.12	614.04	45.24	98.85
3	0.06	200	0.07	0.00011	0.12	564.52	49.21	99.03
4	0.06	200	0.07	0.00012	0.12	522.39	53.17	98.95
5	0.06	200	0.07	0.00013	0.12	486.11	57.14	98.66
6	0.06	200	0.07	0.00014	0.12	454.55	61.11	98.81
7	0.06	200	0.07	0.00015	0.12	426.83	65.08	98.57
8	0.06	200	0.07	0.00016	0.12	402.30	69.05	98.41
9	0.06	200	0.07	0.00017	0.12	380.43	73.02	97.99
10	0.06	200	0.07	0.00018	0.12	360.82	76.98	97.80
11	0.06	200	0.07	0.00019	0.12	343.14	80.95	97.68
12	0.06	200	0.07	0.0002	0.12	327.10	84.92	98.04
13	0.06	200	0.07	0.00021	0.12	312.50	88.89	97.30
14	0.06	200	0.07	0.00022	0.12	299.15	92.86	96.98
15	0.06	200	0.07	0.00023	0.12	286.89	96.83	96.87
16	0.06	200	0.07	0.00024	0.12	275.59	100.79	96.60

Table B-14: Process parameters and the resultant RD for the builds that were used to study the effect of changing PSD and LT for S1 and LT of 80µm for the material 316l-SS

Run#	*LT (mm)*	*LP (W)*	*PD (mm)*	*ET (s)*	*HD (mm)*	*SS (mm/s)*	*VED (J/mm^3)*	*RD (%)*
1	0.08	200	0.07	0.00013	0.12	486.11	42.86	98.52
2	0.08	200	0.07	0.00014	0.12	454.55	45.83	98.74
3	0.08	200	0.07	0.00015	0.12	426.83	48.81	98.40
4	0.08	200	0.07	0.00016	0.12	402.30	51.79	98.47
5	0.08	200	0.07	0.00017	0.12	380.43	54.76	97.85
6	0.08	200	0.07	0.00018	0.12	360.82	57.74	97.60
7	0.08	200	0.07	0.00019	0.12	343.14	60.71	97.34
8	0.08	200	0.07	0.0002	0.12	327.10	63.69	97.21
9	0.08	200	0.07	0.00021	0.12	312.50	66.67	96.89
10	0.08	200	0.07	0.00022	0.12	299.15	69.64	96.79
11	0.08	200	0.07	0.00023	0.12	286.89	72.62	97.39
12	0.08	200	0.07	0.00024	0.12	275.59	75.60	96.77
13	0.08	200	0.07	0.00025	0.12	265.15	78.57	97.03
14	0.08	200	0.07	0.00026	0.12	255.47	81.55	96.29
15	0.08	200	0.07	0.00027	0.12	246.48	84.52	96.37
16	0.08	200	0.07	0.00028	0.12	238.10	87.50	96.41
17	0.08	200	0.07	0.00029	0.12	230.26	90.48	95.92
18	0.08	200	0.07	0.0003	0.12	222.93	93.45	95.22
19	0.08	200	0.07	0.00031	0.12	216.05	96.43	96.26
20	0.08	200	0.07	0.00032	0.12	209.58	99.40	94.98
21	0.08	200	0.07	0.00033	0.12	203.49	102.38	95.36

Table B-15: Process parameters and the resultant RD for the builds that were used to study the effect of changing PSD and LT for S1 and LT of 100µm for the material 316l-SS

Run#	*LT (mm)*	*LP (W)*	*PD (mm)*	*ET (s)*	*HD (mm)*	*SS (mm/s)*	*VED (J/mm^3)*	*RD (%)*
1	0.1	200	0.07	0.00016	0.12	402.30	41.43	97.28
2	0.1	200	0.07	0.00017	0.12	380.43	43.81	96.62
3	0.1	200	0.07	0.00018	0.12	360.82	46.19	96.53
4	0.1	200	0.07	0.00019	0.12	343.14	48.57	96.25
5	0.1	200	0.07	0.0002	0.12	327.10	50.95	96.05
6	0.1	200	0.07	0.00021	0.12	312.50	53.33	95.84
7	0.1	200	0.07	0.00022	0.12	299.15	55.71	95.43
8	0.1	200	0.07	0.00023	0.12	286.89	58.10	95.05
9	0.1	200	0.07	0.00024	0.12	275.59	60.48	95.07
10	0.1	200	0.07	0.00025	0.12	265.15	62.86	95.34
11	0.1	200	0.07	0.00026	0.12	255.47	65.24	94.96
12	0.1	200	0.07	0.00027	0.12	246.48	67.62	94.69
13	0.1	200	0.07	0.00028	0.12	238.10	70.00	94.49
14	0.1	200	0.07	0.00029	0.12	230.26	72.38	94.63
15	0.1	200	0.07	0.0003	0.12	222.93	74.76	93.99
16	0.1	200	0.07	0.00031	0.12	216.05	77.14	94.49
17	0.1	200	0.07	0.00032	0.12	209.58	79.52	94.43
18	0.1	200	0.07	0.00033	0.12	203.49	81.90	95.66
19	0.1	200	0.07	0.00034	0.12	197.74	84.29	94.22
20	0.1	200	0.07	0.00035	0.12	192.31	86.67	94.72
21	0.1	200	0.07	0.00036	0.12	187.17	89.05	94.67
22	0.1	200	0.07	0.00037	0.12	182.29	91.43	94.78
23	0.1	200	0.07	0.00038	0.12	177.66	93.81	94.58
24	0.1	200	0.07	0.00039	0.12	173.27	96.19	94.87
25	0.1	200	0.07	0.0004	0.12	169.08	98.57	94.87
26	0.1	200	0.07	0.00041	0.12	165.09	100.95	94.26
27	0.1	200	0.07	0.00042	0.12	161.29	103.33	94.76

B.2.2. Powder Type 2 (S2)

Table B-16 to Table B-19 are for the Layer Thickness (LT) of 40, 60, 80, and 100µm respectively.

Table B-16: Process parameters and the resultant RD for the builds that were used to study the effect of changing PSD and LT for S2 and LT of 40µm for the material 316l-SS

Run#	*LT (mm)*	*LP (W)*	*PD (mm)*	*ET (s)*	*HD (mm)*	*SS (mm/s)*	*VED (J/mm^3)*	*RD (%)*
1	0.04	200	0.07	0.00005	0.12	1093.75	38.10	91.76
2	0.04	200	0.07	0.00006	0.12	945.95	44.05	94.82
3	0.04	200	0.07	0.00007	0.12	833.33	50.00	97.17
4	0.04	200	0.07	0.00008	0.12	744.68	55.95	98.30
5	0.04	200	0.07	0.00009	0.12	673.08	61.90	98.84
6	0.04	200	0.07	0.0001	0.12	614.04	67.86	98.82
7	0.04	200	0.07	0.00011	0.12	564.52	73.81	98.83
8	0.04	200	0.07	0.00012	0.12	522.39	79.76	98.90
9	0.04	200	0.07	0.00013	0.12	486.11	85.71	98.67
10	0.04	200	0.07	0.00014	0.12	454.55	91.67	98.81
11	0.04	200	0.07	0.00015	0.12	426.83	97.62	98.51
12	0.04	200	0.07	0.00016	0.12	402.30	103.57	98.58

Table B-17: Process parameters and the resultant RD for the builds that were used to study the effect of changing PSD and LT for S2 and LT of 60µm for the material 316l-SS

Run#	*LT (mm)*	*LP (W)*	*PD (mm)*	*ET (s)*	*HD (mm)*	*SS (mm/s)*	*VED (J/mm^3)*	*RD (%)*
1	0.06	200	0.07	0.00009	0.12	673.08	41.27	98.00
2	0.06	200	0.07	0.0001	0.12	614.04	45.24	98.48
3	0.06	200	0.07	0.00011	0.12	564.52	49.21	98.60
4	0.06	200	0.07	0.00012	0.12	522.39	53.17	98.73
5	0.06	200	0.07	0.00013	0.12	486.11	57.14	98.46
6	0.06	200	0.07	0.00014	0.12	454.55	61.11	98.17
7	0.06	200	0.07	0.00015	0.12	426.83	65.08	97.84
8	0.06	200	0.07	0.00016	0.12	402.30	69.05	97.70
9	0.06	200	0.07	0.00017	0.12	380.43	73.02	97.34
10	0.06	200	0.07	0.00018	0.12	360.82	76.98	97.12
11	0.06	200	0.07	0.00019	0.12	343.14	80.95	96.65
12	0.06	200	0.07	0.0002	0.12	327.10	84.92	96.58
13	0.06	200	0.07	0.00021	0.12	312.50	88.89	96.40
14	0.06	200	0.07	0.00022	0.12	299.15	92.86	95.82
15	0.06	200	0.07	0.00023	0.12	286.89	96.83	95.65
16	0.06	200	0.07	0.00024	0.12	275.59	100.79	95.52

Table B-18: Process parameters and the resultant RD for the builds that were used to study the effect of changing PSD and LT for S2 and LT of 80µm for the material 316l-SS

Run#	*LT (mm)*	*LP (W)*	*PD (mm)*	*ET (s)*	*HD (mm)*	*SS (mm/s)*	*VED (J/mm^3)*	*RD (%)*
1	0.08	200	0.07	0.00013	0.12	486.11	42.86	98.05
2	0.08	200	0.07	0.00014	0.12	454.55	45.83	97.93
3	0.08	200	0.07	0.00015	0.12	426.83	48.81	97.69
4	0.08	200	0.07	0.00016	0.12	402.30	51.79	97.62
5	0.08	200	0.07	0.00017	0.12	380.43	54.76	97.10
6	0.08	200	0.07	0.00018	0.12	360.82	57.74	96.62
7	0.08	200	0.07	0.00019	0.12	343.14	60.71	96.51
8	0.08	200	0.07	0.0002	0.12	327.10	63.69	95.70
9	0.08	200	0.07	0.00021	0.12	312.50	66.67	95.27
10	0.08	200	0.07	0.00022	0.12	299.15	69.64	95.39
11	0.08	200	0.07	0.00023	0.12	286.89	72.62	95.00
12	0.08	200	0.07	0.00024	0.12	275.59	75.60	95.10
13	0.08	200	0.07	0.00025	0.12	265.15	78.57	94.49
14	0.08	200	0.07	0.00026	0.12	255.47	81.55	94.51
15	0.08	200	0.07	0.00027	0.12	246.48	84.52	94.40
16	0.08	200	0.07	0.00028	0.12	238.10	87.50	94.69
17	0.08	200	0.07	0.00029	0.12	230.26	90.48	94.70
18	0.08	200	0.07	0.0003	0.12	222.93	93.45	94.09
19	0.08	200	0.07	0.00031	0.12	216.05	96.43	94.40
20	0.08	200	0.07	0.00032	0.12	209.58	99.40	93.96
21	0.08	200	0.07	0.00033	0.12	203.49	102.38	94.24

Table B-19: Process parameters and the resultant RD for the builds that were used to study the effect of changing PSD and LT for S2 and LT of 100µm for the material 316l-SS

Run#	*LT (mm)*	*LP (W)*	*PD (mm)*	*ET (s)*	*HD (mm)*	*SS (mm/s)*	*VED (J/mm^3)*	*RD (%)*
1	0.1	200	0.07	0.00016	0.12	402.30	41.43	96.03
2	0.1	200	0.07	0.00017	0.12	380.43	43.81	95.57
3	0.1	200	0.07	0.00018	0.12	360.82	46.19	95.38
4	0.1	200	0.07	0.00019	0.12	343.14	48.57	95.41
5	0.1	200	0.07	0.0002	0.12	327.10	50.95	94.68
6	0.1	200	0.07	0.00021	0.12	312.50	53.33	94.55
7	0.1	200	0.07	0.00022	0.12	299.15	55.71	93.89
8	0.1	200	0.07	0.00023	0.12	286.89	58.10	94.07
9	0.1	200	0.07	0.00024	0.12	275.59	60.48	94.13
10	0.1	200	0.07	0.00025	0.12	265.15	62.86	94.01
11	0.1	200	0.07	0.00026	0.12	255.47	65.24	93.67
12	0.1	200	0.07	0.00027	0.12	246.48	67.62	94.01
13	0.1	200	0.07	0.00028	0.12	238.10	70.00	93.78
14	0.1	200	0.07	0.00029	0.12	230.26	72.38	93.78
15	0.1	200	0.07	0.0003	0.12	222.93	74.76	93.16
16	0.1	200	0.07	0.00031	0.12	216.05	77.14	93.07
17	0.1	200	0.07	0.00032	0.12	209.58	79.52	93.78
18	0.1	200	0.07	0.00033	0.12	203.49	81.90	94.08
19	0.1	200	0.07	0.00034	0.12	197.74	84.29	93.58
20	0.1	200	0.07	0.00035	0.12	192.31	86.67	94.18
21	0.1	200	0.07	0.00036	0.12	187.17	89.05	93.86
22	0.1	200	0.07	0.00037	0.12	182.29	91.43	93.72
23	0.1	200	0.07	0.00038	0.12	177.66	93.81	93.72
24	0.1	200	0.07	0.00039	0.12	173.27	96.19	93.85
25	0.1	200	0.07	0.0004	0.12	169.08	98.57	94.04
26	0.1	200	0.07	0.00041	0.12	165.09	100.95	92.95
27	0.1	200	0.07	0.00042	0.12	161.29	103.33	93.49

C. MATLAB Code to Generate a Colour Map that Represents the Optimum Location on the Build Platform

```
% 316L-SS -- 150 x 150
% The build platform is approximately 250x250mm^2. However, this
analysis is for the area of 150x150mm^2. So that, in a generated
figure, the x-axis and y-axis is range from 50(origin) to 200.
It means that the first and last 50mm of the build platform is
not included.


clc;clear; close all;

% After counting the number of smaples in location X and putting
them in
% groups: Red, Green and Blue, the percentage is calculated.
% c_ijk: Colour (Red, Green and Blue) percent in each location
on the build
% platform
c_ijk =
{[89;7;4],[71;21;8],[9;11;80];[95;5;0],[60;19;21],[24;24;52];[76
;22;2],[62;25;13],[23;20;57]};

% RGB colour analysis. Red = 255 red, 0 Green and 0 Blue
w = [255 0 0; 0 255 0; 0 0 255];

% Get the colour wiehgt column from matrix W
col1=w(1:3,1);
col2=w(1:3,2);
col3=w(1:3,3);

for i = 1:3
   for j = 1:3
   % Get the matrix of colour percent for each loacation alone
to calculate
   % the weighted value of the colour at each location.
   c_ij=cell2mat(c_ijk(i,j));
    for k = 1:3
    w1=col1(k);
    w2=col2(k);
    w3=col3(k);
    total_w(k) = w1+(w2^2)+(w3^3);
    v_k(k)=c_ij(k)*total_w(k);
    end
    v(i,j)=sum(v_k);
   end
  end
```

```
% Now, the data is normalised to be between 0 and 100
% Normlised_v = ((v(ij)-min(v(:)))/(max(v(:))-min(v(:))))*100

for i = 1:3
   for j = 1:3
   c_ij=cell2mat(c_ijk(i,j));
   Norm_v(i,j)=100-(((v(i,j)-min(v(:)))/(max(v(:))-
min(v(:))))*100);
   % the normalised value = 100 - (...) to change the figure
colour.
   % the red colour for the worst location
   end
end

% Define the size of the matrix Norm_v
[n,m]= size(Norm_v);


% Minimum and maximum values of the plot
% This is useful for setting the limits of the colorbar
bottom = min(Norm_v(:));
top  = max(Norm_v(:));


%interpolation
[rows,columns] = meshgrid(1:m,1:n);
[rows_i,columns_i] = meshgrid(1:.1:m,1:.1:n);
c_i = interp2(rows,columns,Norm_v,rows_i,columns_i,'cubic');

% plot interpolated data
surf(rows_i, columns_i, c_i, 'edgecolor', 'none', 'facecolor',
'interp');
view(2);axis square
set(gca,'YDir','reverse');
colormap jet

% This sets the limits of the colorbar to manual for the second
plot
caxis manual
caxis([bottom top]);

colorbar
```